Investigating the Suitability of Locally Available Materials to Develop Low-Carbon Cementitious Materials for 3D Printing Applications

By

Yazeed Afet Adnan Al-Noaimat

Department of Civil and Environmental Engineering

College of Engineering, Design and Physical Sciences

Brunel University London

A thesis submitted for the degree of Doctor of Philosophy

January 2025

To

My Dad & Mom & Brother

Who have always been by my side and encouraged me

to follow my dreams,

especially this one

Abstract

The environmental impact of traditional OPC has driven the search for sustainable alternatives like alkali-activated materials, calcined clay blends, and recycled aggregates. This doctoral research explores low-carbon cementitious materials using locally sourced construction waste. The work is divided into two parts: developing one-part AAMs with end-of-life brick and LC3 using excavated London clay and recycled aggregates, suitable for cast and 3D-printed applications.

One-part AAMs provide significant environmental benefits due to the elimination of OPC, which can be a potentially suitable alternative to the traditional cement mixture. This part of the thesis investigates the feasibility of using locally available waste material, i.e. brick waste, as part of a one-part AAM binder as an alternative to fly ash (FA). The mortar binder is composed of 40% GGBS and 60% FA, activated using 12% solid sodium silicate to the weight of the binder. Hence, bricks in powder (BP) form were incorporated to replace FA with increments of 10% until full elimination of FA, and bricks in particle form were used to replace natural aggregates by 30%, 50% and 70%. It was demonstrated that BP-based AAMs achieved comparable mechanical performance to FA-based controls. Despite BP's higher crystallinity (70% vs. FA's 50%), pore refinement and accelerated geopolymerisation kinetics enabled the development of comparable strength. Moreover, BP-based AAM exhibited comparable water absorption, freeze-thaw resistivity, and around 65% higher resistivity to high temperature. Replacing natural aggregates with up to 70% brick aggregates (BA) in brick-based one-part AAM showed a maximum improvement of around 17% and 27% for the flexural and compressive strength performances, respectively, and showed better resistivity to freeze-thaw and high-temperature, while increasing the water absorption of the mixtures. Adding 0.1% nano graphite decreased the water absorption by 18%. On the other hand, incorporating BA improved the early-age strength and enhanced the mixtures' shape stability, improving their buildability compared to the mix with natural sand. Moreover, BA incorporation significantly enhanced the compressive strength of the 3D printed samples. From an environmental perspective, one-part geopolymer shows the potential as an alternative low-carbon concrete for conventional concrete, allowing the reduction of CO_2 emissions by around 40%. Moreover, the carbon footprint from replacing fly ash with brick powder or natural sand with brick aggregates did not show observable changes.

On the other hand, LC3 presents another promising low-carbon cementitious mixture that can reduce high amounts of OPC in the binder. This part of the thesis investigates the feasibility of using excavated London clay as calcined clay to develop a 3D printable LC3 mixture composed of 50% OPC, 30% calcined clay, 15% limestone and 5% gypsum. The results revealed the feasibility of using excavated low-grade London clay to develop LC3 mixture, having the highest strength performance when calcined at 800 °C in the LC3 system and showing good pozzolanic reactivity. Incorporating and optimising admixtures (i.e., 0.5, 1 and 1.5% superplasticiser ‘SP’ and 0.4, 0.6 and 0.8% of viscosity-modifying agent ‘VMA’) was compulsory to modify and adjust the fresh behaviour of the mixture to obtain a 3D printable dosage. Adding 1% SP significantly improved the mixture's strength performance, achieving around 44 MPa. Nevertheless, adding superplasticiser produced a too flowable fresh mixture. Incorporating 0.6% VMA was found to balance the workability of the mixture, producing a mixture with low slump, which is suitable for extrudability and buildability. On the other hand, incorporating BA to replace natural aggregates up to 100% in LC3 was found to be beneficial for both the engineering and printing properties of the mixtures. Replacing natural aggregates with BA fully significantly increased the compressive strength from around 34 MPa to 54 MPa. Moreover, the mixtures with BA showed a similar water absorption level with better freeze-thaw resistance while significantly improving the printed samples' mechanical strength. Incorporating BA could have served as a curing agent, allowing LC3 binder hydration to continue through absorbing part of the water from the mixture at the initial stage and releasing it during ageing. This reveals the potential of downcycling BA in LC3 mixtures to develop more sustainable mix formulation. Replacing 50% OPC with limestone-calcined clay and gypsum reduced carbon dioxide by around 40%, whereas replacing natural sand with BA did not show noticeable changes in the carbon footprint.

Overall, this research lays the foundations for the feasibility of using end-of-life brick and excavated London clay after recycling to develop low-carbon cementitious mixtures.

Acknowledgements

All praise and thanks are due to the Almighty Allah who always guides me to the right path and has helped me to complete this thesis.

I would like to extend my heartfelt gratitude to my supervisor, Dr. Seyed Ghaffar, whose unwavering guidance and support have been invaluable throughout this journey. His mentorship went beyond that of a supervisor, as he also served as a source of inspiration and motivation. Also, to thank him for the constructive advice and tips that help in successfully finishing this thesis.

I would like to express my sincere gratitude to Dr. Lee Hosking for his unwavering support throughout my PhD journey. I am especially thankful for the invaluable opportunities he provided, which enriched my experience and broadened my perspective.

I also extend my thanks to the academic staff of the Civil and Environmental Engineering Department for their support and critical discussions throughout the research. In particular: Dr Andrew Fox, Dr Abiy S Kebede, Dr Pedro Martin-Moreta, Dr kangkang Tang, and Prof Xianming zhou.

The technicians of the Civil Engineering Research Centre, Mr Charles Morrison, Mr Andrew Smith, and Dr Nirvan Razaghi-Kashani, are highly acknowledged for their support during the experimental work.

I would like to take this opportunity to thank Prof Bassam Z. Mahasneh, President of Tafila Technical University, for his support and advice to take the thesis in the material construction field.

I would also like to thank my friends and colleagues who have supported me throughout this long journey. Special thanks to Dr Mehdi Chougan for his continuous help and support throughout this PhD.

Finally, and uppermost, I am indebted to my beloved parents, Mr Afet Al-Noaimat and Mrs Roula Al-Kurdi, and my brother, Thamer, for their endless love and support. This work would not be possible without all of them. Also, I would like to extend my appreciation to Rand, who was always there for me during this journey.

TABLE OF CONTENTS

List of Figures

List of Tables

1. CHAPTER 1: INTRODUCTION

1.1. Overview/background

Concrete is the second most widely used material worldwide, made up of cement, fine and coarse aggregates, water and in some cases other admixtures. Concrete plays a foundational role in various structures, making it essential for meeting human needs and facilitating daily life. Its applications range from buildings, roadways, bridges, and highway infrastructures to airfields, tunnels, embankments, and many more. Cement is the main ingredient in concrete, which works as a binding agent to hold the aggregates together. The demand for concrete is increasing significantly with the increment of developmental construction activities, leading to increased demand for cement production and utilising natural aggregates.

Cement stands as the most substantial manufactured product on Earth on a mass basis. In 2022 alone, around 4.1 billion tonnes of Portland cement were produced globally. This figure is unlikely to decline in the near future due to the rapid population growth and urbanisation experienced in many developing countries, which would increase the demand for construction activities in general, and cement specifically. Portland cement has been providing exceptional performance so far. Nevertheless, its production process is a rising concern around the world. Ordinary Portland cement (OPC) production is an energy-intensive process and leads to significant emission of carbon dioxide (CO_2), with the production of one tonne of OPC emitting around 730–990 kg of CO_2 [1], accounting for around 8% of anthropogenic CO_2 emissions [2]. Moreover, the cement industry accounts for 7% of global industrial energy use, making it the largest industrial energy consumer [3]. Although OPC is a low-carbon material compared to other materials used in construction (See Figure 1.1), the massive amounts of OPC used yearly result in this huge environmental impact. This environmental impact associated with cement production can only be expected to increase since the demand for cement is increasing yearly.

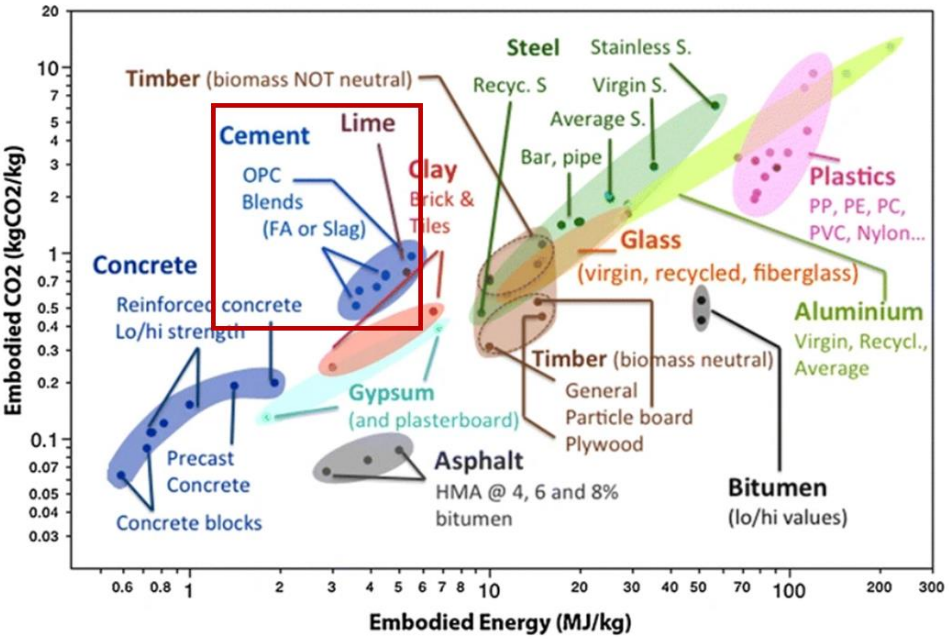

Figure 1.1. Carbon dioxide embodied and embodied energy for typical building materials [4].

There are different approaches to mitigate the environmental impacts of PC production. This includes advanced construction technologies (such as 3D printing technology) and the replacement of OPC with alternative materials to develop eco-friendly green cement. These approaches could mitigate carbon emissions and promote energy conservation. The inclusion of 3D printing technology into construction presents the beginning of the industrial revolution towards automating the construction industry. 3D concrete printing (3DCP) offers various benefits, which include reducing construction time, workforce, cost, and waste materials during the removal of formwork, and enhancing the freedom of architectural designs and the safety of conducted work compared with conventional construction approaches [5,6]. It also reduces the amount of waste from concrete leftovers since it provides the exact quantity of concrete needed to build a certain object. Nevertheless, as mentioned by Wangler et al. [7], 3D printable concrete requires a higher amount of OPC to meet the technology's rheological and engineering demands. In addition, a lower aggregate-to-binder ratio with the absence of coarse aggregates is used in 3D printable mixtures to prevent clogging or blocking the nozzle due to the limited dimension of the nozzle [8,9]. Consequently, neutralising what this technology offers from efficient mix design due to the need for a higher amount of OPC, which leads to emitting more CO_2 into the atmosphere, limiting the environmental and economic benefit of the technology [10], and restricting the utilisation of this technology in current practices. Hence, more sustainable and environmentally friendly binders should be developed to reach this technology's maximum efficiency and allow its construction usage.

In recent years, reducing or completely eliminating the OPC or clinker in a cementitious mixture was one of the most effective ways to reduce the CO_2 footprint associated with cement production. This has directed the industry towards utilising blended cement or cement-free concrete, also known as alkali-activated materials (AAMs), which started to be adopted in many countries more than ordinary OPC. Blended cement is produced by partially replacing OPC with suitable materials that have met certain criteria and characteristics. These materials are known as supplementary cementitious materials (SCMs). When used to replace PC partially, these materials support the properties of the resultant concrete through participating in the chemical reaction of cement as well as through acting as a filler, allowing the development of concrete with similar hardened performance and even better depending on the material used with PC [11,12]. Similarly, AAM is produced using these SCMs, with the difference of the need to chemically activate the binder materials since no cement is presented in the binder [13,14]. Typical materials used as SCMs to partially replace PC in cement-based concrete or as binders in AAM include fly ash (FA), silica fume (SF), and ground granulated blast furnace slag (GGBS) [15–17]. These common materials have been involved in developing sustainable low-carbon cementitious mixtures for cast and 3D printing construction methods [18,19]. Nevertheless, using these common SCMs as main binders may face obstacles in the long run due to their limited availability. SF and GGBS share the problem of limited production quantity [20,21]. While there are comparatively higher FA quantities than SF and GGBS, more than 66% of available FA is unsuitable for use as SCMs because of their low-quality [22]. Moreover, the availability of these SCMs is expected to decrease with the industrial transition towards decarbonisation and the development of cleaner technologies for energy production [23]. Thus, their long-term availability is questionable, and the need to find alternative SCMs of good quality is arising.

When considering developing low-carbon cementitious mixtures, some researchers considered adding additives and admixtures to the mix design for various reasons, such as modifying the workability of the mix by adding superplasticiser [24] or incorporating reinforcing agents like nanomaterials to improve the mixture properties [25]. It became a common practice when developing a mixture for a specific application to consider incorporating additives.

Alongside the massive environmental impacts of PC production for concrete manufacturing, there are high demands on sand for concrete production. Traditional concrete is composed of around 50 – 80% of natural aggregates [26]. Around 40.2 billion metric tonnes of natural aggregate were consumed globally in 2014 alone [27], with approximately 65 – 85% of the natural aggregates consisting of sand and gravel [28]. Due to the high demand and exploitation of sand, the construction industry and academia started seeking alternatives with lower associated costs to be used as aggregates in concrete.

Another serious rising problem in the construction sector is the waste materials generated from the various construction activities, such as excavation and end-of-life building demolition. These wastes are mostly disposed of through landfills, which is considered a costly and ecologically impactful process that consumes valuable land resources [29,30]. Some researchers considered recycling these wastes into particle physical form to be incorporated in cementitious mixtures as a substitute for natural aggregates [31,32]. However, the findings on their impact on cementitious mixture properties were contradictory, and many unanswered questions still need to be fulfilled. Hence, this research was initiated from the need to reduce the environmental impacts induced by the construction sector by developing environmentally friendly cementitious materials exhibiting similar performance to traditional concrete using waste materials.

1.2. Research significance and motivation

As human civilisation advances, the increasing global carbon emissions and energy consumption have become more severe. The construction industry alone accounts for up to 33% of global carbon emissions and 40% of global energy consumption [33]. Alongside the increased demand for OPC production, construction and demolition waste (CDW) amounts are gradually increasing. Around 45% of CDWs, excluding soils, are brick and ceramic wastes [34–36]. Moreover, excavated materials from infrastructure and tunnelling projects are another rising concern [37]. Landfilling these materials is a costly and ecologically detrimental practice that consumes precious land resources [29,30,38,39]. When taking a closer look into the composition of some of these materials, such as brick or clay from excavation projects, their chemical composition suggests their suitability as SCMs, which allow them to participate in concrete reactions, whether when used to replace OPC partially or as a part of a chemically activated AAM binder. Thus, using these wastes as part of the binder presents a suitable approach not only to help mitigate the amount of waste being landfilled but also to limit the carbon footprint associated with OPC production. Nevertheless, studies on construction wastes as binders are still limited. A suitable approach that has been the focus of attention lately is combining the use of innovative construction technologies and green cement-based materials. That could promote energy conservation and reduce carbon emissions [40]. 3D printing concrete is considered a cleaner and more sustainable construction approach, with less waste generation and more efficient production than traditional techniques.

Aside from that, sand is the most extracted material worldwide, estimated to surpass 40 Gt globally [41]. As the demand for concrete rises progressively, sand will eventually be depleted as it is a non-renewable resource. The growing demand for sand exceeded the limits, resulting in ecological deterioration and environmental contamination due to the major geomorphological alteration in sand regions. Hence, it is imperative to employ alternative materials in concrete production to mitigate the over-exploitation of natural sand.

Therefore, the motivation for this work comes from the need to investigate available materials from construction wastes that could present suitable alternatives to common SCMs to mitigate the CO_2 emissions from OPC production and overcome landfilling issues through utilising solid waste streams generated from different construction activities. Also, finding an alternative material to be used as aggregates in cementitious mixtures to mitigate the rising concern of sand depletion and environmental degradation is another driving force of this research. Hence, this work was designed in a way to develop a better understanding of the feasibility of upcycling construction wastes as binder materials and downcycling them to be used as aggregates in the same cementitious mixtures. This project also focuses on understanding the suitability of the developed low-carbon materials for the use in 3D concrete printing technology. It is contemplated that the success of this research would result in the development of two novel sustainable low-carbon cementitious materials for 3D printing applications, containing recycled materials as binder and aggregates, exhibiting similar performance and properties to the traditional cementitious materials. The available studies on brick waste mainly focused on its mechanical performance and workability in AAM. Similarly, studies on excavated London clay were more oriented towards optimising calcination temperature and investigating its mechanical strength behaviour in blended cement or LC3. This is not sufficient to understand their suitability to be used as building materials or as 3D printable feedstock for producing structural elements. Hence, it is crucial to evaluate the different engineering and 3D printing properties, and understand the material science of these materials to provide a comprehensive understanding on the material behaviour in the developed mixtures and the mechanisms behind the mixture performance. Moreover, the combined effect of recycled binder and aggregates on the printing-related properties have not been studied before.

1.3. Research Aims and Objectives

This research aims to study the material science of two different waste materials, namely brick and London clay, and evaluate their effect on the development of two low-carbon environmentally friendly cementitious materials for cast and 3D printing methods. This will contribute to boosting the development of environmentally friendly cementitious materials and 3D concrete printing in the construction sector.

Based on the research aim, the following objectives are formulated:

1. Investigate the feasibility of valorising end-of-life brick in powder form to replace fly ash in a one-part AAM binder, and the suitability of using extra low-grade excavated London clay in calcined form in the LC3 system by investigating the workability, setting time, mechanical strength, and microstructure of the different mixtures.
2. Investigate the effect of undercycling end-of-life brick as aggregates to replace natural aggregates in one-part AAM and LC3 on the fresh, hardened and durability properties of the mixtures.
3. Examine the effect of brick aggregates on the printing properties of the developed low-carbon cementitious mixtures through investigating the open time, shape retention, mechanical strength of 3D printed mixtures and buildability measurement.

The objective of this work is illustrated schematically in Figure 1.2**.** A detailed explanation of the objectives of each chapter is explained in its introduction.

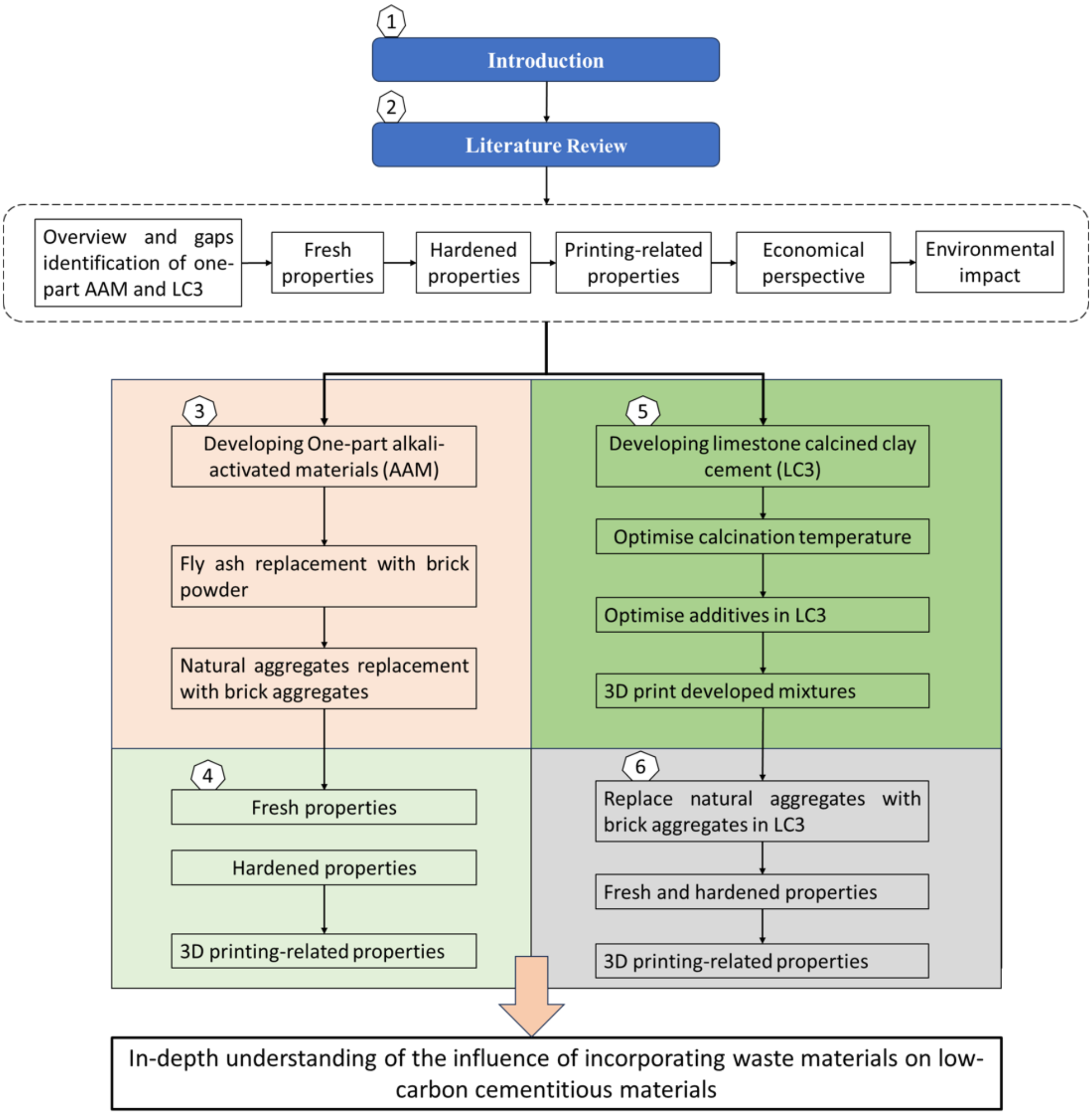

Figure 1.2. Schematic objective chart of the research (the numbers in the figure refer to chapter numbers).

1.4. Novel research contributions

This research contributes to the science through the development of two low-carbon cementitious materials with suitable properties for various construction industry applications. The following contributions were found based on the various materials used in this work:

1. Critical literature reviews highlighting the most widely used materials in one-part AAM and LC3 binders, the potential of using these systems in 3D printing technology, and the potential challenges and the research gaps in these research fields (refer to Chapter 2).

2. Unveiling the suitability of upcycling brick waste to replace fly ash in low-carbon one-part AAMs (refer to Chapter 4).
3. Revealing the feasibility of using excavated low-grad London clay in low-carbon LC3 (refer to Chapter 5).
4. In-depth investigation of the effect of incorporating waste aggregates on the different properties of low-carbon binder systems (i.e., one-part AAM and LC3) (refer to Chapters 4 & 5).
5. Providing a comprehensive understanding of the role of recycled brick aggregates as an internal curing agent to boost the properties development of LC3 mix design (refer to Chapter 5).
6. Optimising low-carbon one-part AAM and LC3 to be suitable for modern fabrication methods, specifically 3D printing (refer to Chapters 4 & 5).

1.5. Outline of thesis

This thesis consists of six chapters. The overview of the chapters is as outlined below:

Chapter 1: Introduction

This chapter provides general background on OPC production problems and the need for developing low-carbon cement. The research motivation alongside the aims and objectives of this project are explained.

Chapter 2: Literature Review

This chapter aims to compile a comprehensive database of the state-of-the-art of the existing work regarding the different existing 3D printable one-part AAM and LC3 mix formulations, with the limitations of the up-to-date conducted work being identified. To do so, this chapter is composed of two different sections. In the first section, a comprehensive review of the impact of the mix designs and ingredients on one-part AAM engineering properties is provided. Similarly, the influence of the different parameters of LC3 mix design on its performance is reviewed in the second section.

Chapter 3: Materials and Methodology

This chapter provides a detailed description of the different materials used throughout the study, as well as a detailed description of the common methodology procedures and analytical methods used in the various phases of this study. Moreover, sample preparation procedures and curing conditions are also included.

Chapter 4: Upcycling and downcycling end-of-life bricks into precursor and aggregates in high-performance one-part alkali-activated materials (AAMs)

This chapter presents a systematic experimental study on the impact of replacing fly ash with upcycled brick powder in a one-part AAM binder. Brick powder replaced fly ash with 10% increment until complete replacement. The study focuses on determining the optimal replacement level to develop AAM with similar properties to fly ash AAM. The developed mixture was selected to replace natural sand with brick aggregate by three ratios, namely 30, 50 and 70%. Then, a comprehensive investigation on the AAM mixtures was conducted. The impact of modifying developed mixtures with nano-materials is also investigated in this chapter. Notably, most studies focused on using brick powder in two-part AAM systems.

Chapter 5: Developing high-performance low-carbon LC3 mixture using excavated calcined London clay and brick aggregates.

This chapter explores the feasibility of using excavated low-grade London clay in calcined form in LC3. The impact of incorporating admixtures to modify the mix design to develop a high-performance mixture is examined and the printability of LC3 is also investigated. This chapter also studies the influence of replacing natural aggregates with brick aggregates on the fresh, hardened, durability and printing properties of LC3 systems.

1.6. Outcomes of this research

The findings of this research have been disseminated through the following scientific publications, book chapters and presentations:

Journal articles:

1) **Yazeed A. Al-Noaimat**, Seyed Hamidreza Ghaffar, Mehdi Chougan, Mazen J. Al-Kheetan, A review of 3D printing low-carbon concrete with one-part geopolymer: Engineering, environmental and economic feasibility, Case Studies in Construction Materials, Volume 18, 30 December 2022, e01818. https://doi.org/10.1016/j.cscm.2022.e01818
2) **Yazeed A. Al-Noaimat**, Mehdi Chougan, Mazen J. Al-kheetan, Othman Al-Mandhari, Waleed Al-Saidi, Marwan Al-Maqbali, Haitham Al-Hosni, Seyed Hamidreza Ghaffar, 3D printing of limestone-calcined clay cement: A review of its potential

implementation in the construction industry, Results in Engineering, Volume 18, 19 April 2023, 101115. https://doi.org/10.1016/j.rineng.2023.101115

3) **Yazeed A. Al-Noaimat**, Mehdi Chougan, Mazen J. Al-kheetan, Marcus H. N. Yio, Hong S. Wong, Seyed Hamidreza Ghaffar, Upcycling end-of-life bricks in high-performance one-part alkali-activated materials, Developments in the Built Environment, Volume 16, 14 September 2023, 100231. *https://doi.org/10.1016/j.dibe.2023.100231*
4) **Yazeed A. Al-Noaimat**, Mehdi Chougan, Abdulrahman Albar, Szymon Skibicki, Karol Federowicz, Marcin Hoffman, Daniel Sibera, Krzysztof, Cendrowski, Mateusz Techman, João Nuno Pacheco, Sang-Yeop Chung, Pawel Sikora, Mazen Al-Kheetan, Seyed Hamidreza Ghaffar, Recycled brick aggregates in one-part alkali-activated materials: Impact on 3D printing performance and material properties, Developments in the Built Environment, Volume 16, 12 October 2023, *100248. https://doi.org/10.1016/j.dibe.2023.100248*
5) **Yazeed A. Al-Noaimat**, Mehdi Chougan, Matteo Sambucci, Marco Valente, Jacopo Tirillò, Abdulrahman Albar, Behzad Nematollahi, Seyed Hamidreza Ghaffar, Optimising limestone calcined clay cement containing excavated low-grade waste clay for 3D printing applications, Magazine of Concrete Research – *Under review*.
6) **Al-Noaimat, Y. A.,** Chougan, M., El-Seidy, E., Albar, A., & Ghaffar, S. H. (2025). Valorising excavated low-grade waste clay in limestone calcined clay cement system for 3D printing applications. Journal of Building Engineering, 106, 112634. https://doi.org/10.1016/j.jobe.2025.112634
7) **Al-Noaimat, Y. A.,** Sambucci, M., Chougan, M., El-Seidy, E., Biblioteca, I., Valente, M., Tirillò, J, Al-kheetan, M. J., Ghaffar, S. H. (2025). Sustainable repurposing of polyvinyl chloride waste as aggregates in limestone-calcined clay cement. *Journal of Cleaner Production*, 144862.

Conference paper

1) **Al-Noaimat, Y.A**., Ghaffar, S.H., 2024. Exploring Low-Carbon Cementitious Materials for 3D Printing Applications: A Comparison Between Limestone Calcined Clay Cement (LC3) And One-Part Alkai-Activated Material (AAM). Digital Concrete 2024 - Supplementary Proceedings. https://doi.org/10.24355/dbbs.084-202408021120-0

Book chapter

1) Ghaffar, S. H., **Al-Noaimat, Y.**, Chougan, M., Al-Kheetan, M., & Mutah, J. (2024). Emerging resources for the development of low-carbon cementitious composites for. *Sustainable Concrete Materials and Structures*, 371.

2. CHAPTER 2: LITERATURE REVIEW

2.1. Introduction

This chapter presents a critical review is presented in this chapter concerning 3D printable one-part AAM and LC3 showcasing the work that has been accomplished on the development of one-part AAM and LC3 in terms of mix formulations, fresh properties, hardened properties, and 3D printing-related properties, to identify the research gaps within the field. In addition, the economical and environmental aspects of the mixtures were reviewed and discussed. It should be noted that this chapter has been presented peer-reviewed journal papers:

1) **Yazeed A. Al-Noaimat**, Seyed Hamidreza Ghaffar, Mehdi Chougan, Mazen J. Al-Kheetan. Case Studies in Construction Materials, Volume 18, 30 December 2022, e01818. https://doi.org/10.1016/j.cscm.2022.e01818
2) **Yazeed A. Al-Noaimat**, Mehdi Chougan, Mazen J. Al-kheetan, Othman Al-Mandhari, Waleed Al-Saidi, Marwan Al-Maqbali, Haitham Al-Hosni, Seyed Hamidreza Ghaffar. (2023). Results in Engineering, Volume 18, 19 April 2023, 101115. https://doi.org/10.1016/j.rineng.2023.101115

Part of the presented literature review chapter was also published as a part of a book chapter.

3) Ghaffar, S. H., **Al-Noaimat, Y.**, Chougan, M., Al-Kheetan, M., & Mutah, J. (2024). Emerging resources for the development of low-carbon cementitious composites for. *Sustainable Concrete Materials and Structures*, 371.

2.2. Challenges and problems concerning 3D concrete printing

The construction industry could experience an evolutionary development by implementing 3D printing technology. The first 3D printing application in the construction sector was in 1997 when various hollow concrete structures were produced [42]. The 3D printing process of concrete elements or components starts with their mix design, followed by their deposition through a pumping system and multi-dimensional movement of a robotic arm or a gantry system in sequential layers [43]. Despite the apparent ease of the printing procedures, this technology requires a printable concrete mixture that does not harden immediately after deposition to avoid cold joints. In order to facilitate pumping and extrusion, printable concrete mixes usually have low dynamic yield stress. However, after extrusion, the extruded mixture should exhibit high static yield stress to enable the concrete to support its own weight and the weight of the successive printed layers [44–47]. Hence, the most appropriate mix for the 3D printing method should be extruded smoothly and provide shape stability by holding the consequent layers' weight.

3D printing of concrete received significant interest in the past few years from industry practitioners and researchers due to its benefits in reducing construction time, workforce, cost, and waste materials during the removal of formwork [5,48]. Many researchers believe that 3D printing offers environmental benefits, cost reductions, and efficiency over conventional concrete structures [49,50]. However, using concrete mixtures compatible with this technology requires 1.5 – 2 times more cement than the conventional casting methods, which leads to more CO_2 being released into the atmosphere [8–10]. The printable mixtures for 3D printing contain a higher amount of binder and fine aggregates than conventional concrete to enhance the shape stability and yield stress [8]. The absence of coarse aggregates from the mixture decreases the segregation and blockage issues [51]. Accordingly, various approaches were considered to decrease the high dependency on OPC and to mitigate the environmental impact associated with OPC production, including partial (blended cement such as LC3) and full replacement (through alkaline activating binder) of OPC in concrete.

2.3. 3D printing of one-part AAM

More recently, researchers have been interested in the 3D printing of alkali-activated materials (AAMs), also known as geopolymers, due to their ability to reduce the CO_2 footprint associated with traditional concrete production [13,52]. Conventional AAM is a two-part mixture produced by mixing an alkaline solution with precursors composed of alumina- and/or aluminosilicate-rich materials such as fly ash and metakaolin. The precursors are activated by alkaline activators such as alkali hydroxide, silicate, and aluminate [14,53–55]. AAM has several advantages over traditional concrete, such as high compressive strength, fire resistance, rapid hardening, salt and acid resistance, and other environmental benefits [56–58]. Despite all the benefits of two-part AAM, some challenges regarding the viscosity and the handling of hazardous alkaline activator solutions for large-scale printing should be considered. Accordingly, using a solid activator to produce a one-part AAM can help solve some of the challenges [59–61]. In addition to water, only a dry combination is required to form one-part mixes, where a solid alkali-activator in powder form is combined with a solid aluminosilicate precursor. Hence, this section reviews the constituents of one-part AAM and highlights the most commonly used precursors and solid activators. The most common techniques utilised for 3D printing AAM are introduced. The effect of different mix formulations and parameters (i.e., precursor type, activator types and dosages, admixtures and additives addition) on the fresh and hardened properties of 3D-printed one-part AAMs are discussed. The environmental and economic feasibility of one-part AAMs and 3D printing technology is also discussed and reviewed compared to more traditional solutions.

2.3.1. 3D printable one-part AAM binder composition

2.3.1.1. Binder

AAMs are composed of natural materials or waste products as precursors, which are activated using alkali or acid reactions. The most commonly used materials as the precursor of AAMs are fly ash (FA), silica fume (SF), ground granulated blast furnace slag (GGBS), and metakaolin (MK) [62]. According to ASTM C-618 [63], FA is a by-product material produced from burning coal, and it is divided into two categories, depending on the chemical composition of coal: class F and class C. The chemical composition of class F should contain silicon dioxide (SiO_2), aluminium oxide (Al_2O_3), and iron oxide (Fe_2O_3), which are equal to or greater than 70% of FA chemical composition, while for class C, they should be equal to or greater than 50% of FA chemical composition [64]. SF is a fine pozzolanic by-product that results from the production of ferrosilicon or silicon alloys in electric arc furnaces, and it is composed mainly of amorphous silica [65]. In contrast, GGBS is a glassy granular material produced by the quick chilling of molten blast furnace slag through immersion in water, with or without compositional modifications, while the blast furnace slag is hot [66]. Moreover, MK is produced by burning (calcining) kaolinite clay at high temperatures between 600 to 900 ˚C [67]. Lately, the focus on employing end-of-life materials to decrease the massive amount of construction and demolition waste (CDW) generated yearly, such as bricks, is receiving significant interest. Due to the brick chemical composition that is similar to FA and the computability of AAM to use any aluminosilicate-rich materials as precursor, end-of-life brick valorising through the use as a binder is being studied widely [68–70].

2.3.1.2. Alkaline activator

The hardening of AAMs takes place through the geopolymerisation or polycondensation reaction after mixing alumina or silicate-rich materials with an alkaline activator [71].

Activators provide alkali cations that work on breaking the Si-O-Si and Al-O-Al bonds in the precursor to form the strength-giving binding phases [72,73]. Depending on the activation method, AAMs can be divided into two-part and one-part AAMs. A solid activator in a one-part AAM can be any material that elevates the pH of the reaction mixture, provides alkali cations and facilitates dissolution [72]. The most used solid activators are anhydrous sodium metasilicate and grade sodium silicate [74]. Solid activators have several benefits over liquid ones: they are easier to handle on-site, free of hazardous highly alkaline liquids, and produced at lower cost with lower environmental impact. Incorporating a solid activator allows for easier mixing procedures similar to OPC, where the solid ingredients are dry mixed before adding the water (Figure 2.1).

Figure 2.1. One-part AAM preparation for 3D printing application [61]

2.3.2. Fresh and hardened properties of one-part AAMs

Several external and internal factors can affect the fresh and hardened properties of AAM mixtures: the external factors include the mixing method, temperature, humidity, and curing regime, while the internal factors include the water-to-solid ratio, and the type, proportion, shape, and fineness of materials used in the precursor. Moreover, the activator’s type, dosage, and molar ratio are also influential parameters. As shown in Table 2.1, the effect of using different mix designs on the fresh and hardened properties of printed and cast AAMs was investigated by many researchers. The effect of using different precursor types, varying precursor proportions, and incorporating retarders, superplasticisers, and other additives to obtain an optimum mixture was also explored. It can be observed that the most commonly used materials in precursors were GGBS and FA. Moreover, changing the variables mentioned above influenced the fresh and hardened properties of the mixture, which are further discussed in this section.

2.3.2.1. Fresh properties

The printing requirements of a mixture are investigated by passing the mixture through the pumping, extrusion, and buildability stages. The fresh properties results and the optimal mix design of 3D printed one-part AAMs obtained from different articles are collated in Table 2.2.

2.3.2.1.1. Pumpability and extrudability

Pumpability is the process that transports workable mix through a pipe from the reservoir to the nozzle under pressure without affecting the materials` properties (workability and yield stress) for the entire transporting time [75]. At the same time, extrudability is defined as the ability of the mixture to be extruded from the nozzle smoothly under pressure in good quality without altering the mixture’s physical properties [76], where a good quality extrusion refers to filaments that have been extruded without any breakage or discontinuity [47]. The requirements of printable material are somewhat contradictory; the mixture must be workable enough to ensure ease of transportation prior to extrusion, and the extruded mixtures must retain their shape by being relatively stiff [77].

The rheological performance of materials and the mix design affect pumpability and extrudability, where the desired mixtures should have low viscosity and optimum yield stress for easy pumping and extrusion, as shown in Figure 2.2 [19]. Muthukrishnan et al. [78] investigated the effect of increasing the activator content on the pumpability of GGBS and FA one-part geopolymer by measuring the static yield strength over time. It was found that increasing the activator content resulted in a faster evolution of yield stress, thus, increasing the pumping energy required. Different articles aimed to determine the effect of various precursor materials and found that enriching the mix with materials containing calcium, like GGBS, decreases the extrudability. Guo et al. [79] found that incorporating up to 10% SF in FA-based one-part geopolymer improves the particle packing and enhances the viscosity. Nevertheless, increasing the SF ratio results in decreasing the viscosity due to its fine particle size. Accordingly, using more than 10% of SF in the mixture may result in the decline of extrudability due to excessive viscosity loss. Shah et al. [80] found that increasing the GGBS percentage in the mix resulted in a decrease in flowability, which could be due to the presence of more nucleation sites at the early stage from the additional calcium that GGBS provides, thus, resulting in the rapid hardening of the mixtures [80]. Additionally, GGBS’s angular shape also plays a role in decreasing the workability [81].

Bong et al. [82] studied the effect of replacing precursor and aggregate separately with wollastonite powder on the workability of FA- and GGBS-based one-part geopolymers. The results showed that increasing the replacement level decreases the spread diameter by forming network structures that can resist the flow due to the needle-like shape of wollastonite. In another study, Bong et al. [83] investigated the effect of replacing fine natural sand with wollastonite microfibre on the extrudability of FA- and GGBS-based one-part geopolymers by printing five layers of square slabs with a total length of 4810 mm for each layer. The mixture with a 10% replacement level was found to have comparable workability to the reference mix, and the researcher successfully extruded the reference mix and the mixture with a 10% replacement level. On the other hand, the pumpability can be improved by increasing the water/binder ratio. However, increasing water content beyond a certain level may result in segregation and pipe blockage [84,85]. On a positive note, incorporating retarders can enhance extrudability by slowing the reactions [80]. In a recent study, Cheng et al. [86] investigated the effect of adding different types of superplasticisers (namely, polycarboxylate (PEC), melamine (M), and naphthalene (N)) with different dosages on the flowability of calcium carbide residue–waste red brick powder-based one-part alkali-activated materials. The authors found that adding 1.5% PC among the different types significantly increased the flowability of the mixtures to a comparable level to that of the OPC mixture. Similarly, Alrefaei et al. [87] studied the effect of incorporating PC, M and N superplasticisers on the mini-slump performance of FA-GGBS-based one-part geopolymer and found that the flowability of the mixtures improved, where PC showed the most significant improvement.

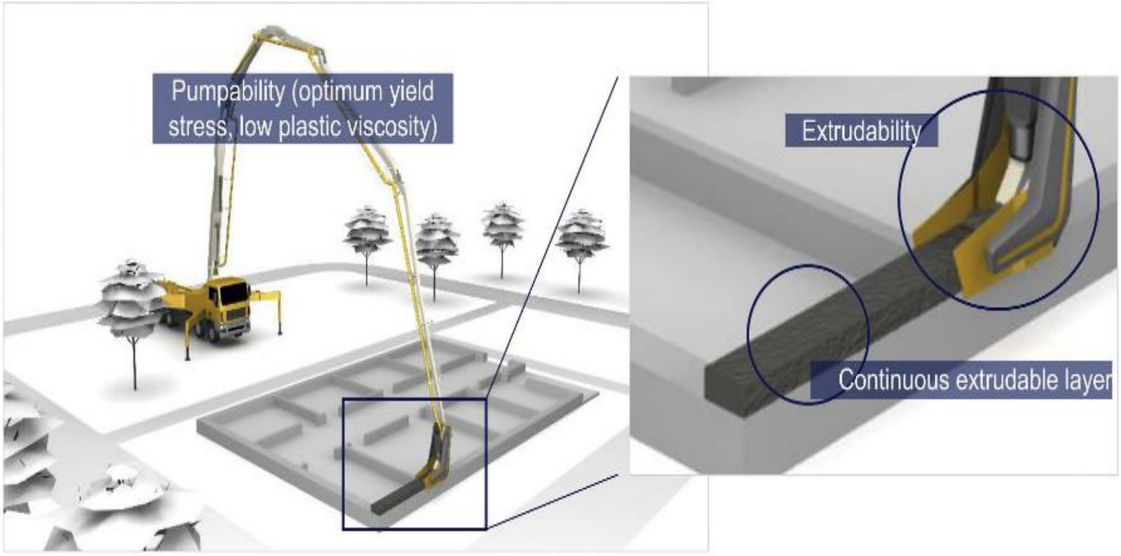

Figure 2.2. Materials properties required for the pumping and extrusion process [19]

2.3.2.1.2. Shape retention

Shape retention is known as the ability of the extruded layer to resist deformation and maintain its cross-section compatible with the nozzle cross-section. The deformation of the deposited layer can result from three main factors: the weight of the layer itself, the weight of the succeeding layers, and the pressure applied during the extrusion process [88]. The shape retention of a mix can be improved by using materials that can enhance the thixotropy property of the mixture. For instance, Bong et al. [89] found that replacing sand with 10% wollastonite enhanced the shape retention ability of the mixture due to the enhancement in thixotropic behaviour and yield stress. While Guo et al. [79] stated that incorporating GGBS in an FA-based one-part geopolymer can enhance the thixotropic behaviour of the mix, thus, enabling the mix to maintain its shape. Additionally, the presence of fine SF particles improves the mixtures' packing density, which results in better yield stress, where the higher yield stress helps maintain the shape of the printed layers. According to Muthukrishnan et al. [78], increasing the activator content enhances shape retention after extrusion by the rapid re-flocculation of the mix. Bong et al. [90] evaluated the shape retention ability of FA- and GGBS-based one-part geopolymer by adding a steel plate on top of a cylinder-shaped mixture and recording the deformation every 30 s prior to adding another steel plate. The results showed that the mixture had a good shape retention ability which collapsed after applying a load that equals around nine times its self-weight. The shape stability of the mixture can be enhanced by incorporating additives, such as MAS, Poly-vinyl Alcohol (PVA) fibres, attapulgite nano clay, and nano graphite platelets [78,91,92]. Further study is necessary to investigate the impact of different mixing times and speeds on the 3D-printed layers’ shape retention.

Table 2.1. Mix formulations of one-part geopolymer

Precursor	Activator Type	Activator percentage (%)	Aggregates size	W/b ratio	S/b ratio	Printing speed	Additives	Method	Printer type	Ref
60 - 85% Fly ash, 15 - 40% GGBS	K_2SiO_4 +KOH	10 – 20	< 2mm	0.35	0.85	90 mm/s	-	3D printed	4 -axis gantry	[93]
50% GGBS, 50% FA **50% GGBS, 50% FA, 10% Act + 0.75% MAS + 1% sucrose**	Anhydrous sodium metasilicate (Na_2SiO_3)	5 – 10	0.1 mm – 1mm	0.36	1.5	10 mm/s	0.5 – 1.5% sucrose 0.75% thixotropic enhancer Magnesium Alumina Silicate (MAS)	3D printed	Three-axis gantry	[78]
50% fly ash, 50% GGBS	Anhydrous sodium metasilicate (Na_2SiO_3)	8 10	0.1mm – 1mm	0.34 0.36	1.5	35 mm/ s	- - 0.5% 1% %	Cast and 3D printed	Gantry	[90]
	Anhydrous sodium metasilicate + GD grade sodium silicate	0 – 7.5% + 2.5 – 10%		0.36			0.5% Retarder			
80 - 90% GGBFS, 0 – 10% **Porcelain ceramic (PC)** **85% GGBFS, 5 – 10% Raw ceramic (RC)**	Anhydrous sodium metasilicate Na_2SiO_3	10	0.2mm – 1.6mm	0.35	2	-	-	Cast	-	[94]

50 – 70% FA, 30 – 50% GGBS **Cured at (20, 30, and 65 C)**	Anhydrous sodium metasilicate Na_2SiO_3	8 – 10	0.1mm – 2mm	0.3	1	-	3 – 5% Sodium tetraborate decahydrate-Borax (retarder)	Cast	-	[80]
70 – 100% FA, 10 – 30% GGBS **60 – 80% FA, 10% GGBS, 10 – 30% SF**	Anhydrous sodium metasilicate Na_2SiO_3	10	40 – 80 mesh	0.3	1.5	-	5% Commercially Attagel thixotropic thickener	3D printed	-	[79]
50% GGBS, 50% FA	Anhydrous (AN) sodium metasilicate Na_2SiO_3 GD grade sodium silicate Na_2SiO_3	10 10	-	0.367	-	-	1% Polycarboxylate (PC1, PC2, PC3) 1% Naphthalene (N1, N2) retarders 1% Sucrose (S) 1% Borax (B) 1% Commercially (RT)	Cast	-	[89]
50% GGBS, 50% FA **Microfibres will replace sand**	Anhydrous (AN) sodium metasilicate + GD Grade sodium silicate sodium Na_2SiO_3 (50:50)	10	0.1mm – 1mm	0.36 0.37 0.377 0.39 0.4 0.425	1.5	30 mm/ s	0 2.2% 4.4% 6.6% 8.8% 13.2% Wollastonite microfibres	Cast and Gantry 3D printed		[83]
Sand replaced (S) **50% GGBS, 50% FA**	Anhydrous	8	840 µm	0.43	1.5 1.35	-	0 10%	Cast	-	[82]

Precursor replaced (GP) **40 – 50% GGBS, 40 – 50% FA, 0 – 20% W**	(AN) sodium metasilicate Na_2SiO_3			0.36	1.2 1.5		20% Wollastonite (W)			
50% GGBS, 10 – 50% FA, 10 – 40% Steel slag (SS)	Na_2SiO_3 + flue gas desulfurization (FGD)	8 + 8	40 – 80 mesh	0.44	1.5	50 mm/s	-	3D printed and cast	-	[95]
100% GGBS	Sodium metasilicate	10%	-	Pastes 0.35 Mortars 0.4	0.83	60 – 100 mm/s	Nanoclay 0 – 0.6% Hydromagnesite nucleation seeds 1 and 2%	3D printed	4-axis gantry	[96]
100% GGBS	Sodium carbonate Na_2CO_3 + Calcium carbide residue (CCR)	8 + 2.5 – 10%	-	0.53	-	-	-	cast	-	[97]
100% GGBS	Na2CO3 + CCR	4 + 2.5 – 10% 8 + 2.5 – 10%	-	0.53 – 0.583	-	-	-	Cast	-	[98]
100% GGBS	Na_2CO_3 + calcined dolomite (CD)	10% + 2 – 10%	-	0.42	-	-	-	cast	-	[99]
50% GGBS, 0 – 50% FA, 0 – 50% brick powder (BP)	Anhydrous sodium metasilicate	10%	Fine sand D50 of 172 µm Coarse sand D50 of 498 µm	0.4	1.5	10 mm/s	Retarder 1% Nano clay 0.5%	3D printed and cast	3-axis gantry	[68]

***Alkali modulus (nSiO2/nNa2O) for anhydrous sodium metasilicate (Na2SiO3) :0.9, and GD grade sodium silicate (Na2SiO3) :2**

2.3.2.1.3. Open time and setting time

Open time is when the material is extrudable after adding water to the mixture; beyond that time, the material loses its extrudability. The suitable open time of the material has to be sufficient to contain the period for which the material is to be deposited. Otherwise, the material will harden in the nozzle or container [91]. Open time and setting time depend mainly on the mix design. Depending on the type of precursors used, the open time and setting time of one-part geopolymers change according to the rate of the mixture reaction mechanisms. One of the main differences between precursors rich in GGBS and other precursors is their setting time, where the presence of rich-calcium material results in the faster setting of the mix [81,100,101]. Figure 2.2 presents the initial setting time of different mixtures obtained from the literature. It can be seen that altering the precursor content has a direct effect on the setting time of the mixtures. The main reason behind the variance in setting time of the mixture is attributed to the amorphousness of the used material and its chemical composition, which plays a big role in the reaction leading to the hardening of the mixture. For instance, Pasupathy et al. [68] investigated the effect of replacing FA with brick powder (BP) by 10%, 30% and 50% on the initial setting time of one-part AAM. The authors found the initial setting time to increase from 102 min to 125 min. The longer setting time, according to the authors, is due to the low geopolymerisation rate in the presence of BP compared to FA. Shah et al. [80] reported that increasing GGBS shortens the setting time of the mix because of the rapid hardening due to the additional reactions that GGBS imposes at the early stage. In addition, Panda et al. [93] stated that the amount of GGBS in the precursor should be controlled since it can change the flow properties, thus, significantly affecting the open time of the mix.

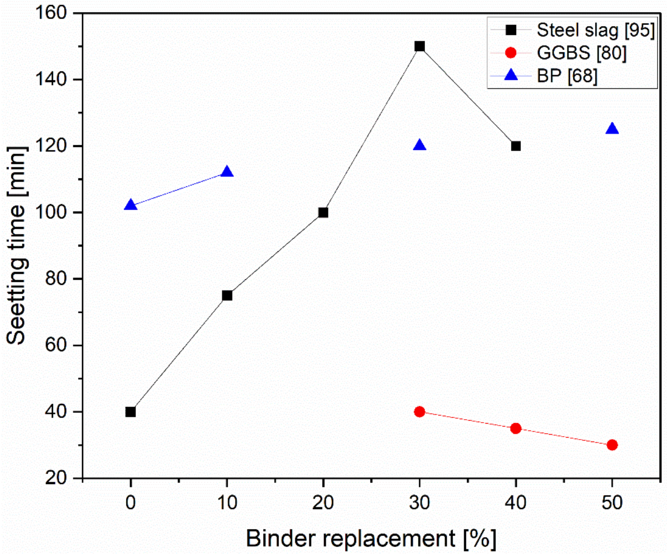

Figure 2.3. Setting time of one-part AAM with different binder replacements [68,80,95]. The base mix of each study is:

Similarly, the activator content has an inverse relationship with open time. Muthukrishnan et al. [78] reported that the increment in activator percentage limits the open time of the mix due to the rapid evolution of yield strength. To extend the open time, they investigated the effect of incorporating a retarder and found it to slow the yield strength development, which increases the open time. Ma et al. [95] studied the effect of replacing up to 40% of FA with steel slag and found an increment in open time, which could be due to the deceleration of the geopolymerisation process caused by the presence of steel slag. However, it was found that using more than 20% replacement level decreased the flowability of the mixture, consequently decreasing the open time, as shown in Figure 2.4.

The studies on the open time of one-part geopolymers are limited. Further research is required to understand the effect of different precursor types, mix designs, additives and retarders on the open time of one-part geopolymers.

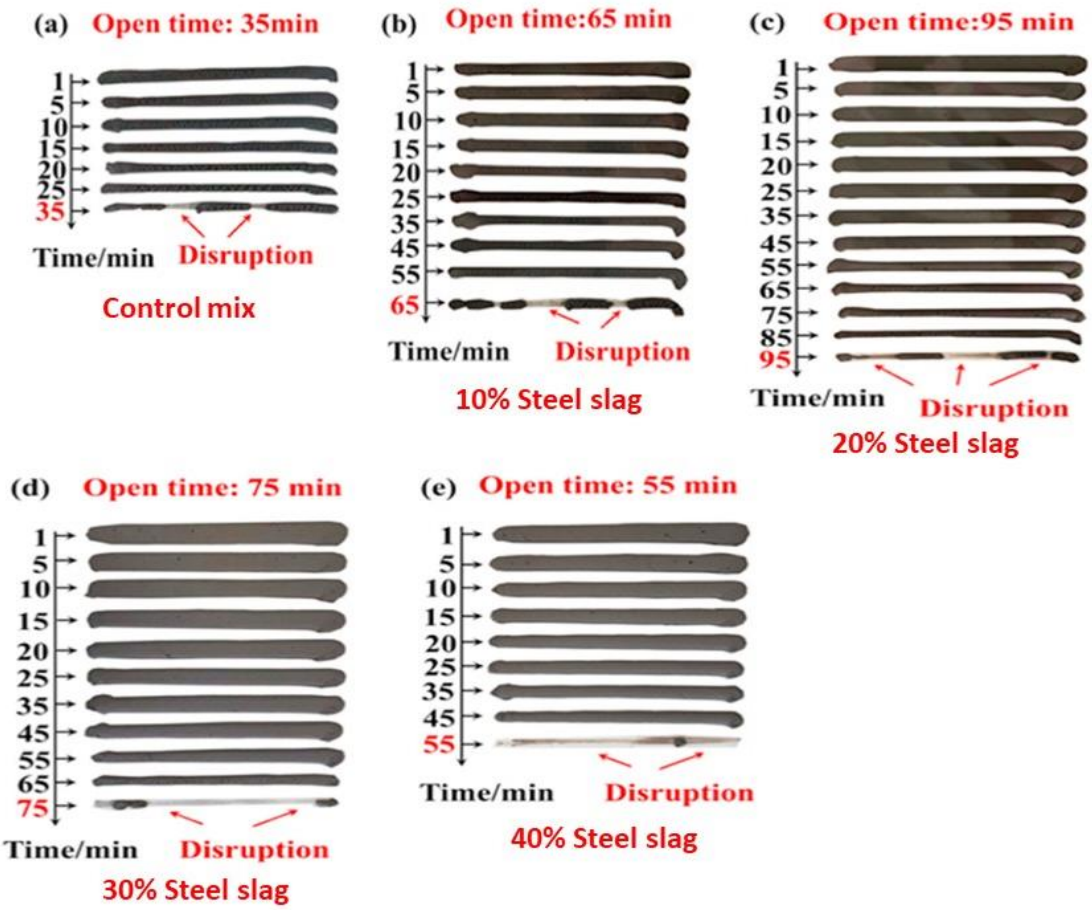

Figure 2.4. Effect of replacing FA with different steel slag content on open time of one-part geopolymer [95]

2.3.2.1.4. Rheological properties

The main rheological properties are plastic viscosity, yield stress, and thixotropy. Yield stress is divided into static and dynamic yield stress. Static yield stress is the shear stress needed to start the mixture's flow. After the flow starts, the needed shear stress for maintaining that flow is called the dynamic yield stress. 3D printable concrete flows when applying external shear stress [102,103], where the mix stops flowing after removing the external force, and thixotropy occurs. Thixotropy is a phenomenon where the mix restores static yield stress by initiating flocculation of the particles due to inter-particle interaction [104]. Rheological properties mainly depend on the mix design of the fresh geopolymer and the shape of the solid ingredients of the mixture. Panda et al. [93] observed that increasing GGBS content in FA-based one-part geopolymer increased yield stress, plastic viscosity, and viscosity recovery, which is due to the chemical composition of GGBS that is rich with calcium. Due to the angular morphology of GGBS particles, the packing density increases, enhancing the mix's thixotropic property.

The reactivity and the composition of the precursor materials influence the rheological parameters. Kaze et al. [105] compared the rheological behaviour of lateritic clay (LAC)- and iron-rich laterite clay (LAI)-based geopolymers. The results revealed that LAI possesses significantly higher yield stress than LAC, which is justified by the higher deformation that LAI exhibited due to the higher interaction rate between its different constituents, since iron (Fe) possesses a higher reaction rate than Si and Al. Thus, iron species quickly precipitate in an alkaline medium to form iron hydroxide gel, accelerating the polycondensation process and producing a more rigid structure. In another study, Kaze et al. [106] studied the effect of different calcination temperatures on the rheology of meta-halloysite-based geopolymer and found that increasing the calcination temperature improved the rheological behaviour of the geopolymer due to the increase of the reactive phases in clay. Ma et al. [95] found that replacing FA up to 100% with steel slag in FA- and GGBS-based one-part geopolymer decreased the rheological properties of the mix. The decrement could be due to the steel slag's low reactivity, which prevented FA and GGBS from reacting with the activator and producing the hydration gels. Most recently, Pasupathy et al. [68] investigated the effect of replacing different ratios of FA with brick powder (BP) on the rheological parameters of GGBS-FA-based one-part geopolymer. The authors reported an improvement in the thixotropy and increment in viscosity with increasing BP content, indicating that adding brick improves re-flocculation ability, as can be seen in Figure 2.5a, where the loss of the ball-bearing effect increased apparent viscosity. Moreover, the static yield stress was also observed to increase with increasing BP content, as shown in Figure 2.5b. Static yield stress is related to the particles’ flocculation, reaction process, and free water content in the paste [107,108]. According to the authors, incorporating BP reduced the reaction rate of geopolymer, which was observed by the longer setting time with increasing BP content. However, due to the irregular shape of BP particles, BP tends to absorb the free water in the mix [109]. That, in turn, accelerates the internal friction between particles and increases the viscosity and shear stress [110], which, in turn, increases the static yield stress.

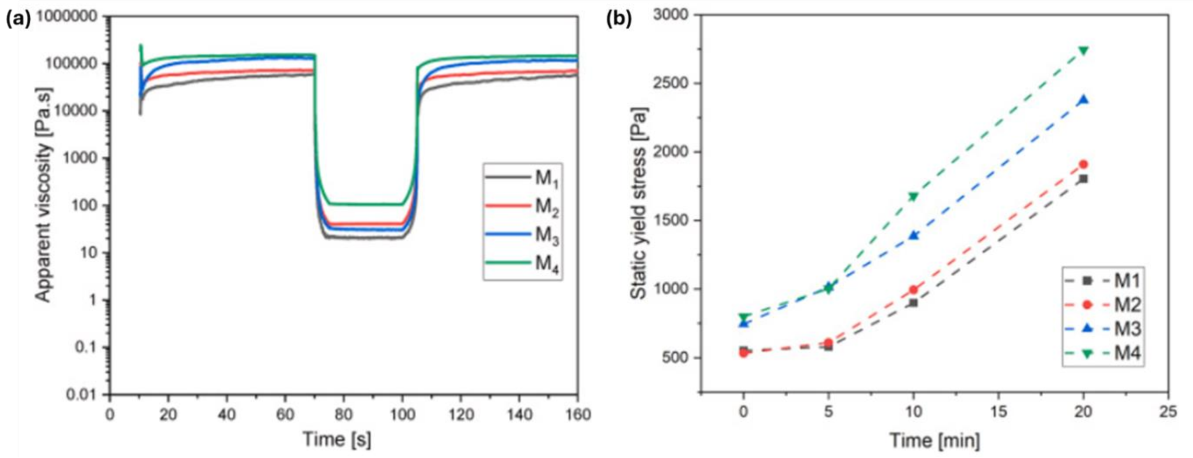

Figure 2.5. (a) Viscosity recovery and (b) static yield stress of different mixtures with varying BP content (M1: 50FA, M2: 40FA 10BP, M3: 20FA 30BP, and M4: 50BP)

Besides the effect of different precursor materials, activator content has an evident effect on the rheological behaviour of the mix. Muthukrishnan et al. [78] found that increasing the activator content significantly increased yield stress and viscosity and improved the thixotropy of the mixture [78]. However, using higher activator percentages may decrease the plastic viscosity of the mix [93]. The activator composition (i.e., alkali modulus) also plays a crucial role in influencing the rheological properties of the geopolymer. According to [111,112], increasing the SiO_2/Na_2O ratio increased the viscosity and yield stress of the geopolymer mixture. Moreover, Bong et al. [83] found that replacing 10% of fine sand with wollastonite microfibre in FA and GGBS-based one-part geopolymer increased yield stress and decreased the plastic viscosity of the mix. The increased yield stress could be due to physical interlock and overlap between wollastonite acicular particles. At the same time, the plastic viscosity decrement could be due to the more elongated particle shape of wollastonite compared to the mixture's other solid particles. Moreover, it was found that substituting sand with 10% fibres had slightly enhanced the thixotropic property and resulted in recovering 80% of the viscosity.

2.3.2.1.5. Buildability

Buildability is the ability of 3D-printed filaments to retain their shape and resist distortion induced by both their weight and the weight of the succeeding layers after it has been extracted from the nozzle [102]. As stated in section 2.2.3.1.1, the mixture must possess high-yield stress after extrusion to retain its shape. In order for the first layer to withstand the weight of the subsequent layers, the mixture should have enough early strength. The buildability mainly depends on the mixture’s rheological properties and object design, including geometry, size, and process parameters [113]. Muthukrishnan et al. [78] investigated the effect of different activator percentages on the buildability of FA- and GGBS-based one-part geopolymer by evaluating the static yield stress development over time when changing activator content. They validated the results by conducting a 3D printing test to determine the maximum number of layers that can be printed before the collapse of the structure or the deformation of bottom layers to 0.5 of the layer's initial width. It was found that increasing the activator content resulted in a faster yield stress growth over time, which improved the retention of the mix and allowed for more layers to be printed. They also investigated the effect of incorporating nano-clay and sucrose and found that adjusting and balancing these additives can allow printing more layers (as shown in Figure 2.6). Although adding 1% sucrose increased the open time, the yield stress development rate and thixotropy were decreased and resulted in limiting the number of layers that could be printed (Figure 2.6c). Furthermore, incorporating 0.75% nano-clay resulted in a better yield strength development and thixotropic behaviour for the mix with sucrose. At the same time, it limited the open time of the mix. Adjusting sucrose to 1.5% resulted in producing a mix with comparable properties to the control mix with adequate open time, which allowed the printing of 120 layers for one patch without failing (Figure 2.6d). Chougan et al. [91] proposed incorporating nano-graphite to enhance the buildability of 3D printed geopolymer.

Bong et al. [90] studied the buildability of FA- and GGBS-based one-part geopolymer when combining 5% anhydrous sodium metasilicate and 5% GD grade sodium silicate activator by printing a rectangular column and found that the mixture had excellent buildability. Moreover, Panda et al. [93] estimated the buildability of a one-part geopolymer by determining its load-carrying capacity in the dormant period. The dormant period before the mix starts setting was found to be less than 30 minutes, referring to the fast development of early strength, which could be due to the initial stage reaction that produced aluminosilicate gel.

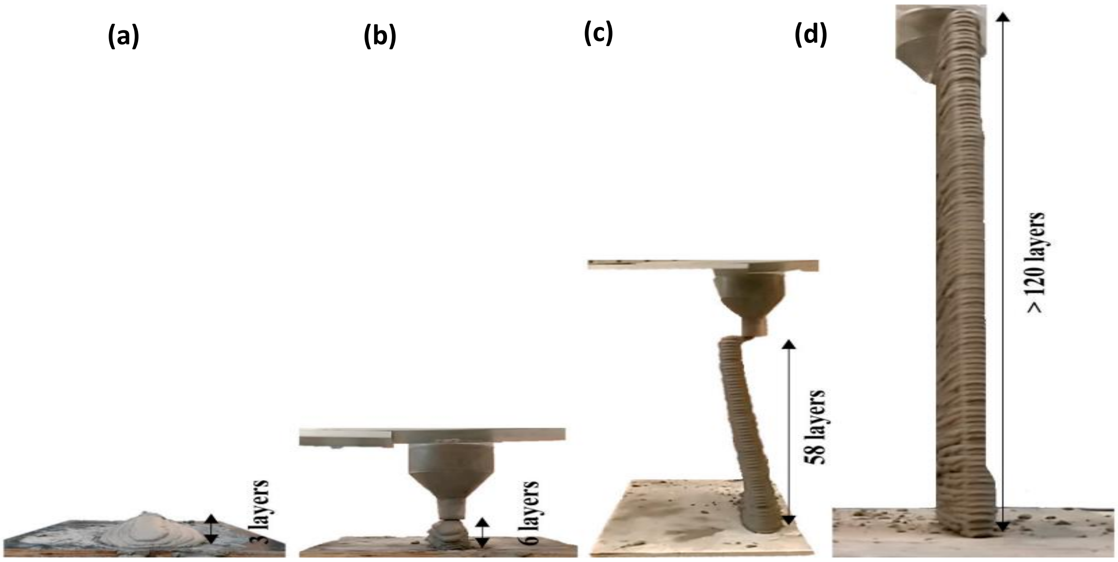

Figure 2.6. Buildability test of a) 5%ACT (activator), b) 7.5%ACT, c) 10%ACT-1%S (sucrose), and d) 10%activator-1.5%S-0.75% thixotropic enhancer one-part geopolymer mixes [78]

Table 2.2. 3D printed one-part geopolymers fresh properties

Optimum mixture	Extrudability	Printability	Thixotropy	Rheological parameters	Buildability	Ref
70% FA, 30% GGBS, 10% activator	-Extruded with no breakage or discontinuity	-	-Increased with increasing GGBS content. -The thixotropy parameter increased with increasing activator content to 15% and decreased beyond that.	-Increased with increasing GGBS and activator level.	-	[93]
50% GGBS, 50% FA, 0.75% (MAS) thixotropic enhancer, 1.5% sucrose	-Increasing the solid activator content caused a decrement in the flowability. -The mixture with a 10% activator could not be pumped. - The addition of sucrose increased the flowability of the mix, while MAS decreased it.	-Increasing the activator dosage and incorporating MAS were found to reduce the open time of the mixture. -The addition of sucrose extended the open time.	-It was improved with increasing activator level. -The addition of sucrose was found to decrease the thixotropic parameter. -The addition of MAS was found to increase thixotropy by 200%.	-Increased with increasing activator dosage. -Yield stress was found to decrease with adding sucrose. -The incorporation of MAS increased the rheological parameters.	-It was found that using the optimum mixture can build more than 120 layers without showing any failure.	[78]
50% GGBS, 50% FA, (5+5)% activator + 0.5% retarder	-The optimum mixture was extruded without any breakage or discontinuity.	-Retarder had prolonged the setting and open time of the mixture.	-The optimum mixture had a strong thixotropy behaviour. It could recover 72% of its initial	-	-94 layers were printed without observing any deformation. -More layers could be printed.	[90]

		-The optimum mixture open time was 65 min.	apparent viscosity within 60 s.			
80% FA, 10% GGBS, 10% SF	-Using more than 10% SF may result in decreasing the extrudability.	-GGBS was found to decrease the initial and final setting time. Thus, limiting the open time for printing.	-Incorporating GGBS and SF was found to improve geopolymer thixotropy. - Increasing both GGBS and SF content decreased the values.	- The incorporation of GGBS and SF was found to increase both yield stress and plastic viscosity. -Increasing the replacement level of GGBS and SF decreased the results.	-	[79]
50% GGBS, 50% FA, 10% micro-fibres	-The control mix and the mixture containing micro-fibres were extruded without any blockage.	-	-The incorporation of microfibres increased the viscosity recovery, indicating the good thixotropy property of the mixture.	-Replacing sand with 10% microfibres increased static and dynamic yield strength while decreasing the plastic viscosity.	-Both the control and optimum mixture were printed successfully without deformation in the bottom layers.	[83]
-	-Increasing SS Improved extrude-ability due to the deceleration of the geopolymerisation process by the presence of less reactive SS.	-The open time increased with SS content up to 20% and decreased beyond that.	-Increasing SS content improved the thixotropy property.	-Plastic viscosity and static and dynamic yield stresses decreased with SS content.	-The buildable height increased with SS content up to 10% and then decreased when printing free wall. -When printing square walls, the buildable height decreased with SS content.	[95]
100% GGBS, 0.4% NC, 2% seeds	-Increasing the NC content to 0.6% led to the extrusion of	-The optimum printing speed was set to 90 mm/s to print layers with the	-NC improved the viscosity recovery behaviour of the mix by 25% due to its thixotropy property.	-Although 0.6 resulted in the maximum yield stress, 0.4% was selected as the optimum.	-15 layers cylinder was printed using the mix with NC to investigate the efficiency of printing speed,	[96]

	discontinuous filaments.	same width as the nozzle inlet.		-NC inclusion resulted in three times higher yield stress without affecting the apparent viscosity. -The incorporation of the accelerator slightly affected the yield stress.	and no deformation was observed. -Twisted column was printed without having any deformation in the bottom layer.	
50% GGBS, 20% FA, 30% BP			-The thixotropy was slightly improved with BP content in the mixtures.	-The addition of BP increased the apparent viscosity and the static yield stress.	-Mixture with 30% BP was selected for buildability and 20 layers were printed without any discontinuity.	[68]

2.3.2.2. Hardened properties of one-part AAMs

Mechanical strength tests on 3D printed specimens were assessed by applying load in three directions; longitudinal, lateral, and perpendicular to the printing direction, which are referred to as X, Y, and Z-directions, respectively. Specimens have been extracted with different dimensions from printed blocks depending on the type of test to be conducted. Different researchers investigated the effect of different mix designs on the hardened properties of printed and cast geopolymers, as shown in Table 2.1. The effect of using different precursor types, varying precursor proportions, and incorporating retarders, superplasticisers, and other additives to obtain an optimum mixture was explored. Table 2.3 shows the mechanical performance and optimal mix design obtained from different articles for 3D-printed and cast one-part geopolymers.

2.3.2.2.1. Compressive strength

Several studies have shown that comparable strength values can still be obtained by controlling the printing parameters and mix design [91,114]. Depending on the mix design, the strength of a one-part geopolymer is often higher when using a calcium-rich precursor. That is in good agreement with the results obtained from different articles shown in Table 3. The more incorporation of GGBS, the higher the compressive strength [91,115,116]. However, increasing GGBS beyond a certain limit causes a decrement in the compressive strength, which could be due to the loss of workability, as illustrated in Figure 2.7(a). Panda et al. [93] found that increasing GGBS content from 15% to 40% significantly increased the compressive strength values of FA-based one-part geopolymer due to the early formation of C-S-H. They also found that strength values tend to increase with increasing activator dosage from 10% to 20% due to the more Si ions available for geopolyermisation. Determining the optimum precursor proportion for a specific activator percentage and water amount may lead to optimised compressive strength [117]. Dong et al. [117] found that the fineness of the materials plays a significant role in improving the mechanical strength of the geopolymer, where using a finer activator significantly increases the compressive values of one-part geopolymer. Moreover, the compressive strength is affected by the used activator type, where the most effective and used solid activator is sodium silicate. Ma et al. [118] found that partially replacing Na_2SiO_3 with Na_2CO_3 decreased the compressive strength of one-part geopolymers due to the decrease in the geopolymerisation degree in the presence of Na_2CO_3. The incorporation of retarders and rheology-modifying admixtures can result in decreasing the compressive strength value. Sun et al. [119] studied the influence of using up to 8% viscosity modifying admixture on the mechanical properties of one-part geopolymer and found that the compressive strength decreases with increasing the additive dosage. The decline in the strength values in the presence of a modifier was attributed to the aeration effect and the creation of a dense polymer film that hinders the contact of silicate powder with the activator [119].

On the other hand, various researchers studied the effect of using waste material to replace aggregates or part of a precursor. Abdollahnejad et al. [120] found that replacing up to 30% of GGBS with fired and unfired ceramic reduced strength values in GGBS-based one-part geopolymer. While replacing natural aggregate may increase or decrease the strength depending on the type of aggregate used [121]. Lately, Pasupathy et al. [68] replaced 10%, 30% and 50% of FA with BP in GGBS-FA-based one-part geopolymer and reported an increment in compressive strength when incorporating 10% of BP. The authors showed that increasing BP content beyond 10% decreased compressive strength at 7 and 28 days for cast and 3D printed specimens. The decreased behaviour could be due to the lower amorphous content of BP, which decreases the reaction rate of the mixture [122].

Figure 2.7b shows the anisotropic compressive strength behaviour in different testing directions. Some studies found that printed specimens exhibit higher compressive strength values when tested longitudinally (X-direction) to the print direction compared to cast specimens and other directions. This can be due to the movement patterns, as the materials move in the direction of printing, allowing for more compaction after placing the particles, compared to the other direction [93]. The characteristics of the printing process result in an anisotropic behaviour dependent on the direction of testing [123,124]. The heterogeneity created by the interaction between layers may explain this anisotropic nature of printed structures. Due to the intense pressure during the extrusion, the 3D-printed object has a denser microstructure than cast concrete. Nevertheless, the printed object has higher porosity with weaker connections at the layer interface [125]. Other studies [83,90] reported higher compressive strength values for cast specimens than those of 3D-printed one-part geopolymers, which could be due to the higher porosity of printed samples than the cast ones.

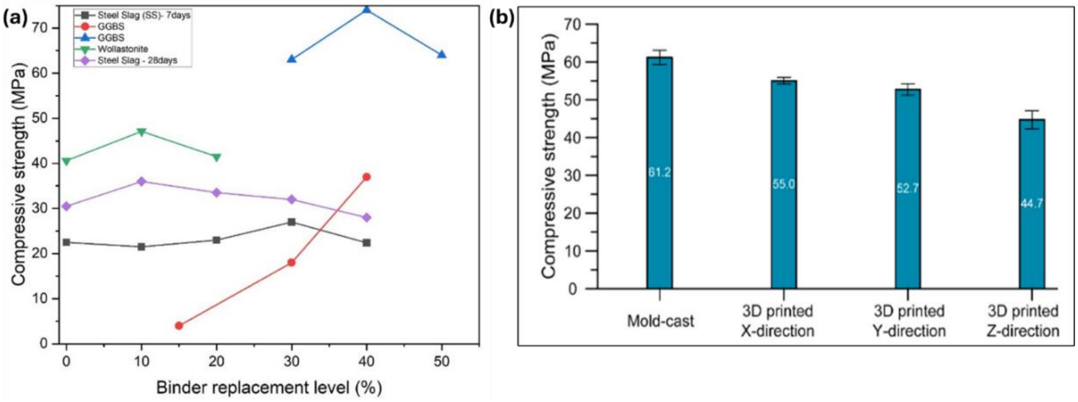

Figure 2.7. Compressive strength of one-part AAM with (a) cast specimens when precursor partially replaced with different materials [80,82,93,95] and (b) different directions on 3D printed optimum mixtures [90]

2.3.2.2.2. Flexural strength

Like compressive strength, flexural strength was found to increase with increasing the activator content and Ca-rich materials [126]. While Shah et al. [80] observed a decrement in the flexural strength when increasing GGBS content, as shown in Figure 2.8a, due to the low water content used in the mix. Moreover, Figure 2.8a presents the effect of replacing precursors with different materials on the flexural strength of cast specimens. Flexural strength was also found to follow an anisotropic behaviour dependent on the testing direction, as shown in Figure 2.8b. Most studies revealed that 3D printed specimens had a slightly higher flexural strength when the load was applied lateral (Y) and perpendicular (Z) to the printing direction. The lowest flexural values are observed when the load is applied in the X-direction, which can be due to the weak interface between layers [127–129]. In 3D printed elements, two different interfaces are produced: a horizontal interface is produced by extruding the subsequent layer on top of the previous layer, and a vertical interface is formed between two layers when the subsequent layer is placed next to the previous layer at the same level. The strength at the centre of the extruded concrete is greater than that at the layer interfaces [125,128]. Different researchers investigated the effect of using fibres to enhance the flexural strength of 3D-printed concrete. They found that incorporating fibre enhanced the printed filaments in perpendicular and lateral directions while not changing the observed anisotropy trend [130,131]. Bong et al. [83] studied the effect of replacing the finest sand with up to 30% wollastonite microfibres on the flexural strength of 3D-printed one-part geopolymer and found that replacing 10% of sand resulted in the highest flexural strength values. The strength was around 4 MPa higher than the reference mix for cast specimens and 1.5 MPa and 0.5 MPa higher for 3D printed specimens in Z- and Y-directions, respectively. The enhancement can be due to the connection of wollastonite particles to the geopolymer matrix after being partially dissolved in the mixture. The presence of these particles in the mixture is supposed to be helpful in crack bridging and crack blocking through the fraction deflection and fibre rupture, which increases the load needed to rupture [88]. Ma et al. [95] found that the lower flexural strength values of 3D printed one-part geopolymers in all directions than the cast specimens are due to the presence of extra air voids during the printing process and the generation of weak interlayers in the bottom.

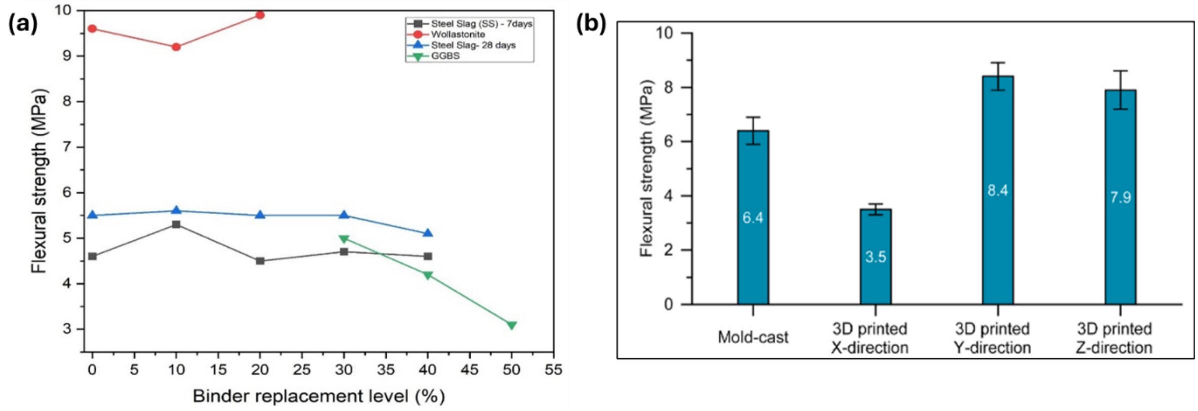

Figure 2.8. Flexural strength of one-part geopolymers with (a) cast specimens when precursor partially replaced with different materials [80,82,95] and (b) different directions on 3D printed optimum mixtures [90]

Table 2.3. One-part geopolymer hardened properties.

Optimum mixture	Compressive strength	Flexural strength	Ref
70% FA, 30% GGBS, 10% activator	-Increased with increasing GGBS and activator. -Strength in the printing direction was the highest.	-	[93]
50% GGBS, 50% FA, 0.75% (MAS) thixotropic enhancer, 1.5% sucrose	- The compressive strength results in all directions were higher than printed geopolymer in other studies at 7 and 28 days.	-A higher strength was obtained at 7 and 28 days compared with similar geopolymers from other studies.	[78]
50% GGBS, 50% FA, (5+5)% activator, 0.5% retarder	-Cast specimens had higher strength values than the printed ones. -The X-direction had the highest value among the other directions. (X-direction load was in the plane of the interfaces between layers). Y-direction was the printing direction, and Z was perpendicular to it.	-Y and Z-direction had higher strength values than the x-direction and the cast specimen. -Y-direction had the highest value, followed by Z, cast specimen, and x-direction, respectively.	[90]
85% GGBFS, 10% PC	-Sealing specimens in plastic bags was found to have the highest strength values compared with submerging and ambient curing methods. -The highest compressive strength was obtained when replacing slag with fired ceramics by 10%. -All the values were lower than the control specimen.	-Specimens sealed in plastic bags had the highest strength. -All values of specimens sealed in plastic bags were slightly lower than the reference mix.	[94]
60% FA, 40% GGBS, 10% activator, 4% retarder	-The strength values increased with increasing slag and activator content. -Using more or less retarder content than 4% decreases the strength values. -Compressive values increased with increasing curing temperature at early ages. -At 28 days, the curing temperature did not affect strength values.	-Increasing slag and activator content resulted in a drop in the flexural values. - Flexural results were found to be decreased when using retarder content other than 4%. -At an early age, flexural strength increased with increasing curing temperature. -At 28 days, flexural strength was not affected by curing temperature.	[80]

50% GGBS, 50% FA, PC1 **50% GGBS, 50% FA, S**	-GD Grade sodium silicate was found to have higher strength values than the anhydrous activator. -The incorporation of superplasticiser (SP) did not affect the mixtures activated with AN, while it reduced the strength values of mixes activated with GD-grade sodium silicate -The incorporation of (R) retarders did not affect the mixes activated with anhydrous sodium silicate (AN), while decreased strength of mixes activated with GD. -The combination of SP and R decreased the compressive strength values compared to using them separately.	-	[89]
50% GGBS, 50% FA, 10% microfibres	-Comparable strength values were obtained with increasing sand replacement levels with microfibres for cast specimens. -For printed specimens, adding wollastonite did not affect the compression performance, where both mixtures exhibited similar strength values. -The highest strength values were obtained in the X-direction (Printing direction)	-For cast samples, flexural strength values increased in the presence of microfibres compared with the control specimen, where the highest value was obtained when replacing 10% sand. -The strength results were comparable to the control specimen for printed specimens. The strength values of the mixture containing wollastonite in the Y and Z directions were slightly higher than the control specimen. -The highest strength values were obtained in Z-direction.	[83]
GP + 10% wollastonite (W)	-Higher compressive values were achieved in mixtures that replaced precursor (GP) with wollastonite (W) than mixtures that replaced sand (S) due to the lower water content in GP. -The highest values for S and GP mixtures were obtained using 10% wollastonite.	-GP had higher flexural strength than S due to the lower water content. -The incorporation of W increased strength in S mixtures while not affecting GP mixtures. -For S mixtures, the highest flexural value was obtained when replacing 20% of sand. While for GP, all the results were comparable.	[82]
-	-At 7 days, the compressive strength increased with increasing SS to 30%. While the 28-day compressive strength decreased with SS content, the highest value was obtained when adding 10% SS.	-The flexural results for 3D printed specimens in all directions were lower than the casted sample.	[95]

	- The results of all directions were higher than the casted specimen, where Y-direction had the highest results among all directions.		
-	-Increasing the CCR ratio (i.e., 7.5 and 10%) decreased the compressive strength of the samples in the different curing methods when immersed in water and aggressive ambient (i.e., Na_2SO_4 and $MgSO_4$). -Compressive strength values significantly decreased when immersing samples in $MgSO_4$ -Compressive strength loss at 84 days increased with increasing CCR ratio when exposing mixtures to Na_2SO_4.	-	[97]
100% GGBS, 8% Na_2CO3, 2.5% CCR	-The compressive strength significantly increased with increasing the activator ratio from 4% to 8%. -For the 4% activator ratio, the incorporation of 5% CCR had the highest development in compressive strength at early ages. However, 2.5% possessed the highest compressive strength at later ages. -For the 8% activator ratio, 2.5% and 5% exhibited the highest compressive strength, while 2.5% had the highest results at 28 days.	-	[98]
100% GGBS, 10% CD	-Increasing CD content increased the compressive strength performance of the mixtures, where 10% achieved the highest values. -All mixtures with the different CD ratios exhibited noticeably higher strength values than NaOH solution-activated slag and less compressive strength than Na_2SiO_3 solution-activated slag.	-	[99]
50%GGBS, 20%FA, 30% BP	-Compressive strength was increased when incorporating 10% BP, whereas increasing BP content decreased the strength at 7 and 28 days for both cast and 3D printed specimens. -Mixture prepared with 30% BP exhibited comparable strength to the control sample. -Printed samples showed anisotropic behaviour in the compressive strength, having the highest values when the load was applied longitudinally to the printing direction compared to lateral and perpendicular.	-	[68]

2.3.3. Economic assessment of one-part geopolymers

One of the main benefits of using 3D printing technology could be the reduction in the overall cost. The involvement of 3D printing provides more economical solutions in terms of material saving, required effort, and energy. Concrete 3D printing (3DCP) does not require formwork, which accounts for 10% of the overall cost. Due to the elimination of formwork, the formwork labour will be no longer needed, reducing the overall cost by 50% or more, as highlighted in [17]. Batikha et al. [132] compared different building techniques and showed that 3DCP is more economical than other construction techniques. According to the study, construction cost is responsible for 55% of the total cost and the material cost for 45% (see Figure 2.9). Other researchers found that the construction cost consumes 70% of the total cost when using a robotic arm for 3DCP [50,133].

The total cost of construction when using 3DPC can also be decreased by employing different approaches, including printing hollow structures and using AAMs to reduce the cost of printing materials [46,134]. Using recycled aggregate, coarse aggregate, and industrial by-product materials can also reduce the total cost [135]. However, Abbas et al. [136] found that producing 1 m^3 concrete with metakaolin geopolymer is three times higher than the total cost of producing it with OPC. This is due to the high cost of geopolymer materials, where sodium hydroxide contributed to 41% of the total cost, metakaolin by about 31%, and sodium silicate by about 19%. Yang et al. [137] showed that the type and content of alkali activators affect the production cost of alkali-activated GGBS. They found that the cost of one-part alkali-activated blast furnace slag foamed concrete was slightly higher than that of OPC concrete. Ma et al. [138] compared the cost of producing 1 m^3 one-part geopolymers prepared with different sodium metasilicate types and 1 m^3 OPC concrete and found that one-part geopolymers had higher costs than OPC concrete. In contrast, Habert and Ouellet-Plamondon [139] compared the economic allocation of one-part geopolymers with OPC and found the possibility of reducing costs by 80% compared with OPC. Vinai et al. [55] compared the costs of production and raw materials of one-part alkali-activated concrete (AAC), Portland cement concrete (PCC), and two-part alkali-activated concrete. The results showed that two-part had the highest cost, while one-part AAC had a slightly lower cost than PCC at all concrete strengths. The low overall cost of one-part AAC is due to the low price of sodium silicate powder, which is four times lower than sodium silicate solution. Based on the above-presented articles, the implementation of solid activators can reduce the overall cost of the one-part geopolymers to a comparable level and even lower than OPC, depending on the used precursor.

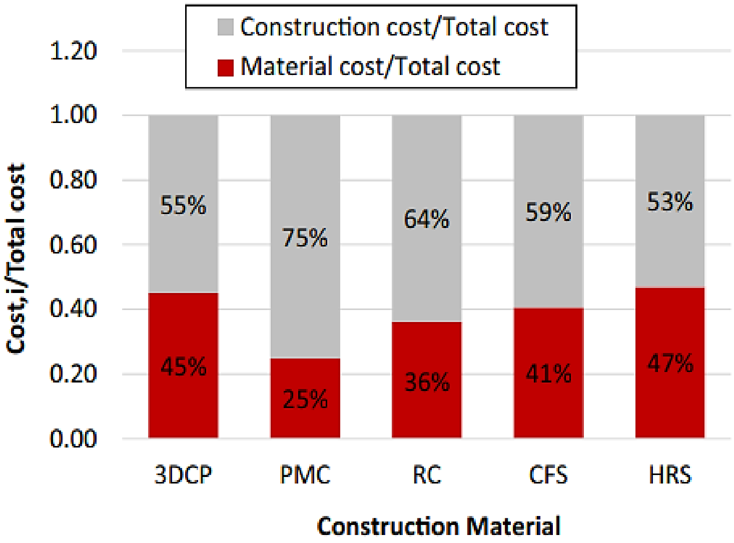

Figure 2.9. The relative percentage of the material cost (USD) and construction activity of total cost (USD/m^2)* [132]

*3DPC: 3D concrete printing, PMC: prefabricated modular construction, CFS: cold-formed steel, and HRS: hot-rolled steel

2.3.4. Environmental impact of one-part geopolymers

3D concrete printing is the most sustainable construction method, which produces a lower amount of CO_2 compared with other types of construction [132]. Mohammed et al. [140] compared reinforced concrete (conventional method) with 3D concrete printing and found that 3D printing concrete produced around 22% less carbon dioxide emissions. Due to the higher amount of cementitious binder in 3D concrete printing technology than in conventional concrete [141], the researchers have focused on finding more environmentally friendly materials instead of cement due to the consumption of around 4% of greenhouse gas (GHG) and to the release of around 8% of the total global CO_2 emissions associated with cement production [4].

Yoa et al. [142] found that using geopolymer in 3D printing decreases the overall CO_2 footprint of concrete production. However, an increase in the use of abiotic resources and depletion of stratospheric ozone was observed. Moreover, Liu et al. [143] found that cast geopolymers had lower environmental impacts than the cast OPC sample, while it did not outperform OPC when printed due to the higher activator content in the mixture. However, when constructing a wall, the environmental impact of the casting technique varied depending on the shape complexity while remaining constant for the 3D printing method [143].

According to the literature, most of the articles used the combination of sodium hydroxide (NaOH) with sodium silicate (Na_2SiO_3) to produce the liquid activator used in two-part geopolymers because the use of NaOH only cannot enhance the strength significantly [144]. Using one-part geopolymers eliminated the need for combining them, resulting in a more environmentally friendly mix than two-part geopolymers. The environmental impact key contributor to geopolymers is the production of alkali activators, as reported in [145] and [146]. The CO_2 emissions produced by activators vary depending on the type of activator, where the CO_2 inventory of Na_2SiO_3 was found to be higher than that of $Ca(OH)_2$ [137]. Furthermore, one-part alkali-activated slag foamed concrete had 85 – 93% lower CO_2 emissions, depending on the type of activator used, compared to that of OPC [137]. The production of 3D printable one-part geopolymer mixes prepared with a solid activator can reduce up to 70% of the carbon emissions and 15% of embodied energy compared with 3D printable OPC having a similar compressive strength value [147]. Panda et al. [93] found that a one-part geopolymer sample had lower CO_2 emissions of around 78%, and the embodied energy accounted for about 15% of that for the OPC-based specimen. Moreover, they revealed that the activator had around 81% of the total energy of the overall mix [93]. Ma et al. [138] calculated the embodied CO_2 index of one-part geopolymers prepared with various types of sodium metasilicate with and without water in their chemical compositions. It was found that one-part geopolymer mixes prepared with different types of sodium metasilicate had lower CO_2 emissions per MPa for 1 m^3 compared to OPC. Although sodium metasilicate with water had the highest CO_2 emission among the other types, it was found to have the lowest embodied CO_2 index when used in the mix [138]. Luukkonen et al. [61] calculated the average environmental impact obtained from different studies and showed that the environmental impact of one-part geopolymers was 24% less than that of OPC, which is lower than the environmental impact of two-part geopolymers, which was 60% of the environmental impact of OPC. It is evident from the different results that using a solid activator to produce a one-part geopolymer is assumed to be an excellent solution to decrease the environmental impacts due to the benefits it presents compared with OPC and two-part geopolymers.

Incorporating a one-part AAM in construction applications can be a potential and feasible solution to meet the goals, of the European Cement Association, of decreasing the carbon footprint of cement to more than half by 2030 [148] due to the use of low-carbon materials in the mix. In addition, using one-part AAMs is comparable and even more economical than OPC in industrial applications.

2.3.5. Interim Section Conclusions and future directions

Implementing a one-part AAM in 3D printing technology offers several advantages over conventional AAM and concrete. The focus of this paper was mainly on the fresh and hardened properties of different mix designs of 3D printed one-part AAMs, their environmental impact, and their cost assessment. From this review, the following conclusions can be drawn:

1- Utilising GGBS in one-part AAMs can enhance the mix's properties. However, it decreases the open time and extrudability.
2- Increasing activator content can improve the rheological properties and mechanical strength of one-part AAMs while decreasing the open time and flowability, thus, limiting the printability of the mix.
3- Retarders and superplasticisers can be used to extend the open time and increase the flowability of a mix, but they will decrease yield stress, thixotropy, and mechanical strength of the mix.
4- One-part AAMs have slightly lower mechanical strength than two-part AAMs but are still stronger than OPC.
5- Depending on the type of materials used in the precursor, one-part AAM can result in reduced costs compared to OPC-based concrete samples. The most expensive material in OPC is cement, while for the AAMs, it is the activator.
6- The state of the art was extensively carried out on developing 3D printable one-part alkali-activated materials prepared using common SCMs (e.g., fly ash and GGBS) as precursors, with few studies focused on alternative materials. More research needs to be executed on different materials and wastes rich in aluminosilicate to expand the dataset on the suitable materials to be used as precursors in AAMs.
7- Incorporating a solid activator leads to around half of the environmental impact produced by a liquid activator, making one-part AAMs a more environmentally friendly mix. It also allows for practical use on a large scale due to eliminating the liquid activator risk.

Based on the presented review, besides the successfully developed one-part AAM mixtures for 3D printing, some challenges need further consideration in future research. Despite the good mechanical behaviour of one-part AAMs, further research is needed to eliminate the mechanical anisotropic behaviour of 3D printed filaments by conducting more studies on the effect of different printing parameters and the incorporation of fibre reinforcement. Moreover, the durability of 3D-printed one-part AAMs needs to be investigated since most studies focus on evaluating the mechanical properties, mainly compressive strength. The effect of incorporating different nano-particles on the fresh and hardened properties can also be investigated. Most researchers focused on investigating the effect of different mix designs on the mechanical and rheological properties of 3D printed one-part AAM. Its good performance and similar preparation procedures to OPC make it a suitable alternative in 3D printing for different industrial applications, including prefabrication and onsite construction. While open time had rarely been investigated and mostly had a narrow window when a solid activator is presented due to the rapid yield stress development, which restricts the use of one-part AAMs in the 3D printing application. Therefore, the effect of different parameters on the open time is to be investigated to develop a one-part AAM mixture with an adequate printing window to address this problem and to be used in building applications. Furthermore, the problem of limited open time for printing needs to be solved by investigating the effect of different types and dosages of retarders and superplasticisers, incorporating various materials in precursors, and changing the preparation parameters.

2.4. 3D printing of limestone-calcined clay cement system (LC3)

Even though SCMs could replace high OPC percentages, their low availability restricted their consideration as a main ingredient in 3D printing applications [20,22]. The abundance of clay and limestone (See Figure 2.10) and the benefits of their combination received significant interest in developing the so-called LC3 mixture. The binder of the LC3 system is mainly composed of clinker, calcined clay, limestone, and gypsum. The LC3 binder is obtained by either co-grinding the components or blending them together until achieving a homogeneous blend.

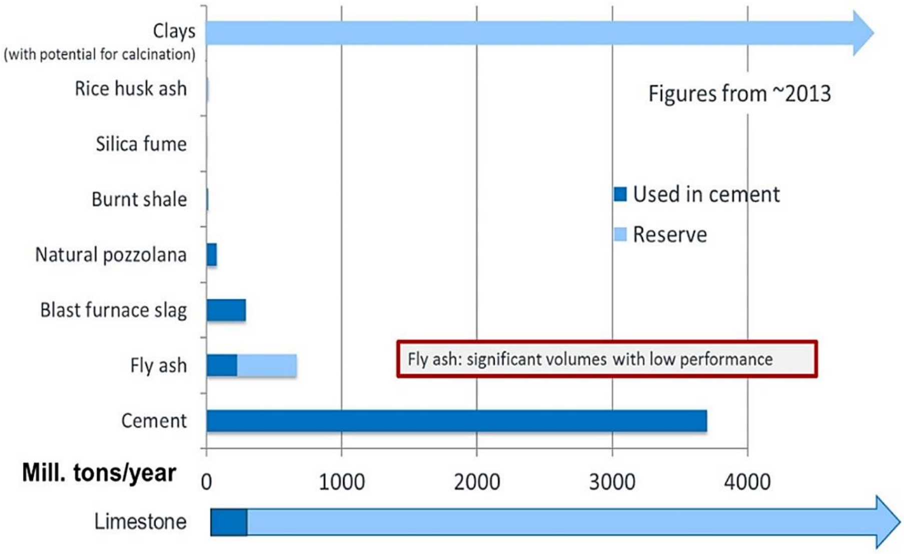

Figure 2.10. Supplementary cementitious materials availability [20]

The high availability, reactive components and chemical composition of calcined clay and limestone attracted researchers' interest, as it showed potential as an alternative for common SCMs to produce a ternary blended cement called LC3. Nevertheless, one of the main constraints facing clay is that despite its worldwide availability, not all clays are suitable for use as a cementitious material. Some standards require clays to meet a minimum chemical composition (e.g. ASTM C-618 [63]) in order to be counted as an SCM. In addition, it is hard to find clay with high kaolinite content. Kaolinite is the most reactive clay mineral and requires lower calcination temperatures than other types of minerals. Although the calcination temperature is half that of OPC, clay needs to be calcinated at elevated temperatures for different durations, depending on the type of clay used, which is considered an energy-intensive process.

Over the last few years, LC3 experienced a fast development due to the ability of limestone and calcined clay combination to replace high OPC percentage (more than 50%) [149,150], generate low CO_2 emissions, enhance the resistance to chemical attacks, and produce mixtures with comparable mechanical performance to conventional OPC after 7 days [151–154]. Due to those various advantages, LC3 was employed in traditional construction applications in many developed countries, where more than 25 buildings were built with LC3, some of which can be seen in Figure 2.11. In India, the most prominent project is the model Jhansi. This house is made of 98% LC3, which used 26.6 tonnes of industrial waste (192 kg/m^2) and saved 15.5 tonnes of CO_2 (114 kg/m^2). These CO_2 savings are similar to the emissions of 10 passengers travelling by plane from Switzerland to South Africa. The Swiss embassy in Delhi was also built with an LC3 blend. Other than India, LC3 was employed in Latin America, mainly in Cuba [155]. The use of LC3 blend in real-life applications presented a turning point to meeting the global goals and vision for sustainable development. The future directions are moving toward sustainability by combining the benefits of 3D printing technology and LC3 blend to lower environmental impact, waste production, and consumption of limited natural resources to manufacture cement.

Figure 2.11. Constructed LC3 buildings (a) Model house in Jhansi, India, (b) Model house in Santa Clara and (c) building at the Swiss embassy in Delhi, India [155]

Despite the evident advantages of LC3, its implementation in 3D printing applications is still new. In the last five years, several studies investigated the employment of LC3 in 3D printing technology to reduce its reliance on OPC as a binder and to enhance mixtures' properties. However, many research gaps need to be fulfilled to allow 3D printing LC3 on large scale. This section focused on reviewing different properties of the 3D-printed LC3 mixtures. The constituents and chemical behaviour of the LC3 system, OPC substitution level, reinforcing and rheology modifier admixtures, and limestone-to-calcined clay ratio, are thoroughly discussed in this section. In addition, the effect of different OPC replacement levels with limestone-calcined clay, clay minerals content (clay grade), sand ratio, and admixtures types and ratios on the fresh and hardened properties of 3D-printed LC3 mixtures are reviewed. The economic and environmental feasibility of LC3 mixtures employing 3D printing technology is also discussed and compared to conventional materials and production methods.

2.4.1. Limestone calcined clay cement (LC3) in 3D printing application

Researchers, on the one hand, have shown that replacing OPC with calcined clay alone produced mixtures with better printability, strength, and shape stability compared to fly ash [156]. In addition, calcined clay was noticed to enhance the cohesion, apparent viscosity, static and dynamic yield stresses, and thixotropy of mixtures [157]. On the other hand, it has been reported that substituting OPC with more than 10% of limestone alone would weaken the strength of the mixture and increase its water absorption [20]. However, the combination of calcined clay and limestone produces mixtures with enhanced mechanical and physical properties and allows the higher OPC substitution than their incorporation individually. The highest compressive strength performance within the first 28 days of curing could be obtained using a 1:2 ratio of limestone to calcined clay [151,152].

Clay is categorised depending on the packing of its octahedral (O) and tetrahedral (T) sheets and their arrangement and ratio in clay layers. Figure 2.12 illustrates the structure and chemical formulation of the most common clay minerals like kaolinite (1:1-type clay), montmorillonite (2:1-type clay), and illite (2:1-type clay). Kaolinite was used in most studies due to its higher pozzolanic reactivity than other clay minerals and the easier removal of water molecules in kaolinitic clays [158]. Prior to the partial substitution of OPC, clays should be activated. Several techniques for clay activation were reported in the literature, including thermal [159], mechanical [160,161] and chemical activation [162]. Thermal activation is the most used technique, by calcining (burning) clay at elevated temperatures between 600 – 900 ̊C for adequate time to remove water molecules from their structure in a phenomenon known as dihydroxylation [158,163]. Owing to the clay chemical composition, mainly alumina and silica, clay gains a pozzolanic reactivity when burnt at elevated temperatures by destroying the crystalline network, leaving silica and alumina in a disordered, amorphous and unstable state. It is worth noting that calcination does not affect quartz and other anhydrous minerals. Thus, the pozzolanic reactivity mainly depends on the thermal treatment condition and content of clay minerals [67,158,164]. Clay's reactivity decreases when increasing the temperature above 900 ˚C due to the sintering effect in the first place and then its recrystallisation into mullite, spinel and cristobalite [67]. The clay calcination efficacy can be measured by characterisation techniques (e.g., X-ray diffraction (XRD)) or reactivity measurements to ensure proper activation without recrystallisation. There are different techniques for measuring the reactivity of calcined clay that provide reliable results, including a new rapid, relevant and reliable (R3) method based on the correlation between chemical activity and the compressive strength in blended cement systems [152] and lime reactivity test [165]. However, more suitable approaches to measuring the calcination quality should be developed since these methods are time-consuming.

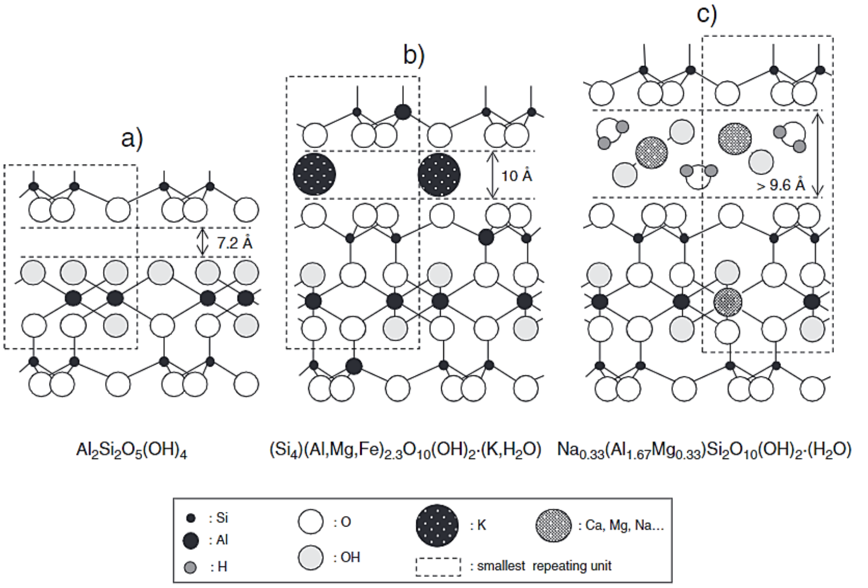

Figure 2.12. Chemical formula and structure of (a) kaolinite, (b) illite and (c) montmorillonite [158]

Calcined clay's chemical and mineralogical compositions and physical properties (i.e., fineness and morphology) may differ when obtained from different suppliers or origins [152,166]. Those differences can occur depending on the type of raw clay, purity of the clay, temperature profile, and calcination conditions, and they may substantially influence the fresh and hardened properties of the LC3 mixture [167–169]. There are several noticeable advantages of using calcined clay in concrete, especially low-grade kaolinite clays. These are (1) low CO_2 emissions released during the calcination process (approximately 0.3 kg CO_2/kg) [20], (2) similar strength behaviour to conventional OPC at an early age [170,171], (3) abundance and ease of obtaining [151,172], (4) lower cost [12,173] and (5) further refinement of mixtures' capillary pores [152,174]. According to Muzenda et al. [163], calcined clay is the main factor in the LC3 system that improves its static and dynamic yield stress, cohesion, adhesion, and plastic viscosity. In contrast, limestone can diminish these characteristics, thus, enabling tailoring the flowability of LC3. According to Tironi et al. [175], when raw clay contains more than 50% kaolinite, the pozzolanic activity of kaolinitic calcined clays appears to depend more on the raw kaolinite crystalline order than on kaolinite content.

2.4.1.1. Chemical reactions and pozzolanic reactivity

Portland cement is mainly composed of 55 – 65% alite ($3CaO.SiO_2$), known as C_3S, 15 – 25% belite ($2CaO.SiO_2$), known as C_2S, 8 – 14% aluminate ($3CaO.Al_2O_3$), known as C_3A, and 8 – 12% ferrite or brownmillerite ($4CaO$- Al_2O_3-Fe_2O_3), known as C4AF. These phases, in the presence of water, react to produce hydration products that include calcium silicate hydrate (C-S-H), portlandite (CH), ettringite (AFt), monosulfate (AFm) and monocarbonate. During the first few days of hydration, alite is the first silicate phase to react, contributing majorly to strength development during the first 28 days. However, belite is responsible for strength development after 28 days due to its slower reaction rate.

Ettringites are formed from the reaction between aluminate, gypsum and water, which further reacts with the remaining aluminate phases forming calcium monosulfoaluminate. Gypsum is added to OPC to control the reaction rate of aluminate through the adsorption of sulfate ions onto aluminate, controlling its dissolution [176,177].

The reaction of limestone-calcined clay consisting of calcined clay, like metakaolin ($Al_2O_3.2SiO_2$, abbreviated as AS_2), with limestone ($CaCO_3$) and $Ca(OH)_2$ forms similar reaction products, as shown in the following equation:

$$AS_2 + 6.4\ Ca(OH)_2 + 0.5\ CaCO_3 + 1.5CaSO_4 + 23.1H_2O \rightarrow 2C_{1.7}SH_4 + 0.5C_4ACH_{11} + 0.5C_6AS_3H_{32} \qquad \text{(Eq. 2.1)}$$

The presence of portlandite (CH) is vital to complete this reaction [151]. Hence, the amount of calcined clay that can react is affected by the amount of belite and alite found in the clinker [151]. Moreover, the reactivity of calcined clay at later ages is affected by the internal relative humidity of the material, where it declines with the decrease in humidity [178]. Low internal humidity would reduce the pore solution in capillary pores in the LC3 system, which limits the growth and development of hydration products to small-size saturated pores. Thus, limiting the space in which the hydration occurs.

The hydration product, calcium alumino-silicate hydrate (C-A-S-H), is formed from the reaction between silicate in calcined clay and portlandite, which mainly depends on the hydration temperature and kaolinite content in the clay [154,179]. In addition, some of the alumina from calcined clay is incorporated in the formation of this hydration product. Along with the pozzolanic reactivity of calcined clay and the filler effect of limestone, the alumina in calcined clay reacts with carbonate in limestone, producing synergy between the materials and resulting in a mixture with superior performance than OPC [151]. Moreover, the reaction between limestone, alumina phases from calcined clays, and cement forms carboaluminate. However, the development of this phase is delayed until the dissolution of sulphates in the pore solution [174]. Calcined clays produce an additional amount of hemi-carboaluminate and monocarboaluminate (AFm phases) in the presence of limestone [151,180]. It has been suggested that alumina dissolution and reaction depend on the available sulphates, unlike silicate reaction which depends on available CH in the system. The rate of reaction and hydration was also shown to be affected by the presence of alkalis, especially at early ages [181].

The reaction behaviour of LC3 compared to OPC was investigated in different studies by conducting isothermal calorimetry to observe the heat evolved during hydration [182,183]. The effect of incorporating limestone-calcined clay to replace OPC on the reaction kinetics was dependent on the replacement level, clay reactivity and sulfate content. In most cases, partially replacing OPC with limestone calcined clay would reduce the main hydration peak intensity. In some cases, the total heat released tends to increase at low replacement levels of OPC, which is expected due to the combined energy release from the hydration of OPC along with the pozzolanic reaction from limestone-calcined clay with the calcium hydroxide (CH) produced from OPC reaction. On the other hand, increasing OPC replacement level with limestone-calcined clay decreases the total energy released, due to the reduction in OPC particles, which reduces the amount of available CH for reacting with the pozzolanic materials.

2.4.2. 3D printed LC3: fresh and hardened properties

Different factors can affect the fresh and hardened properties of the LC3 system, including OPC replacement level, clay type and mineralogical composition, calcination temperature, calcination period, and water-to-binder ratio. The effect of incorporating higher replacement levels of limestone-calcined clay, various clay grade levels, adding other SCMs to the LC3 mixture, different sand-to-binder ratios and different sand gradation on the fresh and hardened properties of 3D printed LC3 mixture was studied by various researchers, as shown in Table 2.4. The effect of using different admixtures types and dosages (i.e., superplasticiser and viscosity modifying agents (VMA)) and the optimum dosages that can improve 3D printing properties were also investigated. It can be observed that all studies on 3D printing LC3 used a limestone-to-calcined clay ratio of 1:2. Adjusting the above-mentioned parameters affected the fresh and hardened performance of the LC3 mixture, as will be discussed in this section.

Table 2.4. Mix formulations of 3D printed LC3 materials obtained from different studies

Binder				**LP:CC ratio**	**Sand/ binder ratio**	**Sand size**	**W/b ratio**	**Admixtures (%-wt.)**	**Ref**
OPC	Limestone (LP)	Calcined clay (CC)	Others						
10 – 100%	0 – 30%	0 – 60% (about 50% metakaolin (MK))	0.3%-wt. Gypsum	1:2	1.5	0.125 – 2mm	0.3	Hydroxypropyl methylcellulose (HPMC)-based VMA 0.24%-wt. of binder Polycarboxylate ether (PCE)-based superplasticiser 1.5 – 2%wt. of binder	[182]
40%	20% 60% for the reference mix	0 – 20% High-grade CC (HGCC) (95% MK) 20 – 40% Low-grade CC (LGCC) (50% MK)	-	1:2	1.5	< 2mm	0.3	methylcellulose-based VMA 0.24%-wt. Superplasticiser 2%-wt. polycarboxylate (PCE)	[184]
35 – 100%	13.3%, 16.7%	26.7%, 33.3%	5 – 15% silica fume	1:2	1 – 4	-	0.48 -0.5 0.48	Polycarboxylate-based, high-range, water-reducing admixture (HRWRA) 0.4%-wt.	[185]
80% 55%	- 15%	- 30%	20% FA -	1:2	1.5	Uniformly-graded < 2mm Well-graded <4.75 mm	0.32 (reference) 0.4	Superplasticiser 0.15 – 0.7% 0.22%-wt. VMA 0.1%-wt. VMA	[186]
40%	20%	40% Low-grade (40 -50% MK)	-	1:2	1.5	<2mm	0.3	2% Superplasticiser 0.14, 0.24, 0.48% VMA	[24]
40%	20%	40% Low-grade (40% MK)	-	1:2	1.5	<2mm	0.3	2%-wt. Superplasticiser 0.14, 0.24, 0.48%-wt. VMA	[187]
40% 40%	60% 20%	-	-	1:2	1.5	>2mm	0.3	2%-wt. Superplasticiser (PCE)	[170]

		20 – 40% LGCC, 0 – 20% HGCC						0.24%-wt. VMA	
40%	20%	30% low-grade, 10% high-grade	-	1:2	1.5	>2mm	0.3	2% superplasticiser 0.24% VMA	[166]
25%	6.818%	13.636% high-grade	54.5% FA	1:2	0.8	>500µm	0.25	0.55% superplasticiser 0.15% VMA 2% fibres of the mix volume	[188]

2.4.2.1. Fresh properties of 3D printed LC3

The fresh state properties of 3D printable LC3 mixtures are considered the main defining parameters for successful 3D printing. These parameters include pumpability, extrudability, printability window (i.e., open time), and buildability [18,189,190]. Table 2.5 presents the fresh properties of the optimum mix design and the effect of changing some parameters on 3D printing as reported in the literature.

Table 2.5. Fresh properties of 3D printed LC3 mixtures

Mix formulation	Extrudability	Open time	Rheological properties	Buildability	Ref
10% OPC, 60% CC, 30% LP, 1.5 wt%. superplasticiser, 0.24 wt%. VMA	-Increasing the replacement level of OPC with limestone-calcined clay resulted in a quick loss of workability over time, where mixtures prepared with 75% and 90% limestone-calcined clay replacement levels had an extrudability window of 15 min. - The extrudability window increased with increasing superplasticiser content from 1.5% to 2% by 20 min for high replacement levels.	-Increasing OPC replacement level with limestone-calcined clay by more than 45% decreased the open time from 120 min to 45 and 25 min for 75% and 90% substitution levels, respectively. -The open time was prolonged by 50 min when increasing the superplasticiser percentage by 0.5%	-	-Mixture prepared with a 90% replacement level of OPC with limestone-calcined clay and 1.5 wt.% superplasticisers had the highest buildability, reaching more than 20 layers. The test was terminated due to insufficient material in the hopper. -Increasing the superplasticiser content weakened the buildability behaviour of the LC3 mixture.	[182]
40% OPC, 20% HGCC, 20% LGCC, 20% LP	-Increasing HGCC content increased the flowability of the mixture.	-Increasing the HGCC content decreased the open time of the mixture. -Mixture with 20% HGCC content had an open time of 30 min, while for 10% and 0%, the open time was 70 and 80 min, respectively.	-Mixture with the highest HGCC content had the highest shear yield stress.	-For a rectangle opening nozzle, increasing HGCC content enhanced the buildability of the mixture, where the mixture containing 20% HGCC is the only mixture that successfully printed a wall of 21 layers without collapsing. - The round opening nozzle showed fewer differences between the theoretical and measured heights of the printed objects and had more stable boundary	[184]

				conditions between the layers than the rectangle opening nozzle. -Only HGCC successfully achieved the designated number of layers (i.e., 18 layers)	
45% OPC, 33.33% CC, 16.67% LP, 5% SF, and 2.5 S/b ratio	-Increasing the sand-to-binder ratio decreased the quality of the extruded filaments, showing voids and discontinuity. -Increasing limestone-calcined clay content to 50% and silica fume to 10% resulted in minor defects on the surface, while other mix formulations were extruded smoothly.	-	-Using limestone-calcined clay to replace 40% and 50% of OPC increased static yield stress by 7 and 15 times, respectively. -Incorporating 5% and 10% silica fume in mixes containing 50% limestone-calcined clay resulted in almost 75- and 86-times higher yield stress, respectively. -Adding limestone-calcined clay and silica fume increased dynamic yield stress, plastic viscosity and structural recovery.	-Reference mixture was un-buildable compared to the mixtures containing SCMs. Incorporating limestone-calcined clay to replace OPC successfully printed the cylinder. However, it did not maintain its shape. -The combination of limestone-calcined clay and silica fume jointly improved the buildability of the mixture. -Increasing the sand-to-binder ratio improved shape retention of the mixture but, at the same time, induced extrusion problems.	[185]
LC3-well-graded sand 0.6% superplasticiser	-Cracks were observed in the LC3 mixture prepared with well-graded sand after a few minutes of printing due to a significant loss of workability. -Increasing the superplasticiser content enhanced the workability of the mixture and increased the spread diameter.	-LC3 prepared with well-graded sand prepared with 0.6% superplasticiser had an open time of 80 min, whereas the reference had 240 min.	- Rheology resistance under compression load was higher for the LC3 mixture compared to the reference. -Increasing superplasticiser content significantly decreased the rheological properties	-A maximum of five layers were printed using the reference mixture. -LC3 prepared with uniformly-graded sand with 0.4% superplasticiser was successfully used to print a 300 mm height cylinder. While adding 0.6% superplasticiser to the LC3	[186]

	-Using 0.6% superplasticiser for LC3 prepared with uniformly-graded sand enhanced the extrusion quality, where no cracks were observed during printing.		under compression load of the LC3 mixture. -Elongational viscosity was much higher for the LC3 mixture than the reference mixture and decreased with increasing superplasticiser ratio. -The LC3 system showed higher yield stress in the penetration test than the reference mixture, having a penetration resistance of 0.5, 4.5, and 7 MPa for reference, LC3 with uniformly-graded sand, and LC3 with well-graded sand mixtures, respectively.	prepared with well-graded sand resulted in similar flowability to the reference mix but increased the buildability to 210 mm before collapsing. -LC3 with well-graded sand containing 0.6% superplasticiser was printed with 76 layers and 1.14 m height.	
LC3-0.24% VMA	-Increasing VMA dosage increased the required pressure for extrusion.	-Increasing VMA dosage from 1.2% to 2% and 4% reduced the open time of the mixture from 90 min to 70 and 50 min, respectively.	-	-Increasing VMA dosage improved the shape stability of the mixture. -Mixture prepared with 0.12% VMA dosage exhibited severe layer deformation and had the worst buildability. -Increasing VMA dosage increased the green strength of the mixtures, where 0.48% VMA achieved high values up to 2.5h.	[24]

40% OPC, 20% LP, 40% low-grade CC	-The mixture prepared with the highest VMA dosage had better cohesion during the visual inspection of the extruded materials. -Increasing VMA dosage increased the extrusion pressure.	-	-Increasing VMA dosage increased the elongational yield stress and shear yield stress.	-Increasing VMA dosage enhanced the shape retention in the first 2h. -A stable shape could be found immediately after extrusion for 0.48% VMA. However, using 0.14% and 0.24% VMA produced a stable shape after 25 min and 60 min, respectively.	[187]
40% OPC, 20% low-grade, 20% high-grade and 20% LP	-Increasing calcined clay grade (MK content) showed a higher extrusion pressure growth rate with time. - After reaching the initial setting time, mixtures prepared with medium and high-grade clay showed significantly high extrusion pressure -Using high-grade calcined clay increased the extrusion pressure, which may bring extruding difficulties.	-Using high-grade calcined clay increased the extrusion shear strength, reducing the mixture's open time.		-The incorporation of high-grade calcined clay enhanced the green strength of the mixtures, which improved the buildability of the fresh mixture in the 3DCP process.	[170]

2.4.2.1.1. Rheological parameters

Yield shear stress, plastic viscosity, and thixotropy are the main rheological parameters investigated by researchers. Yield shear stress can be divided into static and dynamic yield shear stresses, where static yield stress is the stress needed to start the system flow, while dynamic stress is the stress needed to keep the flow [191]. After removing the stress or pressure applied, the flow stops, and thixotropy happens. Thixotropy is the restoration of the mixture’s static yield stress by initiating the flocculation of particles due to inter-particle interaction [104].

The different behaviour of fresh mixtures under static and dynamic stresses could be due to the mixtures' rheology and thixotropy, which depend mainly on the mix design. That is related to the binder composition, particle shape, water percentage, and aggregate gradation and content. Long et al. [185] showed that incorporating limestone-calcined clay increases the static yield stress by 7 and 15 times when replacing 40% and 50% of OPC, respectively. Moreover, the incorporation of 5% and 10% silica fume (SF) into the mixture containing 50% limestone-calcined clay resulted in around 75 and 86 times higher static yield stress, respectively. That is due to the higher water absorption and flocculation induced after adding limestone-calcined clay and SCMs can increase the static yield stress of the mixture [156]. The static yield stress increases due to limestone-calcined clay particles that possess angular geometry, which can increase inter-particle locking [173,192]. Besides the replacement level, adding high-grade calcined clay increases the shear yield stress of the mixtures due to the inclusion of more reactive calcined clay [184,193,194]. For instance, Chen et al. [184] found that increasing metakaolin content in calcined clay increased the shear yield stress, as shown in Figure 2.13. Moreover, incorporating limestone-calcined clay and SF also increase the dynamic yield stress, plastic viscosity, and thixotropy of mixtures [185].

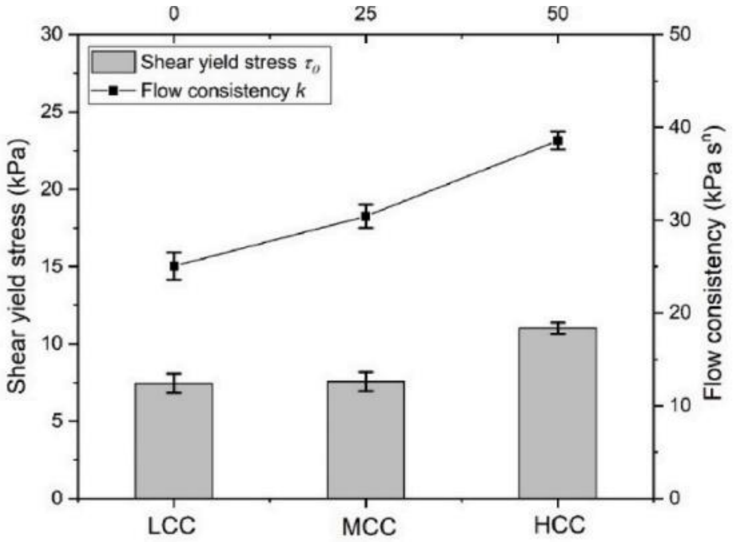

Figure 2.13. Shear yield stress and flow consistency of mixtures LC3 mixtures prepared with LCC: low-grade calcined clay, MCC: medium-grade calcined clay, and HCC: high-grade calcined clay [184].

Replacing OPC with 40% and 50% limestone-calcined clay exhibited a thixotropy recovery of 96% and 67% in the mixture, respectively, compared to 62% in OPC [185]. The better thixotropic behaviour when incorporating limestone-calcined clay is due to the particle flocculation because of its morphological structure, which also increases the yield stress [195,196]. The improvement in the thixotropic behaviour of the mixture could be due to the nature of calcined clay that exhibits a shear-thinning behaviour, which induces a flocculation structure and absorbs a high quantity of free water. After removing the load or shear stress, it can rebuild the intermolecular forces and flocculation structure [163,168]. That is because clay particles are heavily charged, where the faces possess negative charges and the edges positive charges, allowing them to produce scaffolding structures with the hydroxide and calcium ions produced from OPC reaction with water. That, in turn, influences clay particle flocculation behaviour and enhances the thixotropy recovery of the mixture [197]. It is noteworthy that fresh cementitious materials require a high thixotropy in 3D printing for the deposited layers to have enough yield stress to withstand the gradually increasing load induced by the succeeding deposited layers' weight [198]. However, the high thixotropy may result in weak interface adhesion [5,84].

Moreover, increasing the aggregate/binder ratio in the mixture induces a higher static yield stress due to the higher packing density and solid-to-solid contact because of the smaller spacing in the presence of more sand. Increasing the sand percentage in the mixture increases the dynamic yield stress and plastic viscosity but decreases the structural recovery (thixotropy).

This is due to the low binder content, which reduces the flocculation and the formation of hydrates, thus, reducing the structural recovery [185]. Shantanu et al. [186] argued that the impact of sand type and gradation is not significant in the first few minutes, indicating that the rheology effect of the binder is dominant. The authors stated that using well-graded and uniformly graded sand did not exhibit any differences at the first few minutes, whereas LC3 prepared with well-graded sand exhibited significantly higher yield shear stress and viscosity than the uniformly graded sand after 30 min.

The most effective way to enhance the workability and adjust the rheological parameters of a printable mixture could be by incorporating admixtures [64,187,199]. Most of the work on 3D printing LC3 has incorporated additives such as viscosity-modifying agents (VMA) and superplasticisers, as shown in Table 2.4. Superplasticiser addition reduces viscosity and yield stress, which reduces the required extrusion pressure [186]. Nonetheless, the addition time of the superplasticiser (i.e., directly at the beginning of mixing with water or delayed) plays a key role in the rheology of the mixture. Matos et al. [200] found that adding superplasticiser directly with the mixing water significantly increased yield stress by 3.4 times and structuration rate by 2.2 higher than the mix with 10 minutes delayed addition. On the other hand, VMA incorporation improves the rheological parameters and the needed pressure for the extrusion process [24]. It has been reported that VMA increases the plastic viscosity and/or yield stress of the mixture for a fixed dosage of superplasticiser [201]. Although SP and VMA are mostly used together, many studies did not consider the fact that hydroxypropyl methylcellulose (HPMC) as a VMA has the potential to rival superplasticisers in its ability to adhere to cement or other small particles, which can ultimately impact the dispersion of superplasticisers [47,64,202].

2.4.2.1.2. Extrudability and pumpability

Extrudability is the ability to smoothly extrude the printable mixture under pressure from the nozzle without any discontinuity or breakage. On the other hand, pumpability is the transporting process of the mixture under pressure from the reservoir to the nozzle through a pipe without affecting the mixture's properties (i.e., workability and rheological properties). Extrudability and pumpability mainly depend on the mixtures' rheological behaviour (i.e., static yield stress and plastic viscosity). Depending on the type of printer used and if there is no additional pressure, extrudability and pumpability can be considered similar processes. Hence, pumpability and extrudability, in this review paper, were considered to be one process defining one material property due to the fact that recent studies employed printers without any additional pressure input. This property was defined as the ability to print material in a continuous filament and acceptable quality [7,18,88]. The incorporation of limestone-calcined clay mainly lowers the mixture's workability, decreasing the mixture's extrudability. Hence, LC3 printability depends mainly on the replacement ratio. For instance, Chen et al. [182] found that increasing OPC replacement level with limestone-calcined clay up to 90% decreased the mixtures' flow rate due to different rheological performance, where rapid stiffness was observed with increasing limestone-calcined clay content, reducing the workability of the mixture and thus the extrudability. According to the authors, increasing the superplasticiser content can enhance the extrudability of the mixture even at high OPC substitution levels. However, it lowers the mechanical performance of the mixtures.

The rheology, flowability and fresh cementitious mixture strength are strongly related to the corresponding water film thickness (WFT) [203–208] as it could be formed from excessive water on the particles' surface to reduce friction between particles [204]. Incorporating limestone-calcined clay could increase the physical properties of the mixture, including total specific surface area (SSA) and solid friction, which in turn affects WFT. It was reported that packing density was not affected by replacing OPC with limestone-calcined clay, where a slight decrement was observed when incorporating it in a high percentage (i.e., 90% limestone-calcined clay) [182]. In contrast, the SSA of dry binder increased with increasing limestone-calcined clay content, possibly due to the high SSA of calcined clay. Moreover, the higher SSA of LC3 mixes reduced the WFT. According to Chen et. al. [182], the most significant factor affecting fresh properties is the WFT of pastes as a basic indicator incorporating various physical characteristics, i.e., water content, packing density, and SSA.

The grade of calcined clay (i.e., MK content presented in the clay) can also affect the printability and extrudability of the mixture. Increasing the calcined clay grade increases the extrusion pressure growth rate over time. Increasing the MK content, present in the clay, would accelerate the cement particles' phase change from flocculation to structuration [170]. At an early age, most SCMs (including MK) act as fillers, as indicated by Lothenbach et al. [209], since the pozzolanic reaction is generally dependent on the hydrated cement products. One of the main effective properties of fillers is their fineness, which could offer additional surfaces for the nucleation sites for the hydration products.

Increasing the solid percentage (sand content) could lower the quality of the printed mixture, producing more defects in the samples due to the high friction between the solid particles and the low binder volume present in the composite. Long et al. [185] investigated the effect of incorporating different percentages of limestone-calcined clay, silica fume, and sand on the extrudability of the mixture. They found that increasing the sand content in the mixture produced voids and discontinuity in the extruded filament, as shown in Figure 2.14. Moreover, it was found that incorporating high percentages of limestone-calcined clay along with silica fume could result in minor defects on the surface of the extruded filament. Superplasticisers were used in most of the proposed LC3 printable mixtures to enhance their extrudability and flowability by reducing viscosity and yield stresses [24,166,170,184–187].

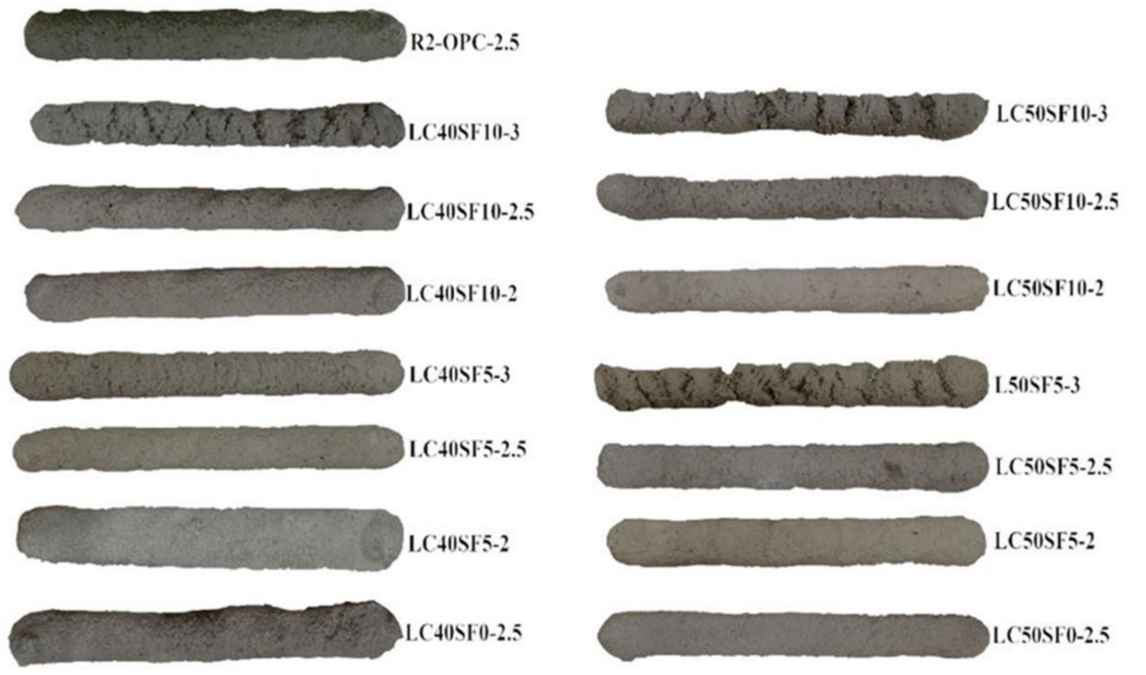

Figure 2.14. Extrudability of LC3 mixtures with different limestone-calcined clay, SF and sand contents [185]

2.4.2.1.3. Open time and setting time

Open time, also known as the printability window, is the period at which the mixture can be printed with acceptable quality through the nozzle without any cracks [202]. The open time and setting time are directly related to the workability and rheological properties of the mixture. Using a pump in the 3D printing process induces high friction, which increases the mixture temperature and results in a faster loss of workability [182]. Pumpability and buildability are significantly affected by the open time, where the mix with low open time may face difficulties during the extrusion process due to the rapid development of yield stress over time. In contrast, mixtures with long open time may limit the structure's buildability while printing due to the low structuration rate.

The setting and open time mainly depend on clay mineral content and OPC replacement level. Incorporating calcined clay containing a high percentage of kaolinite (high-grade clay) decreases the setting time of the mixtures. Chen et al. [170] found that the initial setting time decreased with the higher MK content in the calcined clay, which could be due to the acceleration effect that MK induces in the matrix. The authors showed that the mixture prepared with low-grade calcined clay (40 – 50% MK) had an initial setting time of 147 min compared to those of medium (around 62.5% MK) and high-grade (about 75%) mixtures of 78 and 52 min, respectively. Thus, using high-grade calcined clay shorten the open time of the composite. As explained in Section 4.1.2, that could be due to the acceleration effect in the presence of more MK. Due to clay's porous nature and limestone's high fineness, increasing OPC substitution ratio lowers the workability of the composite [182]. That will decline the flowability and narrow the printability window of the composite.

A suitable way to extend the open time of the mixture is by increasing the superplasticiser content [182]. It has been reported that increasing the replacement ratio of OPC with limestone-calcined clay reduces the open time of the mixture, whereas incorporating higher superplasticiser dosages prolongs it [182]. Another way to extend the open time is by subjecting the mixture to continuous mixing and pumping [186]. On the other hand, incorporating VMA admixture can shorten the open time of mixtures, as shown in Figure 2.15 [24]. Although the open time of the investigated mixtures is long enough, more studies concerning the influence of changing the retarder content and aggregate/binder ratio and incorporating other SCMs and admixtures on the open time of the LC3 mixture are needed.

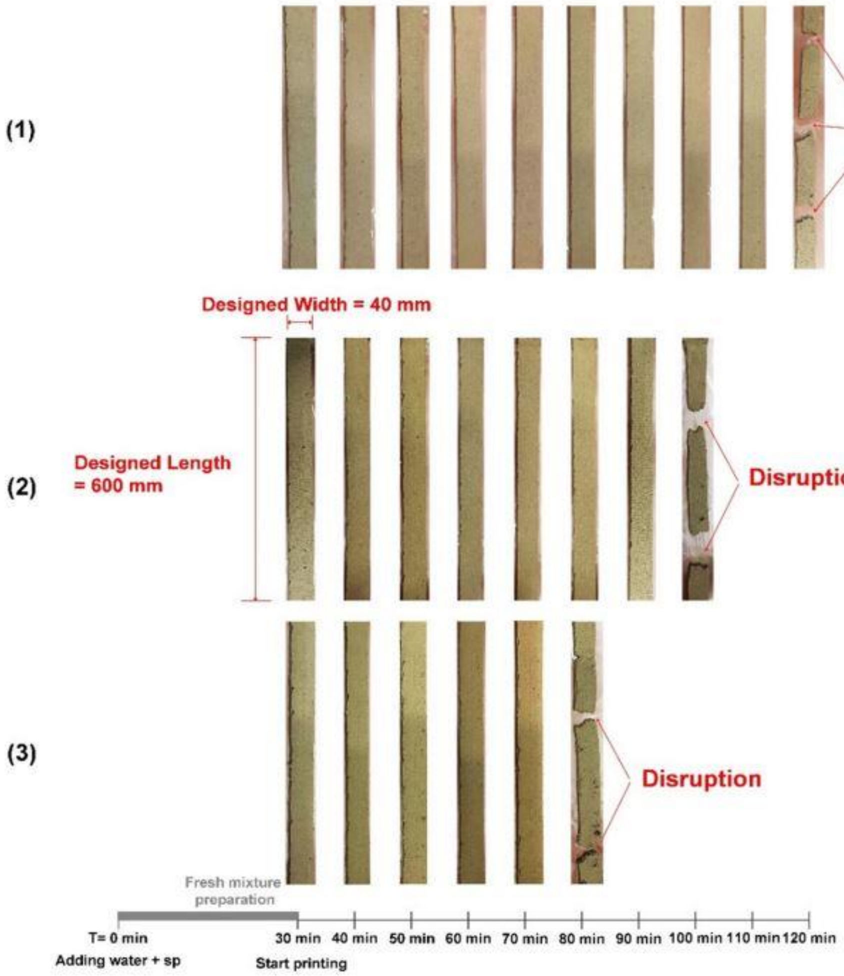

Figure 2.15. Open time of LC3 mixtures containing (1) 0.14%, (2) 0.24%, and (3) 0.48% VMA [24]

2.4.2.1.4. Buildability

Buildability is the ability of the printed mixture to retain its geometry under the loads brought from the upper layers [147]. Buildability mainly depends on the static yield stress [15], which is affected by OPC replacement level, water content, and calcined clay grade. Mixtures that show rapid growth in static yield stress immediately after extrusion have the least deformation during printing successive layers, allowing for better buildability. In addition, buildability is affected by geometrical and material properties. Chen et al. [184] investigated the effect of using two different nozzle openings and heights on the buildability of LC3 mixtures prepared with different calcined clay grades. The first nozzle had a rectangular opening with a height of nozzle opening of 13.5 mm, and the second had a round opening with an 8.5 mm height. The round opening nozzle showed fewer differences between the measured and theoretical height and had more stable layers than the rectangle opening. The authors found that the mixture prepared with the highest content of high-grade calcined clay achieved good buildability in both nozzle shapes. Increasing the substitution level of cement with limestone-calcined clay decreased the workability, which in turn increased the shape stability of the mixture, thus, resulting in a better buildability performance [184]. In another study, Chen et al. [182] investigated the effect of replacing up to 90% of OPC with limestone-calcined clay on the buildability behaviour of the mixture. The authors found that the mixture with the highest replacement level (90%) exhibited the highest buildability performance, reaching more than 20 layers. While mixes with lower replacement levels collapsed due to mix instability induced by plastic deformation in the bottom layers. Increasing the number of printed layers increases the self-weight load on the bottom layers, resulting in their compaction and a decrease in their theoretical height, which increases the designated standoff distance and causes instability when printing the succeeding layers. According to Chen et al. [182], structural instability occurs due to the plastic deformation induced by the self-weight of successive layers, which increases the standoff distance, as illustrated in Figure 2.16. In addition, the authors employed a down-flow nozzle in their study that prints the succeeding layers by a squeezed forming process, increasing the load the bottom layers should withstand. These forces compacted the bottom layers and increased their width, causing a decrement in the contact area between layers and resulting in structural instability. It is reported that the addition time of superplasticiser influences the mixtures' buildability. Matos et al. [200] reported that the direct addition of superplasticiser to LC3 doubled the mixtures' buildability without impacting the open time of the mix compared to that of a 10-minute delayed addition.

Buildability is also affected by the sand-to-binder ratio used in the composite. Sand content in the mixture affects the static yield stress, where the higher the sand percentage, the higher the static yield stress, thus, the better the buildability of the mix. Long et al. [185] showed that increasing the OPC replacement level with limestone-calcined clay from 40% to 50% improved the buildability of the LC3 mixture and allowed for more layers to be printed, but that was not sufficient to maintain its shape and presented large deformations. The authors found that the hybrid incorporation of LC3 and SF can effectively improve the mixture buildability and retain the object shape, as shown in Figure 2.17. Although increasing the sand content can improve the buildability and shape retention of the mixture due to the better static yield stress, extrusion problems (e.g., blockage in nozzle or poor-quality filaments) occur when exceeding certain sand content. The buildability and shape stability of the printed filaments can be improved by incorporating additives like VMA to adjust the mixture's rheological properties. According to [64,88,210], a small dosage is sufficient to improve buildability.

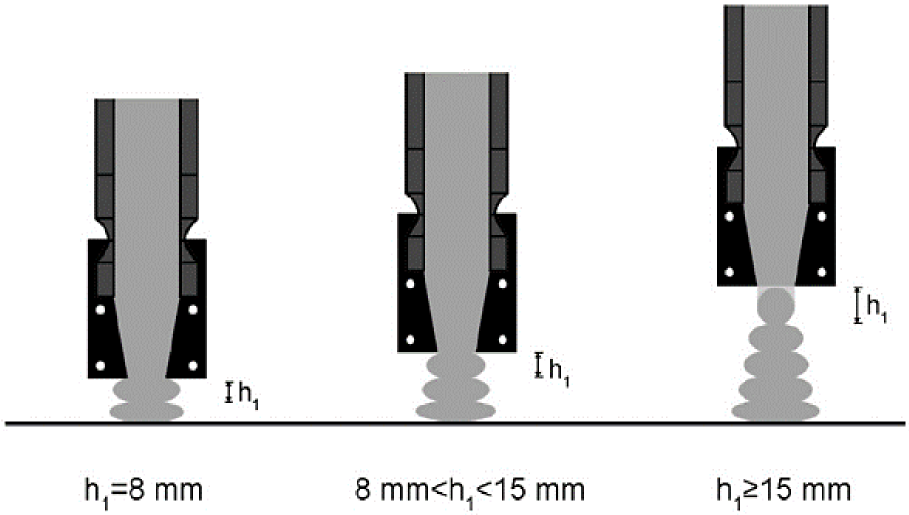

Figure 2.16. Illustration of the increased standoff distance with the more compaction induced from the weight of the top layers [182]

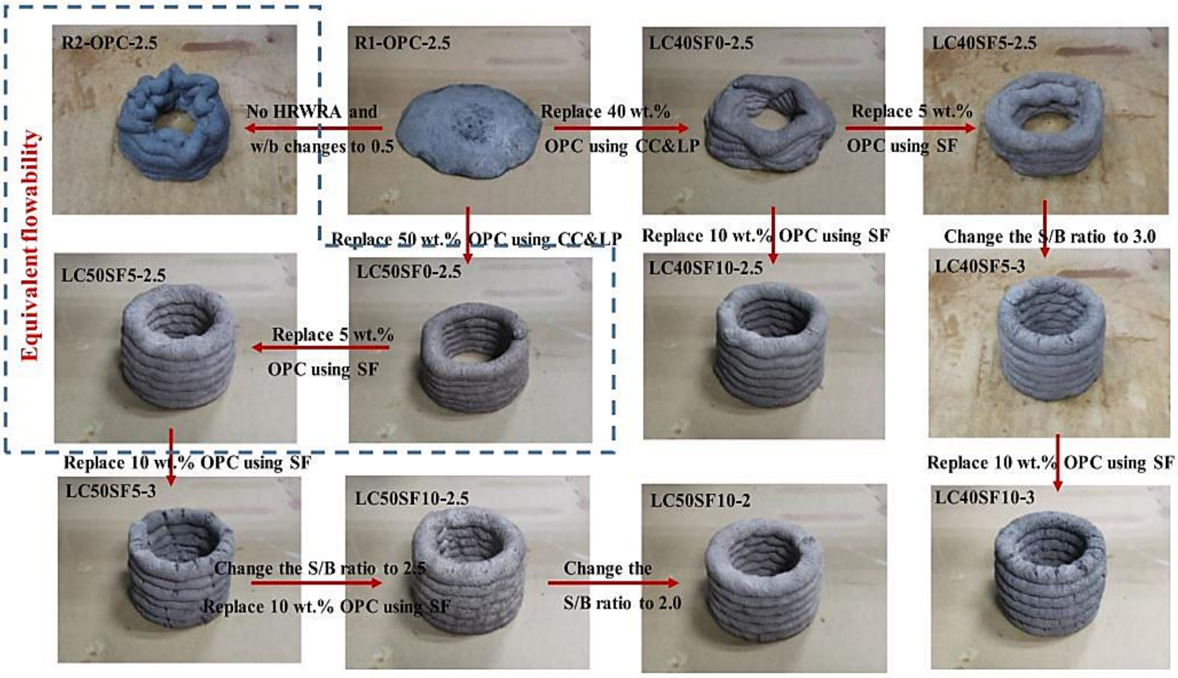

Figure 2.17. Buildability and shape retention of the object using different LC3 mix formulations [185]

2.4.2.2. Hardened properties of 3D-printed LC3

2.4.2.2.1. Compressive strength of cast and 3D printed LC3

The effect of different mix formulations on the compressive strength is presented in Table 2.6. One of the main advantages of limestone-calcined clay is its ability to replace a high amount of OPC, around 40–50%, without having a remarkable reduction in compressive strength. The mechanical performance of LC3 mixtures mainly depends on the OPC replacement level and clay grade, as shown in Figure 2.18, which presents compressive strength results obtained from different studies in the literature for LC3 mixtures with different kaolinite content and replacement levels after 7 and 28 days. For instance, Chen et al. [170] found that the strength development rate and green strength significantly increased with increasing kaolinite content in the calcined clay. At later ages, the compressive strength of cast specimens was found to be more dependent on the MK content in the calcined clay. The authors concluded that increasing the MK ratio could significantly accelerate the initial cement hydration, which results in higher mechanical performance. Moreover, Avet et al. [152] stated that the compressive strength of the LC3 mixture mainly depends on MK content, regardless of the calcined clay's fineness, compositions, and secondary phases. Although calcined clay with high MK content could improve the mechanical performance of mould-cast cementitious mixtures at an early age, using high-grade calcined clay in 3D printing could lower the mechanical performance of the printed samples due to the increased thixotropy that results in forming cold joints. Chen et al. [184] investigated the effect of different grades of calcined clay on the mechanical properties of 3D-printed LC3 and found that LC3 prepared with medium-grade clays (around 70% MK) showed the highest compressive strength performance. The low mechanical performance when incorporating high-grade clays could be due to the high thixotropy that can allow for the easy formation of weaker interfaces and cold joints [5,84]. In 3D printed cementitious materials, it is typical to find a high amount of air voids between two layers with a weak adhesion in the interface, which could be due to the high structuration rate [128,211,212]. According to Avet et al. [153], porosity refinement when incorporating clay with kaolinite content above 65% results in reaching a critical pore entry radius that slows the reaction and restrains hydrated phase participation, which limits the strength at later ages (28 days). Another critical role that can influence the compression performance of the LC3 system is the OPC replacement level. Various studies have shown that replacing OPC with up to 50% limestone-calcined clay can achieve similar mechanical performance. Nevertheless, increasing the OPC substitution ratio declines the compressive performance of the mixture [182,183]. According to Zhou et al. [213], increasing the substitution level of OPC results in forming fewer hydration products (i.e., C-S-H) due to the less OPC presented, thus, reducing compressive strength.

Unlike cast LC3, 3D printed LC3 had anisotropic properties in compressive strength performance when loads were applied in different directions. Chen et al. [184] found that different LC3 mixtures exhibited the highest compressive strength when loads were applied parallel to the printing direction, as shown in Figure 2.19. This anisotropic behaviour could be due to printing quality and the weak interface [93]. The better compressive strength performance parallel to the printing path could be due to the more compaction in the printing direction because of the movement patterns [93]. In addition, layer weight should be taken into account due to its ability to compact layers and cause variation in compressive performance [128]. Compared to cast specimens, on the one hand, 3D-printed samples have a denser microstructure due to intense pressure during printing. On the other hand, 3D-printed specimens and objects have a weaker interface with higher porosity and air content [125,214], which might lower their performance under compression and cause this anisotropic behaviour. Wang et al. [188] investigated the compressive strength performance of LC3-ECC (Engineering cementitious composites), containing a high volume of fly ash and 2% polyvinyl alcohol (PVA) fibres. According to Wang et al. [188], the printed layers experience a tensile loading when it is perpendicular to the loading direction, resulting in weakening the strength performance in the direction parallel to the printing path since it experiences more interlayer forces. Moreover, in the presence of fibre, PVA fibres play a key role in dispersing the stresses when the load is applied laterally or perpendicularly to the printing path, in addition to their bridging effect, which contributes to the anisotropic compression strength behaviour of the printed mixture.

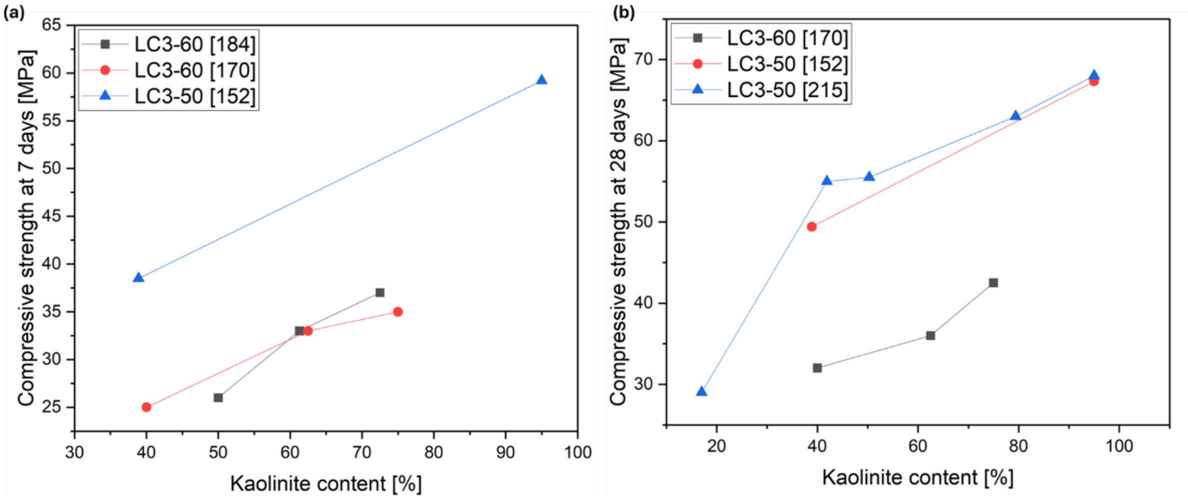

Figure 2.18. Effect of kaolinite content in calcined clay on LC3 strength properties [152,170,184,215]

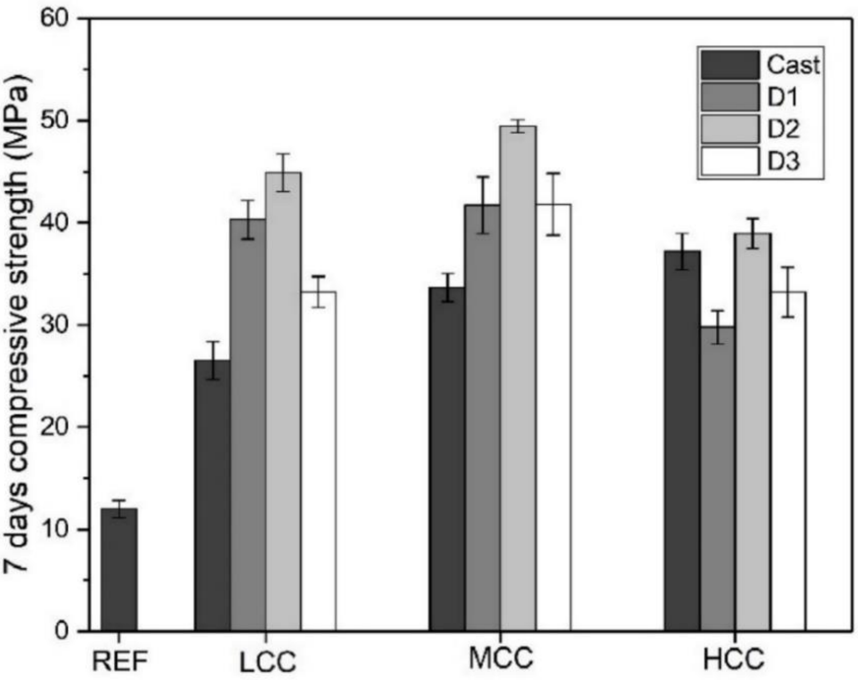

Figure 2.19. Compressive strength of cast and 3D-printed LC3 samples at different directions at 7 days (D1: perpendicular, D2: parallel, and D3: lateral to printing path) [184], where LCC is low-grade calcined clay, MCC is medium-grade calcined clay, and HCC is high-grade calcined clay.

The gradation and percentage of sand can also influence the compressive strength of mixtures. Shantanu et al. [186] claimed that incorporating well-graded sand enhances the compressive strength of the mixture due to better particle packing compared to uniformly graded sand. Similarly, Long et al. [185] showed that increasing the sand content increases the strength performance of LC3 mixtures due to the better packing density of the mixture. However, increasing sand above a certain level might reduce the binder content that covers aggregates, which decreases compressive performance due to a decline in cohesion.

Superplasticiser was incorporated in different studies to enhance the printability properties of LC3 mixtures. However, its incorporation degrades the early-age mechanical performance of the mixture. According to Chen et al. [182], increasing the superplasticiser percentage from 1.5% to 2% reduced the compressive strength by around 50% at 1 day, where the effect diminished at later ages beyond 3 days.

Table 2.6. Compressive strength of 3D-printed LC3 mixtures

Optimum mix formulation	Compressive strength	Ref
55% OPC, 30% CC, 15% LP, 1.5 wt%. superplasticiser, 0.24% VMA	-A significant loss in compressive strength was observed with increasing OPC replacement level with limestone-calcined clay at different test ages. -Increasing the superplasticiser content decreased the compressive strength values.	[182]
40% OPC, 20% HGCC, 20% LGCC, 20% LP	-The LC3 mixture exhibited higher compressive strength values than the reference mixture. -3D printed mixtures exhibited higher strength performance than the cast mixture. -Mixture prepared with 10% HGCC and 30% LGCC had the highest strength values for 3D-printed specimens. 3D-printed specimens containing 20% HGCC achieved lower strength values -The highest compressive strength was obtained when applying load lateral (D2) to the printing direction.	[184]
45% OPC, 33.33% CC, 16.67% LP, 5% SF, and 2.5 S/b ratio	-Increasing limestone-calcined clay content decreased the compressive strength values. -The addition of 5% SF increased the compressive strength. -Mixture prepared with a 2.5 sand-to-binder ratio achieved the highest compressive strength values in all mixtures	[185]
LC3-MS, 0.6% superplasticiser	-The compressive strength results of the LC3 mixture prepared with well-graded sand (MS) were comparable to that of the reference mixture at all test ages. -The LC3 mixture prepared with uniformly graded quartz sand (QS) had comparable compressive strength to the MS and reference mixtures at 1 day, with lower results at 7 and 28 days.	[186]
LC3 – 0.24%VMA	-Reference cast mixture prepared without VMA exhibited higher compressive strength values than the printed mixtures with different VMA dosages. -Increasing VMA dosage from 0.14% to 0.24% increased the strength performance in all directions. Further increase of the VMA dosage to 0.48% decreased the strength values to a lower level than 0.14%. -The highest compressive strength was reported for all printed specimens when the load was applied parallel to the printing direction.	[24]
40% OPC, 20% low-grade, 20% high-grade and 20% LP	-Compressive strength increased with increasing the MK content in the mixture at all test ages. -All mixtures had higher compressive strength than the reference mixture.	[170]
25% OPC, 13.636% CC, 6.818% LP, 54.5% FA	The 3D-printed sample achieved higher compressive strength performance than the cast, with the highest strength in the direction perpendicular to the printing path.	[188]

2.4.2.2.2. Bond strength of 3D-printed LC3

Table 2.7 presents the impact of different parameters that has been investigated on the bond strength of 3D printed LC3. Interlayer bond strength is believed to be a weakness between two adjacent layers in printed structures [198]. Due to a lack of intermixing between the old and new layers, a weak interlayer adhesion occurs, usually referred to as the cold joint [84,216,217]. Thixotropy dominates the formation of weak interlayer bonds (cold joints) from a material perspective [84]. In addition, bond strength can be affected by the time interval between the succeeding layers and the nozzle standoff distance.

Although prolonging the time gap between the layers could offer the extruded filaments more time for the evolution of static yield stress, it can lead to decreased bond strength [15,218,219]. There are no specific time intervals, but the printability window (open time) could be a boundary for dividing the time interval length since cement is a time-dependent material. For short time intervals, Tay et al. [211] confirmed that the adhesion between the layers at the interface is affected by the thixotropy behaviour of the deposited mixtures [211]. While for long time intervals, on the one hand, bond strength may be influenced by the printing environment [218,219]. For instance, different studies revealed that the bond strength of deposited layers could exhibit a noticeable reduction under a drying environment [113,128,212]. Sanjayan et al. [10] and Van Der Putten et al. [220] indicated that the moisture content of the surface of the layer is crucial concerning bond strength. Hence, seeking methods to retain the deposited layers’ surface moisture is essential.

On the other hand, the nozzle standoff distance could be changed depending on the change of layers' height since it is challenging to avoid extruded material deformation. Changes in the distance standoff may cause severe or limited effects on the bond strength of the mixture depending on the difference in the contact surface area between the layers. Chen et al. [166] investigated the influence of using three different time gaps (i.e., 20 s, 1 min, and 10 min) and three nozzle standoff distances (i.e., 0, 5, and 10 mm) on the bond strength of 3D printed LC3 mixture and compared it to cast mixture. The authors found that using a time gap of 20 seconds resulted in around 14% higher tensile strength than the cast mixture. While increasing the time gap to 1 minute and 10 minutes, decreased the tensile strength by 4% and 13%, respectively, compared to the cast specimen. Only a slight decrease in the bond strength resulted from increasing the nozzle standoff distance. The decline in the bond strength with increasing time gap could be due to the increased local porosity in the interlayer zone, as illustrated in Figure 2.20**.** A stiffer layer surface minimises the deformation in the surface of the bottom layer induced by succeeding layer weight, which could limit the interactive bond space between the layers [211]. That, in turn, increases the unfilled area between layers, causing more macro-pores and increasing the porosity in the interface.

Incorporating additives and admixtures could also influence the bond strength of 3D-printed LC3. Most recently, Ibrahim et al. [221] reported that the early age bond strength of the cast and 3D printed samples decreased with increasing superplasticiser content. In contrast, comparable results were obtained for the different ratios for cast samples at later ages. However, for 3D printed specimens, the mixture prepared with 0.8% exhibited higher strength performance at 7 and 28 days than the mixture with 0.6%, which could be due to the difference in the surface moisture content. Moreover, anisotropic behaviour was observed for bond strength depending on the testing direction, similar to compressive strength. Bond strength exhibited comparable values to cast when tested parallel to the printing direction and higher than the perpendicular direction. According to Ibrahim et al. [221], printing parameters and the strength development of materials influence bond strength. The hydration product formation and chemical compatibility of materials improved between the deposited layers when incorporating limestone-calcined clay due to their synergistic effect, silicate minerals' stick nature in kaolinitic calcined clay, and chemical admixtures incorporation significantly strengthened the bonding strength.

Studies on the LC3 interlayer bond strength are limited. Further research is required to illustrate the effect of varying the mix design, calcined clay grade, and limestone to calcined clay ratio on the bond strength of 3D-printed LC3 mixtures.

Table 2.7. Impact of different parameters on the bond strength of 3D printed LC3

Investigated parameters	**Bond strength**	**Ref**
Time intervals	-Increasing the time interval decreased the interlayer bond strength.	[24]
-Nozzle standoff distance (0, 5 and 10 mm). **-Time intervals (20 s, 1 min, and 10 min),**	-The bond strength decreased with increasing the time gap. -Using a time gap of 20 s resulted in higher bond strength for the printed specimen than the cast specimen. Increasing the standoff distance up to 10 mm did not induce a critical effect. -A nozzle standoff distance of more than 10 mm resulted in an inaccurate layers' positioning.	[166]
Superplasticiser addition (0.8 and 0.6%)	- Increasing superplasticiser content decreased the 7-day strength results of the cast and 3d printed samples while slightly affecting the cast's later age bond strength values. - 3D printed specimens with 0.8% exhibited higher strength performance than 0.6% at later ages and were comparable to the cast. - 3D printed specimens exhibited better performance in the lateral direction than in the perpendicular direction.	[221]
25% OPC, 13.636% CC, 6.818% LP, 54.5% FA	-The bond strength was slightly higher in the horizontal direction than in the vertical direction by around 25%.	

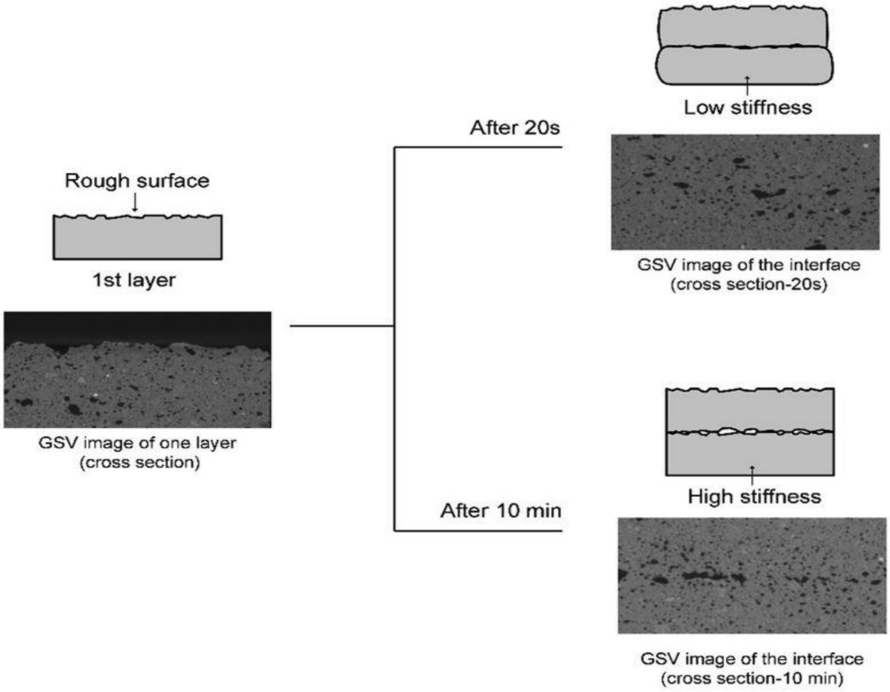

Figure 2.20. The influence of different time gap intervals on the interface of the 3D printed specimens [166]

2.4.2.2.3. Porosity of 3D printed LC3

One of the main advantages of limestone-calcined clay is microstructural refinement induced by the different products formed from the pozzolanic reaction [151,152,169,222]. In addition, the high fineness of limestone particles allows it to act as a filler and reduce porosity [23,223]. The porosity is mainly affected by the water-to-binder ratio, where decreasing the ratio decreases the porosity of the mixture [170]. Kaolinite content in calcined clay can also affect the porosity of LC3 mixture at early ages. Avet and Scrivener [153] investigated the porosity of different calcined clays with various kaolinite content in LC3. The porosity was found to be depended on kaolinite content at early ages (3 days), showing lower porosity values and finer pore microstructure when calcined clay contains kaolinite content of more than 65%. At 28 days, LC3 prepared with calcined clay containing less than 50% kaolinite content showed significant pore refinement, having finer pore microstructure than OPC. The authors have shown that all LC3 mixture containing calcined clay with a kaolinite content of 40% or more had similar critical pore entry radius of 3 – 5 nm. In 3D printing technology, printing parameters, such as time interval and nozzle standoff distance, can affect porosity. Chen et al. [166] investigated the effect of different printing time gaps (20 s, 1 min and 10 min) on LC3 interlayer and local porosity and found that the local porosity increases with increasing time intervals between layers. However, the total porosity of the different mixtures was comparable, except for cast and 10 min time intervals, as shown in Figure 2.21a**.** Extending time gaps between layers could increase the concentration of macropores along the interface (see Figure 2.20), which increases the local porosity value, as shown in Figure 2.21b. According to [211], at short time intervals, the load induced from depositing succeeding layers would rearrange the top surface of the substrate layer, increasing the interacted area between the two layers. However, increasing the interval time would allow more time for the stiffness growth of the substrate layer, which decreases the changes that could occur when depositing the successive layer and, in turn, limits the interacted bond areas between layers and increases macropores formation. In this study, the authors have also studied the effect of different nozzle standoff distances (5 and 10 mm) on LC3 porosity and obtained similar total and local porosity values, as shown in Figures 2.21 (a and b).

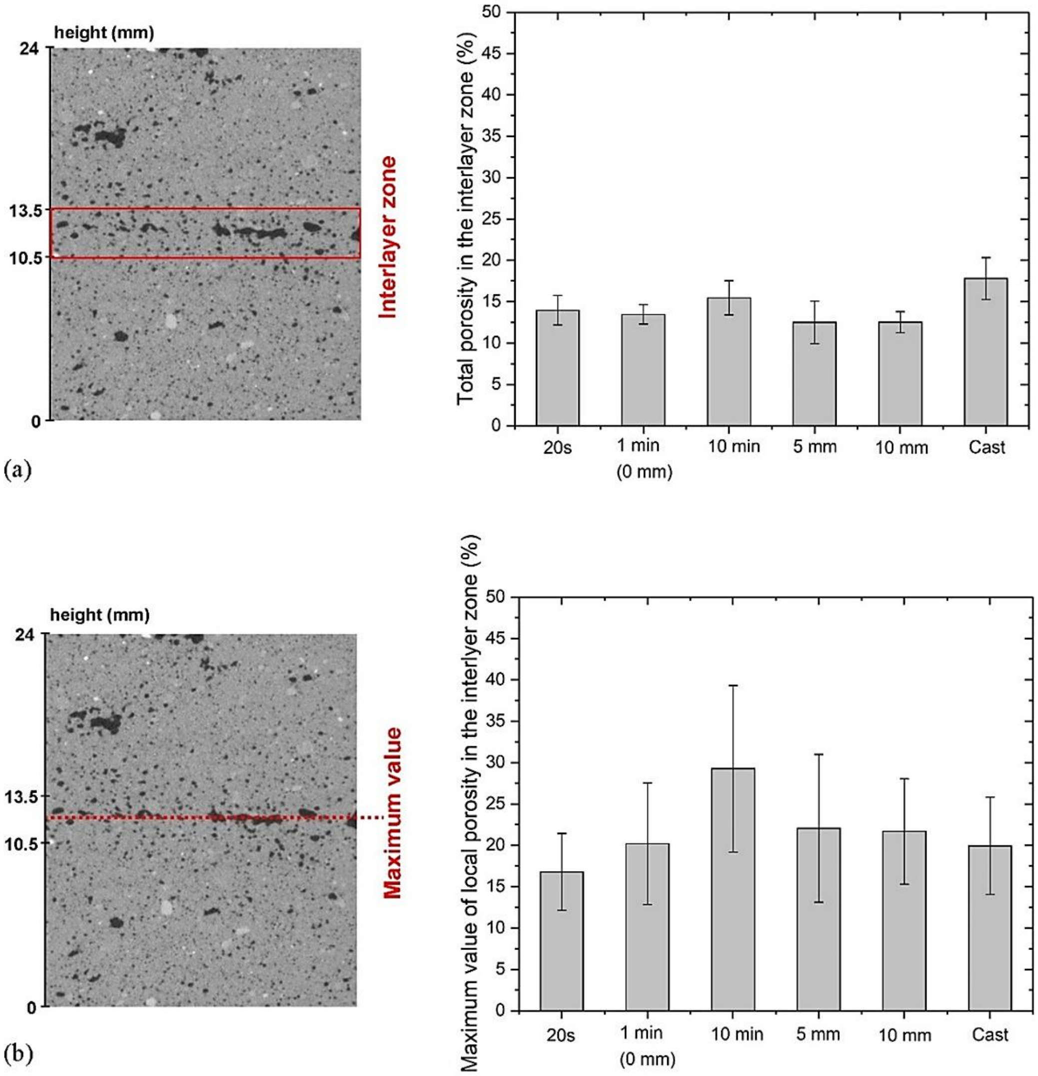

Figure 2.21. (a) Total porosity in the interlayer zone and (b) maximum local porosity in the interlayer zone [166]

VMA was used in different studies to enhance the various properties of the mixtures. Incorporating VMA increases the porosity of the mixture [187,224]. For instance, Chen et al. [24] investigated the effect of adding different dosages of VMA (i.e., 0.14%, 0.24% and 0.48% by weight of the binder) and found that the optimal dosage of VMA is 0.24%, which achieved the lowest porosity. According to the authors, porosity is affected by the adhesion between the two layers, which is affected by the rheological properties of the lubrication layers. The lubrication layer viscosity should not be too low since it would contain higher water content, thus, increasing the porosity. At the same time, the viscosity should not be too high because it would increase the extrusion pressure and the porous microstructure in the layer and the interface [24]. Therefore, it is preferable to control and optimise the used dosage of VMA to avoid degradation in the other properties. Based on the different studies that investigated the effect of VMA dosage on LC3 properties [24,182], the optimum dosage of VMA for 3D printing could be recommended as 0.24% by the weight of the binder with considering optimising the superplasticiser content in the mixture.

2.4.3. Environmental sustainability of LC3

A comparison between different construction methods has revealed that 3D concrete printing produced the lowest CO_2 emissions and it can become the most sustainable construction method in near future [132]. However, the concrete mixture used in 3D printing requires higher amounts of OPC binder than the traditional casting method [141], which makes the research on environmentally-friendly alternatives to OPC vital [4]. The impact of replacing OPC with limestone-calcined clay on CO_2 emissions and energy consumption has been studied using life cycle assessment (LCA) [225]. It was found that replacing cement with limestone-calcined clay significantly lowered CO_2 emissions to 610 kgCO_2/tonne of cement and energy consumption to 4850 MJ/tonne of cement compared to that of OPC of 930 kgCO_2/tonne of cement, 5945 MJ/tonne of cement in traditional cast method. LC3 had also lower CO_2 emissions than pozzolanic Portland cement (PPC) prepared with fly ash that exhibited 680 kgCO_2/tonne of cement but with slightly higher energy consumption, in which PPC requires 4690 MJ/tonne of cement.

Common SCMs are derived from industrial applications and activities, such as fly ash [226,227], silica fume [228], and other naturally obtained SCMs like limestone [229–231].

Clay can be considered an environmentally friendly SCM. However, unlike the other common SCMs, clay needs to be processed and calcinated to be used. The production of calcined clay requires lower energy and generates fewer CO_2 emissions than OPC, which helps decrease the negative environmental impact by using blended cement containing those SCMs with maintaining similar performance. The energy required for clay calcination was reported to be around 60% of that to produce OPC [232]. In addition, CO_2 emissions from clay calcination are almost 30% of that from OPC manufacturing. Long et al. [185] selected mixtures having similar properties to the reference mix to allow for a reasonable evaluation of different mixtures' environmental impact. The results showed that the various composites prepared with limestone-calcined clay and silica fume as a replacement to OPC had around 41 – 50% lower greenhouse gas and 39 – 45% less energy consumption than the reference mixture. Malacarne et al. [233] investigated the environmental performance of LC3 mixtures prepared with four different types of Brazilian clays compared to OPC and found that LC3 had lower greenhouse gas emissions by around 38% than OPC. The authors found an average emission of 516 kgCO_2/tonne of LC3 cement produced. Similar values were also reported in the Indian context of 550 kgCO_2/tonne [232] and the Cuban context of 550–562 kgCO_2/tonne of LC3 cement [234]. The production of LC3 can help mitigate the carbon dioxide amount released into the atmosphere, contributing significantly to climate change.

Unlike OPC production, the main causes of greenhouse gas in calcined clay production are clay extraction and processing, followed by calcination. Different studies reported that calcined clay could be responsible for producing CO_2 emissions in the range of 150–300 g/kg [20,234,235]. Berriel et al. [225] compared the environmental impact between OPC, blended cement containing 15% zeolite and LC3 systems under three different technological levels, namely Pilot (no investment), Industrial (low investment), and Best Available Technology (BAT) (massive investment). The authors found that LC3 had the lowest impact whatever the technological level used, as shown in Figure 2.22. The reduced emissions of LC3 were not only from the calcination process but also from energy savings from LC3 crushing and grinding due to its softness compared to OPC. Although LC3 can reduce emissions, the availability of clay sources plays a significant role in LC3 production. Hence, the environmental impact depends on the transportation type and location distance to the plant.

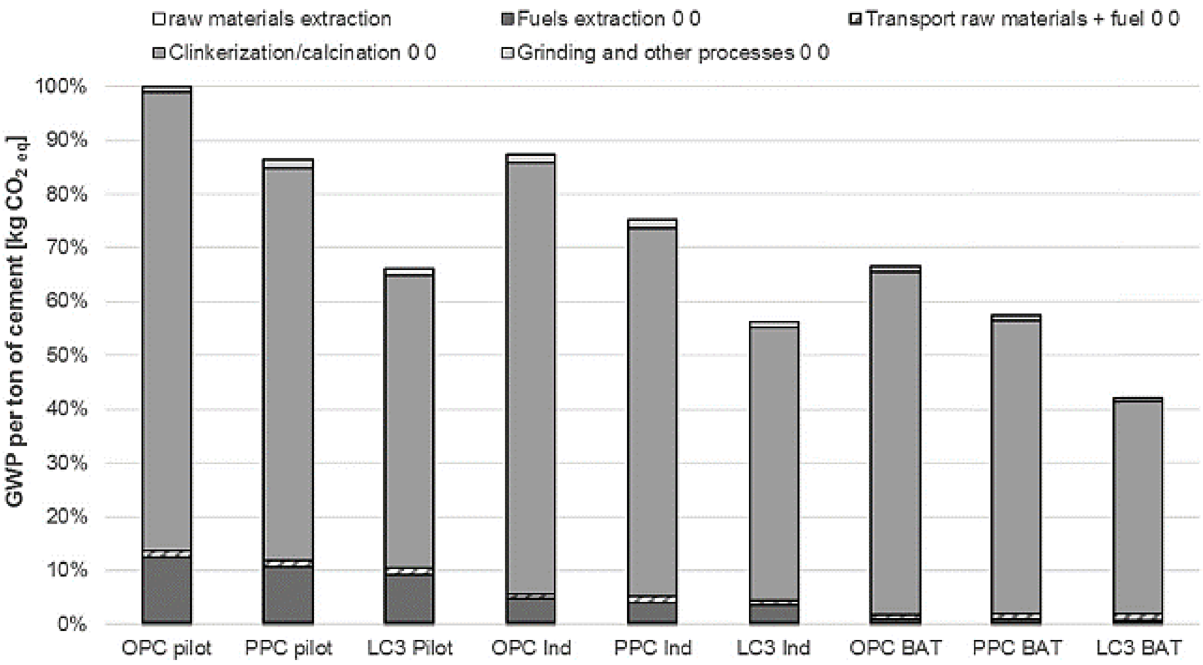

Figure 2.22. Global warming's potential impact on different scenarios of cement production in Cuba [225].

2.4.4. Economic feasibility of 3D printed LC3

Using 3D printing technology could provide potential cost savings. Implementing 3D printing offers suitable economical solutions in terms of required manpower, material saving, and energy. That will also be reflected in lowering the number of co-workers for formwork preparation, decreasing the overall cost by around 50% or more [17]. Compared to the different construction methods, the concrete 3D printing system is more economical, where the overall cost in one of the studies was divided into 55% construction cost and 45% material cost [132]. The total cost of construction can be further decreased when employing the 3D printing method by implementing different approaches, including using alkali-activated materials and blended cement to reduce the cost of printing materials, using 3D printing hollow structures or incorporating industrial by-products and recycled aggregates [46,134,135]. Moreover, the construction cost could change depending on the printing technique, material delivery systems, and process precision. Hence, the machinery and the cost change depending on the method used. The machinery can be categorised into unconventional construction equipment (UCE) and conventional construction equipment (CCE). Often CCE, such as a piston pump, can deliver the material to the print head. While for extrusion and printing, a print head in new equipment with a multi-functional complex design is needed. Indeed, for a successful industrial implementation, a print head should be fitted with sensors that continuously track the evolution of material properties for data feedback and active rheology control and should be flexible to change in size and shape. With all these advancements, print heads will become a substantial cost factor [48]. It is expected that price of 3D printing technologies fall due to the industrial competition [236]. However, some challenges might face the owner of the printers since its new to the construction industry, including the availability of spare parts and the lack of expertise for maintenance. The operational and maintenance cost of a 3D printer was estimated to be 75$/h [8,237].

Different studies have confirmed the economic feasibility of cast LC3 in various scenarios [11,225,238]. The economic assessment differs from one country to another, depending on the locally used materials, since the alternative feasibility must be compared to that of the product that has the potential to replace it. Different factors can influence the economic viability of the material, like transportation mode and distance and availability of the material. In addition, since LC3 is composed of raw material (i.e., clay) that needs to be calcinated and processed, processing plays a significant role. Berriel et al. [225] assessed the economic potential of LC3 prepared using four different types of Cuban calcined clay by performing Capital and Operational Expenditures. The authors indicated that changing technology or fuel type changes production costs. Moreover, depending on the type of transportation used, production cost tends to increase with the transportation distance. Nevertheless, there are limited cost analyses on LC3 compared to other cementitious binders, especially in 3D printing applications.

2.4.5. Section conclusions

Utilising limestone calcined clay cement (LC3) in 3D printing technology presents several advantages over traditional concrete systems. This paper focused on reviewing the materials properties of cast and 3D printed LC3, the environmental impact and cost assessment of cast LC3. The following conclusions can be drawn from this review:

1- The rheological properties and thixotropy of the mixture increase when incorporating limestone-calcined clay, where using high-grade clays or increasing replacement levels could further modify rheological performance. Nevertheless, a higher replacement level and using high-grade clay content can lower the mixture’s flowability, extrudability and open time. Moreover, incorporating additives and admixtures can modify the rheological parameters of LC3, at the same time, influence other printing properties.

2- Increasing the replacement level can enhance the buildability of the LC3 mixture. Similarly, using high-grade clay could improve the buildability. In addition, nozzle shape and geometrical properties affect the buildability of the mixture.

3- Metakaolin content in calcined clay plays a key role in influencing the cementitious mixture's different properties and in the printable mixtures' performance. Although incorporating high-grade calcined clay in cast method is preferable and provide better performance, using high-grade calcined could lower the mechanical performance of 3D printed LC3. Moreover, a high replacement level can also lower the mechanical performance of both cast and 3D printed LC3.

4- Printing parameters (i.e., nozzle standoff distance and time gap intervals), layer surface moisture content and additives incorporation affect the bond strength behaviour of 3D printed LC3 mixture.

5- Production of LC3 mixtures can lower economic and environmental impacts compared to that of OPC. Depending on the substitution level, LC3 allows a 30–50% reduction in CO_2 emissions and energy consumption. However, the economic and environmental feasibility tends to depend on the availability and location of clay sources.

6- While most studies focused on using calcined clays with medium-to-high kaolinite content (>40% kaolinite content) to develop 3D printable LC3 mixtures, incorporating available local low-grade clays (< 40% kaolinite content) as calcined clays could assess with upscaling LC3 mixtures, making LC3 more accessible and economically viable for both cast and 3D printing applications.

The implementation of LC3 in 3D printing applications is still new. Hence based on the presented section, further research studies are needed to fulfil the research gaps. Further research is needed to investigate the effect of different mix designs, additives, admixtures, printing parameters and mixing time on the bond strength and porosity of 3D-printed LC3. Most studies were executed to investigate the mechanical and printing properties of LC3 prepared with calcined clay containing at least 40% kaolinite content. Hence, more studies are needed to understand the impact of utilising locally available low-grade clays with a kaolinite content lower than 40%. Moreover, the durability and flexural strength of 3D-printed LC3 mixtures must be investigated since most studies focus on investigating the compressive strength performance of printed mixtures. Although the open time of LC3 mixtures is suitable for 3D printing, more studies should consider the effects of different parameters and admixtures on the large-scale delivery of the material to the extruding nozzle. Moreover, the impact of incorporating different additives and admixtures on the flowability and slump performance of the mixtures should be further investigated since it could indirectly indicate the performance of the printing mixtures.

2.5. Challenges and research gap

The limitations and challenges after reviewing the literature can be summarised as follows:

1- Most existing studies focused on investigating the different properties of one-part AAM prepared by employing common SCMs, such as fly ash and silica fume. Although their good performance and suitability in AAM, the availability of these materials can be troublesome depending on the regional location. The reliance on these common SCMs makes the development of AAM and its application challenging. In addition, the engineering and printing-related properties of one-part AAM containing brick powder as binder have not been studied thoroughly to understand its suitability as a building material, specifically for the use as a feedstock for 3D printing applications for structural applications.

2- Investigation on recycling brick aggregates in one-part AAM on the different durability properties are limited.

3- Available research focused on developing 3D printable LC3 mixtures with a calcined clay containing at least 40% kaolinite content. However, not all regions have access to clay deposits containing a clay with 40% kaolinite mineral content or more, and locally available clays mostly have lower kaolinite content. Moreover, existing studies have not investigated the various engineering properties of LC3 prepared with low-grade kaolinite content to develop a better understanding of the material performance.

4- There has been no study conducted to investigate the 3D printability of LC3 containing low-grade calcined clay. Hence, more research on locally available clays should be executed to investigate their reactivity in calcined form, and their potential to be used in the LC3 system is needed.

5- The effect of incorporating brick aggregate on the printing-related properties of one-part AAM and LC3 has not been investigated.

Ultimately, the study aims and seeks to contribute to the transition of the construction industry towards greener and more sustainable practices by promoting the adoption of the circular economy framework through repurposing and valorising locally available construction waste to be reused as a construction material.

3. CHAPTER 3: INVESTIGATION OF THE SUITABILITY OF USING BRICK AS BINDER AND AGGREGATE ON THE PROPERTIES OF ONE-PART AAM

3.1. Introduction

This chapter provides a comprehensive explanation of the rationale for replacing fly ash with brick powder and natural aggregates with brick aggregates. It comprehensively investigates the efficiency and suitability of using local waste material in the UK, namely waste brick, in two physical states, powder and aggregate, to partially replace fly ash precursor with 10% increments and natural aggregate by 30, 50, and 70% in AAMs. Moreover, the compatibility and effect of incorporating nano-graphite platelets with 0.1, 0.5, and 1% dosages were investigated. The flowability, mechanical strength, microstructure, water absorption, freeze-thaw resistivity and fire resistivity were investigated on the different mixtures. Moreover, the embodied carbon was assessed as well. It should be noted that the outcomes of this chapter have been published as a journal paper:

1) **Yazeed A. Al-Noaimat**, Mehdi Chougan, Mazen J. Al-kheetan, Marcus H. N. Yio, Hong S. Wong, Seyed Hamidreza Ghaffar. Developments in the Built Environment, Volume 16, 14 September 2023, 100231. *https://doi.org/10.1016/j.dibe.2023.100231*

3.2. Theoretical background

The most common precursors used in AAM (i.e., FA, SF, and GGBS) are not available in some countries and their availability will severely decrease in the upcoming years due to significant efforts toward reduction of carbon dioxide. Thus, it is crucial to introduce alternative binder materials [70]. Meanwhile, construction and demolition waste (CDW) amounts are gradually increasing with the increase in construction industry activities, population, and urbanisation. Around 45% of CDWs, excluding soils, are brick and ceramic wastes [34–36]. Disposing brick and ceramic waste in landfills is a costly and ecologically detrimental practice that consumes precious land resources [29,30,38,39]. The incorporation of recycled brick aggregates (BA) is limited due to their higher porosity compared to concrete aggregates [31]. Various studies have examined brick as an aggregate in mixtures, with mixed results regarding its impact on performance. While incorporating brick aggregate (BA) can diminish durability by increasing the transport properties of mixtures [31,239], it improves thermal and acoustic insulation [239] and decreases drying shrinkage. This is because BA has high water absorption and releases water to the binder matrix as the binder loses water during hydration and moisture exchange with the environment, thereby facilitating internal curing [240,241]. Nevertheless, many outstanding questions regarding the performance of concrete containing recycled brick aggregates remain.

The valorisation of waste materials rich in silica and alumina, such as brick, as precursors in AAMs has been gaining interest in recent years. Bricks contain high Al_2O_3 and SiO_2, similar in composition to supplementary cementitious materials (SCMs) such as fly ash. Therefore, some studies have investigated the feasibility of using end-of-life bricks as a binder replacement in concrete and alkali-activated materials [242–246]. Migunthanna et al. [247] investigated the effect of incorporating different brick powder (BP) percentages in one-part AAM. They found that the mixture containing 40% BP and 60% GGBS achieved a compressive strength of 48 MPa after 7 days of curing. Most recently, Pasupathy et al. [68] investigated the suitability of using brick powder as a precursor in one-part AAM for 3D concrete printing. Their study demonstrated that substituting 10% of FA with BP improved the mechanical properties of cast and 3D printed mixtures by up to 12%. However, further increasing the BP content negatively impacted the strength of the materials. Various studies have examined the properties of cast and 3D-printed one-part AAM made from different precursor materials, but research on brick-based AAM is limited.

3.3. Experimental program

The experimental framework considered in this section to investigate the effect of replacing FA with BP, NA with BA and incorporating nG on the properties and performance of one-part AAM is illustrated schematically in Figure 3.1**.**

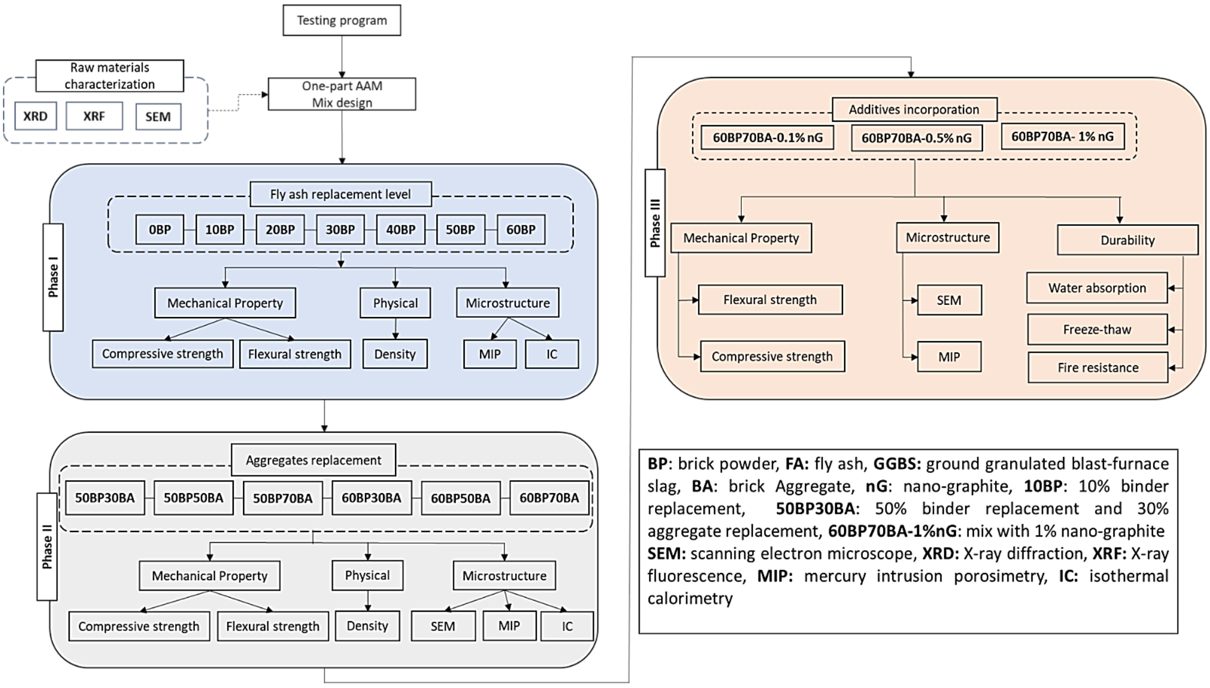

Figure 3.1. Experimental test program

3.3.1. Raw materials

A commercial fly ash (FA) under normal fineness (N) category conforming to BS EN 450-1:2012 [248] was supplied by Cemex, UK. A commercial ground-granulated blast furnace slag (GGBS) was supplied by Hanson Heidelberg Cement, UK, following BS EN15167–1 [249]. Brick powder processed from end-of-life bricks collected from a demolition site near Brunel University London was used as a precursor. The collected bricks were crushed manually using a hammer, followed by automatic crushing using a 100-grinder machine (Retsch, Germany) equipped with a 2 mm mesh (See Figure 3.2a**)**. The obtained material was further crushed and ground using a ball mill (Retsch, Germany) (See Figure 3.2b) containing 8 balls for 5 min with a speed of 500 rpm, followed by sieving through a 125 µm mesh to obtain brick powder (BP). Figure 3.3 presents the preparation process for BA and BP. The alkali activator was sodium metasilicate (SS) powder (Na2SiO3) with a density of 2.61 g/cm^3 and a molecular weight of 122.062 g/mol was supplied by Fisher Scientific, UK. The activator has a SiO2/Na2O alkali modulus of 1.6 and a purity of 97.5%. The mineralogical composition and particle size distribution of FA, GGBS and BP are presented in Figure 3.4. The XRD pattern shows that FA is highly amorphous and contains traces of quartz and mullite. On the other hand, the predominant phase in BP was quartz due to the presence of SiO_2 in clay minerals and the incorporation of sand in brick manufacturing [250]. The crystallinity index (CI) of FA and BP was determined using the Rietveld method and was found to be 50% for FA and 70% for BP. The chemical oxides of FA, GGBS, and BP are presented in Table 3.1. The chemical compositions of BP and FA are comparable for most oxides. Furthermore, the true particle density of FA was determined to be 1.98 g/cm^3 and 2.44 g/cm^3 for BP.

Nano-graphite platelets (nG) Grade K6Nan with a purity of 97.5% and 6–7 nm lamella thickness index were obtained from Nanesa srl., Italy. nG platelets were added to reinforce the developed one-part AAM due to their ability to enhance the cementitious mixtures' mechanical performance and durability.

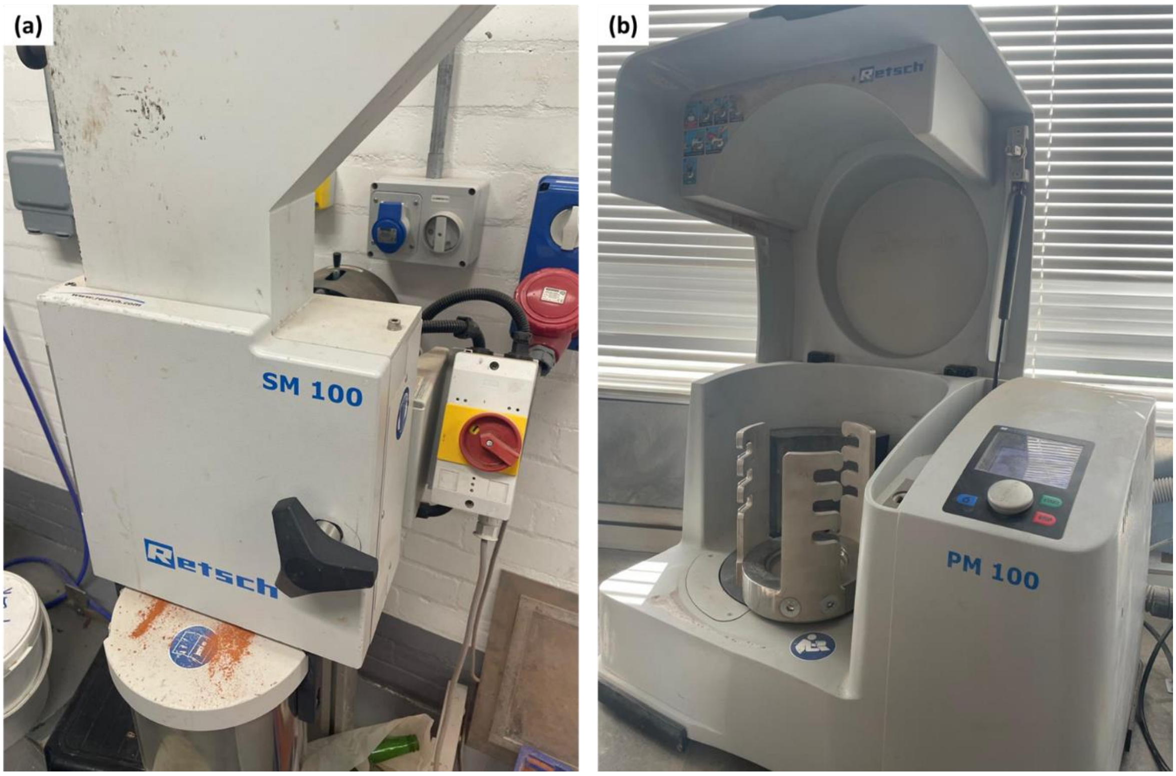

Figure 3.2. (a) Retsch SM100-grinder machine and (b) Retsch ball mill machine.

Figure 3.3. Brick powder and brick aggregate preparation process.

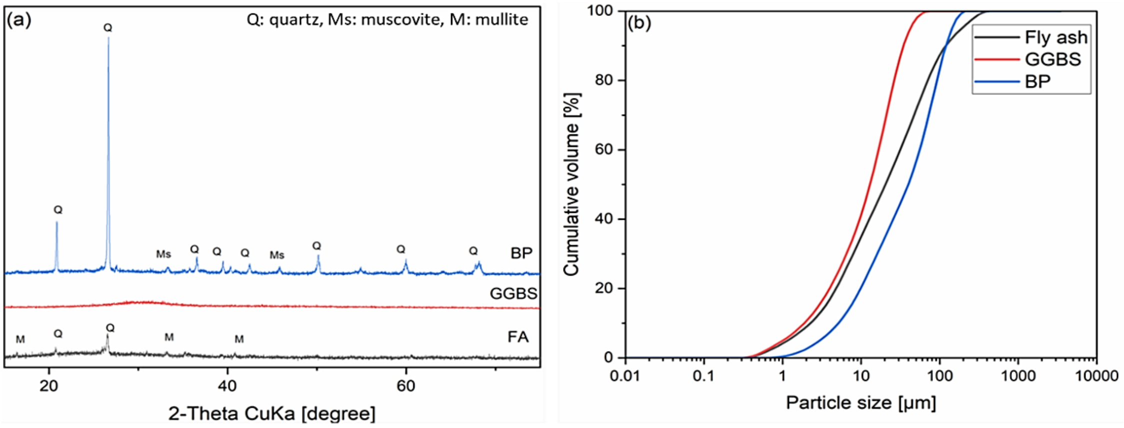

Figure 3.4. (a) XRD pattern and (b) particle size distribution of FA, GGBS and BP.

Table 3.1. Oxide compositions (wt. %) of FA, BP and GGBS obtained from XRF

Material	SiO_2	Al_2O_3	CaO	Fe_2O_3	MgO	K_2O	SO_3	TiO_2	Na_2O	LOI
FA	53.12	23.83	3.82	8.36	1.50	2.51	1.16	0.81	1.10	1.9
GGBS	26.75	9.31	49.05	0.73	7.42	0.40	2.65	0.61	0.30	1.2
BP	64.6	13.1	0.44	7.04	-	2.16	0.62	1.31	-	2.9

Micrographs from scanning electron microscopy (SEM) in Figure 3.5 show that the brick powder is irregularly shaped with rough surface texture due to crushing.

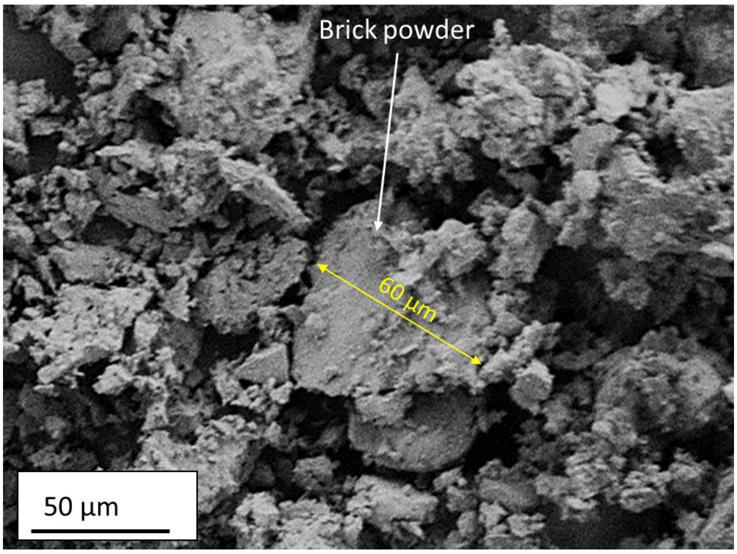

Figure 3.5. SEM image of the microstructure of BP particles

Siliceous river sand was used as natural aggregates (NA), which was supplied and certified for use in concrete according to BS EN 12620:2013 [251]. As mentioned earlier, brick was collected from a demolition site and manually crushed using a hammer. Then, the crushed particles were introduced to automatic crushing. NA and BA were sieved to have a particle size of less than 2 mm. Following sieving, the gradation and particle size distribution range of NA and BA were determined using sieve analysis. Based on sieve analysis, 49% of NA particles passed the 0.5 mm sieve, whereas BA exhibited a particle size with over 90% of particles above the 1.0 mm sieve, as shown in Figure 3.6. The physical properties of NA and BA are shown in Table 3.2. Moreover, optical microscope images were collected for NA and BA, and it was found that NA particles are spherical shaped, while BA are elongated and have a much rougher surface than NA, as shown in Figure 3.7.

In addition, micro silica sand (Sika, Switzerland) with a particle size distribution of 0.06 – 0.3 mm was used as a part of NA in one-part AAM mixtures. Micro silica sand was added to the aggregates in one-part AAM to strengthen the bond between aggregates and matrix to ensure a smooth extrusion process of the mixture from the nozzle.

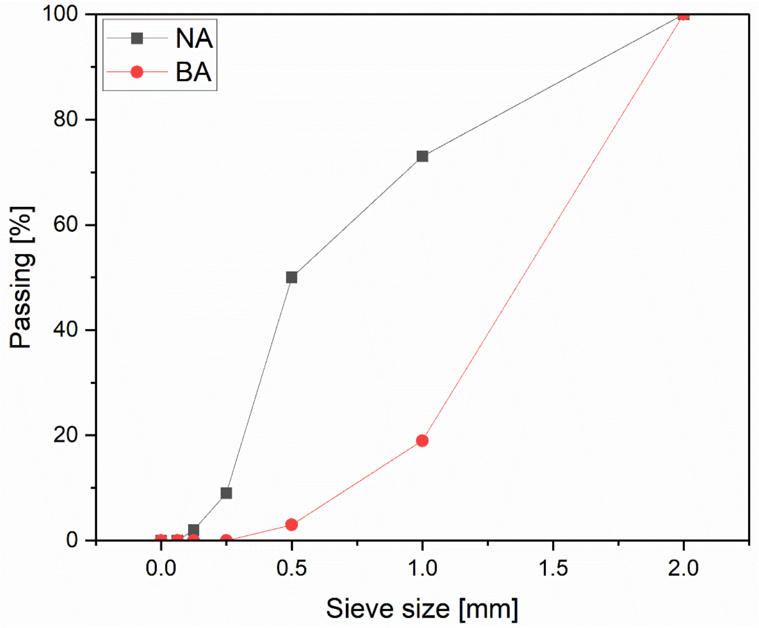

Figure 3.6. Particle size distribution of NA and BA.

Table 3.2. Physical properties of the natural and recycled aggregate

Property	**Fines content**	**Bulk density [kg/m^3]**	**Relative particle density [kg/m^3]**	**Saturated surface-dry density [kg/m^3]**	**Oven-dry density [kg/m^3]**	**24h water absorption [%]**
NA	< 3%	1617	2633	2610	2597	0.53
BA	<0.5%	1130	2634	2330	2144	8.70

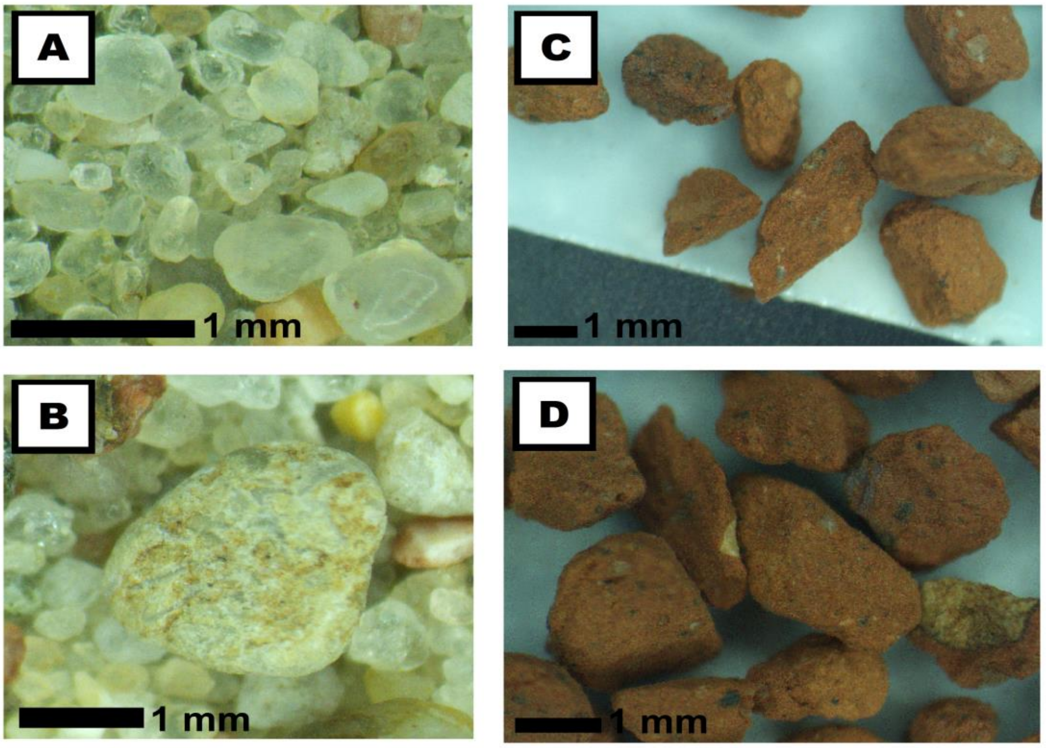

Figure 3.7. Optical microscope images of (a-b) NA and (c,d) BA

Similar to BP, the SEM image showed that brick aggregate (BA) is irregularly shaped with rough surface texture due to the crushing process, as shown in Figure 3.8.

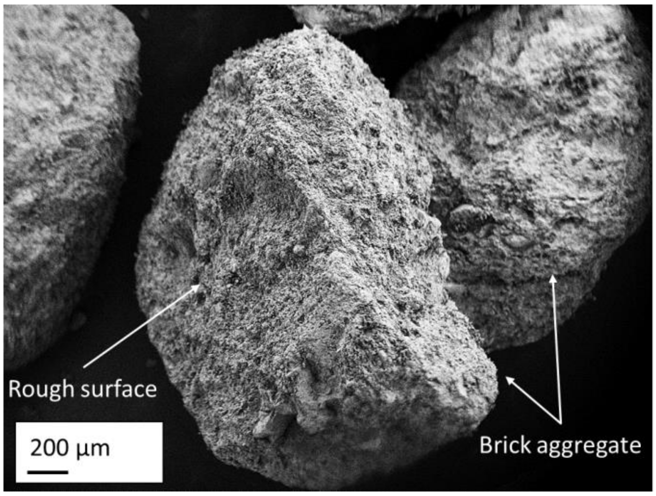

Figure 3.8. SEM image of BA microstructure.

3.3.2. Mix formulations and sample preparation

A total of 16 different one-part AAM formulations were prepared and investigated in three phases, as shown in Table 3.3. Preliminary investigations consisting of flowability, flexural strength, compressive strength, and setting time were conducted to optimise the base mixture precursor. Different binder proportions of 50 – 90% FA and 10 – 50% GGBS were investigated. The results showed that although increasing GGBS content enhanced the mechanical performance of the mixture, setting time and workability of the mixtures decreased. Accordingly, the binder composed of 60% FA and 40% GGBS was selected as the base mixture formulation because of the high mechanical performance and acceptable workability and setting time. The binder in all mixes had a constant 40% GGBS, with the remaining 60% being a combination of FA and BP at a 10% increment. Sodium silicate (SS) was used as the activator at 12% weight of the binder. A water-to-binder mass ratio of 0.4 was used for all mixtures. The aggregate-to-binder ratio was set to 1.2.

In phase II, the natural aggregates were replaced with 30%, 50%, and 70% BA. The rationality behind the selected replacement levels is not to optimise or determine the optimal BA replacement level, but to investigate the overall effect of incorporating BA on the properties of the selected one-part AAM mixtures.

In phase III, nano-functionalised graphite platelets (nG) were added at 0.1%, 0.5%, and 1% weight of the binder. The additive dosages adopted in this study were selected based on the optimal mixture determined from a previous study conducted to investigate the effect of nG incorporation on the properties of 3D printed two-part AAM [91].

The mixtures were prepared in two stages. First, the solid ingredients (GGBS, FA, BP, SS, sand, BA, and nG) were dry-mixed for three minutes. After dry-mixing, tap water was gradually added for a duration of two minutes and mixed for an additional eight minutes. For AAMs reinforced with nano-graphite platelets, nG was dispersed in water for 30 minutes using an ultrasonic homogeniser (U.S. solid, United States). At the end of the mixing process, specimens were cast in prismatic polystyrene moulds (40 x 40 x 160 m^3), heat cured at 60 ̊C for 24 h, then de-moulded and kept in a room environment (20 ± 3 ̊C and 50% RH) until testing. It was reported in previous studies that age does not have a remarkable influence on AAM strength following heat curing [252]. The compressive strength of heat-cured AAM after 3 days was reported to be comparable to that of the conventional OPC cured at ambient conditions for 28 days [253]. It was also reported that heat-cured one-part AAM at 3 days exhibits comparable compressive strength to 28 days of ambient-cured AAM [252]. Hence, based on the previous investigation [252], heat curing was employed in this study to accelerate the hardening of the mixtures.

Table 3.3. Mix formulations for the different phases of the section

	Mixture ID	Binder (wt.%)			Aggregates (wt.%)			SS (wt.%)	nG (wt.%)
		FA	GGBS	BP	River sand	Quartz sand	BA		
Phase I	0BP	60	40	-	85.3	14.7	-	12	-
	10BP	50	40	10	85.3	14.7	-	12	-
	20BP	40	40	20	85.3	14.7	-	12	-
	30BP	30	40	30	85.3	14.7	-	12	-
	40BP	20	40	40	85.3	14.7	-	12	-
	50BP	10	40	50	85.3	14.7	-	12	-
	60BP	-	40	60	85.3	14.7	-	12	-
Phase II	50BP30BA	10	40	50	59.7	10.3	30	12	-
	50BP50BA	10	40	50	42.65	7.35	50	12	-
	50BP70BA	10	40	50	25.59	4.41	70	12	-
	60BP30BA	-	40	60	59.7	10.3	30	12	-
	60BP50BA	-	40	60	42.65	7.35	50	12	-
	60BP70BA	-	40	60	25.59	4.41	70	12	-
Phase	60BP70BA-0.1nG	-	40	60	25.59	4.41	70	12	0.1
	60BP70BA-0.5nG	-	40	60	25.59	4.41	70	12	0.5
	60BP70BA-1nG	-	40	60	25.59	4.41	70	12	1

3.3.3. Experimental tests

The details and procedures for the different tests are presented below.

3.3.3.1. Flowability

The workability of the cementitious mixtures was measured as a means of flowability. A flow table test was conducted to investigate the consistency and workability of the various mixtures according to the procedures described in BS EN 1015:3-1999 [254]. The flow diameter was recorded on the fresh mixture at 0, 5, 10 and 15 min at the end of the mixing process. The flowability percentage was calculated using the following equation (Eq. 3.1):

$$Flowability\ (\%) = \left(\frac{d_{average} - d_0}{d_0}\right) x\ 100 \qquad (Eq. 3.1)$$

Where, $d_{average}$ is the average spread diameter of the fresh mortar in two perpendicular directions, and d_0 is the bottom (large) diameter of the cone.

3.3.3.2. Mechanical strength

Flexural strength (3-point bending) and compressive strength were measured after 3-days of curing following BS EN 196-1 [255]. The tests were performed using a Universal Testing System (Instron 5960) (see Figure 3.9) at a loading rate of one mm/min on prismatic samples of 160 x 40 x 40 mm^3. The flexural and compressive strength results were reported as the average of three and six replicates per mixture, respectively, and the standard deviations were calculated and presented as error bars. The coefficient of variance (CoV) was calculated for the obtained results. The test was conducted at 3 days of curing on one-part AAM mixtures, and at 7 and 28 days of curing of LC3 mixtures.

Figure 3.9. Instron 5960 Universal Testing System.

3.3.3.3. Mercury intrusion porosimetry (MIP)

Pore structure was characterised via mercury intrusion porosimetry using a Quantachrome Poremaster 60. Samples of approximately one cm^3 were placed into the penetrometer assembly, de-aired and filled with mercury up to a pressure of 0.34 MPa in the low-pressure station. The assembly was then transferred to the high-pressure station where pressure was increased to 414 MPa, allowing the detection of pore sizes of down to 3.6 nm, assuming a mercury contact angle of 140^o.

3.3.3.4. Isothermal calorimetry

The heat release during hydration was measured using a TA Instrument TAM Air 3-channel isothermal calorimeter at 25°C for three days. 50 g samples were prepared externally following the same mixing procedures of preparing mortars, then filled into a 125 ml glass ampoule and inserted into the calorimetry device. Due to disturbance caused by external mixing and phase stabilisation, the collected data during the first 45 min were discarded.

3.3.3.5. X-Ray diffraction (XRD)

0BP and 60BP pastes were prepared for investigation by dry mixing the binder and activator for three minutes, followed by adding water and wet mixing for ten minutes. The samples were cured in the same manner as the mortar samples and then ground into fine powder for analysis. XRD measurements were conducted using a Malvern Panalytical Empyrean XRD in the Bragg-Brentano geometry with CuKa radiation (λ = 1.540596 Å). The incoming beam path had a programmable divergence slit, while the diffracted beam path had a programmable anti-scatter slit. Each scan was conducted in the 2θ range of 10° to 75° within a measurement period of one hour.

3.3.3.6. Energy dispersive spectroscopy (EDS)

EDS spot analysis was performed on a Supra 35VP Carl Zeiss EDAX, USA on seven randomly selected regions on a polished paste piece to calculate the Si/Al ratios. The results were averaged, and the standard deviation was calculated.

3.3.3.7. Scanning electron microscope (SEM)

SEM was used to study the microstructure of the different cementitious mixtures (Supra 35VP, Carl Zeiss, Germany) equipped with energy-dispersive X-ray spectroscopy (EDS). The analysis was conducted on small fractured pieces collected from mortar prisms after flexural testing with approximately 6 x 6 x 6 mm^3 dimensions. Prior to SEM analysis, the samples were gold coated for 3 min using an Edwards S150B sputter coater to prevent surface charging effects. Around 15 secondary electron images were taken from each sample at a varying accelerating voltage of five to seven kV to ensure meaningful observations on a working distance (WD) of 25-29 mm.

3.3.3.8. Water absorption

Water absorption was carried out according to BS 1881-122:2011 [256] as a performance indicator for durability [257–259]. The test was conducted on 3-day cured prismatic samples (40 x 40 x 160 mm). Samples were oven-dried at 105 °C for 48 h, weighed, and then submerged in water, and their mass was measured periodically until saturation. The water absorption (%) was calculated as follows:

$$Water\ absorption\ (\%) = \frac{M_t - M_0}{M_0} \times 100 \qquad \text{(Eq. 4.2)}$$

Where M_t (g) represents the sample mass at time t after exposure to water, and M_0 (g) represents the oven-dried mass.

3.3.3.9. Freeze-thaw resistivity

Freeze-thaw (FT) resistance was determined on 3-day cured prismatic specimens (40 x 40 x 160 mm) following the Polish standard PN-85-B-04500 [260]. The specimens were submerged in water for 24 h and then placed in the FT computer-controlled chamber (weisstechnik), as shown in Figure 3.10, for 25 FT cycles at 98% RH. Each cycle involved 4 h of freezing at -20 ˚C, followed by 4 h of thawing at 20 ˚C. A compressive strength test was performed on the samples at the end of 25 FT cycles to determine the strength loss calculated as:

$$Strength\ reduction\ (\%) = \frac{C_1}{C_0} \times 100 - 100 \qquad \text{(Eq. 4.3)}$$

Where C_0 is the compressive strength of the normal cured mixture and C_1 is the compressive strength of the mixture after exposure to the FT cycles.

Figure 3.10. Freeze-thaw computerised chamber.

3.3.3.10. Fire resistivity

Fire resistivity was investigated on the control sample as well as the mixtures selected as the best-performing mix from each phase by exposing the specimens at the age of 3 days to a temperature of 800°C for 1 h using a CARBOLITE CWF 1100 furnace with a gradual temperature increment of 10° C/min from the ambient temperature to the target temperature. At the end of the exposure time, the furnace was turned off, and the samples were left to cool down in the furnace to room temperature under open-air conditions. Then, their mechanical performance was investigated.

3.4. Results and discussions

3.4.1. Effect of replacing fly ash with brick powder

The effect of incorporating BP to replace FA was investigated on the flowability, mechanical strength, pore microstructure, mineralogy and reaction kinetics, and the results are presented and discussed in this section.

3.4.1.1. Flowability measurements

Figure 3.11 presents the flowability of the different one-part AAM mixtures. The main contributor to the cementitious mixtures flowability is the amount of free water available. The term "free water" describes the amount of water that is available to serve as a lubricant between particles rather than being instantly consumed in the chemical hydration of cement or absorbed into the surfaces of small particles. This water improves the mix's flowability by facilitating particle mobility and lowering internal friction. The workability is It is expected that the workability decreases when replacing FA with BP due to its porous nature and high water absorption capacity compared to FA. Interestingly, the flowability results increased at a replacement level of 10%, and decreased with increasing replacement level beyond 10%. The flowability of the mixture is mainly governed by two factors, which are the shape and fineness of the particles. The highly irregular shape and rough surface of BP particles contribute to the decrease in the flowability of the mixture, in contrast to those of the spherical FA particles [261,262]. However, the results of the current study suggest that, up to a certain replacement level (i.e., 30%), the fineness effect of binder materials is dominant over the shape effect on the flowability of the mixtures. Mixtures prepared with more than 30% of BP had slightly lower flowability than the control mixture (0BP), indicating that BP’s shape and porous nature became dominant over the fineness of FA, as shown in Figure 3.11.

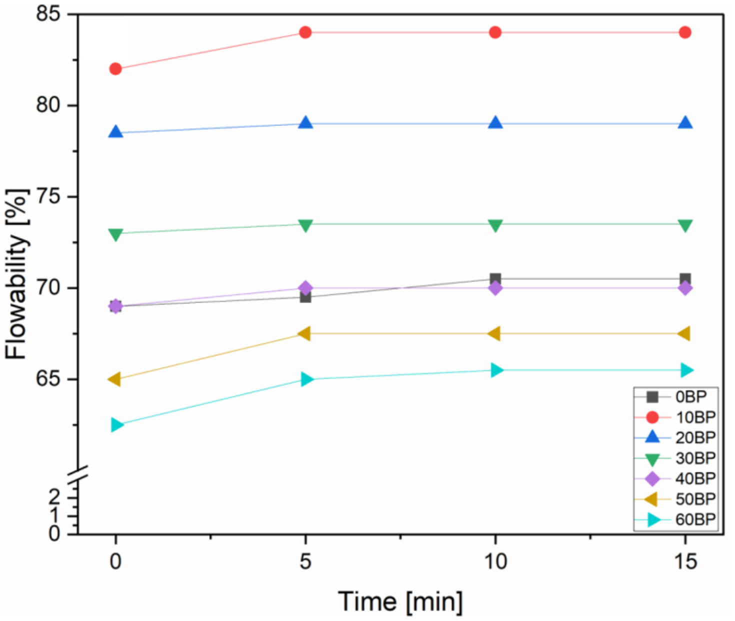

Figure 3.11. Flowability of one-part AAM mortars with different BP content.

3.4.1.2. Mechanical strength

Figure 3.12 presents the mechanical properties of the mixtures as a function of increasing replacement levels of brick powder (BP). Figure 3.12 shows that all mixtures containing BP exhibited 6 – 15% lower flexural strength than the control sample (7.5 MPa), where 20BP had the lowest flexural strength of 6.4 MPa. However, it is worth noting that the amount of reduction in flexural strength did not correlate with the replacement level. All the mixtures have CoV less than 6%.

Similarly, substituting FA with BP reduced the compressive strength relative to the control (0BP). 10BP showed the lowest compressive strength of 33 MPa, which was 20% lower than the control. The lower compressive strength of 10BP could be associated with the high flowability of the mix, as shown in Figure 3.11, which indicates the presence of higher amount of free water in the materials, resulting in the development of a more porous microstructure, which is further discussed later. Interestingly, increasing the replacement level of fly ash beyond 10% with BP led to gradual increase in the compressive strength of AAM. For example, 60BP had a compressive strength of 38 MPa, which is around 16% higher than the 10BP (33 MPa). The results of the different samples had a CoV less than 4%. The increase in compressive strength with increasing BP content could be attributed to the decline in flowability (see Figure 3.11), indicating the better compaction of the mixtures and lower porosity. Moreover, although increasing replacement level increased the compressive strength behaviour, 60BP still showed slightly lower strength performance than 0BP, achieving around 8% lower compressive strength value. This could be explained by the fact that brick powder exhibits less pozzolanic reactivity than fly ash due to the high impurities in its mineralogical composition [263], which will be further discussed in the next sections. That would, in turn, decrease the geopolymerisation rate and reduce the overall strength performance of the mixture.

The density of mixtures slightly increased with increasing BP content. The compressive strength of a mixture generally improves when its density increases since the higher density denotes lower void content. However, the density difference between the mixes before and after BP substitution is negligible (1.9 g.cm^{-3} for 0BP and 2.04 g.cm^{-3} for 60BP) and can be attributed to the higher density of BP (i.e., 2.445 g.cm^{-3}) compared to FA (i.e., 1.995 g.cm^{-3}).

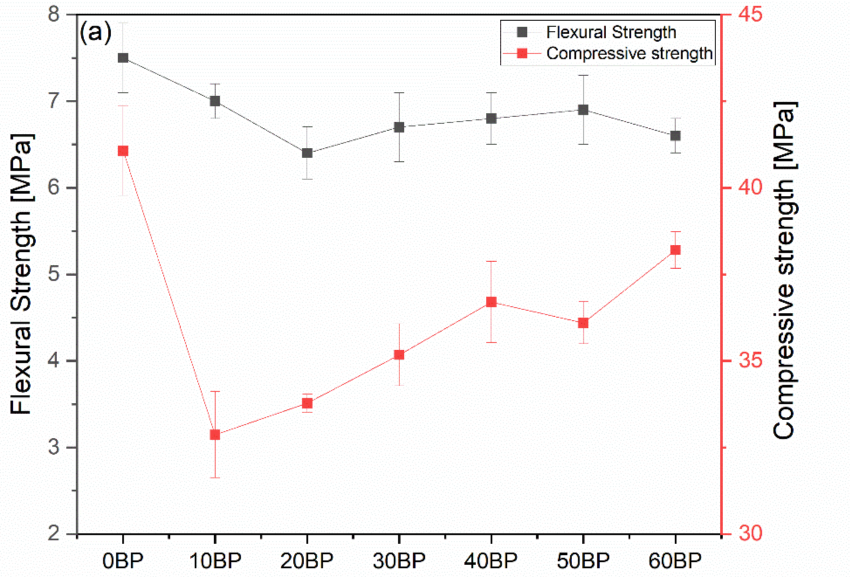

Figure 3.12. Effect of replacing different percentages of FA with BP in one-part AAM mortars on flexural strength and compressive strength. Error bars represent the standard deviation.

Other researchers have studied the effect of incorporating brick powder to replace part of the precursor. These studies have shown similar or better mechanical performance than the control mixes [247,264]. Nevertheless, due to differences in the bricks and mix formulations, a limited comparison can be made between this study and the results obtained in other studies. For example, Migunthanna et al. [247] achieved a slightly higher compressive strength than the results presented here after three days, reaching around 43 MPa when using the same precursor formulation (i.e., 60% BP, 40% GGBS) but with a 10% liquid activator in a two-part AAM. Hwang et al. [264] attained compressive strength up to 50 MPa after three days for mortar containing 60% BP and 40% GGBS in a two-part AAM. Collectively, these studies and the present work show that incorporating BP in AAM is a promising approach, and the mechanical properties indicate that the reactivity of BP is comparable to FA. The mechanical results show that a further increase in BP content in the mixture is possible. However, it was limited to replacing FA in the presented study to maintain high strength performance. As a cementitious material, BP presents a suitable alternative to FA, exhibiting comparable performance and microstructure development. BP is expected to have a low to free value in terms of cost since it is a by-product of the grinding process used to produce accurate dimensions for mortar-free walling in making calibrated brick components [265]. Considering the better mechanical behaviour obtained when increasing BP content, mixtures with the highest substitution ratios (i.e., 50% and 60%) were selected for natural aggregate replacement in phase II.

3.4.1.3. Pore structure analysis

Figure 3.13 presents the pore structure characteristics obtained from the MIP test. It should be noted that the study considered selecting only the control mixture (0BP) and 60BP mixtures to understand the difference between the FA-based one-part AAM and BP-based one-part AAM. Mixture 10BP was also selected to investigate the reason behind the high drop in compressive strength values. It can be observed from the pore volume, which is also known as porosity, curves that although replacing 10% FA with BP increased the pore volume by around 12%, 60BP had slightly lower pore volume than 0BP, as shown in Figure 3.13a. Moreover, Figure 3.13b presents the pore size distribution of the different mixtures. 0BP and 60 BP had similar critical pore diameters, whereas 10BP had a slightly higher peak (Figure 3.13b). These results correlate with the compressive strength results, explaining the reason for the lower compressive strength of 10BP and the incremental trend with increasing BP content to 60%.

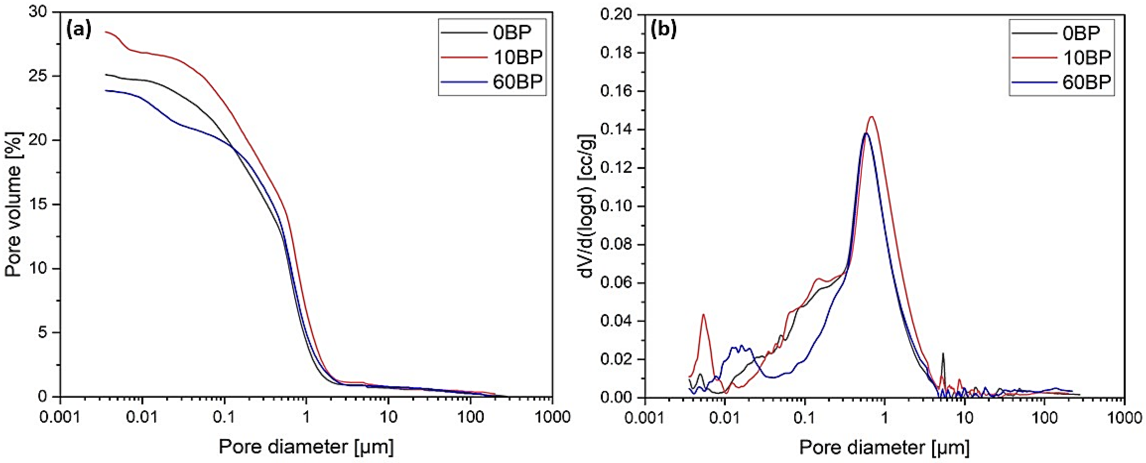

Figure 3.13. (a) Cumulative intrusion and (b) pore size distribution from MIP of the different mortars

To further investigate the pore microstructure, Figure 3.14 shows the composition of the different pores in the mixtures along with their total porosity. The results indicated an increase in the total porosity when replacing 10% FA with BP, while decreasing for higher replacement levels (i.e., 60%) to a lower porosity value than the control mixture (i.e., 0BP). This could be associated with the higher flowability and workability, as reported earlier, which resulted in developing a more porous microstructure in the case of 10BP, whereas the decrement in the flowability indicated the formation of a more compacted microstructure, and thus, resulting in a lower porosity. This could also explain the drop in compressive strength for 10BP and the increment with increasing the replacement level.

For better description, the pore size is defined and divided into three different size ranges: small pores (0.002– 0.05 µm), medium pores (0.05–7.5 µm), and large pores (> 7.5 µm) [266]. It can be observed that the pores were distributed between small and medium pores. The fraction of small pores was observed to increase by around 4% and 10% for 10BP and 60BP than 0B, as shown in Figure 3.14. This could be due to the decrease of geopolymerisation products and active components due to the lower reactivity of BP compared to FA, which is crucial for the pore structure [267]. However, the pore structure of the mortars with BP was found to be more refined, in which 60BP showed around 11% decrement in the medium pore fractions compared to 0BP, which is due to the filler effect of brick powder, which could explain the decrement in the porosity when increasing BP content to 60%.

It should be noted that the presented results do not provide a full understanding of the effect of other replacement levels on the pore microstructure, as the scope was only to justify the compressive strength results and understand the difference between FA and BP in one-part AAM.

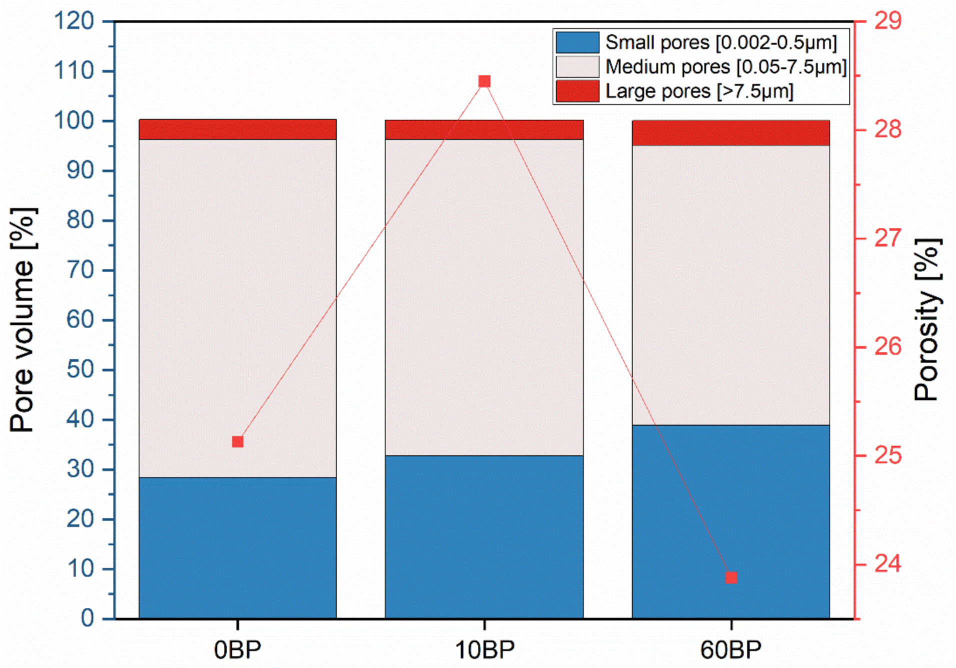

Figure 3.14. Pore volume fractions and porosity of 0BP, 10BP and 60BP mortars.

3.4.1.4. XRD and EDS

The difference between FA-based one-part AAM and BP-based one-part AAM mixtures was further assessed using XRD and EDS to allow a better understanding of the variance in geopolymerisation and phase formation between the different binders. Figure 3.15 shows the

XRD patterns of 0BP and 60BP pastes cured for 3 days. As expected, the main crystalline phase was quartz (Q), derived from raw brick powder (Figure 3.4a). 60BP showed a high peak intensity at 26.6° due to the high amount of quartz presented in BP, which notably decreases the reactivity of the fraction-bearing Al-Si [263]. This high crystallinity nature of BP (i.e., 70%) prevents the particles' complete dissolution and participation in the alkali reaction, lowering the amount of hydration product formed. That could explain the slight reduction in the mechanical strength values of the 60BP mix compared to that of the control sample (0BP). To better understand the effect of crystalline phases on the mechanical properties of the mixture, the Si/Al ratio of 0BP and 60BP pastes were determined using EDS on polished paste pieces. Results showed that the Si/Al ratio of 60BP (i.e. 4.1 ± 0.1) was significantly higher than that of 0BP (i.e., 2.8 ± 0.04) due to the presence of more quartz in the mixture. According to Yusuf et al. [268], excessively high Si/Al ratios (i.e., higher than 3.8) can impair the mechanical performance of the resulting mixture due to excessive production of aluminosilicate gel in the very early stages of the reaction, which prevents proper subsequent development of microstructure [269]. The strength reduction between 0BP and 60BP can therefore be associated with the higher crystalline content and the significant increase in the Si/Al ratio.

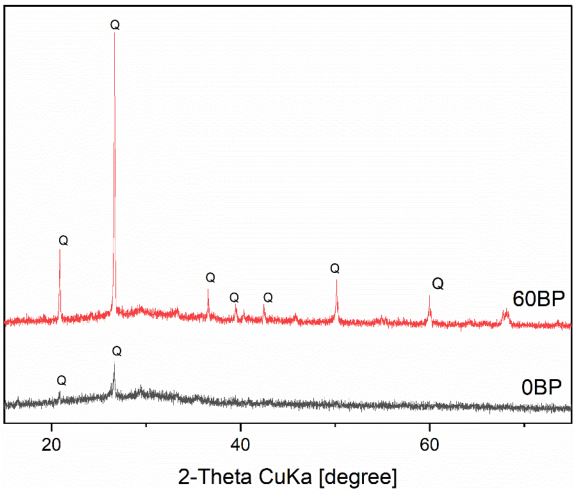

Figure 3.15. XRD patterns of 0BP and 60BP pastes (Q: quartz)

3.4.1.5. Reaction kinetics

The differences in reaction kinetics between FA-based and BP-based one-part AAM in the first 72h were studied using isothermal calorimetry**.** Figure 3.16 shows that the heat flow curves are composed of five stages: (1) dissolution (Peak I), (2) dormant (i.e., the period between the deceleration of the first exothermic peak and the beginning of the second exothermic peak), (3) acceleration (Peak II), (4) deceleration, and (5) steady state [95]. The dissolution peak (I) for 60BP was higher and occurred earlier (Figure 3.16 a(i)) compared to the control. This could be due to the higher silicate content in BP compared to FA (Table 3.1). Moreover, the acceleration peak (II) of 60BP was also seen to occur earlier and at a slightly higher intensity than 0BP (Figure 3.16 aii). These results indicated faster dissolution and the earlier reaction of the dissolved ions in the geopolymerisation process of 60BP. The results are in good agreement with those of EDS, which proves the promotion of gel formation (i.e., acceleration in peak II) in the presence of an excessive Si/Al ratio, as discussed before. Following the deceleration of peak II, the mixtures presented similar heat release behaviour. The reaction kinetics of AAM binders can be reflected through the total heat released during the first 72h reaction. The results demonstrated the comparable reactivity of BP to that of FA, where both mixtures exhibited similar behaviour. However, 60BP had considerably higher total heat released after 72 h than 0BP, as shown in Figure 3.16b.

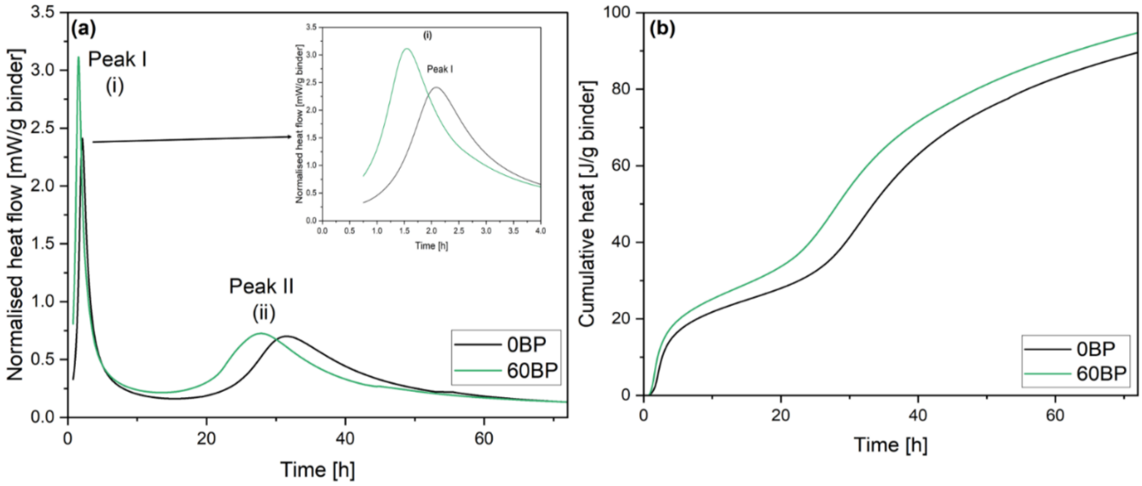

Figure 3.16. Isothermal calorimetry curves of one-part AAM mortars: (a) normalised heat flow and (b) cumulative heat release

3.4.2. Effect of replacing natural aggregates with brick aggregates

3.4.2.1. Mechanical strength

The 30%, 50%, and 70% replacement levels were specifically chosen to gain deeper insight into how varying amounts of brick aggregate (BA) influence the mechanical strength performance of the mixture. It should be noted that the aim was not to optimise the replacement level. Figure 3.17 presents the flexural and compressive strength results of the 0BP, 50BP, and

60BP mixes with increasing replacement levels of natural aggregate with BA. All the mixtures had a CoV less than 7.8% for flexural and less than 5.2% for compression. Incorporating brick aggregate (BA) enhanced flexural strength performance as shown in Figure 3.17a. For example, the 50BP mix containing 30% or 50% BA exhibited almost 27% higher flexural strength than the mix without aggregate replacement and around 13% higher than the control (0BP). At 70% BA, flexural strength was comparable to the control (0BP) but remained around 15% higher than the mix without replacement. For 60BP, replacing 30% of natural aggregate with BA increased flexural strength to a similar level to the reference (0BP) and was around 28% higher than the mix without replacement. Increasing aggregate replacement to 50% and 70% BA resulted in 10% lower flexural strength than the reference (0BP) but 16% higher than the mix without aggregate replacement. The compressive strength of the 50BP mix did not change when up to 50% natural aggregate was replaced with BA. However, 50BP-70BA achieved similar compressive strength to the control (0BP) and 17% higher compressive strength than the mix without replacement. Similarly, the compressive strength of 60BP did not change when 30% natural aggregate was replaced with BA. However, the 60BP-50BA and 60BP-70BA mixes achieved similar compressive strength to the control (0BP) and around 5-8% higher compressive strength than the mix without replacement. It is also worth noting that replacing natural aggregate with BA had a negligible effect on the composites' density. That is due to the comparable densities of natural aggregate (1.82 g.cm^{-3}) and BA (1.981 g.cm^{-3}), as shown in Figure 3.17c. The enhancement in strength performance could be due to the higher water absorption capacity of BA compared to natural aggregate, which absorbed part of the water in the mixture, reducing the overall effective water content of the mixtures from 0.394 for the mix without BA to 0.325 for the mixtures with 70% BA. This would enhance the compactness of the mixture, increasing the mechanical property.

Moreover, the compressive strength of the cementitious composite is affected directly by the physical and textural properties of the aggregates [270]. The improved mechanical performance of mixtures containing BA could be due to the porous and irregular surface texture of BA (see Figure 3.8) that enhances the adhesion between aggregate particles and the paste matrix. In addition, the larger particle size distribution of BA (d50 < 800 µm) compared to natural aggregate (d50 < 300 µm), as shown in Figure 3.6, could also be responsible for the improvement in the strength. It is well known that increasing the maximum particle size of aggregates increases the compressive strength of the resultant cementitious mixture [271,272].

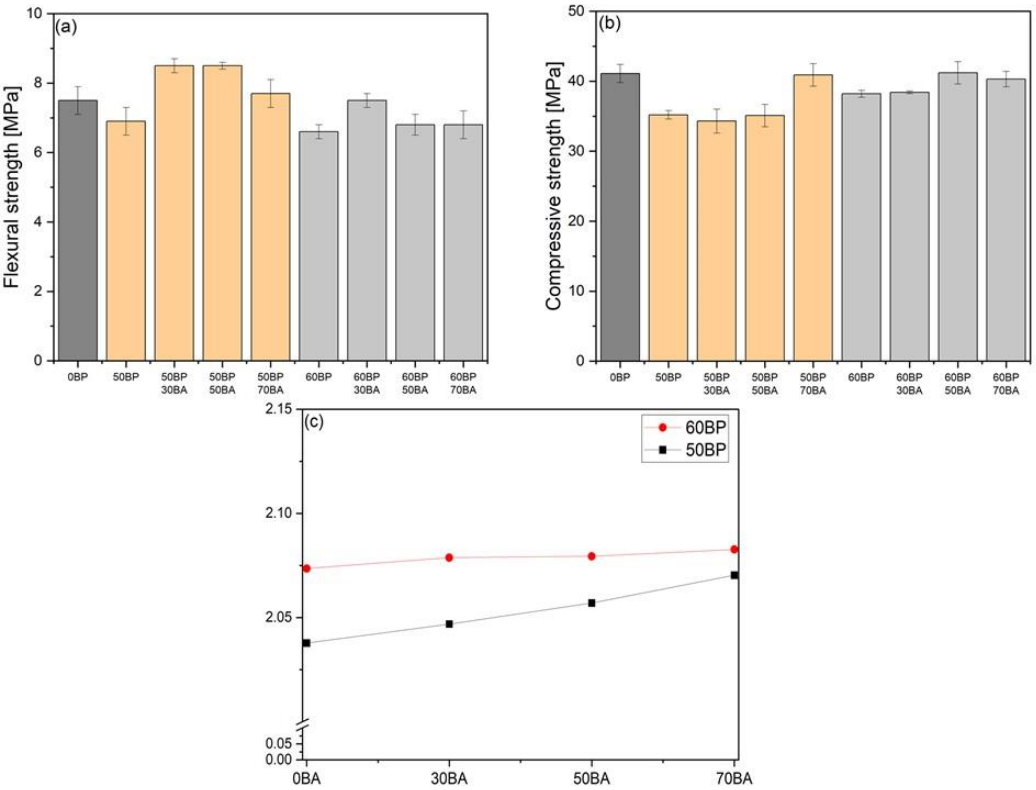

Figure 3.17. Effect of BA incorporation on Flexural strength, compressive strength and density of one-part AAM.

3.4.2.2. Microstructure characterisation

SEM images were captured for the mixture containing 70% BA replacement level to investigate the computability of BA in brick-based one-part AAM and study the interfacial bonding between the aggregate and the matrix. The mixture with the highest replacement level was selected for easier detection of the aggregates in the microstructure of the sample. The images are presented in Figure 3.18. BA can be identified from its porous microstructure compared to the matrix, as can be seen in Figures 3.18a and c. It can be observed from the figures that BA is completely embedded in the matrix, which shows good bonding between BA particles and the paste matrix. From Figure 3.18, the embedment of BA in the paste matrix can be seen clearly without delamination or debonding at the aggregate-paste interface. The strong adhesion and good interlocking of BA with the cement paste allowed effective stress transfer when subjected to external loading, thereby improving the overall mechanical performance.

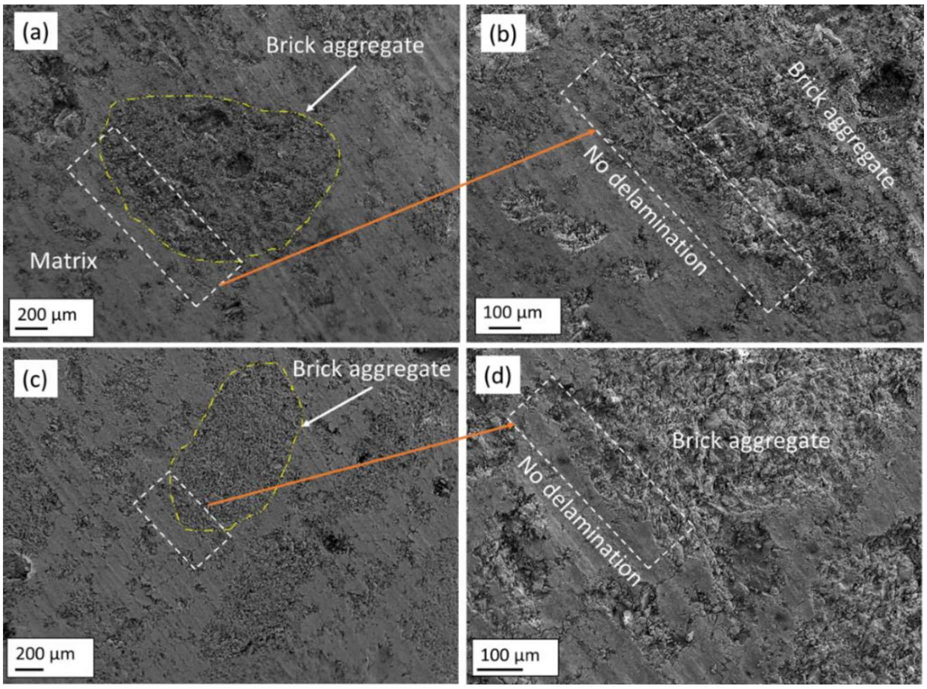

Figure 3.18. SEM images showing the microstructure of 60BP70BA cross-section after flexural strength testing

3.4.2.3. Pore structure analysis

The effect of incorporating 70% BA on the pore microstructure of BP-based one-part AAM mortars was investigated using MIP and compared to 60BP with natural aggregates, and the results are presented in Figure 3.19. The incorporation of BA increased the total intruded volume, thereby indicating a higher porosity (Figure 3.19a). Nevertheless, the dominant peak pore size was observed to shift to a smaller pore radius, which was around 0.4 µm for 60BP-70BA compared to 0.6 µm for 60BP (Figure 3.19b), indicating a finer pore size distribution in the 60BP-70BA composite. That could be due to the slightly higher water absorption capacity of BA [i.e., 8.7] than natural aggregate [i.e., 0.5], which decreased the free water/binder ratio, and thus resulting in a denser microstructure of the paste matrix. This could explain the slight enhancement in the mechanical performance of the mixtures prepared with BA.

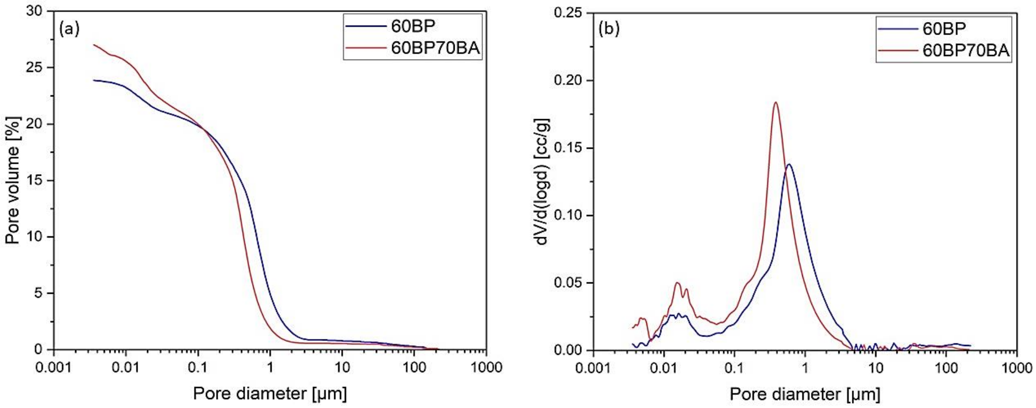

Figure 3.19. (a) Cumulative intrusion and (b) pore size pore distribution from MIP for AAM with and without BA

As mentioned in Section 3.4.1.3, the pores are classified into three different categories depending on their sizes. Hence, to further understand the impact of BA on the pore microstructure of BP-based one-part AAM, the fraction of each pore size that plays a part in the total porosity is provided in Figure 3.20. It can be seen that even in the presence of BA, most of the pores were between small to medium pores. Incorporating BA found to increase the fraction of small pores and decrease the medium and large pores fraction compared to 60BP. The formation of more small pores could be due to the high water absorption capacity of BA particles, since additional water was not accounted for in the mix design, which could have absorbed some of the water, reducing the overall reaction and resulting in the formation of more small pores. The formation of a large number of small pores could result in a refined pore structure, but at the same time, it results in a higher porosity [273]. Moreover, the reduction in medium and large pores is due to the formation of hydration products that would occupy the macro pores, thus refining the pore size distribution [274]. It was reported that the quantity of small pores has minimal impact on the mechanical strength and durability properties compared to medium and large pores [275]. Hence, the reduction in large and medium pores could contribute to the observed increment in compressive strength.

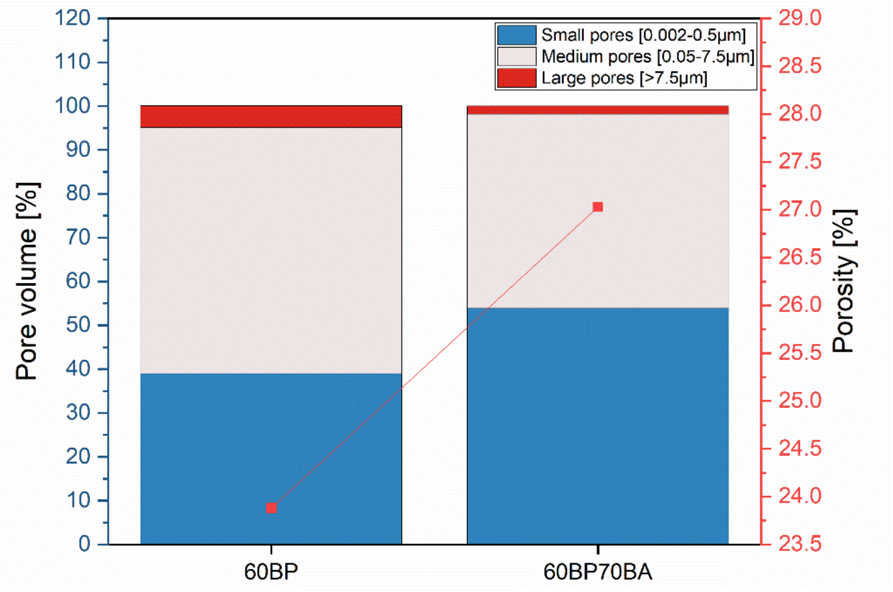

Figure 3.20 Pore volume fractions and porosity of 60BP and 60BP70BA mortars.

3.4.2.4. Reaction kinetics

The effect of replacing natural aggregate with 70% BA on the reaction kinetics of one-part AAM was investigated using isothermal calorimetry. The results (Figure 3.21) show a reduction in heat flow and cumulative heat released with increasing BA percentage. The lower intensity and the delay in appearance of the main exothermic peaks (I and II) with an increasing BA (Figure 3.21a) could be due to the porous nature of BA that tends to absorb slightly higher amounts of water from the mixture compared to the natural aggregates, resulting in a reduction in the free water available for the initial dissolution of the precursor. This will, in turn, delay the formation of reaction products and, therefore, the acceleration peak (II). Another reason could be the Na^+ ions movement restriction due to the lower free water content because of the excessive absorption of BA, which slows down the geopolymerisation process. Figure 3.21b shows a reduction in the total heat released after 72 h, indicating a lower degree of reaction with increasing BA content. Nevertheless, a slight strength enhancement was observed (as described in the preceding paragraphs), which is associated with a more densified microstructure in the presence of BA.

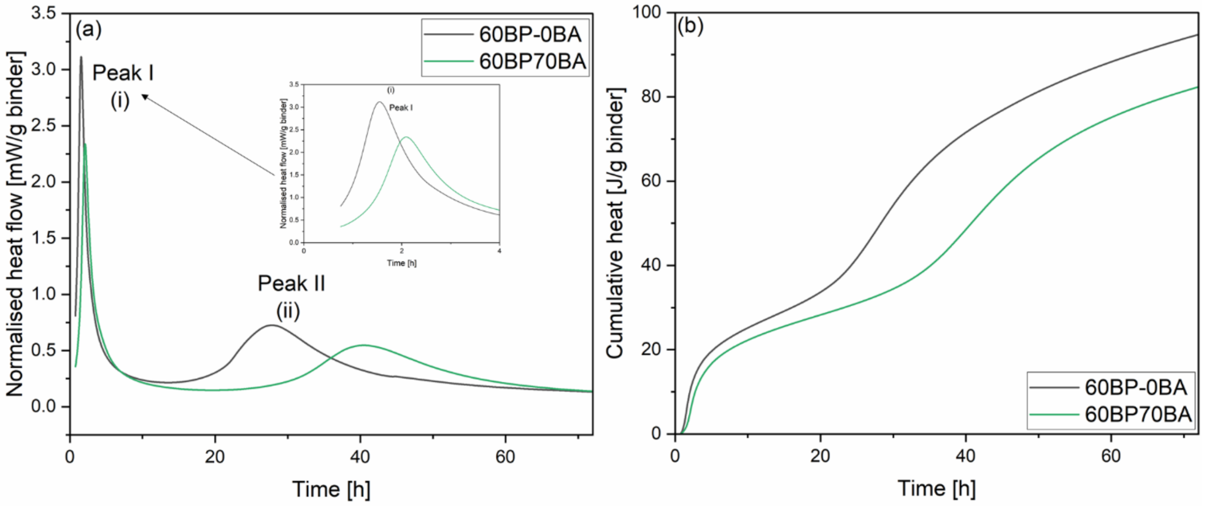

Figure 3.21. Isothermal calorimetry curves of one-part AAMs with NA and 70%BA: (a) normalised heat flow and (b) cumulative heat release

The above-presented results indicate the suitability of completely replacing natural aggregates with BA without showing noticeable differences in one-part AAM properties. Based on the findings above and considering the good performance obtained, the mixture with the highest binder and aggregate replacement level (60P70BA) was selected to study the effect of incorporating nano-graphite platelets in phase III.

3.4.3. Effect of nano-graphite platelets

3.4.3.1. Mechanical strength performance

Figure 3.22 shows that all mixtures modified with nG exhibited strength enhancement. Flexural strength increased by 31%, 37%, and 49% in mixes containing 0.1%, 0.5%, and 1% nG with a CoV of 3.2%, 1.5% and 4.9%, respectively, compared to the mix without nG with a CoV of 7.8% (Figure 3.22a). Compressive strength increased by around 6% and 11% for the 0.1nG and 1nG mixes, with a CoV of 0.98% and 2.69%, respectively, with similar performance for 0.5nG with a CoV of 2.77% compared to the control that had a CoV of 2.77% (Figure 3.22b**)**. The strength enhancement is mainly due to crack-bridging phenomena caused by the presence of nG in the microstructure of AAM [91]. Furthermore, the distinct flaky shape and high fineness of nG particles facilitate their bonding with the cementitious matrix [276]. The presence of stiff nG particles is expected to improve the mechanical performance of the composite, especially flexural strength, by controlling microcracking development and propagation induced by loading. Although incorporating 0.1% slightly enhanced the compressive strength, adding 1% did not show a significant difference compared to 0.1%. The slight enhancement could be due to the high surface area and morphology of nano-graphite platelets, which enhanced the mixtures' interconnected mechanism. However, the agglomeration effect after adding a high nanomaterial content could limit the cementitious mixture's enhancement.

Chougan et al. [91] studied the effect of incorporating up to 1% nG in 3D-printed two-part AAMs and reported similar behaviour, whereby compressive and flexural strength increased by 14% and 46%, respectively. Under compression, cracks initiate and propagate orthogonal to the local tensile stress and parallel to the loading direction. According to the authors, the improved strength is attributed to three mechanisms. First, the nG particles mitigate stress concentrations in the matrix due to their high elastic modulus and spatial distribution. That helps in spreading stresses over a larger region and prevents localised failure. Second, the crack-blocking/bridging effect of nG prolongs the initiation and delays the propagation of cracks. Crack intersecting nG will require higher fracture energy to propagate through [277]. The third mechanism is the additional (C-A-S-H) gel formed due to greater nucleation sites offered by the nG particles [278,279].

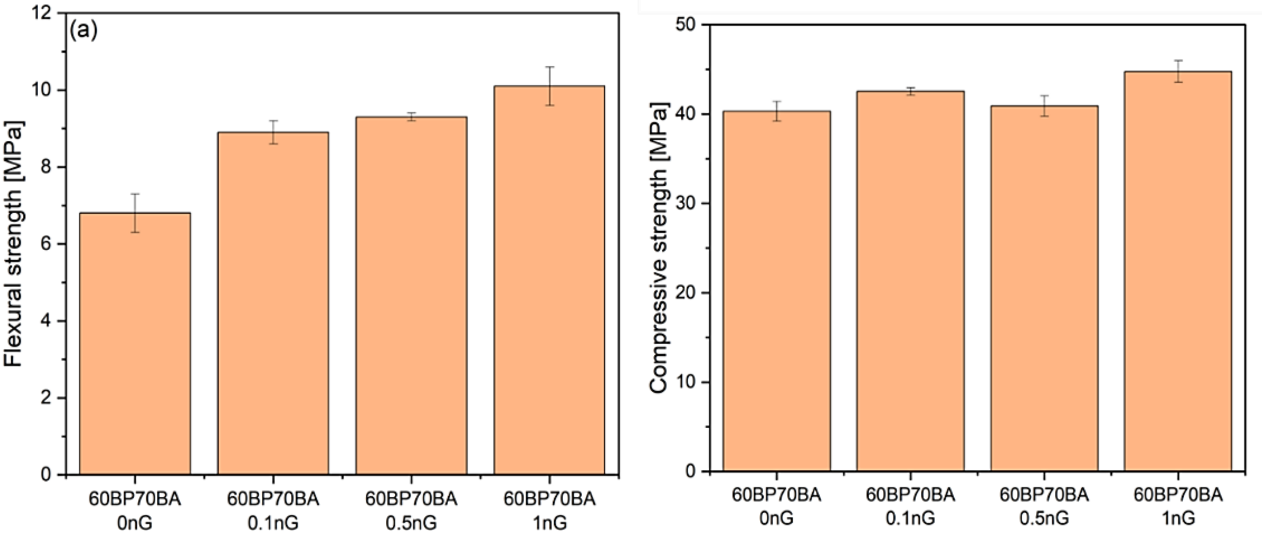

Figure 3.22. Effect of different nG dosages on (a) flexural strength and (b) compressive strength. Error bars represent the standard deviation

It can be observed that nG enhancement is more significant in flexural strength than in compressive strength performance. Figure 3.23a illustrates the schematic enhancement mechanism of mixtures containing nG under the flexural strength test. Under 3-point bending flexural strength test, the cementitious prism experiences tensile stress at the bottom of the sample and compressive stress at the top of the sample. Failure starts with the formation and spread of microcracks in the tensile zone because cement is naturally weak in tension, as can be seen in Figure 3.23a, causing a localised tensile cracking. Incorporating nG additive provides support and reinforcement to the tensile region through its crack bridging and blocking phenomena, improving the flexural strength behaviour of the mixture. On the other hand, when applying compressive load on cement, a combination of shear cracking and pore collapse occurs, where stress concentrations form at pre-existing defects and spread through the sample less directionally than flexural failure and cracks, as shown in Figure 3.23b. Thus, reducing the efficiency of nG particles in improving the mixture stress resistivity because the failure process depends more on the bulk material qualities and shear behaviour than on localised tensile cracking. That could explain the better improvement of flexural strength in the presence of nG particles than the compression strength performance.

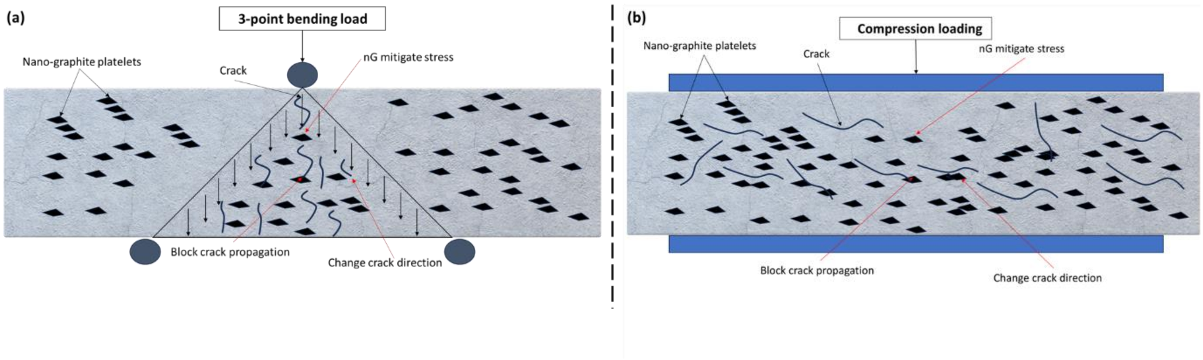

Figure 3.23. Schematic illustration of the performance of nano-graphite modified one-part AAM under (a) flexural strength and (b) compressive strength tests.

3.4.3.2. Microstructure characterisation

Figure 3.24 provides SEM micrographs of the mixture with 1% nG additive. It can be seen that nG particles were completely embedded in the matrix. Figure 3.24a reveals that nG offers platelet–matrix interactions in the microstructure of the mixture, which are essential for enhancing the composite's mechanical performance. Looking closer, it can be seen that nG platelets improved crack resistance inside the matrix of the cementitious microstructure through its crack-bridging phenomena, as shown in Figure 3.24b, which is essential for enhancing the mixtures’ mechanical strength. The crack bridging process, in which nGs span across emerging microcracks to efficiently reduce crack opening displacement, is clearly shown in Figure 3.24(b). Furthermore, Figure 3.24(c) demonstrates nG's ability to mitigate stress and stop the crack propagation through altering the crack direction by spreading the stress over a larger area. This can be observed closely in Figure 3.24(d), which indicates that the nGs modifies the local stress field and causes crack deflection. Moreover, Figure 3.24(e) shows that nG particles obstruct the crack path, preventing it from propagating. This contributes to increasing the strength performance of the mixture by raising the energy needed for crack propagation.

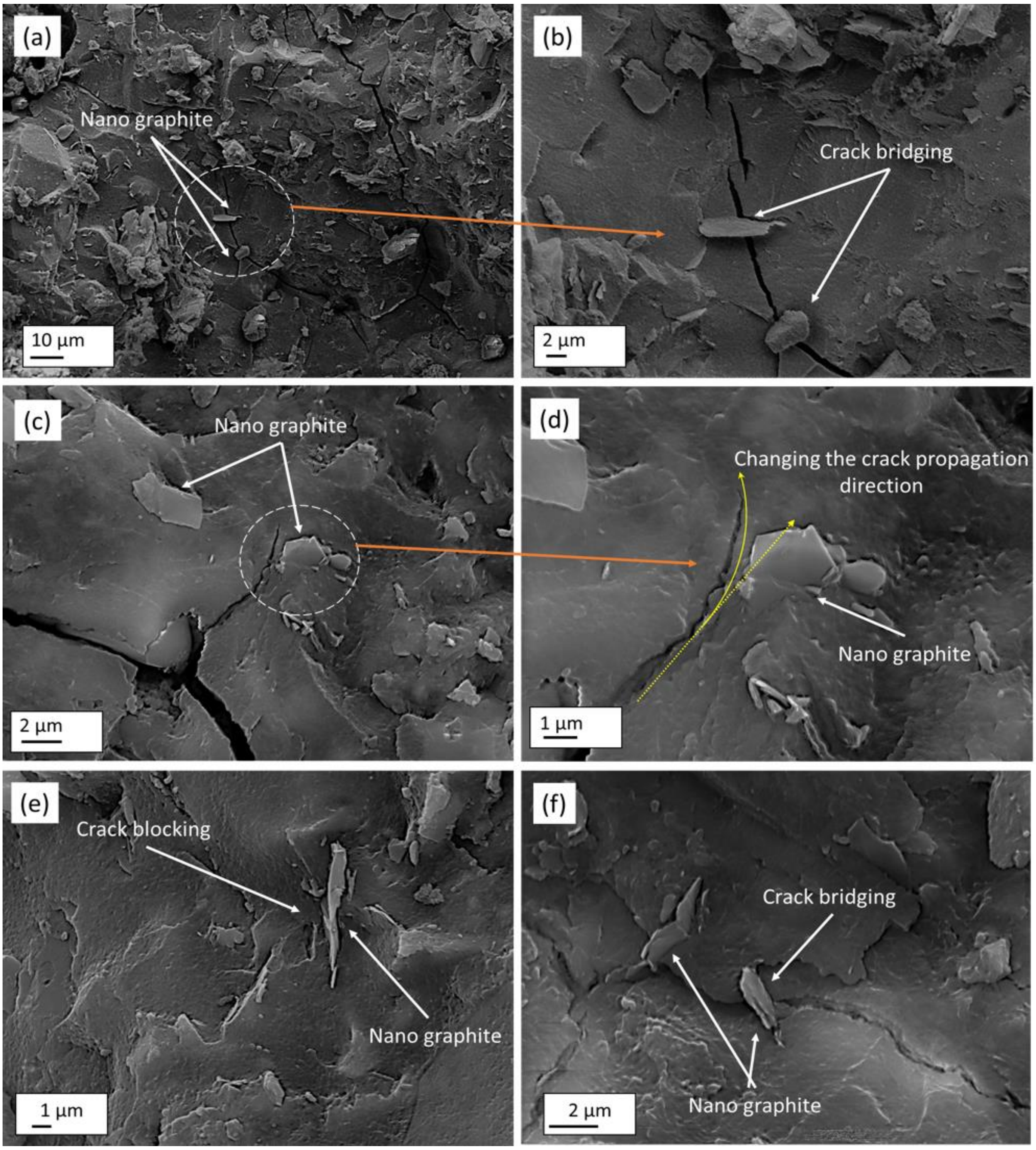

Figure 3.24. Microstructure of 60P70BA with 1% nG addition after flexural strength test.

3.4.4. Water absorption

Figure 3.25 presents the water absorption for the control (0BP), 60BP, 60P70BA, and 60P70BA with different nG dosages. The incorporation of brick in the mixture increased water absorption due to its highly porous structure. The considerable difference between 0BP and mixtures prepared with BP and BA at the early stages of the test is due to the high capillary absorption of brick [280]. Another interesting observation is that 60BP reached full saturation after 60 min compared to 6 h for the control (0BP). According to ASTM C-1585, the first six hours are regarded to be the rapid absorption stage, whilst the second day and beyond are the slow absorption stage. According to Zhuang et al. [281], the capillary pores water absorption process is the main contributor to the rapid absorption stage. Therefore, it can be indicated that the higher the amount of small pores, the greater the initial water absorption rate. Hence, in this study, the MIP results (Figure 3.14) showed that the 60BP mixture contained more small pores than the 0BP mixture, leading to increased capillary suction. This may explain why the mixture with BP absorbed more water in the first few hours than the FA mix. Yet both mixes exhibited similar water absorption of around 14%, which is because both mixes had similar total porosity. Incorporating 70% BA increased total water absorption to around 15.5%, mainly due to the higher porosity and absorption of the mixture prepared with BA compared to natural aggregate (Figure 3.19a).

Incorporating nano-graphite platelets significantly improved the resistance to water absorption and reached values lower than the control (0BP). 60P70BA-0.1nG attained the lowest absorption, with a reduction of 102% and 18% after 5 min and 72 h, respectively, compared to the mix without nG (60P70BA). The remarkable reduction in water absorption for mixes with nG can be attributed to the hydrophobic nature of nano-graphite particles, which act as a transport barrier and inhibit water ingress into AAM [282]. Chougan et al. [283] found that incorporating 0.2% nG lowered the water absorption values by 80%. Dua et al. [282] showed that incorporating 5% nano-graphene decreased the average water absorption by 75%. However, this study showed that water absorption increased at nG dosages higher than 0.1%. For example, the mix with 1% nG displayed significantly increased water absorption values comparable to the mix without nG (60P70BA). This could be due to poor dispersion causing agglomeration and clustering of excess nG particles, thus reducing their overall effectiveness [284,285].

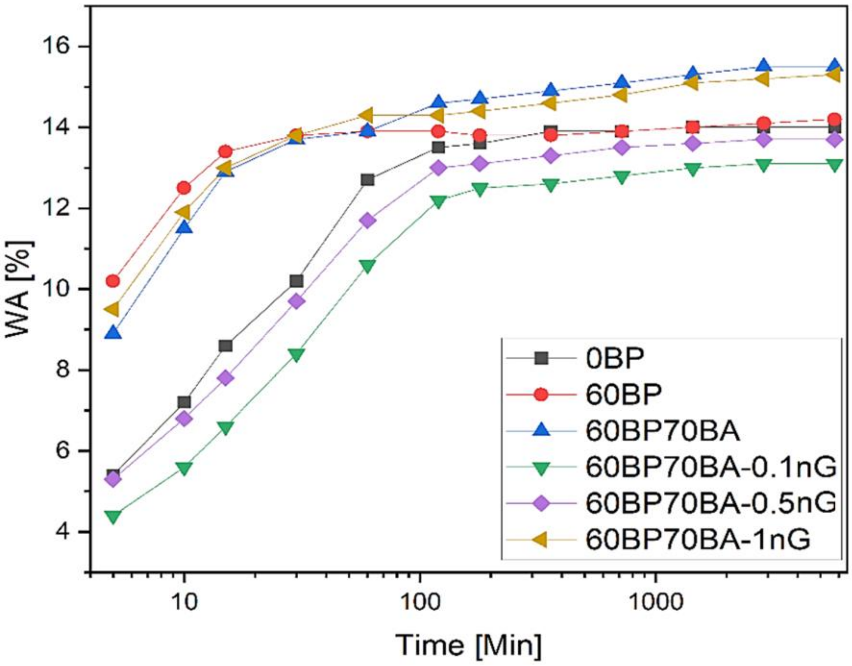

Figure 3.25. Water absorption results of the different mixtures

3.4.5. Freeze-thaw resistance

Figure 3.26 shows that the AAMs experienced compressive strength reduction ranging from 5 to 55% after exposure to freeze-thaw (FT) cycles**.** It is interesting to note that the control (0BP) suffered the highest strength reduction (55%), while mixes incorporating BP, BA, and nG showed a lower reduction in compressive strength after completing the FT cycles. The main reason for the strength reduction following the freeze-thaw cycles is the crack initiation during freeze cycles. During the freezing process, entrapped water expands as a result of transforming into ice, which leads to the widening and rupturing of the pore structure of the AAM, thus, deteriorating the mechanical performance. Hence, the damage induced by FT cycles varies depending on the free water present in the system [286]. In other words, the higher the water absorption level of the mixture, the higher the strength loss. According to Guo et al. [287], replacing FA with BP significantly reduced pore size and total porosity. The volume and size of pores affect durability [288]. For example, a finer pore structure reduces water ingress, resulting in better resistance to FT [289]. In this study, the finer microstructure and the slightly lower porosity in 60BP (Figure 3.13b) could explain its better resistance to FT compared to 0BP. Furthermore, the presence of unreacted BP particles in the microstructure could work on absorbing part of the water in the mix, providing additional space for the expansion during the freezing process of water, which prevents the formation of internal stress within the matrix. Thus, improving the resistivity to freeze-thaw in the presence of BP.

Incorporating BA results in a more densified microstructure compared to 60BP, as revealed by MIP (Figure 3.13), can explain the better performance in the FT test. In addition, better resistance could be associated with the porous structure of BA that offers space for expansive mechanisms of freezing water to relieve the pressure induced by ice formation rather than stressing the microstructure of the mixture. It was found that incorporating nG additives up to a certain limit improves the freeze-thaw resistivity of one-part AAM mixtures. The mix containing 0.1% nG showed the best performance with a compressive strength reduction of only 5%. The presence of hydrophobic nG decreases water absorption and, thus, less ice formation. In addition, the crack-bridging effect of nG helps to control crack initiation and propagation induced by water expansion during the freezing process. However, increasing the nano-graphite dosage degrades the resistance to FT, which is in line with the higher water absorption observed in Figure 3.25, which increases the amount of freezable water [290]. Moreover, the mass loss of all mixtures was within the standard deviation range.

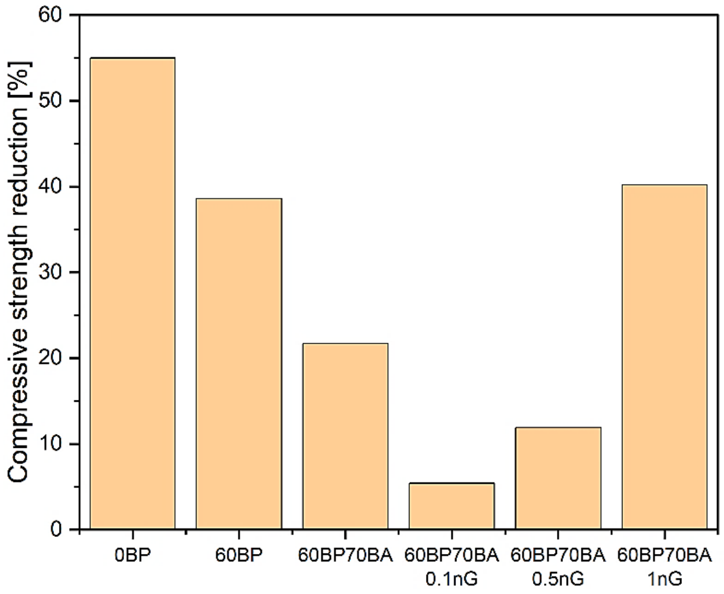

Figure 3.26. Compressive strength loss after freeze-thaw test

3.4.6. High temperature resistance

The reduction percentages in compressive strength after exposing the specimens to a temperature of 800 °C for 1h are presented in Figure 3.27. The highest strength reduction of around 21% was observed for the mix prepared with 1% nG, which had a compressive strength value of 36.4 MPa after being exposed to elevated temperature. It can be noticed that the control mix (0BP) showed a significantly higher reduction compared to the mixtures prepared with brick powder (BP) and brick aggregates (BA). The results indicated that the incorporation of brick in powder and aggregate form enhanced the high temperature resistivity of the mixture. That is in good agreement with the results reported in [291]. Giannopoulou et al. [291] measured the compressive strength reduction of two-part waste brick-based AAM when exposed to 800 °C for 2 h and did not observe any reduction in the strength. The authors suggest that the observed behaviour in the compressive strength of brick AAMs after exposure to elevated temperatures resulted from structural rearrangements in their matrices caused by water evaporation, dehydroxylation, and phase transformations [58,292,293]. The water evaporation and the loss of structural water could result in the initiation of micro-cracks, which can weaken the structure and decrease the compressive strength of the mixtures [294]. According to Tu et al. [295], the dehydration, decomposition, pore pressure accumulation and crack development could be behind the deterioration in the strength performance. However, the lower reduction in the case of mixes prepared with BP could be due to the high absorption capacity of the porous brick particles, which possibly decreased the micro-crack growth due to presence of more water in the system. That, in turn, could also explain the further enhancement of high temperature resistivity when incorporating BA, in addition to BA's rough and porous surface that provided better interlocking and required higher pressure for micro-crack development.

The compressive strength performance of mixtures prepared with 0.1% and 0.5% nG increased after exposure to heat, which can be attributed to more geopolymerisation reactions occurring in the AAM after being heated. That is in good agreement with the results reported in [296–298]. However, for the mix prepared with 1% nG, the significant reduction in compressive strength can be due to the excessive addition of nG that prevented the complete dispersion of the particles, resulting in agglomeration and clustering of the particles which reduces its overall effectiveness [284,285]. In addition, the unreacted and poorly dispersed excessive nG worked on absorbing water and led to a drier mixture due to the high specific area of nG particles. This also leads to a less densified mix. That, in turn, would facilitate the growth of micro-cracks when exposed to elevated temperature and reduce the compressive performance of the mixture. It can be indicated from the results that end-of-life brick in powder form as binder could be used to produce high temperature-resistant AAM, and up to 0.5% nG could be incorporated to further modify the high temperature resistivity of the mixture.

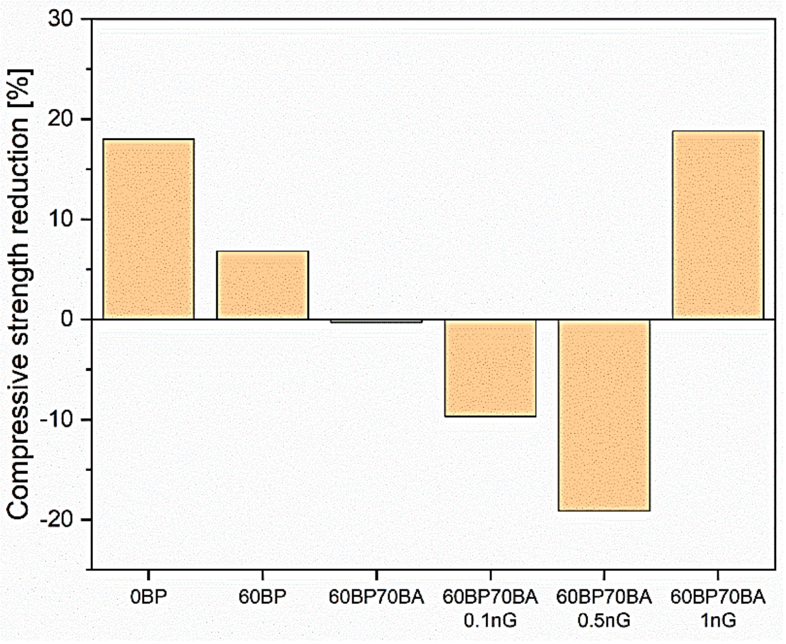

Figure 3.27. High-temperature resistance of one-part AAM mixes

The observed behaviour after exposing the samples to elevated temperature could be better discussed in terms of the effect of high temperature on the samples' microstructure, as illustrated in Figure 3.28. The main contributor to strength and microstructure deterioration is the pore pressure accumulation and moisture transportation within the microstructure. The trapped water movement and evaporation at high temperatures can lead to damaging the pore structure [253]. When exposing the samples to elevated temperature, the propagation of cracks and the formation of additional cracks take place as the temperature rises due to the accumulated pore pressure in the compacted microstructure of the mixtures. Moreover, the presented pores rupture further and expand, resulting in an expansion of the width of the pore. That, in turn, would negatively impact the mixture and cause a loss of strength in the mixture. This explains the reduction in compressive strength. Nevertheless, one-part AAM at elevated temperature experiences further geopolymerisation, which causes strength gain through filling the presented and expanded pores [299]. The production of new crystalline phases and viscous sintering works to overcome the strength loss induced by the formed cracks by compacting and strengthening the microstructure through filling the pores and improving the interparticle bonding, leading to a denser and durable structure [300,301]. Depending on the type of materials used in the mixture, the structural rearrangement and phase transformation differ, which would explain the different behaviour obtained in this study. For instance, BP-based one-part AAM had less change in compressive strength performance than the FA-based mix, which could be because the mix with BP had more unreacted particles and quartz, which could have dissolved at high temperatures, allowing for additional geopolymerisation within the microstructure.

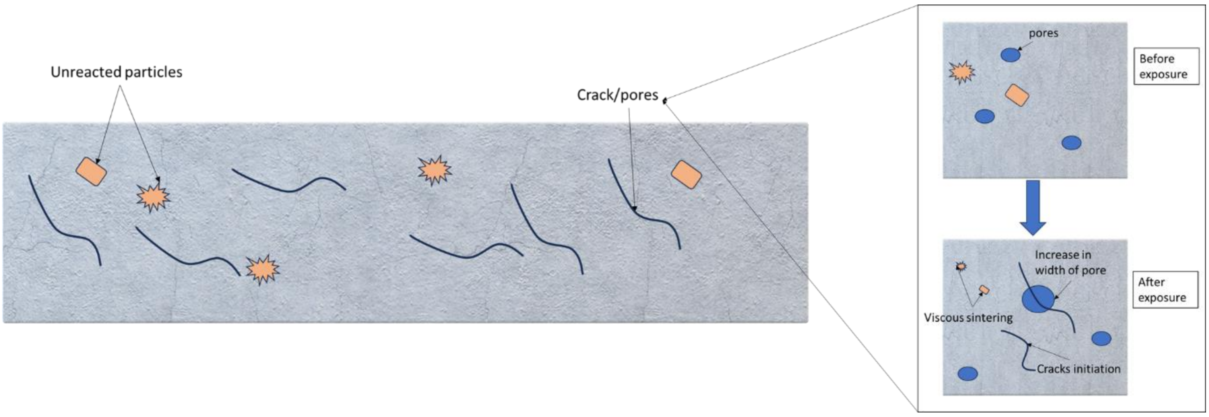

Figure 3.28. Schematic illustration of the microstructure of the samples before and after exposure to high temperature.

3.4.7. Embodied carbon footprint of the different mixtures

The embodied carbon emissions from producing 1 m^3 of a one-part AAM mixture are calculated in this section. The reduction in embodied carbon emissions from substituting fly ash with brick powder, and natural sand with recycled brick aggregates in alkali-activated materials (AAMs) are calculated.

The embodied carbon emissions associated with fly ash extraction are notably higher than those of recycled brick powder, which is a by-product of construction waste and requires less processing. The transition to recycled materials in concrete formulations presents an opportunity for substantial reductions in CO_2 emissions, aligning with global efforts to minimise the environmental impacts of the construction sector. This section explores the change in CO_2 emissions when recycled brick powder fully replaces fly ash in a 40% GGBS and 60% fly ash-based binder. Moreover, the changes after substituting up to 70% of natural sand with brick aggregates are also presented. The functional unit on which the comparison was made is 1 m^3. It should be noted that only processing energy and emissions (i.e., crushing, grinding and sieving) to produce brick powder and brick aggregates will be counted in the calculation. Generally, natural materials, such as sand, have a slightly higher CO_2 footprint than recycled materials due to the higher energy required for their extraction and processing.

The environmental coefficients of natural sand and BA were obtained from the life cycle inventory of the materials from the Ecoinvent 3.10 database with datasets related to single production processes in a European allocation, and the data of the different materials are presented in Table 3.4. For brick powder, the environmental coefficient was considered as the environmental impact of the energy required for crushing the materials.

Table 3.4. The quantities for producing 1 m^3 of one-part AAM, referring to materials, are expressed in kg.

Process	FA	60BP	60BP-30BA	60BP-50BA	60BP-70BA	EC
OPC	0	0	0	0	0	0.878
GGBS	377.4	377.4	377.4	377.4	377.4	0.0729
FA	566.1	0	0	0	0	0.0368
BP	0	566.1	566.1	566.1	566.1	0.028
Sodium silicate	113.2	113.2	113.2	113.2	113.2	1.21
Water	377.4	377.4	377.4	377.4	377.4	0.0003
Natural sand	1415.2	1415.2	990.6	707.6	424.6	0.0129
BA	0	0	424.6	707.6	990.6	0.007

The calculation of the CO_2 emissions reduction was done by adding up the CO_2 emissions of each ingredient in the mixture, which is calculated by multiplying the quantity of the material needed in the production of 1 m^3 by its environmental coefficient. The total CO2 emissions were calculated in terms of global warming potential (GWP) using the following equation:

$$GWP_i\ [CO_2] = \sum M_j \times EC_j \qquad \text{[Eq. 3.2]}$$

Where GWP_i represents the global warming potential for a specific mixture, j denotes the individual components, M_j represents the amount of the components in the mixture and EC_j is the environmental coefficient of the components.

Table 3.5 shows the results of the GWP calculations for the different one-part AAM mixtures. The GWP from a C40 concrete mixture, composed of 350 kg of OPC, 175 kg of water, 1194 kg of sand and 614 kg of gravel, was also calculated and presented as a benchmark for comparison reasons. Even though AAM mixtures investigated in this study had a low aggregate-to-binder ratio (i.e., 1.2), it can be seen that all one-part AAM mixtures emitted around 40% lower CO_2 emissions than the C40 mixture. That indicates that one-part AAM presents a suitable low-carbon alternative to OPC-based concrete. It can also be seen that the carbon impact of brick-based one-part AAM (i.e., 60BP) (198.7 kg CO_2/m^3) was slightly lower than fly ash-based one-part AAM (203.7 kg CO_2/m^3). Taking into consideration the comparable mechanical strength performance of both mixtures alongside the better durability behaviour of the mixture prepared with BP, the slight reduction in GWP makes brick powder a suitable alternative to fly ash to develop a more sustainable mixture, which not only slightly reduces the emissions associated with FA but repurposes waste material. The results agree with those of Liang et al. [302], which found that reusing waste red brick powder reduces CO_2 emissions when replacing FA. On the other hand, replacing natural sand with BA did not seem to cause an observable reduction in the carbon footprint of the mixtures, where the highest reduction was when replacing 70% of natural sand with BA, which reduced the GWP by 3%. According to Fořt et al. [303], recycling construction waste could decrease the overdependency on natural aggregate while providing limited environmental benefits. This is in good agreement with the calculation presented in this study, which shows that the only environmental benefit from recycling brick waste is to limit the depletion of natural resources.

Table 3.5. Carbon footprint estimation (GWP) of the composites.

Mix	**C40**	**FA**	**60BP**	**60BP-30BA**	**60BP-50BA**	**60BP-70BA**
GWP [$KgCO_{2eq}/m^3$]	330.68	203.7	198.7	192.9	194.5	195.8

3.4.8. Chapter conclusions

This study investigated the effects of end-of-life waste brick on the properties and performance of one-part alkali-activated materials (AAM). Brick was used in powder form to partially replace fly ash precursor and in aggregate form to partially replace natural aggregate. The mixture with the highest substitutions of brick powder (60%) and brick aggregate (70%) was further modified by incorporating 0.1 to 1% nano-graphite additive. The one-part AAMs' mechanical performance, reaction kinetics, microstructure, water absorption, and freeze-thaw durability were studied. The following conclusions were drawn:

- Brick powder is reactive and can completely replace fly ash in one-part AAM. This produced lower compressive strength (6-20%) and flexural strength (6-15%). In addition, one-part AAM prepared with BP had more small pores and fewer medium pores than the FA-based one-part AAM, which explains the higher water absorption in the first few hours. Yet, both mixtures exhibited similar water absorption of around 14% due to their similar total porosity of around 24-25%. In addition, BP-based one-part AAM found to induce higher heat due to the high silica in brick powder than FA. Moreover, an improved freeze-thaw resistance was observed compared to the fly ash-based one-part AAM. Furthermore, brick-based AAM had better high-temperature resistivity with only 6% compressive strength reduction.
- Replacing natural aggregate with brick aggregate improved compressive strength (up to 17%), flexural strength (up to 27%) and freeze-thaw resistance. It also enhanced the high-temperature resistivity of the composite, showing no reduction in compressive strength. This is due to the irregular surface texture of the brick aggregate that gave better adhesion with the paste matrix and a denser aggregate-paste interface.
- Incorporating 70% BA increased water absorption from around 14% to 15.5%, which is due to the higher total porosity, which increased from 24% to around 27% in the presence of BA because of its porous nature.
- The addition of 0.1% nano-graphite enhanced compressive strength by 6% and increased flexural strength considerably by 31% through its crack-blocking/bridging mechanism. The improvement was more noticeable in flexural strength results due to nG ability to prevent localised tensile cracking under flexural stress, unlike compression stress, which initiates cracks in different directions.
- Nano-graphite decreased water absorption by 18% and improved freeze-thaw durability due to its hydrophobic nature. Moreover, nano-graphite addition modified the mixtures' high-temperature resistivity, allowing the AAM to gain more strength rather than a reduction compared to before exposure to elevated temperature. However, increasing the nano-graphite dosage led to degraded performance, presumably due to a lack of dispersion of particles and agglomeration within the AAM matrix.
- The carbon footprint calculations showed the suitability of one-part AAM as an alternative low-carbon concrete to conventional OPC-based concrete, reducing the emissions by around 40%. It also revealed that recycling brick into powder form to replace fly ash does not provide a noticeable reduction in the overall carbon emissions,

whereas it slightly reduces the carbon emissions when fully replacing fly ash. However, it presents a suitable approach to reduce the volume of materials being landfilled. Similarly, recycling the brick waste as an aggregate replacement does not provide observable reductions in the carbon footprint.

Overall, this study succeeded in upcycling bricks obtained from construction sites and re-using them as construction materials in different forms in one-part AAM. This study also provided a pathway and a framework for the steps and methodology to develop an eco-friendly cementitious mixture from recycled waste.

4. CHAPTER 4: Recycled Brick Aggregates in One-Part Alkali-Activated Materials: Impact on 3D Printing Performance and Material Properties

4.1. Introduction

The main purpose of this chapter to comprehensively investigate the printing-related properties of brick-based one-part AAM with up to 50% brick aggregates. The effect of BA inclusion on flowability, slump height, mechanical strength of 3D printed specimens, microstructure, shape stability, and buildability were investigated on the different mixtures. It should be noted that the outcomes of this chapter have been published as a journal paper:

Yazeed A. Al-Noaimat, Mehdi Chougan, Abdulrahman Albar, Szymon Skibicki, Karol Federowicz, Marcin Hoffman, Daniel Sibera, Krzysztof, Cendrowski, Mateusz Techman, João Nuno Pacheco, Sang-Yeop Chung, Pawel Sikora, Mazen Al-Kheetan, Seyed Hamidreza Ghaffar. Developments in the Built Environment, Volume 16, 12 October 2023, *100248*. *https://doi.org/10.1016/j.dibe.2023.100248*

4.2. Methodology and experimental program

The schematic overview of the experimental programme considered for this section to study the effect of BA incorporation on the fresh, hardened and printing properties is presented in Figure 4.1**.**

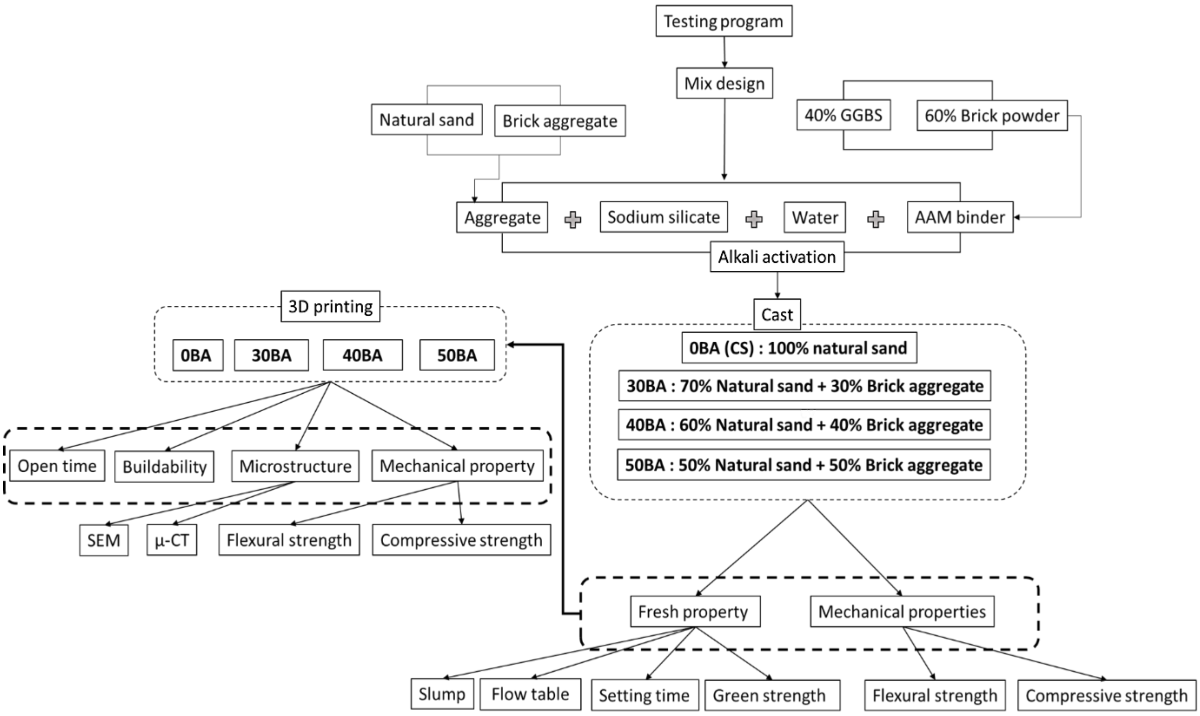

Figure 4.1. Illustration of the experimental testing program

4.2.1. Mix formulation, casting and 3D printing of specimens

The mix formulation of the four different 3D printable compositions prepared and investigated are given in Table 4.1. Based on the previous section results, the optimum precursor developed, which corresponds to the best-performing mixture in their study, was selected to investigate its various printing properties. In all samples, the precursor content was kept constant and equal to 60% BP and 40% GGBS, with an aggregate-to-binder ratio of 1.2 and a water-to-binder ratio of 0.4, as shown in Table 4.1. The solid sodium metasilicate (Na_2SiO_3) activator (SS) with a constant content of 12% of the weight of the precursor was used for all mixtures. The replacement ratios of NA with BA were 30%, 40% and 50%-wt. (by weight). Most of the research on recycled aggregate concrete accounts for the water absorption of the RA (either the aggregates are saturated before use, which is not a feasible option for fine recycled aggregates, or the water absorbed by the BA is calculated and added to the mix [304]). In this paper, the water absorbed by the BA was not accounted for when defining the mix design (that is, the effective w/b ratio was not defined beforehand – e.g. by being imposed as equal to that of the mix without BA). This was deliberate since, as long as the concrete is properly extruded, any water absorbed would be beneficial to buildability and to the hardened state properties of the mortar, improving its overall behaviour. Therefore, the following rationale was followed:

- The mix 0BA was defined first;
- Mixes containing BA were produced with the same total water of the mix 0BA;
- If the mixes were not extrudable or buildable or if any fresh state measurement deviated significantly from that of mix 0BA, the water content was iteratively changed;
- After all mixes are defined, the effective water content was calculated by subtracting the water absorbed in the first 30 minutes after mixing, which was determined as 91% of the 24-hour water absorption for the BA following the test protocol presented in [305] and assumed as 100% of the 24-h water absorption for the NA due to the small water absorption of this aggregate;
- It was found that no adjustments to the total water were needed.

The mixtures were prepared in two stages. First, the dry ingredients, including precursor, aggregates, and activator, were inserted together into the mixer and dry-mixed for 3 min.

Following dry-mixing, water was added gradually to the mixture while being mixed within a duration of 2 min and mixing continued for 8 min more (i.e., 10 min of wet-mixing in total). Ten min of mixing time was employed to ensure mixture homogeneity. The mixing procedure was conducted in control room conditions (20 ̊C and 40% RH) to ensure consistency. Following mixing, fresh mixtures were poured into prismatic polystyrene moulds with a dimension of 40 x 40 x 160 mm^3 immediately for the conventional cast method or fed to the printer hopper. After casting or printing, specimens were oven-cured at 60 C for 24 h, followed by ambient temperature until the test age. It was reported in previous studies that age does not have a remarkable influence on AAM strength following heat curing [252]. The compressive strength of heat-cured AAM after 3 days was reported to be comparable to the conventional OPC cured at ambient conditions for 28 days [253]. It was also reported that heat-cured AAM exhibits comparable compressive strength to that of 28 days of ambient-cured AAM [252].

Table 4.1. Mix formulations of the different mixtures

ID	**Binder (wt.%)**		**Aggregates (wt.%)**			**SS (wt.%)**	**Total water ratio**	**Effective water ratio**
	BP	GGBS	Natural aggregate	Quartz sand	BA			
0BA	60	40	85.3	14.7	0	12	0.4	0.394
30BA	60	40	59.7	10.3	30	12	0.4	0.37
40BA	60	40	51.18	8.82	40	12	0.4	0.36
50BA	60	40	42.65	7.35	50	12	0.4	0.35

4.2.2. Printing process

A three-axis gantry-type extrusion-based 3D printer was used as illustrated in Figure 4.2a. The extrusion system is composed of (i) an auger connected to a three-axes rail system, moved and controlled by a computer program in the printer software. (ii) A hopper with a top opening of 185mm, through which the materials were fed. (iii) A circular nozzle with an outlet diameter of the extruder of 25 mm. The maximum printing space in the extruder gage is with the length, width, and height of 1400, 1200, and 800 mm, respectively. An illustration of the extruder and the printing process of one-part AAMs are presented in Figure 4.2. The nozzle standoff distance and printing speed and nozzle standoff distance were 10 mm and 42 mm/s, respectively.

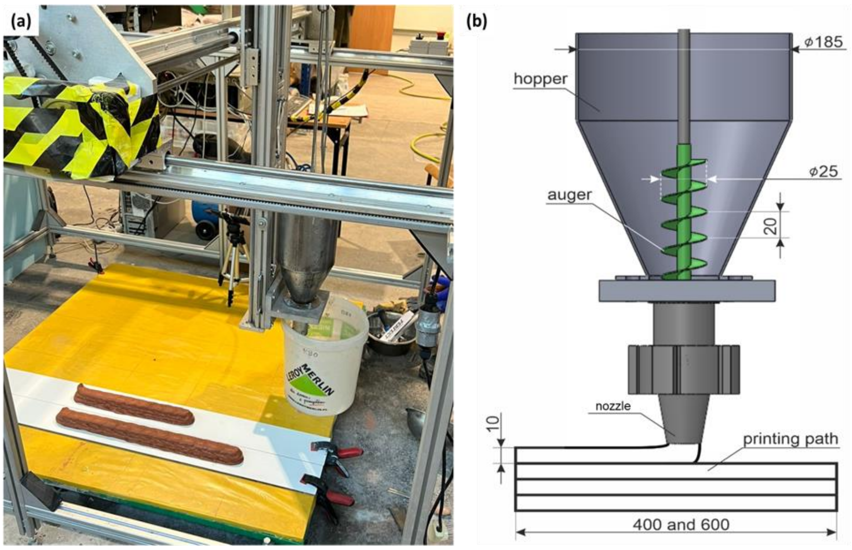

Figure 4.2. (a) Extrusion-based 3D printer and (b) illustration of the extruder parts.

4.3. Experimental methods

The procedures of the specific test methods used in this section are presented below.

4.3.1. Slump height measurements

Slump height measurements were conducted to assess the workability of the fresh cementitious mixtures as an indicator of their ability to retain their shape. A mini-slump test was also assessed to determine the workability of the fresh mixture following BS EN 12350-2:2009 [306]. Mini-slump cone apparatus was used with a height, top and bottom diameter of 50, 70 and 100 mm, respectively. The slump value was recorded, directly after end of the mixing process, as the flow height reduction after one minute of pouring the fresh mixture into the cone. Furthermore, the relative slump value (Γ_p) was measured following the ASTM C-1437 [307] using the following equation (Eq. 4.1):

$$\Gamma_p = \left(\frac{d}{d_0}\right)^2 - 1 \qquad (Eq. 4.1)$$

Where d is the average spread diameter of the mixture in two perpendicular directions and d_0 is the bottom cone diameter.

4.3.2. Green strength

Green strength refers to the early age strength of cementitious mixtures in their fresh state before hardening. The “green” strength of the AAM specimen was conducted by the uniaxial unconfined compressive test (UUCT) and digital image correlation (DIC) system (GOM ARAMIS). The test was performed on a small compression test stand (Figure 4.3). The stand has an installed force sensor with a range of up to 500 N (HBM C9C 0.5 kN) coupled to an HBM MGC Plus AB22A bridge. A loading rate of 15 mm/min was assumed for the performed test. Tests were conducted on the cylindrical specimens (d=60 mm, h=120 mm), 30 minutes after water contact. Mix preparation and tests were made in a laboratory condition at a temperature 20° (±2°) and relative humidity of RH=55% (±5%). For each type of sample, four specimens were tested. A similar test approach for green strength evaluation has been used by other authors [308–312]. In addition, the compressive test device was equipped with an LVDT sensor to control the displacement of the specimen. The deformation of the specimen during the compression test was recorded by DIC system, which controlled the displacements of 9 markers placed on the specimen. During the test, results from the force sensor were recorded by the DIC system via an analogue connector. The system configuration between HBM MGC Plus AB22A and GOM ARAMIS allows for full analysis of force-strain relationships in GOM Correlate software. Figure 4.3a shows the test stand for UUCT with ARAMIS system test.

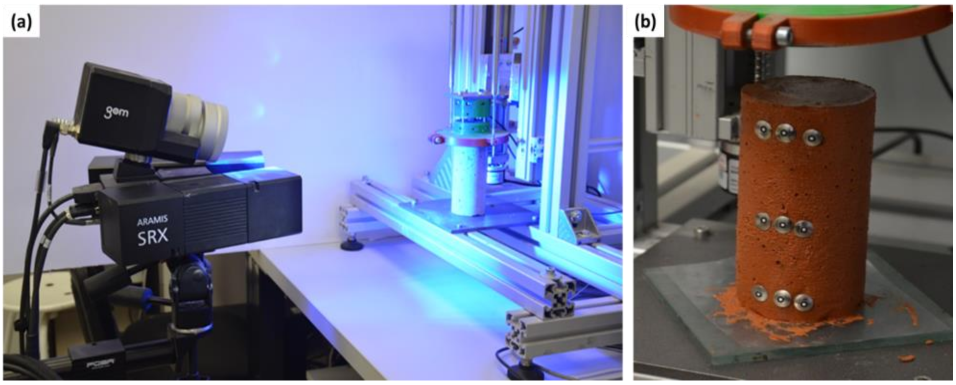

Figure 4.3. (a) Test stand for UUCT with ARAMIS and (b) demoulded specimen before the test

Similar mixing procedures were used to prepare the fresh mixture with the difference that the samples were moulded in plastic cylindrical form with a diameter of 60 mm and height of 120 mm. Before starting the test, the specimen was demoulded, and set up on the bench and 9 markers were placed on the specimen surface (Figure 4.3b).

The green strength was evaluated based on the DIC system. The green compressive strength [kPa] was calculated according to Eq. 3.

$$\sigma(\epsilon) = \frac{N_{(\epsilon)}}{A_{(\epsilon)}} \qquad (Eq. 4.2)$$

Where $N(\epsilon)$ is the force (N) measured by the HBM C9C 0.5kN force sensor, $A(\epsilon)$ is the area measured by the DIC system.

The Young's modulus was calculated according to Eq. 4 for the linear part of stress–strain curve between strains $\epsilon_u = 0.06$ and $\epsilon_d = 0.04$. For all obtained data, the values of the coefficient of variation (CoV) were calculated.

$$E = \frac{\sigma_{0.06} - \sigma_{0.04}}{\epsilon_u - \epsilon_d} \qquad (Eq. 4.3)$$

Where:

$\sigma_{0.04}$ and $\sigma_{0.06}$ are the compressive stress for strains equal to 0.04 and 0.06, respectively.

4.3.3. Mechanical strength

For assessing the mechanical anisotropic behaviour of the printed samples, the tests were conducted on cut prisms from the printed samples in lateral (v) and perpendicular (h) directions to the printing path, as shown in Figure 4.4.

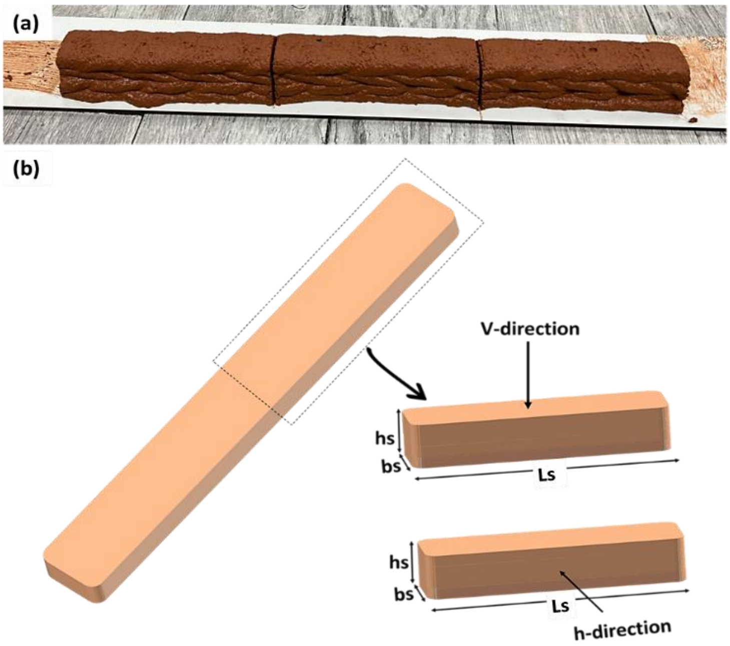

Figure 4.4. (a) 3D printed line cut into prismatic samples for mechanical properties and (b) illustration of loading directions.

To maintain uniformity of the cast and printed samples, a straight line with a cross-section of 40 mm x 40 mm was printed, and subsequently, three prisms measuring 160 x 40 x 40 mm³ were cut and extracted for mechanical testing, as shown in Figure 4.5**.** The extracted samples were polished using sandpaper to smoothen the surface and the dimensions of the polished samples were measured prior to testing to ensure accurate calculation of results. Then similar procedures to the cast were followed.

Figure 4.5. 3D printed line cut into prismatic samples for mechanical properties.

4.3.4. Setting time

The initial setting time of the different mortars was determined immediately after the mixing process finished. The fresh mixture was poured into a cone, and a Vicat apparatus (see Figure 4.6) was used to record the setting time of the mixtures following BS EN 480-2:2006 [313] and ASTM C191-08 [314]. A cone with a height, top and bottom diameter of 40, 70 and 80 mm, respectively, was used. The Vicat needle penetration was recorded every 5 min until a four mm needle penetration depth was reached

Figure 4.6. Vicat apparatus and the cone for setting time assessment.

4.3.5. Open time

Open time, also known as printability window, refers to the period during which the freshly prepared material paste demonstrates adequate workability for printing. Various studies estimated the open time of the fresh pastes using Vicat, slump, or rheology tests at predetermined intervals [18,76,315]. In this study, the open time was assessed by printing simple lines of 150 mm x 26 mm, having a resting time of 5 min until the printed line showed discontinuity, as shown in Figure 4.7.

Figure 4.7. Straight lines extruded to assess the open time of the mixture.

4.3.6. Microstructure analysis

X-ray micro-computed tomography (micro-CT) was employed for non-destructive investigation of the volumetric microstructural characteristics of the printed materials. Through micro-CT scanning, a series of cross-sectional images were acquired, as depicted in the second image of Figure 4.8. The primary focus of employing micro-CT was to examine the pore characteristics, which involved segmenting the pore regions using the modified Otsu method. The resulting binarized images were then stacked to generate a 3D volumetric representation of the pore volume, as illustrated in Figure 4.8. In this study, a micro-CT image resolution of 22.12 µm/pixel was used, which proved sufficient for capturing both micro and macro pores that can impact the physical and mechanical properties of the materials. For the investigation, samples were scanned with enough height to include the interlayers of the printed samples. The pore structures of the printed samples were analysed using the micro-CT data obtained.

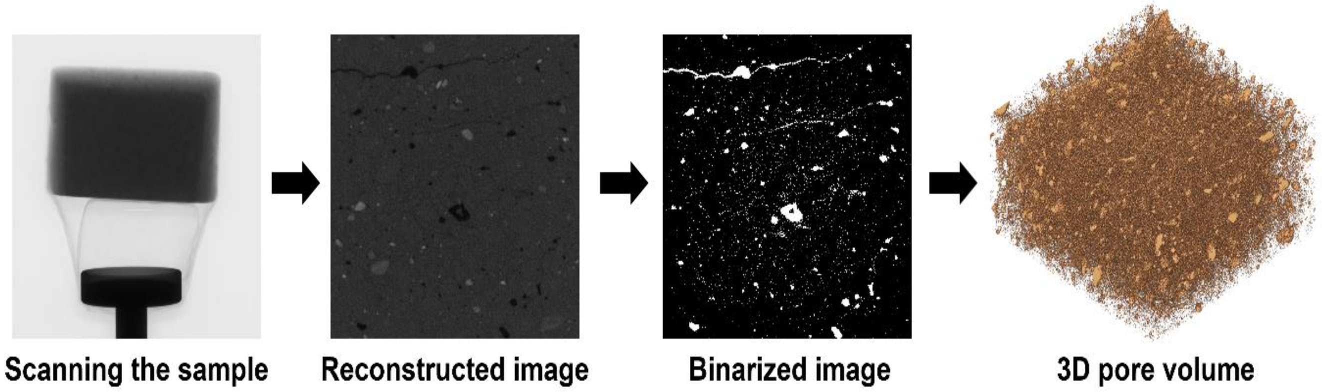

Figure 4.8. Micro-CT imaging to segment the pore volume (Note: in the binarized image, the white represents the pore part within the specimen.)

4.3.7. Buildability

The buildability of the different samples was investigated following an ad hoc testing method through 3D printing cylindrical structures with a diameter of 150 mm using 5500 g of fresh mixture. The same printing parameters of mechanical properties assessment were utilised for this test. For buildability, one batch of materials was prepared for each mixture, and the printing continued until failure or material finishes. The quality of the printed cylinders was investigated visually in terms of vertical distortion, maximum height, and layer deformation. The buildability and outer-surface finish of the different mixtures were investigated on high-quality pictures. The maximum height of each printed sample and the reduction at the bottom layers were measured using Image software to allow for accurate and meaningful measurements.

4.4. Results and discussions

4.4.1. Effect of brick aggregate on one-part AAM fresh properties

4.4.1.1. Flowability and slump measurements

The most critical parameter to anticipate the successful 3D printing of cementitious-based materials is their fresh properties. The fresh properties of AAM, including flowability, shape stability and workability, are significantly affected by the characteristics of the aggregate, such as surface texture, volume fraction, size and gradation [316]. The flowability percentage and slump measurements of each mixture are presented in Figure 4.9. As shown in Figure 4.9a, **t**he results indicated that the flowability of all mixtures diminished when BA was used to partially replace NA. The maximum reduction was registered for the samples with 50% substitution of natural aggregates, in which the flowability decreased from 65% for 0BA to 48% for 50BA. Similarly, both relative slump value and slump height decreased as the incorporation ratio of the BA increased, as shown in Figure 4.9b. This behaviour is due to BA's geometry and roughness and the option of not accounting for the water absorbed by the BA when defining the mixes. There are four types of water in the fresh mixture, which are (i) adsorbed water on the particle surface, (ii) free water, (iii) water filling the gaps between the particles [196], and (iv) water absorbed by the BA, which is relevant due to its large water absorption. The fluidity of the mixture is influenced only by the free water when the mixture's overall water content is constant. Since the total water of the mix was fixed, this means that the amount of free water decreases when BA are used due to its high water absorption capacity. It is important to note that BA particles have a rough and elongated shape that can significantly hamper the workability and flowability of mixtures. This is due to the increased friction between components, which is not a concern for NA particles with a spherical and round shape. Although there is still no specific standard produced to indicate the acceptable or required values of flowability and slump height, it was reported by Tran et al. [317] that appropriate 3D printable mixtures can be developed with a slump of 15 – 30 mm and flowability of 210 – 240 mm. Hence, the slump height in this study suggests that the mixtures with BA may have excellent shape retention and buildability. However, the flowability loss can result in difficulties in extruding the mixtures and might lead to a blockage in the extrusion system during printing. These aspects are discussed in the next section.

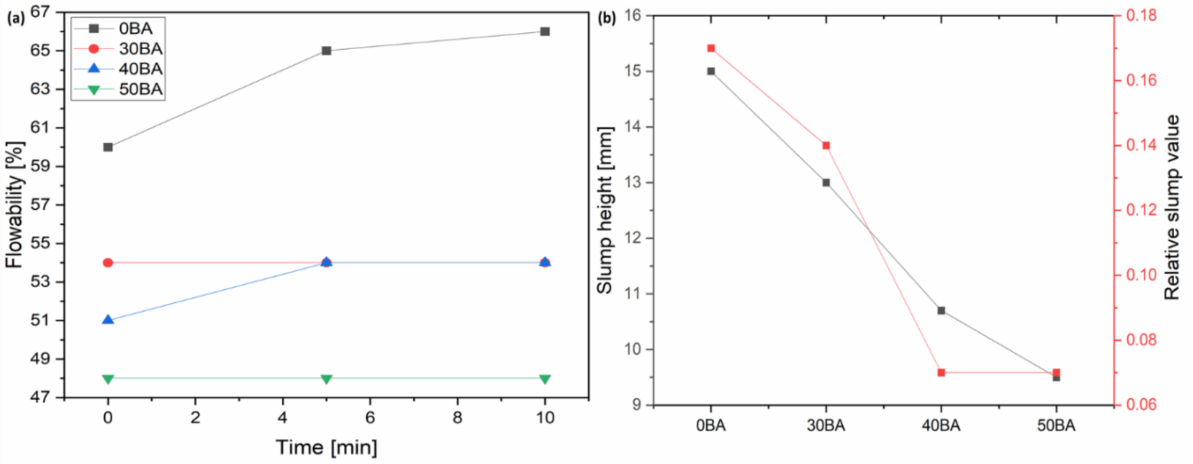

Figure 4.9. Fresh properties of one-part AAMs with different BA content: (a) flowability as a function of time and (b) slump height.

4.4.1.2. Green strength

The green strength was evaluated based on the DIC system and the green compressive strength [kPa] was calculated. During the test, the specimen diameter was measured automatically by the DIC system using markers placed on the sample. The ARAMIS device allows to precisely determine the green compressive stress (σ) – strain (ϵ) curves for each mix, as presented in Figure 4.10. The maximum compressive stress (σ_{max}) and Young's modulus are reported in Table 4.2.

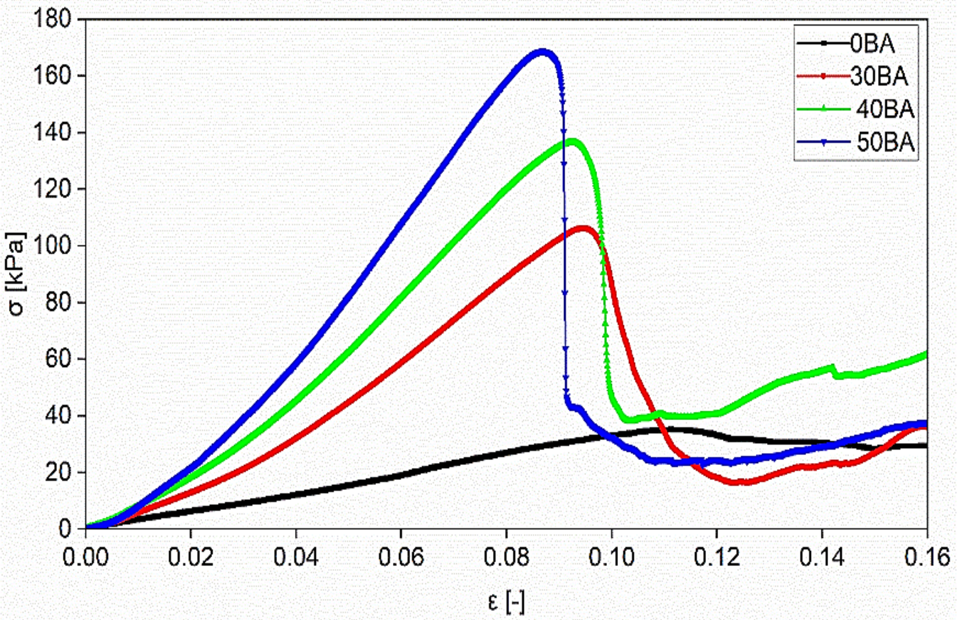

Figure 4.10. Stress-strain relationship for tested specimens

Figure 4.11 shows the failure mechanism of the examined specimens. The photos were obtained by GOM Corelate 2022 ARAMIS software. Despite the addition of brick aggregates (BA), the failure pattern was unaffected. The specimens showed a shear failure pattern, which was evident from the visible diagonal shear crack on each specimen. Moreover, it is important to mention that the lateral deformation decreases with the increase of the percentage of BA added because the BA content affects the directional dependency of the pores, which is attributed to the mechanical behaviour of the specimens.

Table 4.2. Comparison of the maximum compressive stresses and Young's modulus

Mix	BA replacement ratio [%-wt.]	σ_{max} [kPa]	CoV [%]	$\varepsilon(\sigma_{max})$ [-]	E [kPa]	CoV [%]
0BA	0	35.16	9.79	0.111	341.48	6.11
30BA	30	106.28	4.49	0.095	1 334.25	9.47
40BA	40	136.46	8.91	0.093	1 828.51	7.48
50BA	50	168.69	6.15	0.087	2 465.31	7.29

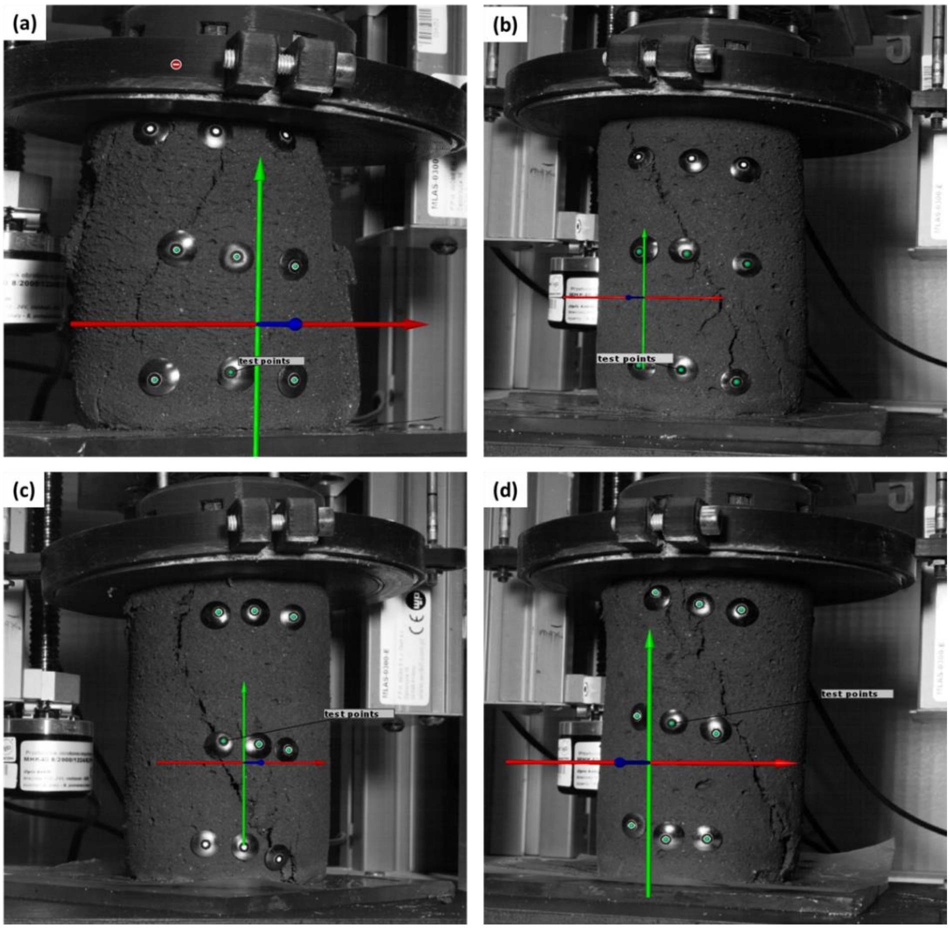

Figure 4.11. Failure mechanism of the specimens (recorded by ARAMIS system): (a) 0BA; (b) 30BA; (c) 40BA; (d) 50BA

Figure 4.12 shows the relationship between maximum green compressive stresses (σ_{max}), green Young's modulus and the BA incorporation. The data has been analysed by linear regressions. The results show a linear relationship between the incorporation ratio of the BA and the mechanical properties. The σ_{max} increased with increasing the BA content in the mix (R^2=0.99, see Figure 4.12). The mixes with 30%, 40% and 50% of brick aggregate (BA) content had σ_{max} increase of 202.2%, 288.1% and 379.7%, respectively. The Young's modulus value increased with the addition of BA, with a linear regression (R^2=0.98). The mixes with 30%, 40% and 50% BA content had increased Young's modulus by 290.7%, 435.5% and 622.0%, respectively. Increasing BA content significantly increased the green mechanical properties of AAM mixes (up to 379.7% for compressive strengthσ_{max}, up to 622.0% for Young Modulus). The failure pattern was similar for all BA content. Nevertheless, the lateral deformation decreased with the BA content.

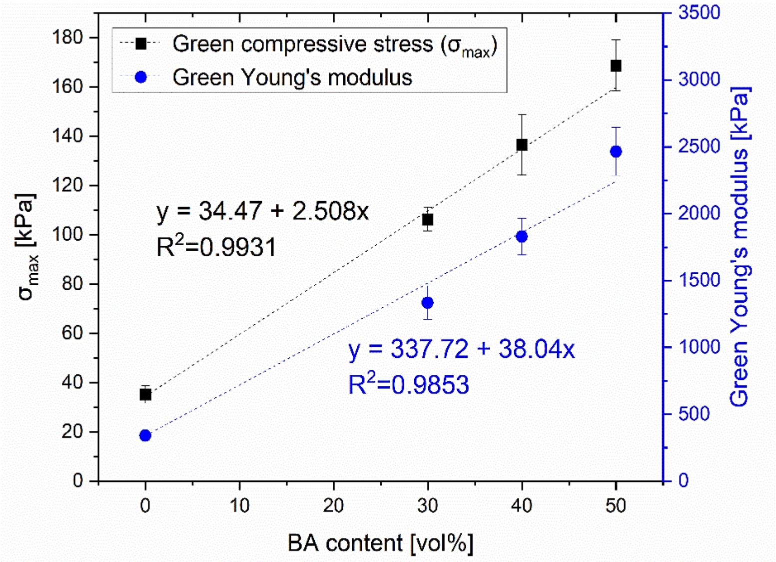

Figure 4.12. Relationship between the BA content and the maximum green strength and green Young's modulus

Several studies have proposed different methods to define the fresh properties of the cementitious mixtures, some of which, for example; rheology tests, are unable to fully evaluate the mix properties for 3D printing applications due to test specifications. Recently, a more realistic fresh property test, i.e., the green strength test, has been widely used as a practical tool to anticipate the shape retention and buildability of cementitious composites. However, for alkali-activated materials, further research is needed to assess the data on green strength [68,197,318–323]. The maximum green strength value of 35.16 kPa was registered for the reference mix (0BA), similar value (i.e., 34.84 kPa) was obtained in a study conducted by Casagrande et al. [312]. However, incorporating BA gradually increased the green strength to 106.28 kPa, 136.46 kPa, and 168.69 kPa for 30BA, 40BA, and 50BA, respectively. Research on incorporating waste brick aggregate on the fresh performance of cement-based or AAM mixes is limited [68,324,325]. The remarkable increase in the green strength of the BA mixtures can be associated with the early-age strengthening phenomenon caused by the incorporation of BA. This has been proven in several studies in which the incorporation of BA significantly reduces slump values [324,325]. Moreover, according to Pasupathy et al. [68], incorporating ground brick waste causes a substantial enhancement in the static yield stress. Their results indicated that the aforementioned static yield stress enhancement is due to the high water absorption capacity of the brick waste in the composition, which ultimately diminishes the mixture's ball-bearing ability. The increase in green strength and Young’s modulus observed in the present paper is a natural consequence of using a rough and porous aggregate with high water absorption capacity, particularly at early ages (7.9% at 30 min), and not compensating for this water absorption in the mix design. In line with the green strength results, the green Young’s modulus of the mixtures gradually increased from 341.48 kPa for the reference mix (0BA) and reached 1334.25 kPa, 1828.51 kPa, and 2465.31 kPa, for the 30BA, 40BA, and 50BA, respectively. It's worth noting that previous studies reported green Young modulus values ranging from 27.92 kPa [311] to 488 kPa [312], which is broadly dependent on the mix formulation specifications. Achieving high values of green mechanical properties is a good indication of the mixtures' improved buildability (as discussed in section 4.4). However, it is worth noting that the high water absorption of the used recycled aggregate and the nature of alkali-activated materials lead to a remarkably decreased open time (see section 4.1.3).

4.4.1.3. Setting and open time

Different studies reported a direct relationship between the initial setting time and the open time of cement-based materials [18,326], which is essential for the large-scale 3D printing process [327]. In this study, the impact of different BA content on the initial setting time and open time of the AAM mixtures were investigated and the results are presented in Figure 4.13. Similar to the flowability and slump measurements, the setting and open times were shortened when incorporating BA. It can be seen that increasing BA content from 0% to 50% gradually decreased the setting time from 45 min for 0BA to 35 min, 30 min, and 25 min for 30BA, 40BA, and 50BA, respectively. A similar trend was observed for the open time, in which the extrusion open time values decreased from 30 min for 0BA to 15 min for 50BA. This behaviour is mostly caused by the water absorption over time of the brick aggregates, which reduced the amount of free water in the mixture, decreasing the particles' flocculation. That, in turn, resulted in a drier mixture, increasing the pressure required for the needle to penetrate and for the layer to be extruded for the open time. These results are in good agreement with the results obtained in flowability and slump measurements (see Figure 4.9) and with the green strength results.

According to BS EN 197-1:2011 [328], the initial setting time of 42.5 strength class OPC should be greater than 60 min. It can be seen that none of the mixture met this criterion, having the longest initial setting time of 45 min for 0BA. It should be noted that for 3D printing, open time is more crucial factor compared to setting time.

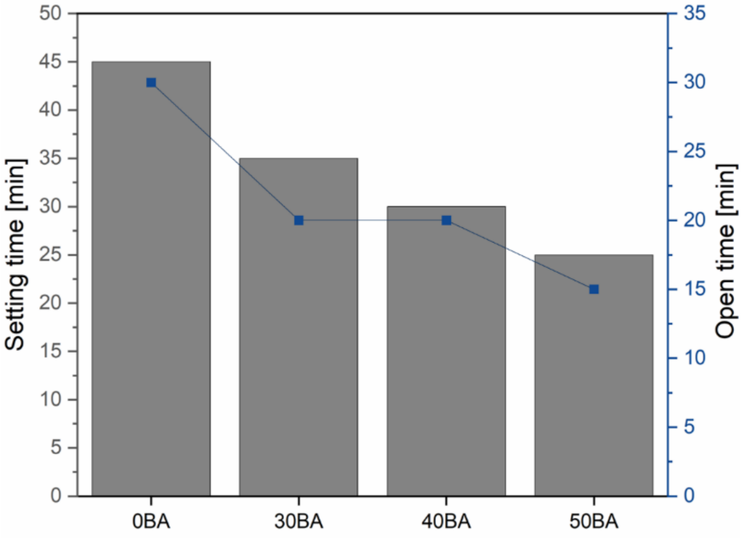

Figure 4.13. Setting and open time of the mixtures with different BA content

4.4.2. Mechanical properties

Compressive strength is one of the most critical and important mechanical properties of concrete. The compressive strength of 28 day cured concrete, according to ACI 318M-05 [329], should reach at least 28 MPa to be used in basic engineering applications. This criterion was considered to understand the suitability of the cast and 3D printable mixtures investigated in this study for engineering applications.

Figure 4.14 shows the flexural and compressive strengths and the oven-dry density of cast and 3D printed one-part AAM with and without BA. All mixtures met the criterion to be used in engineering applications. As per previous investigations, the printed samples are expected to exhibit anisotropic mechanical behaviour due to the formation of voids between the successive layers [330,331]. Accordingly, the flexural and compressive strength of the 3D printed specimens were measured in lateral (h) and perpendicular (v) directions to the printing path to investigate the anisotropic behaviour (Figure 4.4b). Both flexural and compressive strength results increased with increasing BA content without noticeable differences in the oven-dry density of the samples. Figure 4.14a shows that incorporating BA enhanced the flexural performance of the mixtures. The 50BA sample exhibited the highest performance for both cast and 3D printed samples regardless of the loading direction, which exhibited around 41%, 47%, and 24% higher flexural strength for the 50BA cast specimen, as well as printed samples in lateral and perpendicular directions, respectively, compared to their corresponding values for 0BA. Similarly, compressive strength results gradually increased with increasing BA content. The highest compressive strength performance was achieved by 50BA, where the compressive strength was increased by 18%, 39%, and 38% for the cast specimen, lateral (h-direction) and perpendicular (v-direction) directions, respectively, compared to 0BA, as shown in Figure 4.14b. As in the case of green strength, the higher strength values with increasing BA content could be due to the lower amount of water in the system, confirmed by the workability results in section 4.3.4.1.1. This can result in better compactness and fine microstructure of the mixtures. Based on the findings of the previous chapter (chapter 4), incorporating BA decreased the dominant peak pore size distribution, reflecting the denser microstructure in the presence of BA. It is generally known for cementitious-based materials that the denser the mixture, the higher the strength [332].

Another reason could be BA's rough, irregular surface and porous structure that enhances the adhesion between the matrix and aggregate particles (see Figure 4.15). This was confirmed by SEM images, which showed the satisfactory embedment of BA in the matrix and the good interlocking between the matrix and the aggregate (see Figure 4.15). When exposed to external loading, the good interlocking and adhesion of the binder paste with BA allowed for efficient stress transmission, increasing the overall mechanical performance [333].

The flexural strength results of the different 3D printed mixtures depend on the testing directions, where 3D printed samples exhibited lower strength when applying the load in perpendicular (v-direction) direction to the printing path compared to both cast and lateral direction (h-direction), as shown in Figure 4.14a. Applying the load perpendicularly (v-direction) to the printing path showed relatively higher and comparable results to the cast sample. Similar directional behaviour was obtained for compressive strength, as shown in Figure 4.14b. However, regardless of the loading direction, the 3D printed samples exhibited higher compressive strength values than the cast specimen. According to Nerella et al. [128], two types of compaction are presented for 3D printed structures and elements: compaction from the extrusion process and weight compaction of deposited layers. The high level of compaction during printing leads to the production of samples with less porosity and denser structures, ultimately improving mechanical performance compared to the conventional cast method. The compressive strength of the printed samples was also dependent on the testing direction, where applying load lateral (h-direction) to the printing direction showed higher strength values than the perpendicular direction (v-direction) for the different mixtures. A similar anisotropic mechanical behaviour was observed in previous studies [68,78,83,90,93]. Those studies investigated the mechanical performance of 3D printed samples in three directions, which are longitudinal, perpendicular and lateral to the printing path. The findings of those studies were contradictory, in which some reported the highest strength when the load was applied in the longitudinal direction, followed by lateral, and finally perpendicularly to the printing path [68,83,309], conflicting with the findings of the presented study. On the other hand, similar findings to this study were reported by other researchers, i.e., showing that printed samples exhibited the highest strength performance in the lateral direction [78,90]. According to Panda et al. [134], mimicking micro-mechanics of mixtures' material can explain this mechanical anisotropic behaviour, where applying load laterally to the printed filament allows for the uniform distribution of load throughout the cross-section. However, in the case of applying load in a transverse direction, the beads start to separate from each other, lowering the specimens' strength. Hence, this anisotropic behaviour could be due to the difference in compaction between the directions, indicating that the self-weight of the material was insufficient to compact the filaments properly and resulted in lower performance perpendicular to the printing direction (see section 4.3). The high strength observed in the lateral direction (h-direction) can be because of the better interlocking induced by the layer deposition pattern, in which the rotational movement of the auger in the extrusion system causes an upward twisting in the deposited filaments (see Figure 4.4a), increasing the contact area and the interlocking between the deposited and subsequent layer, which allows for the uniform distribution of load on the cross-section of the sample. Thus, enhancing the ability of the printed samples to withstand loads and increasing their strength performance.

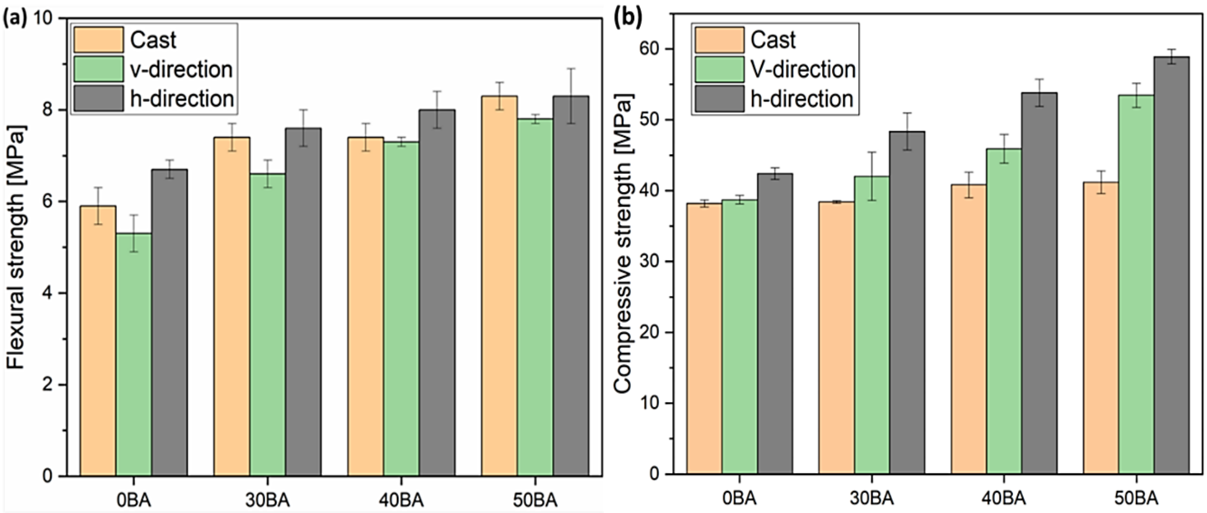

Figure 4.14. (a) Flexural strength and (b) compressive strength of cast and 3D printed brick-based one-part AAM containing different brick aggregate (BA) percentages. Error bars present the standard deviation.

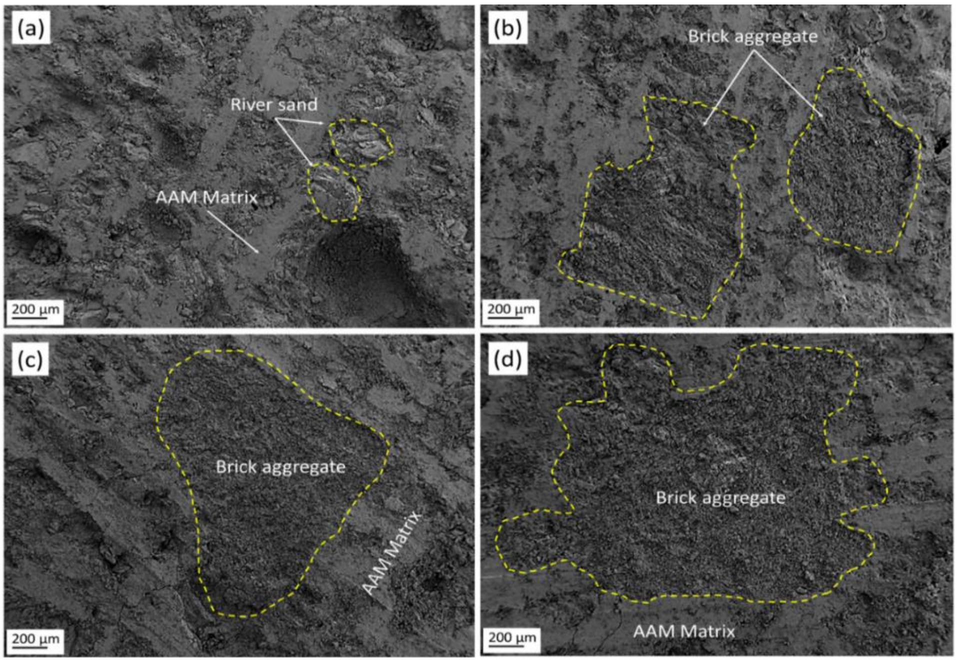

Figure 4.15. SEM images obtained from samples extracted from the printed lines of (a) 0BA, (b) 30BA, (c) 40BA and (d) 50BA

4.4.3. X-ray micro-computed tomography

The micro-CT technique was employed to investigate the microstructural characteristics of the printed materials. Specifically, the samples designated as 0BA, 30BA, 40BA, and 50BA were analysed to explore the influence of different mixtures on the material properties, particularly with regard to pores. In the x, y, and z directions, a volume of 1000 x 1000 x 500 voxels was examined for each composition. Figure 4.16 presents the pore volume for each specimen. Only pores larger than the pixel size used (22.12 μm) were considered, resulting in calculated porosity values of 3.2%, 3.8%, 3.7%, and 5.4% for the 0BA, 30BA, 40BA, and 50BA samples, respectively. These porosity values indicate that there are no significant differences in porosity among the samples based on the amount of BA contents, although the 50BA sample shows slightly larger porosity than other cases. To conduct a more comprehensive analysis, several aspects of pore structures were examined. Figure 4.17a illustrates the distribution of pore sizes in the printed specimens. It can be seen that the 0BA sample exhibited more uniformity and homogenousity pore structure sizes than those containing BA. This finding suggests that an increase in BA content results in the production of specimens containing pores within a specific size range. Figure 4.17b displays the spatial distribution of the pores throughout the height of the specimen. Despite the slightly larger overall porosity observed in the 50BA samples, this figure reveals that the local porosity values are generally consistent, indicating a uniform pore structure quality in the printed samples.

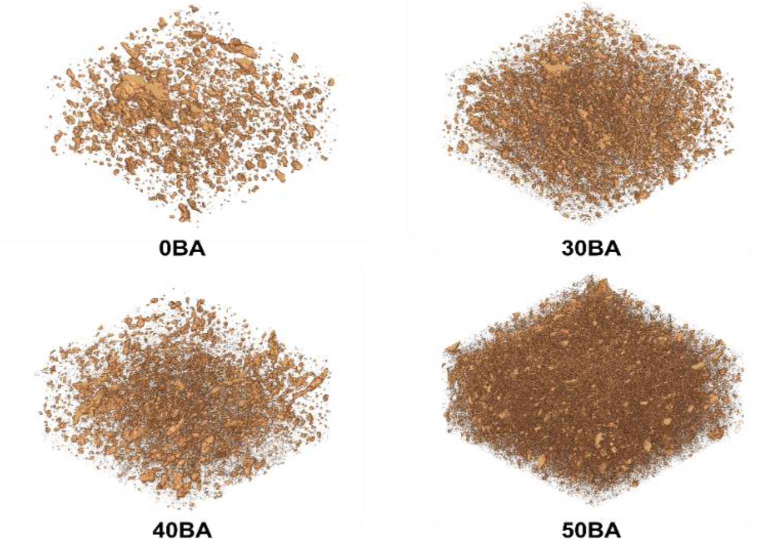

Figure 4.16. Pore volume image of each specimen.

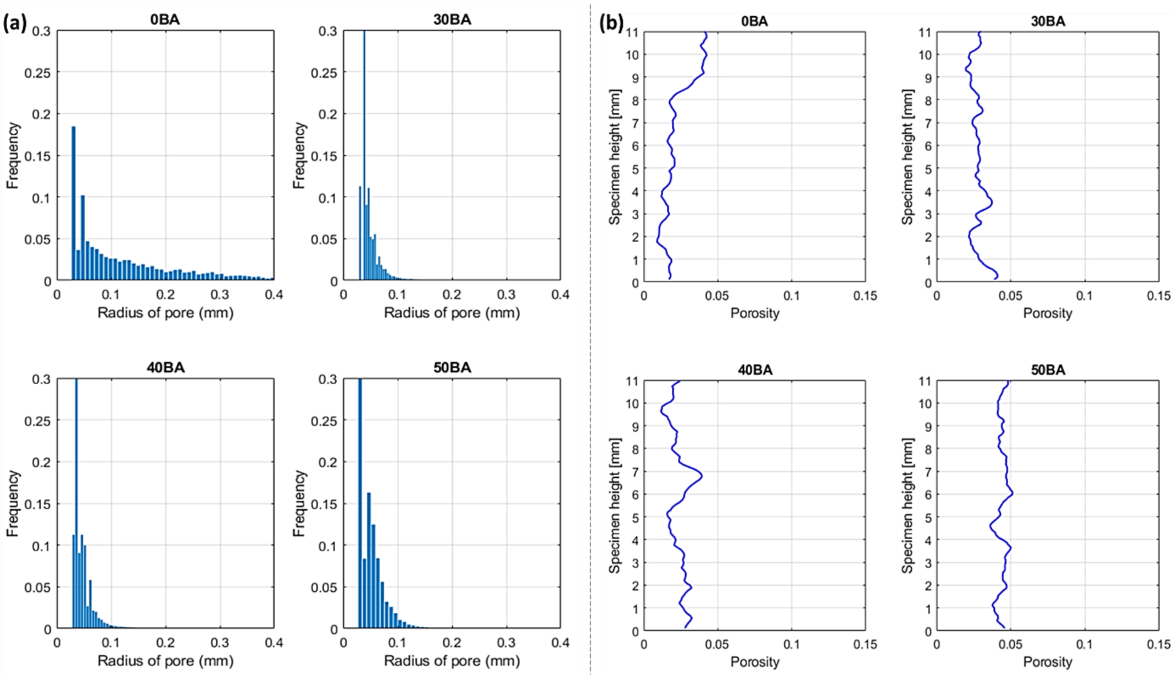

Figure 4.17. (a) Pore size distribution of the specimens and (b) the spatial porosity according to the specimen height in each specimen.

The micro-CT data was also utilised to investigate the effect of BA on pore shape. Figure 4.18 presents the sphericity of pores based on their size and the relative solid density of the samples. Sphericity serves as an indicator for pore shape, where a sphericity value of 1 indicates a perfect sphere and lower values indicate increasing anisotropy. Figure 4.18a demonstrates that the reference sample (0BA) contains more isotropic pores than samples with BA content. Among the BA samples, no significant variation was observed based on the BA amount; however, an increase in BA content correlated with a higher degree of anisotropy. This suggests that the quantity of BA affects pore structures, including shape, potentially influencing the mechanical properties of printed materials [331]. Those results could explain the directional anisotropic mechanical behaviour of the 3D printed samples, especially for the 50BA sample. The pore shape of 50BA indicated a relatively higher pore anisotropy than other samples, which can explain the high variance between the lateral and perpendicular testing directions in compressive strength results of 50BA (see section 4.3.4.2). Besides pore characteristics, the micro-CT data can be utilized to analyse the relative solid density of the samples. The grayscale values in the reconstructed micro-CT images indicate the relative solid density, where higher grayscale values correspond to a denser phase. Figure 4.18b illustrates the average pixel values at different specimen heights. The figure suggests that, overall, the measured relative solid densities appear to be uniform, although there is a slight increase in density with higher amounts of BA contents. To summarise, the micro-CT data enables effective examination of pore and solid characteristics of the materials based on their BA contents.

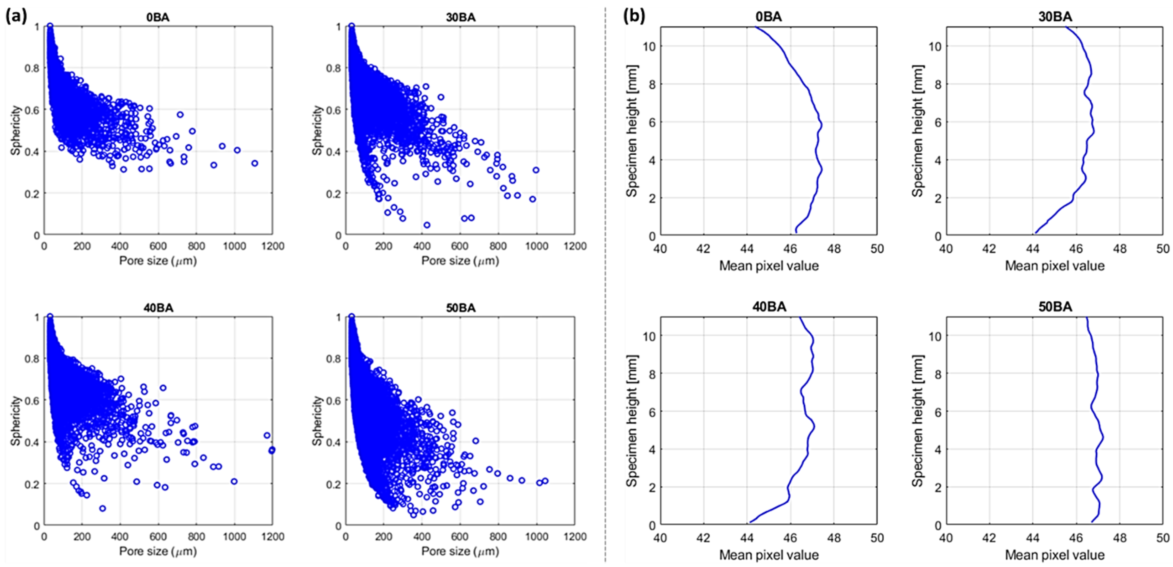

Figure 4.18. (a) Sphericity of each specimen according to the pore sizes and (b) Relative solid density along the specimen height (Note: the mean pixel value of the micro-CT image indicates the relative density of the solid phase.)

4.4.4. Buildability

Figure 4.19 presents the printed cylinders of 5500 g of the different mixtures for the buildability test. The buildability test was executed through continuous printing until a failure was observed. Following printing, the maximum printing height of each cylinder was also measured. It can be seen that mixtures prepared with BA exhibited better buildability than the control mixture. As shown in Figure 4.19a, the control mixture could be printed up to nine layers before collapse. However, layer deposition was terminated due to the excessive deformation in the bottom layer, which leads to structural instability and failure if further layers were deposited. The behaviour of the control sample was predicted from slump height and green strength results, which showed a high reduction in height without applying any load, and low green strength, indicating that the mixture did not develop enough stiffness to sustain the weight of the successive layers. Replacing natural aggregate with BA enhanced the buildability, where 30BA and 40BA exhibited good buildability performance, reaching 13 layers and exhibiting an experimental height of 123 mm and 125 mm (see Figure 4.19 b) and c), respectively, which is comparable to the theoretically designed height of 130 mm. It is noteworthy that the number of layers deposited stopped at 13 layers, not because this was the buildability threshold of the mixtures, but because the fixed amount of materials (i.e., 5500 g) did not allow any more printing. Hence, more than 13 layers could have been printed without showing any deformation or collapse. Moreover, increasing the BA content to 50% reached 13 layers without showing any deformation in the bottom layers or collapse (see Figure 4.19d), having almost similar experimental height (i.e., 129 mm) to the theoretically designated height (130 mm). The improvement in buildability could be mainly attributed to the reduced free water content in the presence of BA due to its high water absorption capacity, improving the mixtures' shape stability and buildability. Moreover, the enhanced interlocking between the binder and aggregates and the increased friction because of rough and porous microstructure of BA improve the green compressive strength, allowing the extruded layers to withstand more loads, and thus preventing bottom layer deformation and radial distortion.

It can also be observed from the figures that with increasing BA content, the radial distortion decreased, where above 30% BA, the objects exhibited a perfect cylinder shape. Furthermore, it can be seen that some cracks occurred at the 12th layer, which is due to the finishing of the fresh batches prepared for the buildability test.

As mentioned in section 3.1.1, pumpability and dynamic yield stress can be evaluated through flowability, while buildability and static yield stress can be measured through slump measurement. Thus, it can be indicated that the greater the BA content, the higher the static yield stress and the better the buildability of the mixture. That could explain the excellent shape retention without showing noticeable radial distortion with increasing BA content (i.e., 40BA and 50BA) compared to 30BA. The excellent buildability of mixtures with BA confirms the feasibility of utilising end-of-life brick in aggregate form in the concrete 3D printing application to promote recycling construction and demolition waste.

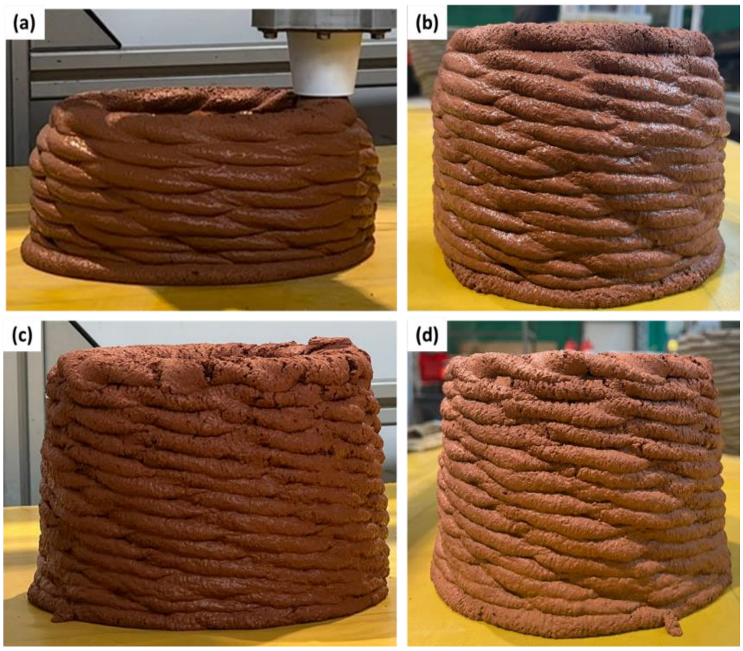

Figure 4.19. Buildability of the different 3D printed one-part AAM: (a) 0BA, (b) 30BA, (c) 40BA, and (d) 50BA.

4.4.5. Section Conclusions

This study investigated the feasibility of recovering end-of-life bricks in a powder physical state as a binder as well as 1 -2 mm particles as a natural aggregate replacement to develop one-part alkali-activated materials for 3D printing applications. Recycled brick aggregate was incorporated with different percentages in the AAM mixtures comprised of 60% brick dust and 40% GGBS as binder, and their impact on fresh properties, which determines the mixture's printability, was evaluated. Hardened properties and buildability of the different mixtures were also evaluated. According to the results, the following conclusion can be made:

1) Incorporating brick aggregate decreased slump measurements and height, flowability and setting time while increasing the green strength and green Young's modulus. This could be due to the high water absorption of brick aggregates and the decrease in the ball-bearing effect when replacing the spherical and round-shaped natural aggregate with irregular brick particles.
2) Flexural and compressive strength increased with increasing brick aggregate content for both cast and printed specimens. Printed samples showed anisotropic mechanical behaviour, having the highest flexural and compressive strength performance when the load was applied laterally to the printing direction (h-direction) compared to both the cast sample and the perpendicular direction.

3) Flexural strength of the printed specimens had comparable strength values to cast when the load was applied perpendicular (v-direction) to the printing path. In contrast, the printed samples' compressive strength was higher than the cast mixture.
4) Micro-CT results indicated that incorporating brick aggregates led to having comparable porosity and solid density between the different contents and the mixture with natural sand while increasing the pore structure's anisotropy. However, increasing the brick aggregate content to 50% increased the calculated porosity of the mixture. Moreover, the pore shape was also found to be dependent on brick aggregate content, where the 50% replacement level showed the highest degree of anisotropy, which could be the reason for the directional anisotropic behaviour of the mixtures under compression and flexural strength tests.
5) Replacing natural aggregate with brick aggregate improved the buildability of the mixtures, exhibiting a higher number of layers without showing any failure compared to the control mixture, which showed a high deformation in the bottom layer.

This work proves the suitability and compatibility of using brick in aggregate form as an alternative to the limited natural aggregate in brick-based one-part AAM. This research project also provided a successful framework to develop an eco-friendly feedstock for 3D printing applications.

5. CHAPTER 5: DEVELOPING AND OPTIMISING LC3 CONTAINING EXCAVATED LONDON CLAY FOR 3D PRINTING

5.1. Introduction

This chapter focuses on optimising a 3D printable LC3 mix using excavated London clay, examining the effects of calcination temperature on the reactivity of calcined London clay and admixture addition on the properties and printability of the LC3 mixture. Different dosages of superplasticisers (SP) and viscosity-modifying agents (VMA) will be tested for fresh properties, reaction kinetics, and strength. 3D printing trials will assess shape stability, print quality, and buildability. While many studies have developed 3D printable LC3 mixtures, these typically use clay with at least 40% kaolinite. To the authors' knowledge, the printability of an LC3 mix made with low-grade excavated London clay has not been previously explored. It should be noted that the outcomes of this chapter have been published as a journal paper:

5.2. Theoretical background

Low-grade clay minerals, particularly those with kaolinite content below 40%, have been identified as promising candidates for producing pozzolanic calcined clay for LC3 production [24]. These clay minerals typically contain components such as kaolinite, montmorillonite, and illite [334]. In recent decades, the analysis of clay materials found in the Earth's crust concerning their pozzolanic activity and their potential as SCMs in cementitious mixtures has gained significant interest. However, there is a notable lack of studies investigating the performance of these clays in their calcined form [335–337], highlighting a significant technical gap in evaluating the suitability of these locally sourced waste materials. Given the diverse origins of the excavated materials, it is essential to optimise calcination conditions, such as calcination temperature and residence time, on a case-by-case basis [184,334,338]. Recent research has increasingly focused on the potential of utilising excavated clay waste as SCMs. In the UK, tunnelling excavation activities in West London from a major rail infrastructure project are expected to result in over 5 million m^3 of excavated materials, of which the majority is London clay waste [339]. London clay refers to the clays present in the geological formation of the London Basin. It mineralogically differs from kaolinitic clays, having various clay mineral fractions containing relatively low kaolinite content within the range of 10–30% [339]. Studies on investigating the suitability of using London clay are still limited. For instance, Dhandapani et al. [339] investigated the suitability of using excavated London clay obtained from three different locations with a kaolinite content of around 27% to replace 50% and 70% of OPC. The authors of this study found that London clay exhibits better pozzolanic reactivity when calcinated at 800 ℃. Moreover, the studies on London clay in calcined form didn’t consider evaluating the different engineering properties of the resultant mixture, which could offer insights into the suitability of any earth crust clay. In addition, there have been no studies conducted to evaluate the 3D printability and printing-related properties of cementitious mixtures developed using excavated London clay.

5.3. Experimental program

The overview of the experimental programme is illustrated in Figure 5.1.

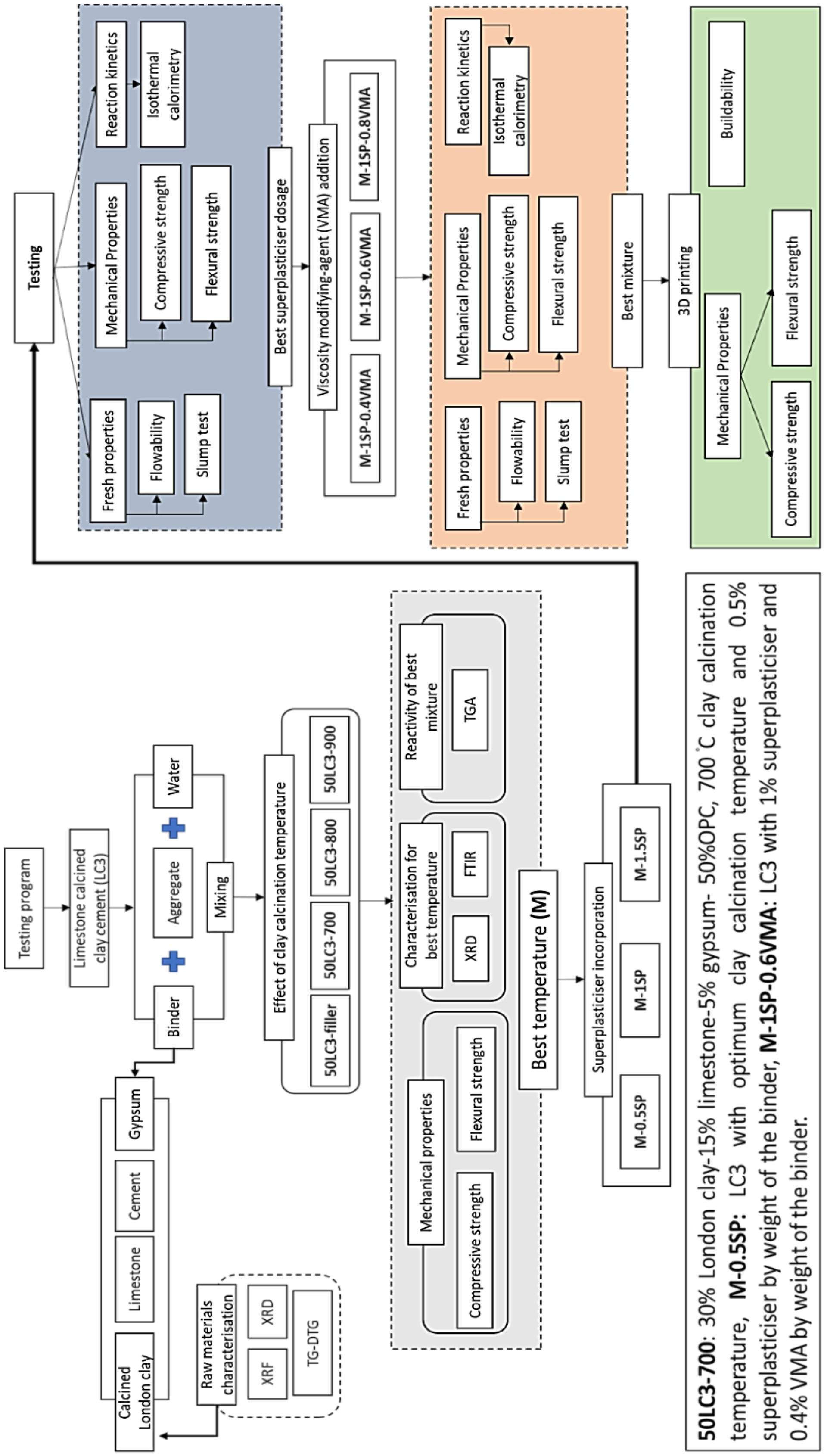

50LC3-700: 30% London clay-15% limestone-5% gypsum- 50%OPC, 700 °C clay calcination temperature, **M-0.5SP:** LC3 with optimum clay calcination temperature and 0.5% superplasticiser by weight of the binder, **M-1SP-0.6VMA**: LC3 with 1% superplasticiser and 0.4% VMA by weight of the binder.

Figure 5.1. A schematic illustration of the experimental program

5.3.1. Materials

A commercial OPC (CEM I 42.5 N) was employed following BS EN 197-1 [328]. London clay was provided from the HS2 excavation site in West Ruislip, West London. The as-received clay samples were oven-dried in an oven at 105°C for 72 h prior to being crushed manually using a hammer into smaller particles. The clay particles were introduced to automatic crushing using a Retsch 100 grinder machine (Germany) (see Figure 3.2a), equipped with a 1 mm mesh. The obtained materials were further ground using a Retsch ball mill machine (Germany) (see Figure 3.2b) containing eight balls for 3 min with a speed of 500 rpm, followed by sieving through a 125 μm mesh to obtain clay powder. The preparation process of clay powder is shown in Figure 5.2. Limestone powder with 99% calcium carbonate purity was supplied from Normin Industrial Minerals, Oman. Table 5.1 shows the chemical oxides of London clay and LP obtained using XRF analysis. The particle size distribution (PSD) curves obtained using laser diffractometry of OPC, London clay, calcined London clay, and LP are presented in Figure 5.3. The gypsum (British Gypsum, UK) was incorporated into the LC3 mixture to promote the reaction of the aluminates from the added SCMs beyond the primary calcium silicate reaction. Gypsum addition shifts the hydration reaction of the aluminate peak to later times, which prevents the flash setting of the mixture [340]. Sika® ViscoCrete® 510 P polycarboxylate powder (Sika, Germany), with a bulk density of 0.6 g/cm^3 and a pH value of 4, was used as a superplasticiser in the LC3 mixture. The used PCE-based SP powder is a high-performance superplasticiser and water reducer. The addition of SP was to reduce the water content and improve the workability and fresh properties of the LC3 mix. Moreover, hydroxypropyl methylcellulose (HPMC)-based VMA white powder supplied by Alfa Aesar, USA, was utilised as VMA in LC3 mixtures.

To produce calcined London clay (CLC), the clay powder was subjected to different calcination temperatures, as will be determined later in this chapter, using an electric chamber furnace (CARBOLITE CWF 1100). The temperature was raised from room temperature to the target calcination temperature at a heating rate of 10°C/min and then maintained for 1 hour. Afterwards, the samples were introduced to rapid cooling at ambient temperature.

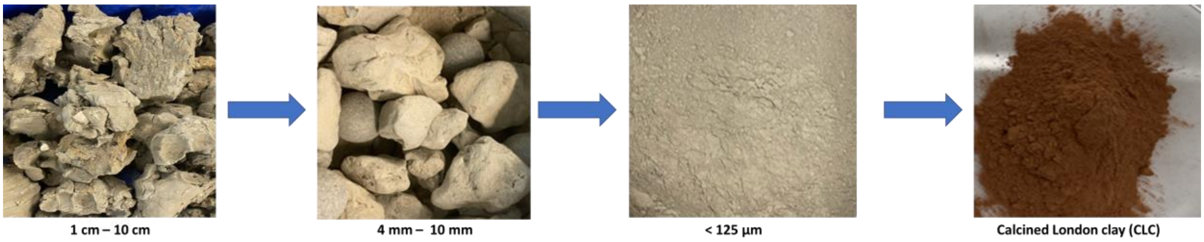

Figure 5.2. Excavated London clay processing and calcination.

Table 5.1. Chemical composition of limestone and raw London clay (%).

	SiO_2	Al_2O_3	Fe_2O_3	K_2O	CaO	P_2O_5	SO_3	MgO	LOI
Limestone	10.3	4.2	2.9	0.7	49.2	-	-	1.93	30.1
London Clay	56.4	14.4	5.9	2.9	1.4	0.9	0.5	0.7	5.8

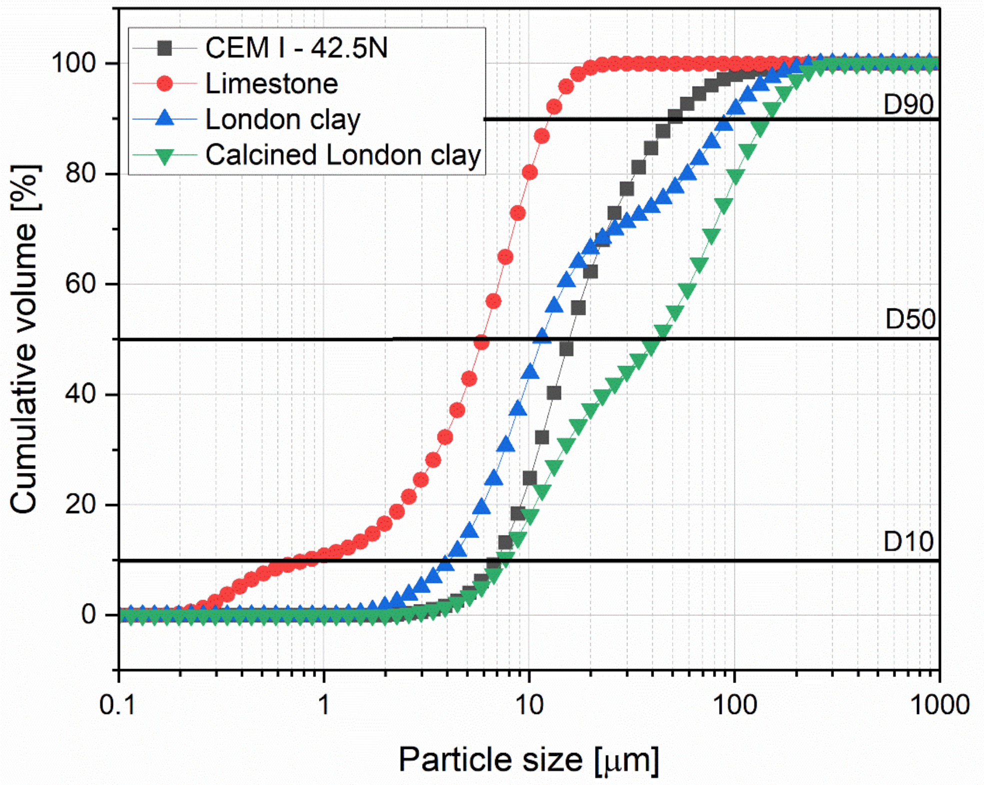

Figure 5.3. Particle size distribution of LC3 binder materials

5.3.2. Sample preparation and mix formulations

A 50% replacement ratio (comprising 30% calcined London clay (CLC), 15% limestone, and 5% gypsum) was used to design LC3-50 mixtures. LC3-50 mixtures were prepared by mixing source ingredients, including OPC CEM I 52.5 N, CLC, limestone, and aggregates, in a planetary mortar mixer (Kenwood, Germany) for approximately 3 min at 100 rpm (dry-mixing stage). Afterwards, the required amount of mixing water was gradually added into the mixer, and mixing continued for another 5 min at 350 rpm (wet-mixing stage). The aggregate/binder and the CLC/limestone ratios were fixed to 1.5 and 2, respectively. For LC3 mixtures containing SP and VMA, precise amounts of SP (i.e., 0.5 wt%, 1 wt%, and 1.5 wt% by the weight of the binder) were poured into the mixer in the dry mixing stage, while the specific amounts of VMA (i.e., 0.4 wt%, 0.6 wt%, and 0.8 wt% by the weight of the binder) were added to the mix at the end of the wet mixing stage, and the mixing continued for an additional 3 min. For LC3 mixtures with SP and VMA, a water/binder ratio of 0.3 was used for enhancing the mechanical properties, while a ratio of 0.5 was used for control mixtures to guarantee adequate workability for casting. The resulting LC3 mixtures were cast in 40 x 40 x 160 mm^3 prismatic polystyrene moulds or fed into the hopper of a 3D printer for the printing process. Both cast and printed samples were placed in a control room at 20 ± 3°C and 40% relative humidity for 24 h (air-curing). The cast specimens were then de-moulded and immersed in a controlled water tank at 20 ± 3°C (water-curing) until the testing age. Table 5.2 displays the mixture formulations, divided into three phases. Phase (I) aimed at optimising the calcination temperature to obtain the highest pozzolanic reactivity from CLC, Phase (II) aimed at optimising the SP ratio, and Phase (III) aimed at optimising the VMA percentage while maintaining the optimal SP ratio. It should be noted that one extra mix formulation was considered in Phase I to be investigated under mechanical strength testing, which had filler instead of CLC in the binder to provide more understanding of the involvement of CLC in improving the strength behaviour of the mixture as an indication of its participation in reaction.

Table 5.2. LC3 mix formulations

Mixture ID	**Binder (%)**				**Aggregate-binder ratio**	**W/B ratio**	**Additives (%)**	
	OPC	**Limestone**	**CLC**	**Gypsum**			**SP**	**VMA**
Phase (I) – Calcination temperature optimisation								
50LC3-700°C	50	15	30	5	1.5	0.5	0	0
50LC3-800°C	50	15	30	5	1.5	0.5	0	0
50LC3-900°C	50	15	30	5	1.5	0.5	0	0
Phase (II) –SP optimisation (50LC3-800°C=M)								
M	50	15	30	5	1.5	0.5	0	0
M-0.5SP	50	15	30	5	1.5	0.3	0.5	0
M-1SP	50	15	30	5	1.5	0.3	1	0
M-1.5SP	50	15	30	5	1.5	0.3	1.5	0
Phase (III) –VMA optimisation (50LC3-800°C=M)								
M-1SP	50	15	30	5	1.5	0.3	1	0
M-1SP-0.4VMA	50	15	30	5	1.5	0.3	1	0.4
M-1SP-0.6VMA	50	15	30	5	1.5	0.3	1	0.6
M-1S-0.8VMA	50	15	30	5	1.5	0.3	1	0.8

5.3.3. Experimental methods

The procedures of the specific test methods used in this section are presented below:

5.3.3.1. X-ray diffraction (XRD)

X-ray diffraction (XRD) was used to determine the mineralogical compositions and phases of the different materials and mixtures and to investigate the changes in London clay after calcination. XRD measurements were conducted using a Malvern Panalytical Empyrean XRD in the Bragg-Brentano geometry with CuKα radiation ($\lambda = 1.540596$ Å). The measurement was conducted for 12 h, covering a 2θ range of 10° to 75°. The incoming beam path had a programmable divergence slit, while the diffracted beam path had a programmable anti-scatter slit.

5.3.3.2. Fourier Transform Infrared Spectroscopy-Attenuated Total Reflectance (FTIR-ATR)

The impact of thermal activation on the chemical bonds of the London clay before and after the calcination process was registered using FTIR-ATR (PerkinElmer Spectrum one Spectrometer, UK). The attenuated total reflection instrument with a 3x bounce diamond crystal at a 45° incidence angle was employed to obtain infrared spectra in the 4000–550 cm^{-1} range with a resolution of 4 cm^{-1}. Measurements were taken after drying the clay powders, and the average result was reported based on testing a batch of three samples per composition.

5.3.3.3. Reactivity test

TGA was conducted using a Setsys Evolution analyser (Setaram Instrumentation, Caluire, France), equipped with alumina crucibles. The sample (50 ± 2 mg) was heated, using inert atmosphere (nitrogen), from room temperature to 800 °C at a heating rate of 10 °C/min. Lime/CLC paste (10 g) was prepared by dry mixing reagent grade calcium hydroxide (> 95%, Alfa Aesar, Haverhill, MA, USA) and the analyte powder in a 1:1 mass ratio. Then, 10 g of water was added, achieving a solid-to-liquid ratio of 1. The fresh paste was divided into two batches for reactivity analysis at 7 and 28 days. The samples were stored in plastic containers and left in an oven at 40 °C to maintain high humidity and minimise carbonation's effect. Before testing, the blend was manually pulverised. Acetone with a purity of 99.5% was added during the milling operation to block the hydration. The excess solvent was removed using a vacuum pump filtering system by collecting the powder on a Whatman540 qualitative filter paper (Whatman®, Maidstone, UK) with a diameter of 8 μm. Prior to TGA testing, the sample was pre-dried at 60 °C for 3 h. A high reactivity pozzolanic calcined clay, metakaolin (MK) with a kaolinite content of 95%, was also prepared and tested to evaluate the pozzolanic quality of CLC with respect to commonly used SCMs and validate the reliability of the method employed in this study.

When subjected to TGA, a blended paste of lime and pozzolana exhibits three distinct characteristic peaks due to simultaneous reactions caused by the consumption of calcium hydroxide by the pozzolanic powder [341,342].

- Mass loss around 200 °C. This peak is attributed to the dehydration of C-S-H gel. Depending on the nature and reactivity of the pozzolan, the pozzolanic powder starts consuming the lime available in the paste to produce C-S-H gel as hydrated product. As the pozzolan fixates the lime over time to form the hydrate gel, the amount of CH phase in the test sample decreases and the amount of hydrated phases that present this weight loss increases.
- Mass loss around 500 °C. This peak is ascribed to the decomposition (dehydroxylation) of unfixed calcium hydroxide from the pozzolanic powder.

$$\underset{74g/mol}{Ca(OH)_2} \rightarrow \underset{56g/mol}{CaO} + \underset{18g/mol}{H_2O}$$

The amount of calcium hydroxide from TGA dehydroxylation ($CH^{dh-loss}$) was calculated using Eq. (5.1) in accordance with the stoichiometry of the reaction above:

$$CH^{dh-loss} = \frac{H_{500°C}}{MW_{H_2O}} \times MW_{Ca(OH)_2} = H_{500°C} \times 4.11 \qquad Eq.(5.1)$$

where $H_{500°C}$ is the mass loss due to the lime dehydroxylation around 500 °C, MW_{H_2O} and $MW_{Ca(OH)_2}$ are the molecular mass of the water and the calcium hydroxide, respectively.

- Mass loss around 700 °C. For a reliable assessment of the pozzolanic activity, the carbonation that lime undergoes by the interaction with the surrounding carbon dioxide was considered in the analysis. Calcium hydroxide converts in calcium carbonate in accordance with the following reaction:

$$\underset{74g/mol}{Ca(OH)_2} + \underset{44g/mol}{CO_2} \rightarrow \underset{100g/mol}{CaCO_3} + \underset{18g/mol}{H_2O}$$

The mass loss around 700 °C is therefore associated to the decomposition of calcium carbonate. The loss in the decarbonation region was converted into calcium hydroxide loss ($CH^{dc-loss}$) using Eq. (5.2) following the stoichiometry of the CH carbonation reaction [343]:

$$CH^{dc-loss} = \frac{H_{700°C}}{MW_{CO_2}} \times MW_{Ca(OH)_2} = H_{700°C} \times 1.68 \qquad Eq.(5.2)$$

where $H_{700°C}$ is the mass loss due to the calcium carbonate decomposition around 700°C, MW_{CO_2} and $MW_{Ca(OH)_2}$ are the molecular mass of the calcium carbonate and the calcium hydroxide, respectively.

Then for each curing age, the pozzolanic activity (PA) of the pozzolan powder, expressed as the maximum amount of lime that the powder can fixate, was calculated using Eq. (5.3)**:**

$$PA\ (\%) = \frac{CH^{i} - CH^{dh-loss} - CH^{dc-loss}}{CH^{i}} \times 100 \qquad Eq. (5.3)$$

Finally, from PA values and the initial mass of powder analysed via TGA, the amount of calcium hydroxide reacted per gram of pozzolan (g CH^{fixed}/g pozzolan) was then determined. This parameter was compared with the classification proposed by Borges et al. [344] categorising the SCMs into "inert", "pozzolanic", and "highly pozzolanic" based on their *g* CH^{fixed}*/g pozzolan* value.

5.3.3.4. Buildability

Similar to the previous chapter, a cylinder was printed in a circular path, measuring 150 mm in diameter. However, four batches of mix (i.e., 8000 g of fresh mixture) were used, which can extrude a total of 23 layers. The buildability of the mixture was evaluated by comparing the maximum height of the printed object after 23 layers, as well as vertical/radial distortion and layer deformation.

5.3.4. Printing process

Similar to the previous chapter, a gantry 3D printer equipped with a custom-designed auger extruder was employed. The samples were printed using a 20 mm circular-shaped nozzle with a motion speed of 15 mm/s and a 10 mm nozzle standoff distance.

5.4. Results and discussions

5.4.1. Clay calcination profile

The effective calcination temperature range, ensuring the decomposition of the clay, was determined using TGA. TGA of as-received London clay was measured using a heating rate of 10 °C/min from 30 °C to 1000 °C (Insturment SDT Q600) with an N_2 flow rate of 30 °C/ min in the heating chamber to avoid carbonation. TGA was also used to determine the kaolinite content of the raw London clay. The dehydroxylation of kaolinite minerals occurs from 400 to 600 °C [153,158]. The kaolinite content ($\mathrm{wt.\%_{kaolinite}}$) is calculated using the mass loss during the dehydroxylation ($\mathrm{wt.\%_{kaol\text{-}OH}}$) using the following equation:

$$\mathrm{wt.\%_{kaolinite}} = \mathrm{wt.\%_{\,kaol-OH}} \times \frac{\mathrm{M_{kaolinite}}}{2\mathrm{M_{water}}} \qquad Eq.(5.1)$$

where $\mathrm{M_{kaolinite}}$ is the molecular weight of kaolinite and $\mathrm{M_{water}}$ is the molecular weight of water.

The mass loss curve in the TGA test is presented in Figure 5.4, where London clay exhibited a total mass loss of around 7% when heated up to 1000 °C. London clay exhibited three phases. The initial phase change occurred around 176 °C, exhibiting a mass loss of around 1.5%, which is primarily attributed to the evaporation of free water. A substantial mass loss of around 2.5% in the temperature range of 566-899 °C was observed and it is linked to the dehydroxylation of clay minerals and transformation into an amorphous structure, suggesting that calcining the clay within this temperature range is crucial for its activation. Hence, the calcination temperatures were selected to be within this range. The analysis of mass loss between 400 to 600 °C revealed a kaolinite content of 16.8% in the used clay.

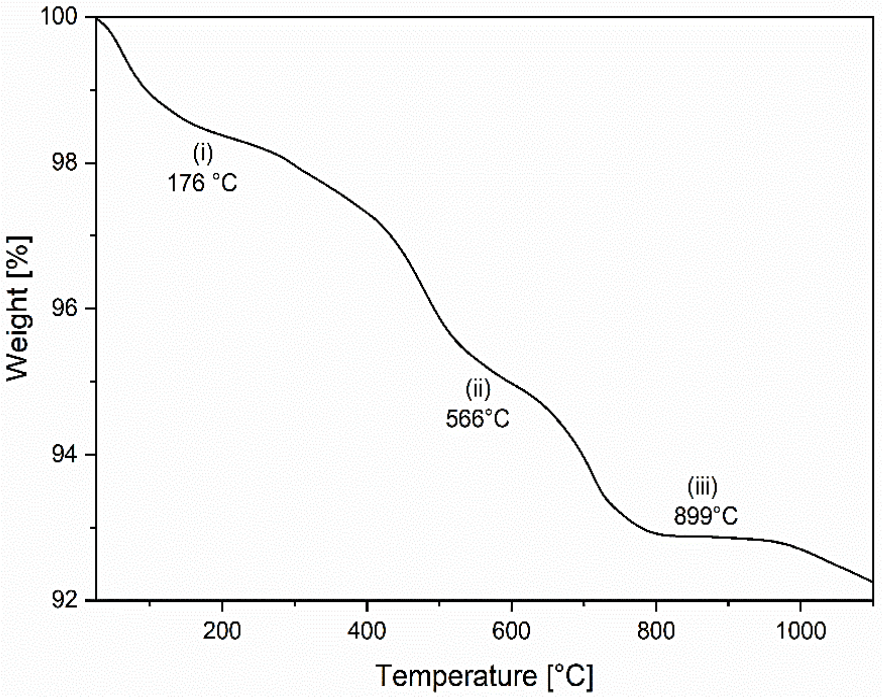

Figure 5.4. TGA curve of raw London clay

5.4.2. Effect of calcination temperature

5.4.2.1. Mineralogical composition changes of clay

The changes in London clays’ mineralogical composition and decomposition after calcination at different temperatures were investigated using XRD and the patterns are shown in Figure 5.5a. The XRD pattern of the raw London clay shows that it is mainly composed of quartz with low-intensity peaks of 1:1 kaolinite clay mineral and 2:1 illite/smectite clay minerals. The presence of impurities, such as quartz and feldspar were identified, which are considered to be inert in terms of pozzolanic reactivity. The presented peaks of feldspar were attributed to potassium feldspar (k-feldspar) according to the ICDD database, which agrees with the chemical composition presented in Table 5.1, which shows that London clay contains 2.9% K_2O in its chemical composition. Calcination of London clay at a temperature of 700 °C caused the disappearance of kaolinite clay minerals at 12.1°, 25°, 30.9° and 60.5° 2ɵ and calcite peak at 29.9° 2ɵ with a decrement in the intensity of the other peaks. Increasing calcination temperature to 800 and 900 °C did not induce significant changes to the XRD patterns, where the illite peaks still presented even after calcining London clay at 900 °C. It can be seen that quartz and feldspar peaks remained unchanged. Similar observations were obtained by Zhou et al. [345], which found that a higher calcination temperature of 1000 °C is needed to allow the dihydroxylation of 2:1 clay minerals (i.e., illite peaks) in excavated London clay. However, it should be noted that the clay used in the authors' studies was obtained from a different location than the clay used in this study.

Similarly, the changes in the clay mineral structure as a function of the calcination process were analysed using FTIR spectra on both raw London clay and CLC. The FTIR spectrums of London clay before and after calcination are presented in Figure 5.5b. For the raw London clay, the absorption bands at 3698-3623 cm^{-1} are mainly assigned to the symmetric stretching vibration of the inner surface hydroxyl group [346] and the absorption band at 3623 cm^{-1} is associated with the internal hydroxyl stretching of clay minerals [347]. The aforementioned bands completely disappeared after calcination, due to the dehydroxylation of clay minerals [345]. The absorption bands at 1622-1424 cm^{-1} are attributed to the stretching of the hydroxyl group in the molecular water. The bimodal absorption band observed at 993 cm^{-1} is related to the stretching of planar Si-O of the different clay minerals (kaolinite, illite, smectite and montmorillonite) [345]. The decline in the peak intensity after calcination at 700°C represents the transformation of the raw London clay into a disordered amorphous structure [348].

Moreover, the absorbance at 911 cm^{-1}, respectively, is a distinctive peak of kaolinite, montmorillonite, and illite, as well as an internal bend of –OH groups. The disappearance of those peaks after calcination is because of the dehydroxylation of clay minerals. The Si-O stretching bands of quartz at 1160, 794, and 693 cm^{-1} are visible at all calcination temperatures, indicating the stability of quartz under calcination. As the calcination temperature increases, the stretching vibration band of Si-O at 993 cm^{-1} shifts slightly to a higher position, which could be due to the formation of a three-dimensional amorphous silica framework [345]. Further increasing the calcination temperature caused a minimal effect on the This is consistent with the XRD results, confirming the dehydroxylation of the clay minerals. Hence, it can be indicated from both XRD and FTIR curves that increasing the calcination temperature above 700 °C did not induce any change to the mineralogical patterns and chemical bounds of CLC.

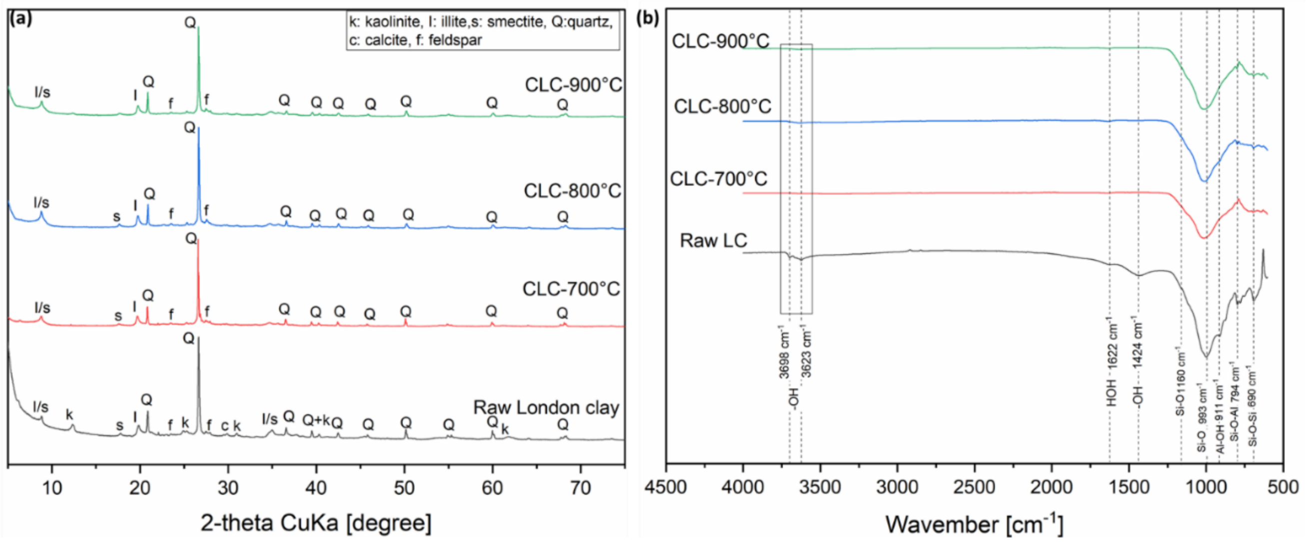

Figure 5.5. (a) Mineralogical phases change and (b) FTIR-ATR spectrums of London clay before and after calcination at different temperatures.

5.4.2.2. Mechanical strength properties

Table 5.3 presents the flexural and compressive strength results of LC3 mixtures prepared using CLC calcinated at different temperatures. To better understand the reactivity of CLC and its impact on the strength performance in the system, an LC3 sample prepared with an inert filler material (i.e., quartz silica) instead of CLC was also prepared, referred to as 50LC3-filler. LC3 mixtures had higher compressive strength than the filler sample after 7 and 28 days. The higher compressive strength of LC3 mixtures indicated the participation of CLC in the reaction through its pozzolanic reaction, producing more hydration products and enhancing the compressive strength of the mixtures. Moreover, it can be observed that using CLC calcinated at 800 °C exhibited around 5% and 14% higher flexural and compressive strength values, respectively, than 700 °C and around 6% and 16% higher flexural and compressive strength performance than 900 °C, indicating the better pozzolanic reactivity of the CLC at this temperature. Furthermore, the densities of different mixtures were comparable of a 2.08–2.12 g.cm^{-3}. Hence, based on the results, 800 °C achieved the highest pozzolanic reactivity and, therefore, it was chosen as the optimum calcination temperature and used to study the effect of additives incorporation to modify the mixture in the next stages of this study. This is in good agreement with the findings of [339,349] and contradicts those of [345]. However, it should be noted that a direct comparison cannot be made between the current study and the other studies because of the difference in the geological location origin, clay microstructure and kaolinite content of the used clay. In addition, the difference in the mix design, including water content, aggregates size and ratio, restricts the direct comparisons to the strength behaviour obtained in other studies. Based on the strength results, 800 °C can be considered the optimal calcination temperature for excavated London clay.

Table 5.3. Flexural and compressive strength of LC3 samples containing CLC calcinated at various temperatures

Mix	**Flexural strength [MPa]**		**Compressive strength [MPa]**	
	7 days	28 days	7 days	28 days
50LC3-Filler	4.4 ± 0.2	7.1 ± 0.1	8.3 ± 1.5	17.4 ± 0.7
50LC3-700	4.4 ± 0.1	6.9 ± 0.1	9.4 ± 0.5	19.1 ± 1.3
50LC3-800	4.9 ± 0.3	7.5 ± 0.3	9.9 ± 0.4	22.6 ± 1.0
50LC3-900	4.2 ± 0.3	7.1 ± 0.5	9.3 ± 0.6	19.3 ± 1.1

Note: The numbers indicate Average ± Standard Deviation.

5.4.2.3. Pozzolanic reactivity

To further understand the reactivity of London clay calcined at 800 °C, which was selected to be the optimal temperature based on flexural and compressive strength, the pozzolanic reactivity of the CLC was evaluated using TGA to determine the amount of CH consumption by CLC. Figure 5.6 shows the TGA analysis of lime-MK and lime-CLC pastes after 7 and 28 days of hydration. The thermograms display the three main phases of weight loss of the samples: dehydration of C-S-H, decomposition of CH, and decomposition of $CaCO_3$. The black curves show the percentage of mass loss in each region, while the red curves indicate the temperature range of the main dehydration/decomposition reactions. By analysing the TGA thermograms, it is possible to notice that, regardless of the type of pozzolan examined, as the hydration age advances (from 7 to 28 days), the extent of the mass loss due to the C-S-H dehydration (around 200°C) increases, the weight loss due to the CH decomposition (around 500°C) gradually decreases, and the effect of carbonation (around 700°C) becomes more significant. This is due to the reaction between lime and pozzolanic powder, which gradually consumes the available calcium hydroxide, generating C-S-H hydration products over time. However, the fraction of calcium hydroxide that remains unreacted in the paste undergoes carbonation, which increases significantly with the hydration age [350].

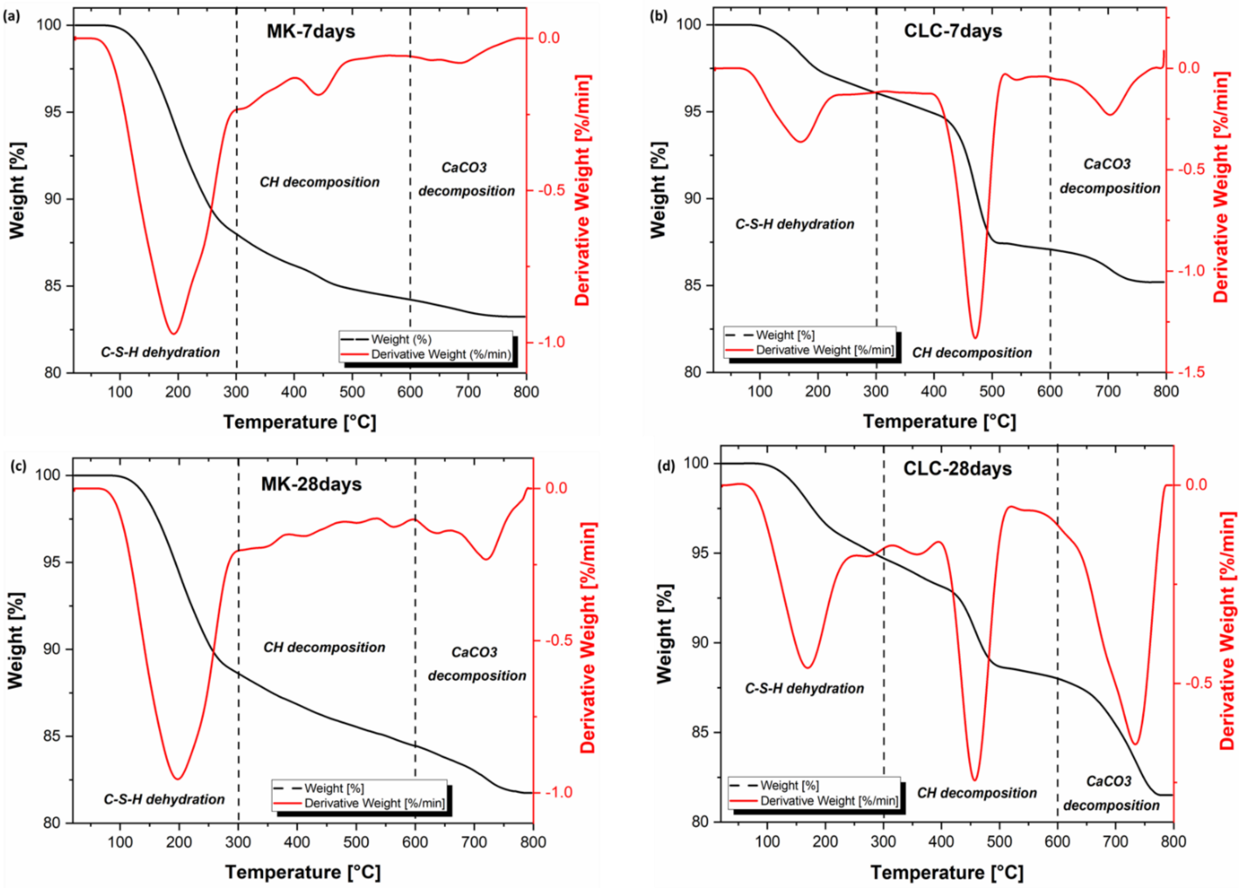

Figure 5.6. TGA thermograms of (a) lime-MK paste at 7 days, (b) lime-CLC paste at 7 days, (c) lime-MK paste at 28 days, and (d) lime-CLC paste at 28 days. CH: Calcium hydroxide ($CaOH_2$).

Figure 5.7a displays the pozzolanic activity (PA) values for MK and CLC at 7 and 28 days. MK powder, as expected, shows very high pozzolanic reactivity. Indeed, net of carbonation phenomena, it consumes the whole amount of calcium hydroxide available in the paste after 28 days. However, almost all the lime present in paste is fixed after 7 days, indicating the ability to carry out its reactivity at the early age of hydration [351]. CLC also highlights the same behaviour of almost complete reactivity to lime at 7 days, but the overall PA is on average 20% lower than the MK. The presence of quartz (inert behaviour) in the mineralogical composition of clay-based materials can limit their pozzolanic reactivity [352]. The PA determined in this study for CLC showed a similar performance to that studied by Zhou et al. [345], which investigated the PA of excavated London clay obtained from an excavation site in East London. Zhou et al. [345] studied the effect of calcining excavated London clay at different temperatures (namely 600, 700, 800, 900 and 1000 °C) on the pozzolanic reactivity of CLC. The authors found that calcining excavated London clay had the highest reactivity at 800 and 900 °C, where both temperatures combined a similar amount of CH, which was identical to this study of around 0.65 g of CH/ g of pozzolana. On the other hand, CLC investigated in this work shows greater activity performance than other clay powders, from scientific literature, obtained as waste and mining by-product. Yanguatin et al. [336] reported pozzolanic reactivity values lower than 50% in excavated waste clays from Bogota (Colombia). Cao et al. [353] investigated the PA of sandstone clay by-product from Queensland quarry (Australia). The calcinated powder (600 °C for 1 h) reached a reactivity of 31 %. For a calcination time of 2 h, the PA was 68%, which is similar to the reactivity of the CLC examined in this study. Based on the classification implemented by Borges et al. [344], CLC can still be classified as a material with pozzolanic activity (Figure 5.7b) and, therefore, has the potential to be used as a supplementary cementitious material in cement binders. To further improve the reactivity of CLC, possible routes are (a) enhancing the amorphousness of the powder or (b) optimising its fineness. It is widely accepted that an increase in specific area (decrease in particle size) will expose a greater surface to chemical reaction enhancing reactivity. Furthermore, amorphous structures provide more reactive than crystalline ones [265].

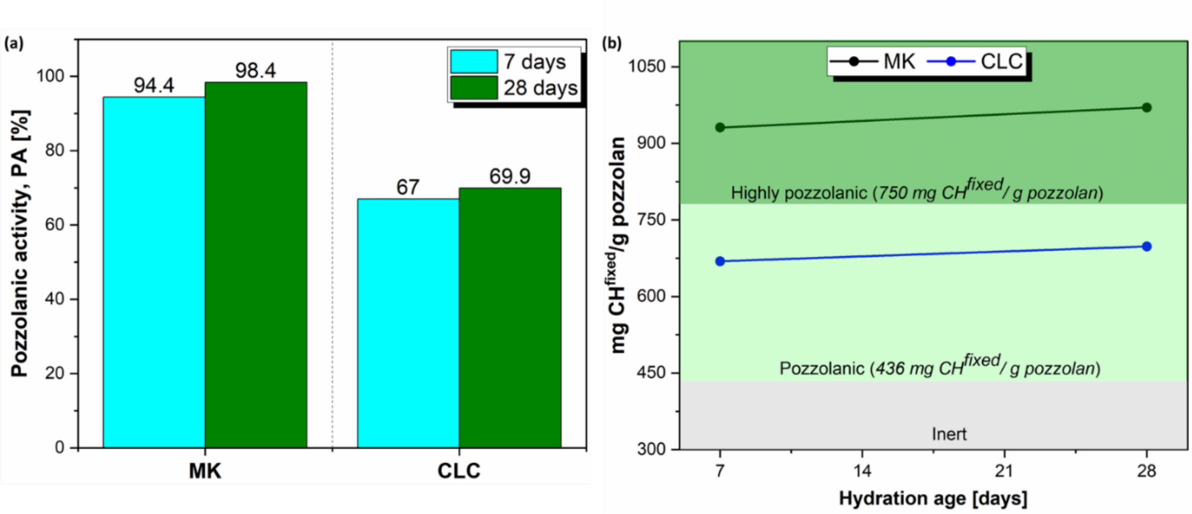

Figure 5.7.Results of TGA analysis: (a) PA values at 7 and 28 days and (b) amount of limed fixed for gram of pozzolan powder. CH: calcium hydroxide

5.4.3. Effect of superplasticiser addition on LC3

5.4.3.1. Fresh properties

The impact of incorporating SP was studied on the fresh properties and mechanical performance of LC3 mixtures prepared with London clay calcined at 800 °C. Incorporating superplasticiser allows the reduction of water-to-binder content while maintaining the workability of the cementitious mixture. The flowability and slump height reduction of the LC3 mixtures were significantly affected by incorporating SP, resulting in a high spread flow diameter. Even without dropping the flow table, the flowability of the mixtures couldn't be measured. Hence, the flowability of mixtures with SP was interpreted as greater than 290 mm, which is the diameter of the flow table apparatus. Moreover, the slump height reduction increased significantly from 5 mm for the control mixture without SP (i.e., M) to 38–43 mm for different SP contents. According to Li et al. [354], a possible reason for the increase in the flowability of the cementitious mixture in the presence of SP can be related to the increase in water filament thickness (WFT). The WFT is affected by the packing density. In the presence of SP, the packing density would increase, decreasing the minimum voids ratio and increasing the excess water ratio in the mix. Hence, increasing WFT and consequently the workability of the mixture. Another possible reason could be the role that SP plays as a dispersing agent, which decreases the cohesiveness of the mixture through its dispersive action [354]. According to Kai et al. [355], the negative ion groups on the SP main chains induce an electrostatic reaction with the calcium ions and hydration products on cement particles' surfaces, making the cement particles adsorb PCE molecules. When being adsorbed to the cement particle, this would allow the PCE SP chain to create a physical barrier around the particles, restricting them from getting in contact with other particles and agglomerating, inducing a steric effect. This, in turn, reflects on the workability of the mixtures. Hence, in this study, even though the w/b ratio was decreased, the higher workability of the mixtures could be attributed to higher packing density and the dispersion action of SP.

5.4.3.2. Mechanical strength properties

Figure 5.8 presents the flexural and compressive strength of LC3 mixtures prepared with different SP contents. Increasing the SP content enhanced the flexural and compressive strengths of the LC3 mixture significantly, where the LC3 mixture containing 1 wt% SP exhibited the highest flexural and compressive strengths of 10 MPa and 44 MPa, respectively. This enhancement is attributed to water-reducing capacity of SP that allowed to lower the water content of the LC3 mixtures from the ratio of 0.5 for the control mixture (M) to 0.3 for those containing SP. Thus, allowing for better compaction of the mixture and production of a more densified mixture with lower porosity. Incorporating SP at low dosage (i.e., 0.5%) might result in insufficient dispersion, resulting in incomplete hydration of cement particles. Increasing SP dosage from 0.5% to 1% was beneficial for the strength performance of the LC3 mixture, allowing for better dispersion of the particles and contributing to better packing density and hydration products. According to Zeyad et al. [356], the enhancement of strength performance with increasing SP dosage in cementitious mixtures could be attributed to the delay in setting time and the longer retention of fresh behaviour and properties of the mixture, consequently allowing the mixture to exhibit a self-compaction ability and thus improving the strength. Although increasing SP dosage enhanced the strength performance, there is a content threshold at which the additive would behave oppositely after exceeding it. That prevents sufficient particle interaction, and thus declines the formation of the strength-giving hydration products, limiting the strength performance of the mixture, as can be seen for the LC3 mixture prepared for 1.5 wt%. Hence, it can be indicated that 1 wt% SP is the optimum dosage.

Based on mechanical properties test results, the mixtures containing 1 wt% SP (the M-1SP mixture) was selected as the optimum mixture for the next stage.

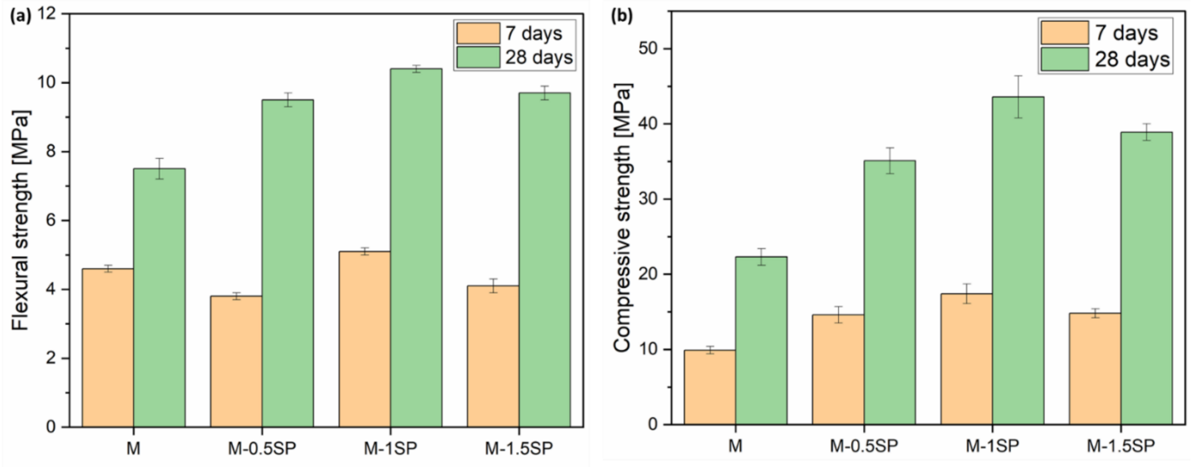

Figure 5.8. (a) Flexural strength and (b) compressive strength of LC3 samples with different SP contents.

5.4.3.3. Reaction Kinetics

Isothermal calorimetry was used to investigate the effect of incorporating different dosages of SP on the reaction kinetics of the mixtures up to 72 h, and the results are presented in Figure 5.9**.** Figure 5.9a shows that all normalised heat flow curves are composed of five stages, which are (1) the initial period, (2) the dormant period, (3) the acceleration period for the main peak, (4) the deceleration period and (5) the steady state [357]. Incorporating SP prolonged the dormant period and decreased the intensity of the main peak significantly, as shown in Figure 5.9a**.** This can be mainly attributed to the reduction of the water content in the mixtures prepared with SP. The dormant period was also prolonged from around 3.5 h for the mix without SP to approximately 8, 13 and 23 h for mixes with 0.5, 1, and 1.5 wt% SP, respectively. In addition, the acceleration period took longer to reach the maximum peak intensity with SP content (see Figure 5.9a). Moreover, the cumulative heat release decreased with SP content, as shown in Figure 5.9b, which indicates the hydration dilution effect in the presence of SP. The retarding and prolonging effect of SP in the LC3 mixture is due to the formation of complexes between the carboxylate groups of polycarboxylate ether (PCE)-based SP and calcium ions (Ca^{+2}) in the pores solution [358], which inhibits the water and ions exchange at the cement-solution interface [359,360] and that hinders the anhydrous grains dissolution [361]. Although isothermal calorimetry curves proved the retardation of hydration in the presence of SP, the compressive strength performance of the different mixtures with SP improved at 7 and 28 days (see Figure 5.8). As stated earlier, this could be due to the lower water content, which resulted in developing a mixture with lower porosity, and, thus, higher strength performance.

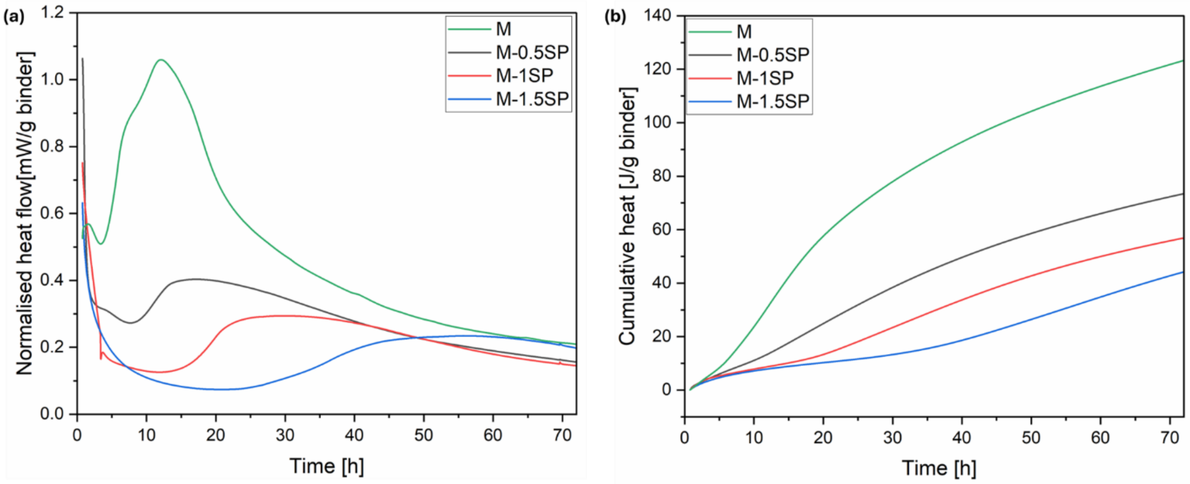

Figure 5.9. Isothermal calorimetry curves of LC3 mixtures with different SP dosages: (a) normalised heat flow and (b) cumulative heat

5.4.4. Effect of viscosity modifying agent incorporation on LC3

5.4.4.1. Flowability and slump height measurements

The LC3 composite containing 1 wt% SP (the M-1SP mixture), which showed better hardened properties among other LC3 compositions, was selected to study the effect of incorporating a VMA. Table 5.4 presents the slump height reduction and flowability percentage of LC3 mixtures with and without VMA incorporation. It is evident that increasing the VMA dosage contributes to retaining the height and shape of the mixture since it decreases the slump height reduction (see Table 5.4). Moreover, the flowability was decreased with increasing the VMA dosage in the mixture. The highest reduction in slump and flowability was registered for the mixture with 0.8 wt% VMA, in which the slump height reduction decreased from 43 mm for M-1SP (i.e., mix without VMA) to 6 mm for M-1SP-0.8VMA, and the flowability decreased from more than 290 mm to 135 mm. For a fixed dosage of SP, the addition of cellulose-derivative VMA (HPMC used in this study is a cellulose-based VMA) can increase the plastic viscosity and/or the yield stress of the mixtures, where the increment is found to be much more significant for plastic viscosity from a macroscale perspective [201,362]. From a microscale view, Chen et al. [24] identified two mechanisms that impact the fresh properties of LC3 in the presence of VMA, which are the flocculation and water retention effects of VMA. Both mechanisms are dependent on the competitive adsorption of the SP and VMA and surface coverage of binder materials and fine particles in the system. The possible flocculation mechanism of VMA in the presence of PCE-based SP are bridging flocculation and depletion flocculation. It was reported that VMA enhances cement grain flocculation by providing more contacts and bridges between particles. This occurs when a high-molecular-weight polymer adsorbs onto multiple cement particles, physically holding them together, promoting green strength development and increase yield stress of cement suspension [24,201,363]. The depletion flocculation occurs due to the depletion of non-adsorbed polymers from a volume exclusion shell around large particles. The difference in the concentration of polymers in the bulk solution compared to the depleted zone results in an increase in the osmotic pressure within the system, causing it to flocculate. That leads to an increase in the yield stress of the suspension [201,364]. On the other hand, the retention of free water by VMA is due to the formation of hydroxyl bonds by hydroxyl groups (-OH) and ether groups (R-O-R) via combined water molecules. Hence, the VMA chain wraps the free water in the suspension [365]. That, in turn, increases the mixture's viscosity [24]. These two mechanisms explain the observed reduction in the workability of the mixtures with increasing the VMA dosage.

Table 5.4. Workability evaluation of LC3 mixtures with different VMA dosages

Mix ID	Slump height reduction [mm]	Flowability [%]
M-1SP-0VMA	43	>190
M-1SP-0.4VMA	20	70
M-1SP-0.6VMA	8	45
M-1SP-0.8VMA	4	35

5.4.4.2. Mechanical strength properties

Figure 5.10 presents the flexural and compressive strength performance of the different LC3 mixtures with and without VMA addition. Both flexural and compressive strengths of mixtures containing different VMA contents are comparable all of which are higher than the value registered for the mix without VMA (i.e., the M-1SP mixture) after 7 days of curing. The flexural strength results at 28 days were comparable for the mixtures with 0.4 and 0.6 wt% VMA to that of the mix without VMA, while a slight decrease for the M-1SP-0.8VMA mix was observed. The results indicated that incorporating VMA did not affect the flexural strength of the LC3 mixture, as shown in Figure 5.10a.

On the other hand, the compressive strength was affected significantly by adding VMA and decreased by around 24 – 29% for different mixtures compared to the mix without VMA after

28 days, as shown in Figure 5.10b. Another interesting observation can be seen in both flexural and compression results when incorporating VMA, which is the higher performance at 7 days compared to the mixture without VMA. A similar impact on the compressive strength was reported in [24,86,224]. Figueiredo et al. [224] investigated the effect of adding different dosages of HPMC-based VMA up to 1% to OPC paste and found the compressive strength to decrease significantly in the presence of VMA. According to the authors, a higher capillary porosity region was observed in mixes containing VMA, which could be filled with water due to its water retention effect. The entrapped water could have been released as the mixture aged and the hydration progressed. This, in turn, increases the void volume in the mixtures prepared with VMA, contributing to the decrement in the compressive strength performance of cementitious mixture in the presence of VMA. Similarly, Chen et al. [24] found the compressive strength performance of the 3D printable LC3 to decrease with increasing VMA ratio. According to the authors, incorporating VMA lowered the heat flow induced by the hydration of the cementitious mixtures. This is in good agreement with the results obtained in this study.

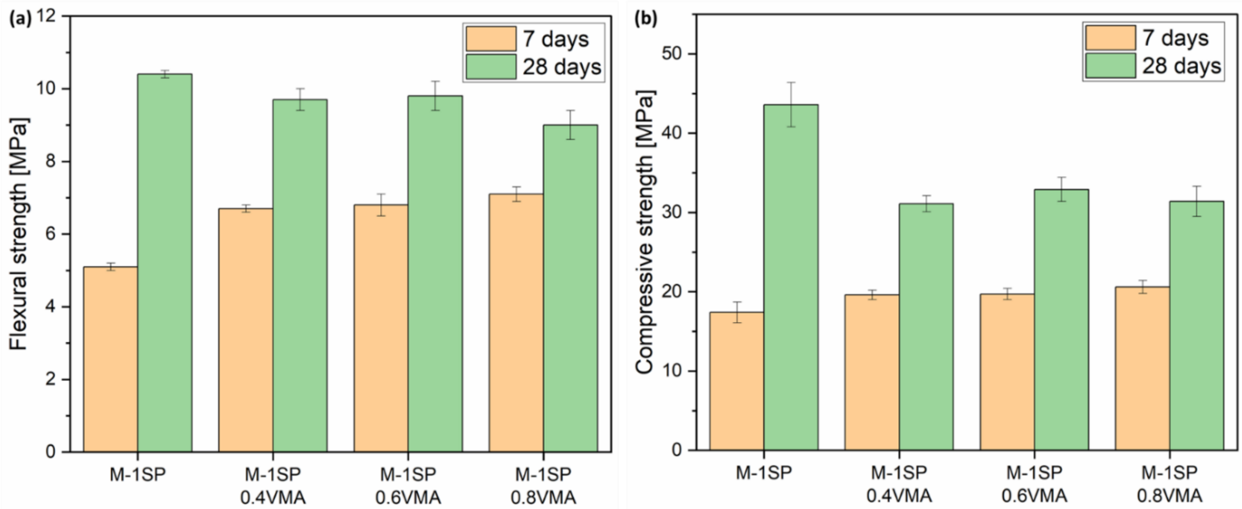

Figure 5.10. (a) Flexural strength and (b) compressive strength of LC3 mixtures with different VMA contents

5.4.4.3. Reaction kinetics

The effect of incorporating VMA on the normalised heat flow and cumulative heat induced from the reaction using isothermal calorimetry, and the curves are presented in Figure 5.11. The heat flow curves are composed of four stages, which are (1) the initial period, (2) the dormant period, (3) the acceleration period, and (4) deceleration followed by a slight slope due to the formation of AFm phases [357]. It can be detected that increasing VMA content slightly decreased the reaction speed at the acceleration period and delayed the time in which the main peak occurred, along with a decrease in the peak intensity. The following peak and the slope also slightly decreased, as shown in Figure 5.11a. Similarly, the cumulative heat release decreased with increasing VMA dosage in the mixture, as shown in Figure 5.11b. These observations are consistent with the results reported elsewhere [86]. Many researchers believe that the adsorption of cellulose-derivative VMAs onto hydrated phases, such as C-S-H and portlandite, is the primary cause of delayed hydration [201,366,367]. The cellulose derivative VMAs have a substantial effect on the precipitation of C-S-H through a three-step process by (1) reducing the number of initial C-S-H seeds formed, (2) slowing down the formation of the C-S-H shell around the C_3S, and (3) leading to the formation of a thicker and more permeable C-S-H layer [367]. Therefore, the compressive strength reduction with adding VMA can also be associated with the retardation of hydration. Although the M-1SP-0.6VMA mix showed a higher retardation effect, it exhibited marginally higher strength than the M-1SP-0.4VMA mix. The observed strength behaviour might be attributed to the better mix consistency of M-1SP-0.6VMA compared to M-1SP-0.4VMA mix, resulting in a less porous microstructure, resulting in the observed strength behaviour.

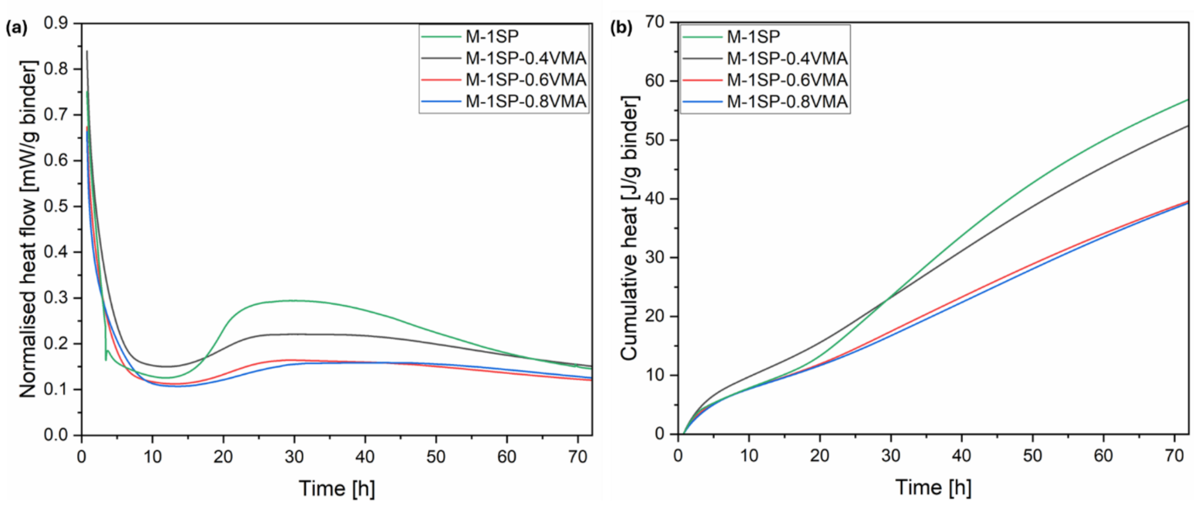

Figure 5.11. Isothermal calorimetry curves of LC3 mixtures with different VMA dosages: (a) normalised heat flow and (b) cumulative heat.

5.4.5. 3D printing-related properties

5.4.5.1. Modifications and shape stability evaluation

In this study, a rectangular object was printed for each composition, and three prisms were extracted to evaluate their mechanical properties. The rectangular objects were also used to visually assess the mixture's shape retention and printing quality after printing a certain amount of fresh mixture, i.e., 2.2 kg. Based on the visual assessment, the M-1SP-0.4VMA mix was considered printable. However, the overflow of the fresh mixture during the extrusion reduces the shape stability of the structure, as shown in Figure 5.12a. The M-1SP-0.6VMA mixture (Figure 5.12b) exhibited acceptable printing quality and better shape retention than the M-1SP-0.4VMA mixture. The M-1SP-0.8VMA mixture was not printable (see Figure 5.12c). These behaviours are consistent with the slump height reduction and flowability percentage results discussed in Section 5.2.3.4, in which the mixtures tend to get dryer with increasing VMA dosage. The lower workability of the M-1SP-0.8VMA mix makes the formation of the lubrication layer to ease the extrusion process challenging. However, once the lubrication layer is formed, the layers show significantly high viscosity, increasing the required pressure to extrude the filaments [84]. That could explain the discontinuity in the extrusion of the M-1SP-0.8VMA mix. Chen et al. [24] used HPMC to develop 3D-printable LC3 and investigated the optimum dosage of HPMC. The authors found the optimum dosage to be 0.24% of the binder weight, which enhanced shape retention [24]. It should be noted that Chen et al. used low-grade clay with 40-50% kaolinite content [24]. This could be a factor changing the optimum VMA dosage required for the LC3 mixture.

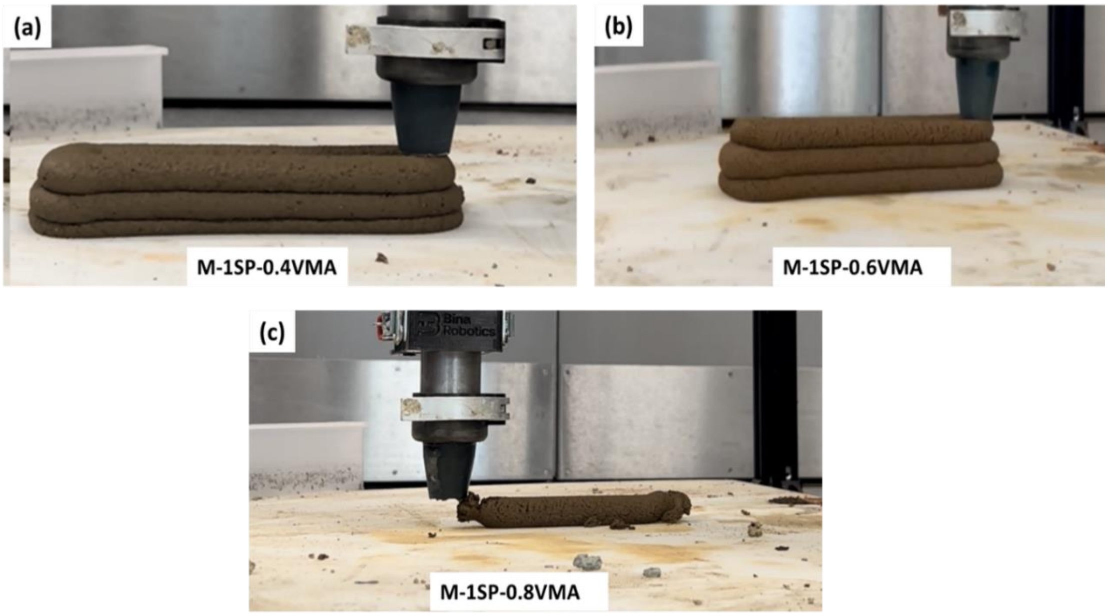

Figure 5.12. Printing quality and shape stability of (a) M-1SP-0.4VMA, (b) M-1SP-0.6VMA and (c) M-1SP-0.8VMA

5.4.5.2. Mechanical strength properties of 3D printed samples

Table 5.5 presents the flexural and compressive strength results of cast and 3D printed mixture containing 0.4 wt% and 0.6 wt% VMA. The cast sample exhibited higher flexural and compressive strength performance than the 3D printed sample at both 7 and 28 days. The printed samples exhibited around 20–27% lower flexural strength values than their cast counterparts, while they exhibited around 20–28% lower compressive strength performance than their correspondent cast samples at 7 and 28 days (see Table 5.5**)**. The lower flexural and compressive strengths of the printed specimens could be due to a thin water layer on the surface of the extruded layers (known as the wet surface effect), which weakens the bonding between the adjacent layers. This thin water layer can be considered part of the lubrication layer, whose formation depends on the amount of free water in the system [24]. Similar to the cast results, the strength performance of the printed mixtures improved when increasing the VMA dosage from 0.4 wt% to 0.6 wt%. Increasing VMA dosage increases the amount of water being retained and decreases the amount of free water in the system, which hinders the formation of the lubrication layer, as discussed in Section 5.2.3.4. According to Chen et al. [24], the rheological properties (i.e., viscosity) of the lubrication layer play a key role in the adhesion between the two adjacent layers because the lubrication layer remains on the surface of the extruded layer after depositing the filament. Therefore, the lubrication layers' viscosity should not be too low or too high since low viscosity might indicate containing a higher water content in the lubrication layer. That, in turn, increases the porosity in the interface [24]. Hence, in this study, the mix with 0.4 wt% VMA might have had a lower viscosity than that of the mix with 0.6 wt% VMA, which could explain the slight enhancement in the strength performance.

Table 5.5. Flexural and compressive strengths of cast and 3D printed mixtures.

Mixture ID	Flexural strength [MPa]				Compressive strength [MPa]			
	7 days		**28 days**		**7 days**		**28 days**	
	Cast	**Printed**	**Cast**	**Printed**	**Cast**	**Printed**	**Cast**	**Printed**
M-1SP-0.4VMA	6.7±0.1	5.1±0.2	9.7±0.3	7.1±0.2	19.7±0.6	15.2±0.6	31.1±1	22.7±1.1
M-1SP-0.6VMA	6.8±0.3	5.5±0.1	9.8±0.4	7.3±0.3	19.9±0.8	15.9±0.8	32.9±1.5	24.9±1.3

Based on the visual inspections of shape stability and the mechanical performance of the modified mixtures with VMA, the M-1SP-0.6VMA mix was selected to investigate its buildability in the next section.

5.4.5.3. Buildability

The buildability of the developed M-1SP-0.6VMA mix was investigated through 3D printing of a cylinder that consists of 23 layers with a 150 mm diameter. Moreover, the open time of the selected mixture was investigated through extruding a straight line every 5 min until the mixture set. The mixture found to have an open time of 65 min. According to ACI 318M-05 [329], CEM I-42.5 should have an initial setting time longer than 60 min. Hence, from the open time, it can be indicated that the mixture has longer initial setting time than 60 min, which meets the criterion of the standard. The mixture was successfully printed and attained the designed 23 layers without showing any failure or collapse, having minimal radial distortion. It should be noted that more layers could have been deposited without any issues. However, the fixed amount of materials (i.e., 8000 g of fresh mixture) did not allow for extruding more layers. Hence, 23 layers weren’t the buildability threshold. As shown in Figure 5.13**,** the optimised LC3 mixture had good shape retention with a smooth finishing at the top, which is consistent with the slump height reduction results (see Figure 5.13). Nonetheless, some slight segregation/cracks were observed on the outer surface of the printed cylinder. These segregations are due to the faster evaporation of water at the sides of the extruded filaments due to the increased friction between the mix and the auger, which increases the mixture's temperature, causing a plastic shrinkage and the segregation at the outer surface of the filaments. In addition, water evaporation occurs at the printed mixture surfaces due to insufficient protection at the interface between the printed layers and the sides due to the absence of moulding [368]. Hence, the presented cracks are due to plastic shrinkage, which occurs immediately after mixing. Although shrinkage represents a significant limitation for concrete printing, this work focuses on developing a 3D printable LC3 mixture using low-grade excavated London clay waste.

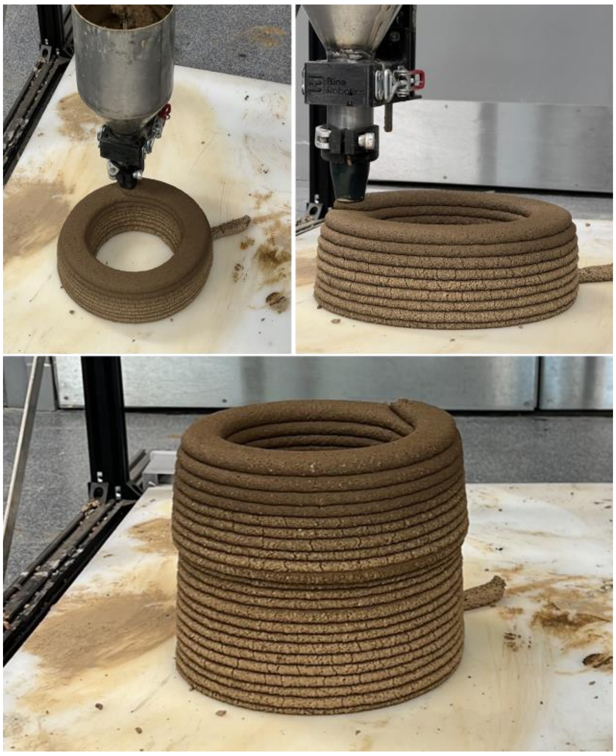

Figure 5.13. Buildability performance of the M-1S-0.6VMA mixture

5.4.6. Chapter Conclusions

This study investigated the potential of using low-grade local excavated London clay waste in calcined form along with limestone to partially replace OPC for 3D printing applications. The effect of different calcination temperatures (i.e., 700, 800 and 900°C) for London clay was investigated. The mixture with the optimised calcination temperature of London clay was considered for the incorporation of different SP dosages (i.e., 0.5, 1 and 1.5 wt%) to enhance the workability of the mixture. The mixture containing the optimum SP content was then selected for incorporating different dosages of VMA (i.e., 0.4, 0.6 and 0.8 wt%) to counterbalance the SP effect and enhance the extrudability of the mixture for 3D printing process. The slump height reduction, flowability, reaction kinetics and mechanical performance of the mixtures were investigated. The results of this study present the potential for an alternative source of clay obtained locally to be used in cementitious mixtures and the following specific conclusions can be drawn from this study:

1. The optimal calcination temperature to fully activate London clay was found to be 800 °C for 1 hour, which exhibited around 15% higher strength values than the other temperatures.
2. The incorporation of SP significantly increased the slump reduction height and flowability.
3. Incorporating SP and decreasing the water content retarded the hydration and decreased the cumulative heat that evolved from the reaction. However, the strength performance significantly increased at 7 and 28 days due to the lower water content in the mixture. On the other hand, the optimal SP dosage to provide the highest strength was found to be 1% to the weight of the binder.
4. Incorporating VMA decreased the slump height reduction and flowability of the mixture. Moreover, VMA incorporation decreased the heat evolved from the reaction and retarded the hydration of the mixture. On the other hand, VMA addition did not affect the mixtures' flexural strength but led to a reduction in the compressive strength. This is due to the retardation of the hydration effect when incorporating VMA.
5. VMA incorporation was beneficial for the fresh behaviour of the mixtures, which resulted in better shape stability and printing quality. However, adding 0.8 wt%. VMA showed discontinuity and difficulties in extruding, possibly due to the lower free water content in the mixture that made the formation of the lubrication layer challenging.
6. 3D printed specimens exhibited around 20-28% lower flexural and compressive strengths than the cast samples at 7 and 28 days. The lower strength behaviour of the printed samples could be due to the weaker adhesion bond between the adjacent layers due to a thin water layer on the filaments' surface.
7. The optimum mixture containing 1 wt% SP and 0.6 wt% VMA (the M-1S-0.6VMA mixture) was successfully printed and achieved the designed 23 layers in the buildability test without showing any failure or discontinuity. Moreover, the mixture had an open time of 65 min, which suggests the suitability of the developed mixture for medium- to large-scale applications.

Overall, the results indicated the feasibility of employing low-carbon cement containing excavated London clay waste for 3D printing applications. Moreover, the used methodology lays a pathway to develop an LC3 mix formulation with suitable properties for 3D printing applications.

6. INFLUENCE OF INCORPORATING BRICK AGGREGATES ON THE ENGINEERING AND PRINTING PROPERTIES OF LC3 PREPARED USING EXCAVATED LONDON

6.1. Introduction

This chapter investigates the effect of replacing up to 100% natural aggregates with brick aggregates on the fresh, hardened, buildability and printing properties of LC3 mixture containing excavated London clay. The sample preparation process and the various mix formulations investigated were highlighted, and specific tests and procedures used for each study were introduced in each section. It should be noted that the outcomes of this chapter have been published as a journal paper:

Al-Noaimat, Y. A., Chougan, M., El-Seidy, E., Albar, A., & Ghaffar, S. H. (2025). Valorising excavated low-grade waste clay in limestone calcined clay cement system for 3D printing applications.

6.2. Methodology and experimental program

Figure 6.1 illustrates an overview plan of the experimental program.

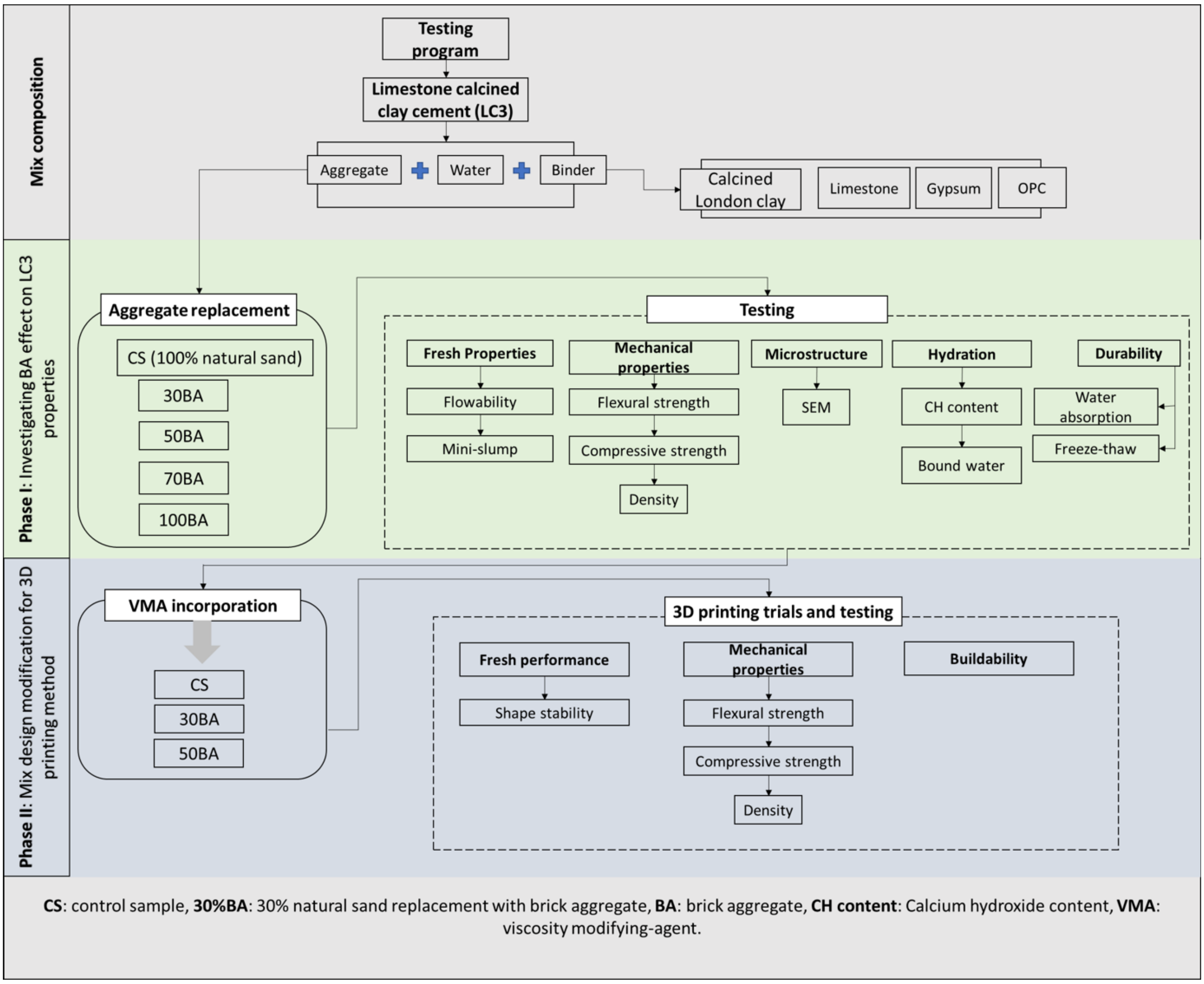

CS: control sample, **30%BA**: 30% natural sand replacement with brick aggregate, **BA**: brick aggregate, **CH content**: Calcium hydroxide content, **VMA**: viscosity modifying-agent.

Figure 6.1. Schematic overview plan of the experimental testing program.

6.2.1. Mix formulations and sample preparation

A commercial OPC (CEM I 52.5 N) was obtained from CEMEX, UK, following BS EN 197-1 [328] was used in this chapter to prepare LC3. A total of five different mix formulations were used in this study to investigate the effect of incorporating BA to replace NA in the LC3 mixture, which are presented in Table 6.1. The reference mix formulation used in this section was selected from the previous section results, which had the best-performing mechanical strength and printability performance, which is LC3 made with 1% SP and 0.3 water-to-binder ratio. The binder was kept constant for all mixtures with an OPC replacement level of 50%, CLC content of 30% and limestone content of 15%, (making a CLC/limestone ratio of 2:1), and gypsum content of 5%. SP was fixed as 1% by weight of binder for all mixtures. An aggregate/binder ratio of 1.5 was used for all mixtures. The replacement levels of NA with BA used were 30, 50, 70 and 100% by weight. BA have a significantly higher water absorption capacity of 8.7% than that of sand at 0.5%. Although it was reported that incorporating dry recycled brick aggregate without considering compensating for their water absorption improves the properties of the cementitious mixture [369], this study considered adding extra water to compensate for the water absorption of BA particles. Even though, it was reported that compensating for BA's water absorption would degrade the cementitious mixture's behaviour [325], it might behave differently in LC3 since calcined clay's later age reactivity is affected by the internal relative humidity of the mixture [178]. When incorporating additional water, BA absorbs water in its porous structure and starts releasing it slowly while the LC3 mixture continues to age [370], working as an internal curing agent by providing extra internal moisture that enables the mixture's hydration and pozzolanic reactivity of calcined clay to elongate, and thus, improves the mechanical strength a durability properties of the mixture. Therefore, this study considered adding extra water to compensate for BA's water absorption as a hypothesis that it will be released to allow the hydration to proceed.

For 3D printing LC3 mixtures with different BA content, an HPMC-based VMA was incorporated into the mixtures to modify their viscosity, cohesion, and water-retention properties. The compatibility of cellulose-based VMA with polycarboxylate (PCE)-based superplasticiser has been reported in previous studies [24,201]. However, when PCE and HPMC are presented together in the mixture, their competitive adsorption in the suspension cannot be avoided. The VMA dosage chosen for each mix was the minimum amount needed to facilitate the extrusion process while still enabling the mixture to retain its shape. The dosage was added based on the initial weight of the binder.

Table 6.1. LC3 mix formulations with and without BA

Mix	**Binder (%)**				**Aggregates (%)**		**w/b ratio**	**Extra water (g)**	**Total W/b ratio**	**Effective W/b ratio**
	OPC	CLC	LP	Gypsum	NA	BA				
0BA	50	30	15	5	100	-	0.3	-	0.3	0.3
30BA	50	30	15	5	70	30	0.3	25.2	0.34	0.3
50BA	50	30	15	5	50	50	0.3	42	0.36	0.3
70BA	50	30	15	5	30	70	0.3	58.8	0.38	0.3
100BA	50	30	15	5	-	100	0.3	84	0.42	0.3

*1% SP by weight of binder was considered for all mixtures.

The LC3 mixtures with and without BA were prepared by dry mixing solid ingredients (OPC, CLC, LP, gypsum, SP, NA and BA) for 3 min in a Kenwood mortar mixer (Germany). Followed by gradually pouring the required amount of mixing water, including the water absorption of BA particles, and wet mixing for 5 min. For mixtures prepared with VMA, for 3D printing, VMA was added to the fresh mixture at the end of the 5 min wet-mixing process with SP, and the mixing continued for an additional 3 min. Mixtures were cast in prismatic polystyrene moulds at the end of the mixing process with a dimension of 40 x 40 x 160 mm^3 or fed to the printer for extrusion and cured in control room conditions at 40% relative humidity and 20 ± 3℃ for 24 h. The cast and extruded specimens were immersed then in a controlled water tank at 20 ± 3℃ until test age.

6.2.2. 3D printing process

The 3D printing of the modified mixtures was conducted using a three-axis gantry-type extrusion-based 3D printer equipped with a custom-designed auger extruder, as shown in Figure 6.2, consistent with the previous section. The samples were printed using a 20 mm circular-shaped nozzle with a motion speed of 15 mm/s and a 10 mm nozzle standoff distance.

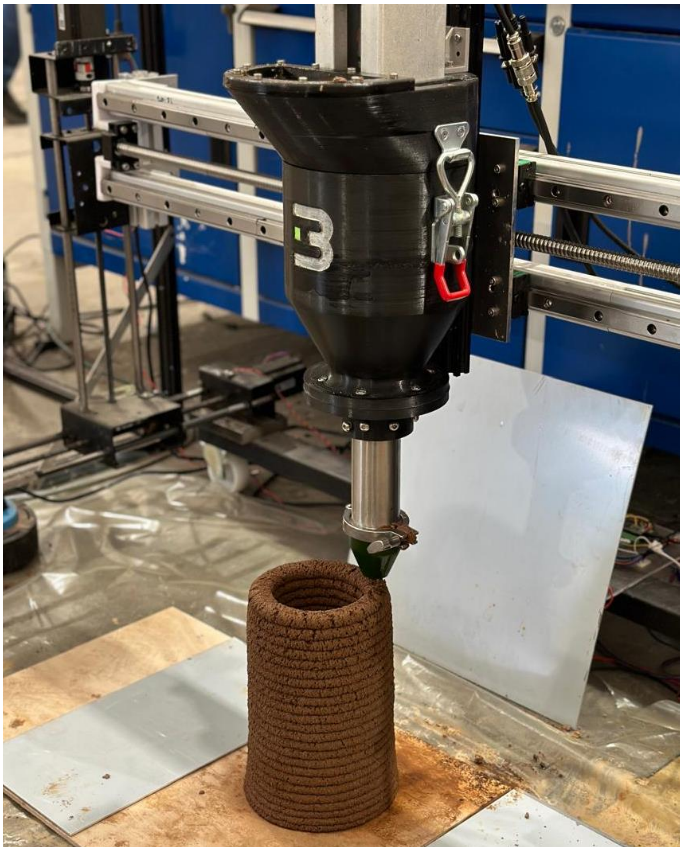

Figure 6.2. Extrusion-based 3D printer

6.2.3. Specific experimental methods

The specific test methods used in this section are outlined below:

6.2.3.1. Thermogravimetric analysis (TGA)

The reaction kinetics of the different mortars were investigated by determining Portlandite content using Thermogravimetric analysis (TGA). TGA was performed on mortar powder using an SDT Q600 instrument with a heating rate of 10 °C/min from 30 °C to 900 °C. To do so, LC3 mortars with and without aggregates were mixed and cured similar to the procedures mentioned earlier. After 28 days, the different mixtures were crushed and ground. The grounded product was then sieved using a 63.5 µm sieve. The total calcium hydroxide (Portlandite) content was determined after 28 days from the mass loss in the temperature range of 400 – 500 °C, which is attributed to the portlandite dehydration, including the mass loss at the temperature range of 600 – 800 °C, which is assigned the decomposition the calcium hydroxide that undergone carbonation and transformed into calcium carbonate. The following equation was used to calculate the total calcium hydroxide content in the different mixtures:

$$CH\ content = \frac{74}{18} \times WL_{CH} + \frac{74}{44} \times\ WL_{CC} \qquad \text{(Eq. 5.2)}$$

where CH represents calcium hydroxide, WL_{CH} and WL_{CC} represent the percentage of weight loss by the dehydration of calcium hydroxide (CH) and calcium carbonate (CC), respectively.

The bound water content was also calculated from TGA curves to investigate the formation and growth of hydration products. The bound water was calculated from the mass loss at the temperature range of 110 – 300 ̊C.

6.2.3.2. Buildability and filaments quality investigation

An ad-hoc testing method of 3D printing cylindrical objects was used to investigate the buildability of the different mix formulations with and without BA. The cylinders were printed with a 150 mm diameter and using a fixed amount of material, consisting of four batches of each mix, which makes around 8000 g of fresh mixture. The buildability of the mixtures was evaluated by investigating layer deformation and radial or vertical distortions. In addition, the final height of the printed object was assessed to the theoretically designed height from the computer model.

6.3. Results and discussions

6.3.1. Effect of incorporating brick aggregates on LC3 properties.

6.3.1.1. Flowability and slump height measurements

Figure 6.3 presents the flowability percentage and slump height reduction of the mixtures prepared with different BA content as an indication of the workability of the mix. The LC3 mixture prepared with NA had an excessive spread diameter greater than the mini-slump table diameter. Therefore, it wasn’t presented in the bar graph results and was considered greater than 290 mm (>190%), which is the diameter of the mini-slump table. The workability of the mixtures decreased with increasing the BA content in LC3 mixtures. For instance, increasing the replacement level of aggregates from 30% to 50% reduced the flowability by 25%, reaching 150% from 175%. The workability and fresh properties of the cementitious mixture are significantly affected by the aggregate's characteristics, including size, shape and surface texture [316]. The BA used in this study exhibits a water absorption capacity of 8.7% determined following the procedures in BS EN 12620:2013 [251]. Depending on BA'S raw materials and production process, its porosity and water absorption can be as high as 40% [370]. Even though the water absorption of BA was compensated for in the mix design, the workability still decreased. The main reason behind the decline in workability is BA's geometry and surface texture compared to NA's. BA particles have irregular and elongated shapes with a rough surface texture, which increases the friction between the different ingredients in the mixture and resistance to flow, which, in turn, significantly declines the workability. This effect is significant when increasing the replacement level from 70% to 100%, which exhibited a significant drop in workability, reaching a flowability of 65% from 130% and a slump height reduction of 10 mm from 30 mm. That is because of the complete replacement of NA with spherical and round particles that act as rollers and improve the flow of the mixtures with BA particles that have a rough and irregular microstructure which hinders the flowability of the mix.

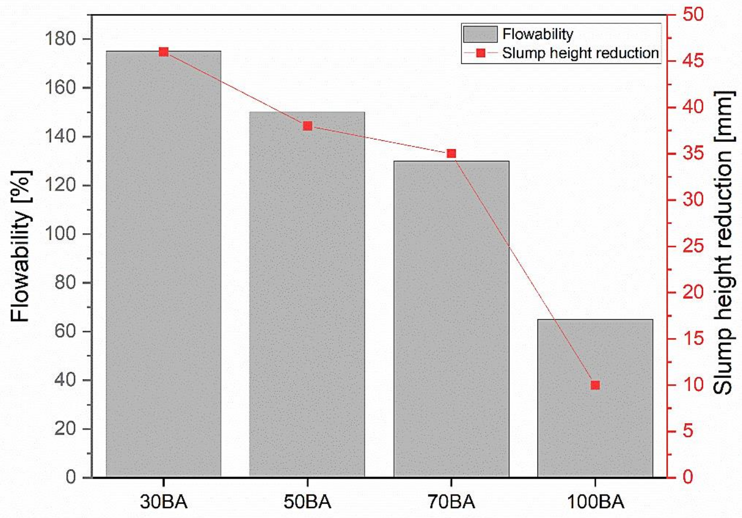

Figure 6.3. Flowability and slump height reduction of LC3 mixtures containing BA.

6.3.1.2. Mechanical strength

Flexural and compressive strength performances of the mixtures prepared with different BA content were investigated at 7 and 28 days, and the results are presented in Figure 6.4. A clear incremental trend can be observed in both flexural and compressive strength results when the replacement level of NA with BA is increased. Figure 6.4a shows that LC3 mixtures with BA achieved 22 to 87% and 8 to 36% better flexural strength performance than the reference mixture at 7 and 28 days, respectively. Similarly, compressive strength results showed a 20 to 87% and 36 to 62% improvement compared to the control mixture after 7 and 28 days, respectively, as shown in Figure 6.4b. The highest flexural strength was reported for the LC3 mixture with 100% BA, which achieved 12.5 MPa, whereas compressive strength was found to be comparable for mixtures with replacement levels of 50% and above, reaching around 54 MPa, which is higher than the natural sand and 30BA mixes. According to ACI 318M-05 [329], compressive strength of concrete should be at least 28 MPa after 28 days to be considered for engineering applications. It can be seen that mixtures meet this requirement.

Previous studies showed contradictory behaviour for incorporating BA to replace NA in cementitious mixtures [371,372]. For instance, Zhang et al. [372] showed that incorporating 30% BA decreased the compressive strength of concrete by around 18%. According to Zhang et al. [372], the reduction in strength performance was related to BA's weaker crushing index than NA's. It should be noted that the authors considered adding extra water to compensate for the water absorption of BA. Bektas et al. [370] reported similar strength behaviour when replacing natural sand by up to 20% in cement mortar. However, the authors didn't consider compensating for the water absorption of BA in the mix design. Some studies considered compensating for the water being absorbed by BA particles by adding extra water or soaking BA in water until saturation [369,373], while others did not consider compensating for the water being absorbed. Huang et al. [369] considered comparing the effect of replacing NA up to 100% with BA in two states (dry state and after pre-soaking in water for 24 h) on the performance of cement mortar and found that using BA in a dry state enhanced the strength performance of the mortars compared to that of pre-soaked BA which declined the properties of the mortar. The authors reported around 20% and 80% higher strength for flexural and compressive strength, respectively than the mixture prepared with NA. That is in good agreement with the results presented in this study, however, this study considered compensating for BA's water absorption.

According to Briki et al. [178], chemical shrinkage progressively empties the capillary pores after setting, decreasing the internal relative humidity of the mixture. That, in turn, slows down the calcined clay reaction rapidly after 7 days. The authors found that calcined clay's reaction increases with increasing water content or the saturation level of capillary pores. However, this improvement in reaction would slow down after 28 days, even in the presence of more solution in the capillary pores [178]. According to Ge et al. [373], incorporating BA in cementitious mixtures decreased the internal humidity loss over time. Moreover, pre-wetting BA was found to further slow the internal relative humidity loss over time by transferring the water from BA to the cementitious matrix with ageing. Hence, in this study, the inclusion of extra water to compensate for BA's water absorption may not have changed the saturation level of the fresh mixture since BA would absorb the excessive water from the fresh mixture (around 4-12% to the binder weight for the different replacement levels). Nevertheless, BA particles might reduce the loss in internal relative humidity with ageing through releasing some of the water being held in their microstructure. Consequently, LC3 mixtures prepared with different BA content contain additional water, which could participate in LC3's hydration and reaction at later ages. That allows BA to work as an internal curing agent during ageing by releasing some of the initially absorbed water during self-desiccation, allowing the hydration to continue. Moreover, if the water remained inside the BA particles and was not used for cement hydration, it would make the BA particles denser by filling the pores [371]. These previous observations and explanations could explain the higher strength development of LC3 mixtures prepared with BA than that of NA in this study.

Another reason for the improvement of mechanical strength in the presence of BA could be due to the BA particle’s porous and rough texture and irregular shape, which could enhance the adhesion between the aggregates and the paste matrix. According to Xing et al. [270], the aggregates’ characteristics, such as textural and physical properties, also affect the cementitious mixtures' mechanical strength. Hence, the strong adhesion of the BA and its effective interlocking with the cement paste plays a crucial role in enhancing the overall mechanical performance of the material. When the composite material is subjected to external loading, the strong adhesion and interlocking mechanisms allow for the efficient stress transfer between the paste and BA, contributing to the material's improved mechanical strength behaviour.

Moreover, the strength improvement could be related to the higher content of larger particles in BA particle size distribution (d50 < 1.4 mm) than NA (d50 < 0.5 mm), since it is well-known that compressive strength of the cementitious mixture increases with increasing aggregates’ particle size distribution [272].

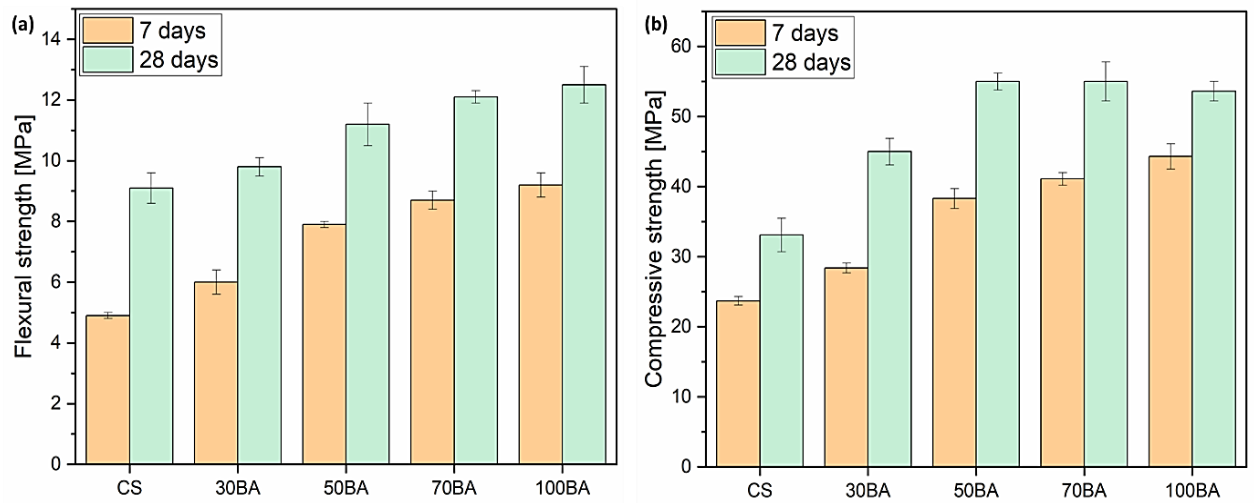

Figure 6.4. (a) Flexural and (b) compressive strength of the different LC3 mixtures after 7 and 28 days.

6.3.1.3. Microstructure characterisation

In this section, only the microstructure of 100BA, which presented significantly higher strength performance than the control sample, was investigated using SEM in comparison to 0BA in order to identify the compatibility of high amount of brick particles in the LC3 mixture and to develop a better understanding of the adhesion and interlocking mechanisms between LC3 matrix and recycled aggregates. Figure 6.5 presents the SEM image of 0BA and 100BA. It can be observed that BA particles are entirely and perfectly embedded in the microstructure of the LC3, without showing any delimitation. This can indicate a good bonding with the paste without showing debonding at the interface between the aggregates and matrix. The good bonding and interlocking of BA with the matrix could be due to the rough surface and porous structure of BA particles, which facilitated the bonding between the aggregates and the matrix, leading to forming a dense microstructure. Similar observations were made by El-Seidy et al. [374], which investigated the effect of fully replacing natural aggregates with BA. They found that BA incorporation allows the development of a more cohesive and denser microstructure due to the rough surfaces of BA particles. Such interconnectivity between the aggregates and the cementitious matrix would contribute to improving the effective stress transition with the microstructure of the mixture, allowing the mixture to resist more load. This could explain the higher strength performance in the presence of BA, as explained earlier.

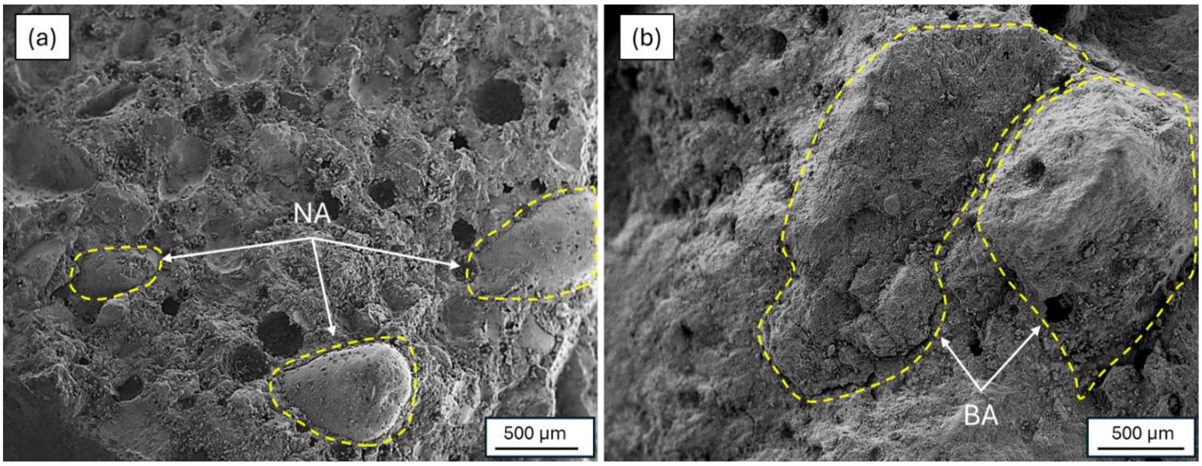

Figure 6.5. SEM images for the microstructure cross-section of (a) 0BA and (b) 100BA mixtures after mechanical strength testing.

6.3.1.4. Calcium hydroxide consumption and hydration products

The effect of BA incorporation on the LC3 hydration was investigated by determining the amount of hydration products as a means of calcium hydroxide (CH) content and by calculating the bound water content. Huang et al. [369] determined the effect of incorporating BA on the hydration of cement by calculating the mass loss associated with CH using TGA curves as the total mass loss from CH dehydration and calcium carbonate (CaCO3) decarbonation. Similarly, in this study, the total CH content (%) in the powdered mortars was calculated as the summation of CH dehydration percentage and calcium carbonate decarbonation, and the results are presented in Table 6.2. It can be observed that the CH content increased in the presence of BA. This is due to the internal curing effect of BA, which promoted the continuous hydration of the mixtures and allowed for the formation of more portlandite and hydration products. Nevertheless, the CH content decreased with increasing BA content in the LC3 mix from 30% onwards. This could indicate the consumption of CH in the reaction to produce more hydration products, which could explain the significant increase in the strength performance of the mixtures in the presence of BA. Huang et al. [369] reported that BA incorporation promotes continuous hydration through its internal curing impact in the mix and increases the CH content in the mixture. It should be noted that the authors investigated the effect of BA on plain OPC mortar, which explains the reason behind the higher CH content in the presence of BA. However, in this study, due to the high substitution of OPC with calcined clay and limestone, the internal curing effect in the presence of BA allows the continuous pozzolanic reaction with CH and the production of more hydration products since calcined clay reactivity is affected by the internal relative humidity [178]. On the other hand, the decrease in CH content with BA content suggests a better pozzolanic reaction of calcined clay and limestone in the mixtures, and the development of more hydration products, which could be another added explanation for the better mechanical strength of the mixtures. Moreover, despite BA's large particle size, their high silica and aluminate content could allow their surface to provide additional nucleation sites, allowing the paste matrix to provide better interlocking with BA particles and better bonding in the microstructure, as was shown in Figure 6.5.

The formation of additional hydration products was also confirmed by the values of bound water content, which was found to be higher in the presence of BA. The bound water content is one of the most commonly used methods to monitor the hydration of cementitious materials. According to Huang et al. [369], the TG weight loss at the temperature range of 110 – 300 ̊C is due to the loss of the bound water from the chemical decomposition of the various hydration products, such as C-S-H and AFm. The mass loss associated with bound water was calculated, and the results are presented in Table 6.2. It can be seen that the bound water content was around 16 – 25% higher than the control sample. That is due to the formation of additional hydration products due to the better hydration in the presence of BA, which increases the amount of chemically bound water content. The bound water increased when replacing up to 50% of NA with BA. That indicates that the mixtures were able to bind more CH and produce more hydration products. Nevertheless, further increasing BA content to more than 50% decreased the amount of bound water content in the mixture, indicating that 50% was the threshold. However, it is still higher than that of the control sample. Moreover, it could be suggested that the activated clay minerals have already reacted during the hydration, and extra water for replacement levels above 50% is not needed due to the low amount of kaolinite presented in excavated London clay. Even though compressive strength didn’t decrease at 70% and 100% replacement levels (see Figure 6.4), which indicates that particle size and physical characteristics of BA play a major role in the strength development.

Table 6.2. CH content and bound water of the different LC3 samples with and without BA.

Mix ID	CH content [%]	Bound water [%]
CS	12.1	2.4
30BA	20.9	2.9
50BA	16	3
70BA	12.6	2.8
100BA	10.6	2.5

6.3.1.5. Water absorption

The primary contributors to material deterioration necessitate both the presence and permeation of water within the mixture. Water presence could result in freeze-thaw harm to the cementitious mixture, while also transporting chlorides, sulfates, and other detrimental ions. Consequently, the absorption of the cementitious mixture profoundly impacts its durability and service life. The water absorption of LC3 mixtures with different BA content was investigated, and the results are presented in Figure 6.6.

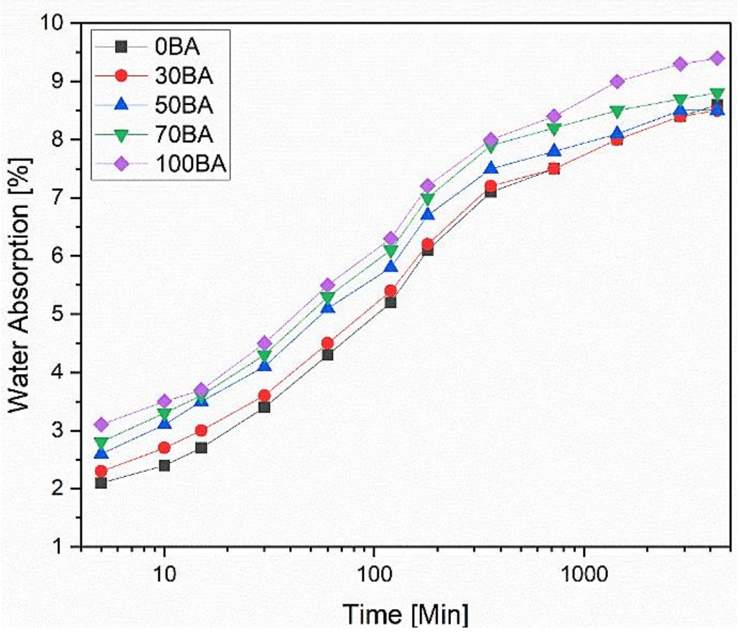

Figure 6.6. Water absorption of LC3 mixtures with different BA content.

A clear trend can be observed from the results, where the water absorption increased with BA content. Interestingly, the LC3 mixture prepared with 30% BA initially exhibited slightly higher water absorption percentages than the mix with NA. However, LC3-30BA exhibited water absorption percentages similar to the control sample after 60 min. Similarly, the LC3 mixture prepared with 50% BA showed similar behaviour to that of 30% BA, where the mix initially exhibited higher water absorption percentages, and after some time, the mixture's water absorption values reached values similar to those of the control sample. This trend was observed for all samples, where mixtures with BA after 5 min exhibited 10%, 24%, 33%, and 48% higher water absorption than 0BA mixtures for 30, 50, 70 and 100% BA content, respectively. As was mentioned in AAM chapter (See section 3.4.4), the rapid absorption stage takes place in the first few hours, whilst the second day and beyond are the slow absorption stage. The main contributor to the rapid absorption stage is the capillary pores' water absorption process [281]. Hence, the higher initial water absorption rate with BA content could be explained by the high porous surface of BA.

After 72 h, the LC3 mixture prepared with 30 and 50% BA achieved similar water absorption values to 0BA, while the 70BA mixture had around 2% higher water absorption percentage than the control sample, which is negligible. On the other hand, 100BA achieved around 9% higher water absorption value than the control sample. Similar findings were reported elsewhere [375]. Dang et al. [375] found that replacing 50% of fine NA with recycled BA and compensating for BA water absorption resulted in around 30–40% higher water absorption percentage than the control sample. Other studies observed higher water absorption percentages when incorporating BA to replace NA [374]. El-seidy et al. [374] found that replacing 50% and 100% of NA with BA in two-part alkali-activated materials resulted in 8% and 25% higher water absorption, respectively, compared to the mixture prepared with NA. The BA used in El-seidy et al. study has a water absorption capacity similar to the BA used in the current study. Similarly, Tavakoli et al. [376] found that replacing 100% of sand with BA in concrete increased the water absorption percentage by around 46% compared to that prepared with sand. It should be noted that a limited comparison can be made due to the differences in BA characteristics and mix formulations. Compared to this work, the current study showed that incorporating different BA content has no or slight influence on the water absorption properties of the LC3 mixture, even for a 100% replacement level. This behaviour could indicate the good compaction and the densified microstructure of LC3 mixes with different BA content (see Figure 6.5).

6.3.1.6. Freeze-thaw resistivity

Freeze-thaw resistivity is one of the primary indicators to ascribe cementitious mixture durability, which is the ability to resist cyclic freezing and melting. During exposure to freeze-thaw cycles, the aqueous solution in the microstructure and capillary pores of the cementitious mixture transforms into ice and expands in the microstructure by around 9% of its volume. This expansion causes unfrozen water to move into any available voids and eventually causes hydraulic pressure [377]. The matrix's irregular and non-homogeneous pores may compensate for the hydraulic pressure to a certain degree. However, once the pores are filled, the matrix may experience internal pressures due to the expansion of water upon freezing. When the pressures and forces induced from frozen water exceed the stress capacity of a cementitious matrix, microcracks may be initiated and propagate throughout the mixture's microstructure, degrading the mixture's strength properties [41]. In addition, the expansion of the frozen water leads to rupturing and widening the pore structure, thus declining the strength properties of the cementitious mixture. Therefore, the deterioration of the properties depends mainly on the presence of free water in the system [286]. The higher the water absorption, the greater the strength loss. Figure 6.7 presents the compressive strength reduction after exposing the LC3 mixtures with different BA content to freeze-thaw cycles. Strength reduction was found to be 6.7% – 8.9%. The strength reduction percentages of the different samples were comparable. Although, LC3 mixtures containing BA showed similar or higher water absorption percentages than the control sample (0BA), mixtures containing BA exhibited slightly lower strength reduction percentages compared to the 0BA mix. This slightly better behaviour in the presence of BA can be associated with BA's porous microstructure, providing space to ease the induced pressure from forming ice. In addition, the microstructure of the LC3 mixture could be more densified in the presence of BA particles due to the good interlocking and adhesion between the paste matrix and BA (see Figure 6.5), which, in turn, increased the resistivity to freeze-thaw cycles. That is in line with the observations obtained by [378]. On the other hand, the slight increment in the strength reduction when increasing the replacement level from 50% to 100% could be due to the higher water absorption capacity of the mixtures, which allows them to retain more water within their structure and that would increase the volume of water which will freeze during the cycles and thus the strength reduction would decrease.

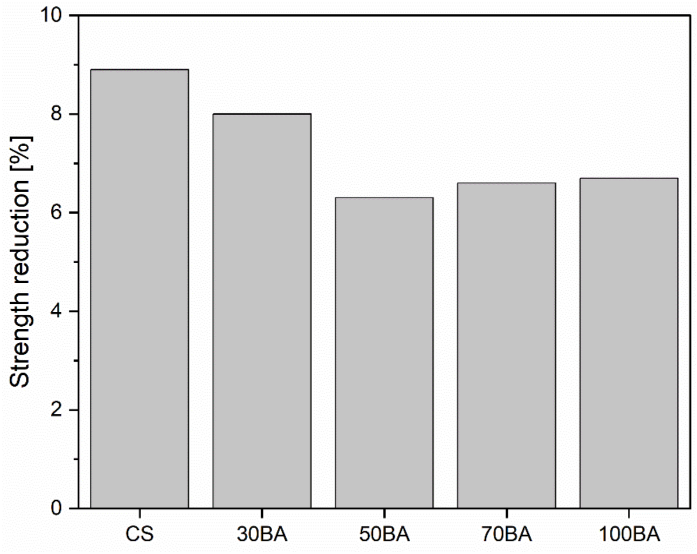

Figure 6.7. Strength reduction percentage after exposure to freeze-thaw cycles.

Huang et al. [369] reported that replacing natural aggregates (NA) with brick aggregates (BA), while accounting for BA’s water absorption, degraded the properties of cement mortars. However, the findings of the current study indicate an opposite trend. The results presented in this work showed that the additional water included in the mix design to compensate for BA’s water absorption was beneficial to the hydration of LC3 and resulted in developing a more densified mixture that exhibited better performance compared to that of the natural aggregates. This shows that compensating for BA's water absorption directly affects the mechanical strength, water absorption and freeze-thaw properties of the LC3 mixture for all replacement levels. However, it can be seen that above 50% replacement level, the performance of the mixtures in all tests slightly decreased but stayed higher than that with NA. This suggests that the extra water for up to 50% replacement level has already facilitated the hydration process and consumption of the activated kaolinite clay in the reaction. However, because excavated London clay has low kaolinite content, adding more water for replacement levels above 50% won’t enhance internal curing but will instead reduce the quality of the mixture.

6.3.2. Embodied Carbon emissions of the different LC3 mixtures

The carbon footprint of the different mixtures in terms of GWP for producing 1 m^3 of the cementitious mixture is calculated in this section. The embodied carbon achieved from substituting 50% of OPC with limestone-calcined clay blends is calculated. The changes also from the substitution of natural sand up to 100% with recycled brick aggregates in the LC3 mixture are calculated.

Similar to section 4.2.7, the functional unit on which the comparison was made is 1 m^3. The calculation of the CO_2 emissions reduction was done by adding up the CO_2 emissions of each ingredient in the mixture, which is calculated by multiplying the quantity of the material needed in the production of 1 m^3 by its environmental coefficient.

The environmental coefficients of natural sand and BA were obtained from the life cycle inventory of the materials from the Ecoinvent 3.10 database with datasets related to single production processes in a European allocation, and the data of the different materials are presented in Table 6.3. For excavated London clay, the environmental coefficient was considered as the environmental impact of the energy required for processing the clay and for the calcination process.

Table 6.3. The quantities for producing 1 m^3 of concrete referring to materials are expressed in kg.

Process	EC [$KgCO_{2eq}$/ kg]	OPC	LC3	LC3-30BA	LC3-50BA	LC3-70BA	LC3-100BA
OPC	0.878	875.5	437.75	437.75	437.75	437.75	437.75
CLC	0.278	0	262.65	262.65	262.65	262.65	262.65
Limestone	0.00552	0	131.33	131.33	131.33	131.33	131.33
Gypsum	0.00838	0	43.78	43.78	43.78	43.78	43.78
Water	0.0003	262.65	262.65	262.65	262.65	262.65	262.65
SP - Polycarboxylates	1.274	8.76	8.76	8.76	8.76	8.76	8.76
River sand	0.0129	1641.6	1641.6	1149.12	820.8	492.48	0
Brick aggregates	0.007	0	0	492.48	820.8	1149.12	1641.6

Table 6.4 shows the results of the GWP calculations for the different mixtures. It can be seen that the carbon impact of the LC3 mixture (489.8 kg CO_2/m^3) was much lower than the OPC mixture (801.1 kg CO_2/m^3), having around 40% reduction in CO_2 emissions. This significant reduction is due to the replacement of OPC, which is the main reason for the massive environmental impact of concrete, contributing to around 95% of the mixture's environmental impact. This agrees with Kanagaraj et al. [379], which reported that LC3 emits around 47.5% lower emissions than OPC concrete. It can be indicated that replacing OPC with a limestone-calcined clay blend provides significant environmental benefits and allows the development of a low-carbon cementitious mixture. On the other hand, replacing natural aggregates with BA did not provide noticeable environmental benefits. As reported in section 4.2.7, the main benefit of recycling brick waste to replace natural sand is to decrease the overdependency on natural resources and reduce the amount of waste being landfilled.

Table 6.4. Carbon footprint estimation (GWP) of the composites

Mix	**OPC**	**LC3**	**LC3-30BA**	**LC3-50BA**	**LC3-70BA**	**LC3-100BA**
GWP [kg CO2 / kg]	801.1	489.8	486.9	484.9	483.0	480.1

6.3.3. Printability and printing properties of LC3 system containing BA

6.3.3.1. Workability modification of LC3 mixtures

The investigated LC3 systems with up to 50% BA exhibited high flowability and slump height reduction due to the inclusion of extra water to compensate for BA particles' water absorption, as explained in Section 5.3.2.1.1. It should be noted that the authors excluded mixtures containing 70% and 100% BA from printing trials due to difficulties in their extrusion and to avoid clogging the nozzle of the hopper due to their high particle-to-particle packing. Hence, LC3 mixtures with up to 50% BA content were considered for modification and 3D printing trials. It is well known that the high flowability of the mixtures would be beneficial for the mixture's extrudability. Nevertheless, high flowability would not allow the mixtures to retain their shape after extrusion, preventing the mixtures from forming the desired shape or object [380].

It is reported in the literature that VMA can reduce the workability of the cementitious mixture through two different mechanisms, i.e., flocculation and water retention [24]. It was reported that incorporating cellulose-derivative VMA can increase yield stress and plastic viscosity [201,362], which is beneficial for the extrudability and shape retention of the cementitious mixture. Hence, in this study, HPMC-based VMA was employed to modify the fresh properties of various mixtures, aiming to achieve a composition capable of retaining its shape. The optimum dosage of VMA was determined following a trial-based approach by incorporating different dosages and investigating its effect on the shape retention of each mixture. That was done by conducting printing trials to print a rectangular object consisting of four layers, as shown in Figure 6.8, which presents the effect of different VMA dosages on the shape retention of an LC3 mixture prepared with 30% BA content. It can be seen that incorporating 0.25VMA %-wt. improved the mixture's consistency and shape retention. However, it was not enough to allow the mix to develop sufficient early strength to withstand the weight of the subsequent layers, showing excessive deformation in the bottom layer, as seen in Figure 6.8a. Increasing the VMA dosage to 0.4 wt.% improved the shape retention of LC3-30BA significantly, allowing the print of four layers without showing any failure, as shown in Figure 6.8b. Hence, this dosage was selected as the optimum for LC3-30BA. The same approach was considered for the other mixtures, and the optimum dosage was found to be 0.5, 0.4% and 0.4 %-wt for CS, 30BA and 50BA, respectively. According to Chen et al. [24], increasing VMA content to a certain level can improve the shape retention of the extruded filaments. The better shape retention was attributed to the relatively higher green strength development with increasing VMA dosage, in which the authors found that increasing VMA dosage from 0.12 wt.% to 0.24 wt.% and 0.48 wt.% allowed the development of 5 times and 6 times higher green strength, respectively. Thus, the cementitious mixture can withstand more loads when depositing subsequent layers. Hence, in this study, the better shape retention is due to the higher green strength development with increasing VMA content. Moreover, when combined with PCE, HPMC-based VMA can significantly increase the thixotropy of cementitious mixture [381], which allows the mixture to achieve faster rigidification to sustain more stress, and thus retain the weight of the subsequent layers.

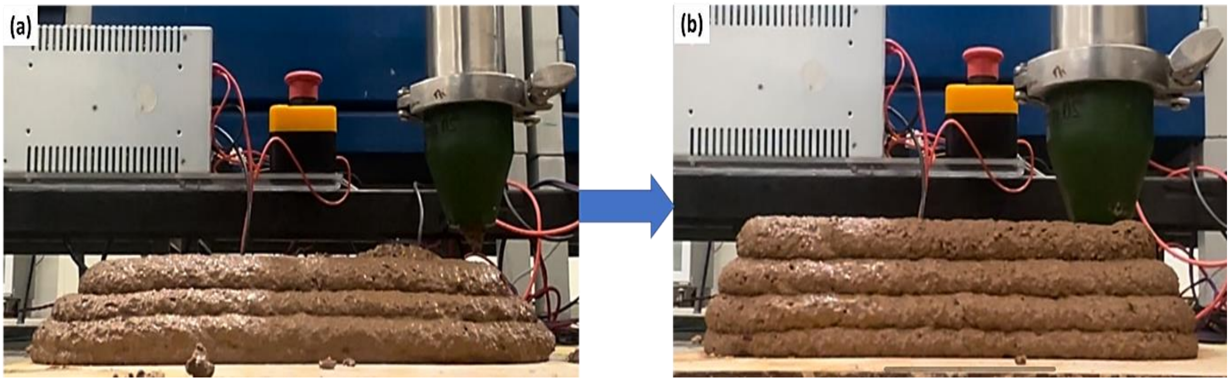

Figure 6.8. Shape retention of LC3-30BA with (a) 0.4VMA %-wt. and (b) 0.5VMA %-wt.

6.3.3.2. Open time

According to BS EN 197-1:2011 [328], the initial setting time of CEM I class 52.5 should be longer than 45 min. However, it should be noted that the open time is a more crucial factor for 3D printed concrete than initial setting time, since the needed time of the mix before setting differs depending on the targeted application. The open time of the modified mixtures was determined, and the results are presented in Table 6.5. All mixtures had suitable open time, indicating their suitability for large-scale applications. It can be seen that the mixture prepared with NA had the highest open time, whereas incorporating BA decreased the open time of the LC3 mixture. This is aligned with the findings of the previous chapter, which found that incorporating BA up to 50% significantly decreased the open time of one part of the alkali-activated material. The reduction was attributed to the high water absorption of

BA, which decreased the amount of free water in the mixture, however, it should be noted that no additional water was accounted for in the previous chapter. Based on the physical properties of BA (see Table 3.3), BA absorbs around 91% of the maximum water absorption capacity of the BA particle within the first 30 min. Although extra water for BA absorption was accounted for, BA absorbs most of it within the first 30 minutes, resulting in similar free water levels as in the CS mix with NA. Hence, it can be indicated that the decrease in open time could be related to the BA's particle morphology and coarser particle shape compared to that of NA, which increases the frictional resistance of the mixture during extrusion and, thus, lowers the open time of the LC3 mixtures with BA.

Table 6.5. Open time of the modified LC3 with NA, 30% and 50% BA

Mix ID	CS-0.5%-wt. VMA	30BA-0.5%-wt. VMA	50BA-0.4%-wt. VMA
Open time in minutes	80	60	55

6.3.3.3. Buildability

The buildability of the modified LC3 mixtures with and without BA was investigated through 3D printing a cylinder using a fixed amount of materials (8 Kg). It should be noted that further VMA modifications were considered when needed to find the optimum VMA dosage that makes the LC3 mixtures buildable without collapsing or failing. For instance, it was found that incorporating 0.4% VMA was sufficient and allowed the mix to retain its shape during the printing trials for a rectangular object with four layers (see section 6.3.3.1). Nevertheless, 0.4%-wt. VMA dosage for LC3-30BA was insufficient to allow the mixture to retain its shape in the buildability test, in which the bottom layers could not develop enough green strength to sustain the load induced from the subsequent layers, resulting in the collapse of the cylinder, as shown in Figure 6.9a. Hence, the VMA dosage of LC3-30BA was increased from 0.4% to 0.5%-wt., and the buildability of the mixture was re-assessed. 30BA mix containing 0.5%-wt. was extruded and could retain the designated object shape, as shown in Figure 6.9b. The better shape retention, as explained earlier, is attributed to the higher green strength in the presence of higher VMA dosage. Therefore, the modified VMA dosages are 0.5%, 0.5% and 0.4% for CS, 30BA and 50BA, respectively.

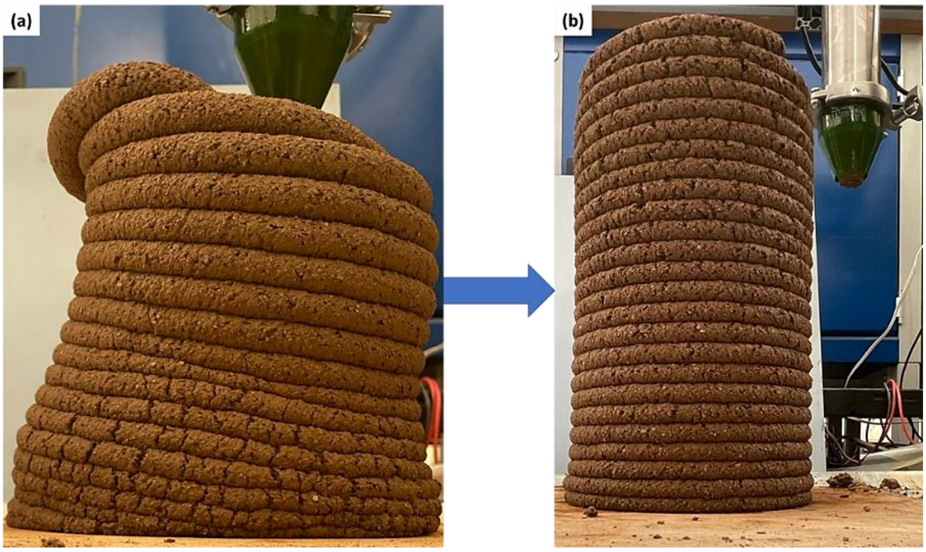

Figure 6.9. Shape retention of 30BA using (a) 0.4%-wt and (b) 0.5%-wt. VMA dosages.

Figure 6.10 presents cylinders of the different modified mixtures, which contain 0.5%, 0.5%, and 0.4% VMA for CS, 30BA, and 50BA, respectively. The buildability test was conducted until the fixed amount of fresh mixture was consumed, and the experimental height and layer number of the various mixtures were measured. All cylinders were printed without any discontinuity in printing or showing lateral deformation and achieved adequate shape and layer thickness, as seen in Figure 6.10. Moreover, all cylinders had a comparable experimental height to the designated theoretical height, in which all layers maintained their designated thickness (i.e., 10 mm).

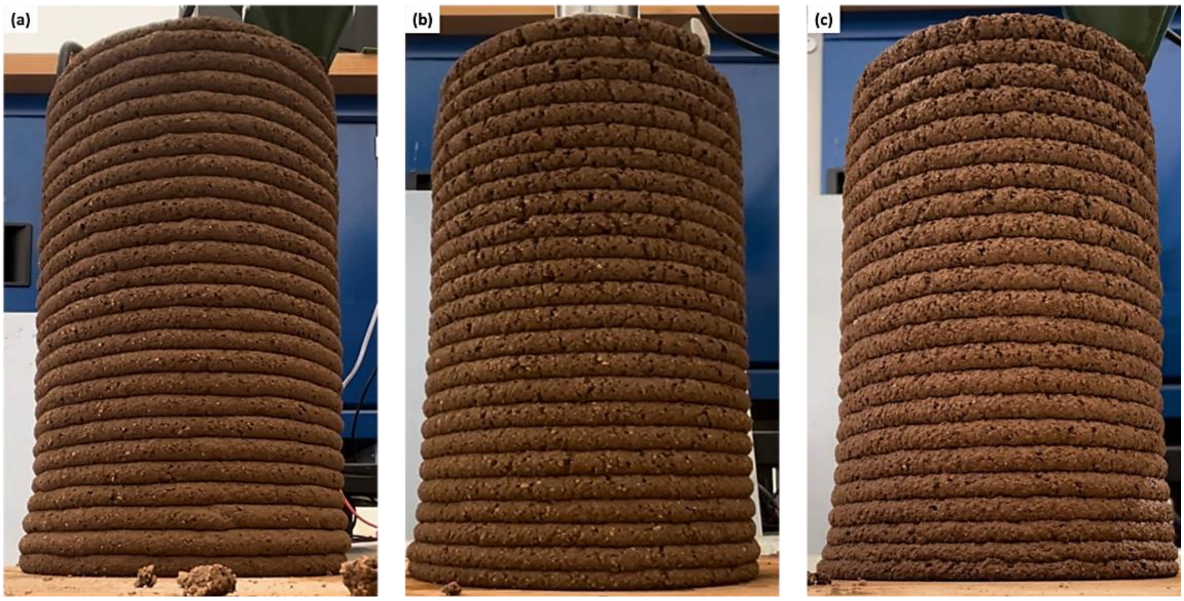

Figure 6.10. Buildability of (a) CS, (b) 30BA, and (c) 50BA.

Although the different LC3 mixtures were modified to be buildable, incorporating BA to replace NA was found to cause some tears in the filaments. It should be noted that the printing parameters, such as printing speed and nozzle size, were kept constant for all the mixtures. The cylinders were examined more closely to understand the reason behind these tears better, as seen in Figures 6.11 – 13. Some tears and voids were observed in all cylinders but increased when BA was incorporated. The cylinder prepared with CS mix showed fewer tears than those containing BA. During the printing process of the CS mix, the mixture was extruded smoothly without showing any cracks. Nevertheless, cracks immediately started showing on the outer surface of the filaments of the CS mix, which could indicate that plastic shrinkage is taking place due to the fast evaporation of the free water in the system. On the other hand, the filaments of the cylinders printed using mixtures containing BA showed tears during the extrusion process. These tears could be attributed to the irregular particle shape of BA, at which its edge might have got stuck (hanged) on the side of the nozzle's outlet, slightly delaying the extrusion and leading to form a small void in the extruded filament. Nevertheless, the formation of additional cracks from shrinkage weren't observed on the cylinders prepared with 30BA and 50BA mixes. This indicates that the water absorption of BA was more dominant over water evaporation, which would allow for maintaining the moisture within the layers and, thus, prevent plastic shrinkage from taking place. As discussed earlier, BA would start releasing water over time. Hence, once the available water in layers evaporated, BA would work on releasing some of the water it initially absorbed, preventing the cracks from occurring. Ge et al. [382] investigated the effect of replacing fine NA with recycled fine BA on the drying shrinkage properties of self-compacting concrete. They found the shrinkage to decrease with increasing the replacement level. Shrinkage, according to the authors, is mainly attributed to the loss of water in the reacted and hydrated binder materials, which results in capillary stress and surface tension. Using recycled fine BA with porous microstructure and high water absorption capacity could result in more effective internal curing [382]. That could explain the absence of cracks attributable to shrinkage in the presented study for the cylinder printed with BA. It should be noted that the shrinkage property isn't part of the current study, hence further research should be conducted. On the other hand,

Figure 6.11. Layers' printing quality of LC3 with NA (CS mix).

Figure 6.12. Layers' printing quality of LC3-30BA mix.

Figure 6.13. Layers' printing quality of LC3-50BA mix.

6.3.3.4. Mechanical properties of 3D printed LC3 mixtures

Figure 6.14 presents the flexural and compressive strength results of cast and 3D printed modified LC3 mixtures with and without BA. presents the flexural and compressive strength results of cast and 3D printed modified LC3 mixtures with and without BA. As per previous investigation, it is expected that VMA incorporation decreases the flexural and compressive strength of LC3 samples [187]. Nevertheless, this study focuses on the impact of BA incorporation on the strength properties of the LC3 mixture. Moreover, the 3D-printed specimens are expected to achieve lower strength performance than the mould-cast specimens. Similar to the results reported in section 5.3.2.1.2, LC3 containing BA maintained higher strength performances than the LC3 mix with NA. The highest strength performance was reported for LC3-50BA for cast and 3D printed samples, exhibiting around 28% and 34% higher flexural strength performance for cast and 3D printed samples, respectively, than the control sample. Similarly, 50BA exhibited around 55% and 40% higher compressive strength for cast and 3D printed specimens, respectively, compared to the control sample. Moreover, as expected, printed specimens exhibited slightly lower flexural and compressive strength performance than the cast specimens. 3D printed specimens exhibited around 16%, 14% and 14% lower strength performance than the mould-cast specimens for CS, 30BA and 50BA, respectively. Rahul et al. [125] reported lower compressive strength performance for 3D printed specimens than the mould cast concrete. According to the authors, the decreased compressive strength performance is attributed to the weaker interfaces developed between the layers in 3D printed specimens with the increased porosities between filaments. Consequently, cracks may be initiated from these weak interfaces under load, causing a failure at lower stress values than the cast specimens. Hence, the lower mechanical strength behaviour of 3D printed samples in this study compared to cast could be attributed to the weaker interfacial bonding between the layers. Similar findings were reported by Ibrahim et al. [221], who found that 3D printed LC3 specimens maintain slightly lower strength performance than the cast specimens. It should be noted that most studies investigated the flexural and compressive strength performance of mould cast LC3 specimens, and the literature lacks findings on the strength behaviour of 3D printed LC3. Hence, comparisons in this study are limited.

As previously mentioned, ACI 318M-05 [329] requires concrete to achieve at least 28 MPa after 28 days to be considered for engineering applications. It can be indicated that modified cast and 3D printed LC3 mixture with NA does not meet this requirement. On the other hand, cast and 3D printed modified LC3 with 30 and 50% BA met the requirements.

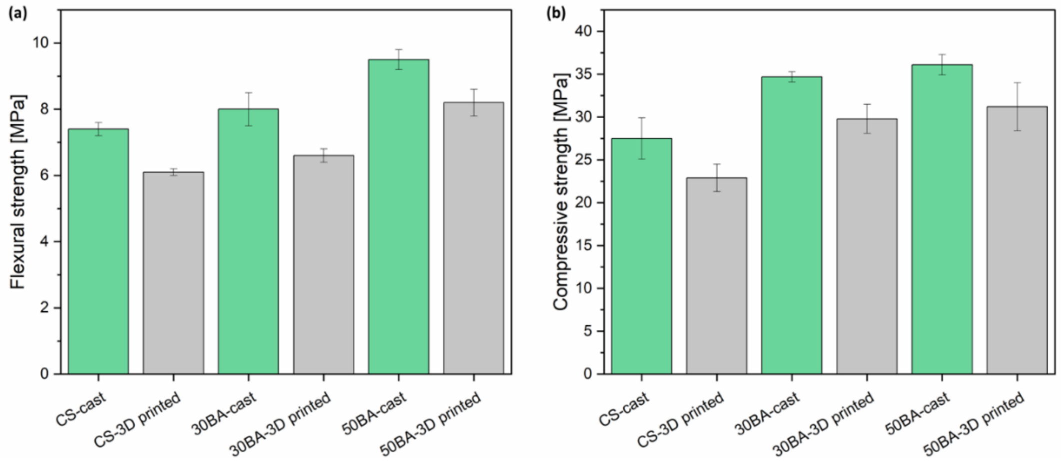

Figure 6.14. (a) Flexural and (b) compressive strengths of cast and 3D printed modified CS, 30BA and 50BA.

6.4. Conclusions

This study investigated the effect of replacing natural aggregates with brick aggregates on the properties of limestone calcined clay cement with applications focused on the cast and 3D printing processes aimed at producing medium to large-scale building blocks and structural elements. Recycled brick aggregates were incorporated to replace up to 100% natural aggregates in the casting method, and their effect on fresh properties, mechanical strength, and durability were investigated. On the other hand, brick aggregates were used to replace up to 50% of natural aggregates in 3D printing applications due to the high particle-to-particle packing, which didn’t allow for further replacements. The mixtures were further modified to retain their shape, and the impact of brick aggregates on buildability, printing quality, and mechanical strength was evaluated. Based on the findings of this study, the following conclusions can be made:

1. Brick aggregate inclusion leads to reduction of workability of the LC3 mixtures even though additional water was counted in the LC3 mix design due to BA’s porous microstructure.
2. The incorporation of brick aggregates plays a significant role in enhancing the mechanical strength of LC3 mixtures. Acting as an internal curing agent, it initially absorbs water and then releases it with ageing, facilitating further hydration. Furthermore, the angular shape and rough texture of brick aggregates also contribute to the improved mechanical strength behaviour of the LC3 mixtures, due to mechanical entanglements and interlocking.
3. The water absorption of LC3 mixtures initially increased with the increase in BA content. However, LC3 mixtures with up to 70% BA showed similar water absorption percentages at 28 days. Moreover, the Incorporation of BA enhanced the resistivity of the LC3 mixture to freeze-thaw, indicating its potential benefits in terms of durability.
4. Global warming potential calculations showed that using LC3 can allow reducing around 40% of CO2 emissions of the OPC-based mixture. Moreover, brick aggregate incorporation didn’t have a noticeable impact on the global warming potential calculations.
5. Shape retention of LC3 mixtures with and without BA was modified using VMA additives. Incorporating optimum dosages of VMA (i.e., 0.5% for CS and 30BA, and 0.4% for 50BA) allowed all mixtures to be buildable and achieve the designed shape.
6. Brick aggregate incorporation can overcome the torsions induced after depositing the layers. Nevertheless, some voids can occur due to the irregular/angular shape of BA.

Overall, this study revealed the suitability of repurposing end-of-life bricks into aggregates to improve the engineering and printing properties of low-carbon cementitious mixtures. This work also provided a framework to develop cementitious mixtures with suitable engineering properties for 3D printing applications.

7. CHAPTER 7: CONCLUSIONS AND FUTURE PERSPECTIVES

Highlights:

- Mitigating OPC environmental impact and the amount of construction and demolition waste being landfilled;
- One-part alkali-activated materials and limestone calcined clay cement as low-carbon alternatives to OPC;
- Valorising end-of-life brick through recycling into SCM;
- Valorising excavated London clay by repurposing to be used as SCMs;
- Examining the fresh behaviour, mechanical strength, durability and printing properties of developed low-carbon cementitious mixtures;
- Understanding the effect of replacing natural sand with recycled brick aggregate on the low-carbon mixtures properties;
- Develop 3D printable one-part AAM and LC3 containing upcycled waste materials;

This chapter presents a concise summary of the main outcomes of this research project. The aim of this chapter is to provide an overall evaluation to ascertain the project's research work's success. The project's results have been used to establish future prospects and critical directions for additional research.

Keywords: AAM, LC3, recycled aggregates, recycled binders, properties, 3D printing.

7.1.Introduction

Cement production significantly contributes to global CO_2 emissions, constituting approximately 8% worldwide [2]. With the ongoing expansion of the construction industry, there has been a substantial increase in the demand for natural resources, specifically sand, resulting in environmental deterioration and resource scarcity. Simultaneously, the construction sector generates substantial waste and secondary materials, a significant portion of which is disposed of in landfills, further amplifying its environmental impact.

This research project has made a significant contribution to the field of low-carbon materials in the construction industry. It has achieved this by developing innovative low-carbon cementitious mixtures, primarily composed of recycled construction wastes as binders and aggregates. These mixtures can be used in various construction materials as an alternative to traditional cementitious mixtures, thereby mitigating the overreliance on cement and natural resources.

The successful utilisation of waste materials in AAM and LC3 mixtures broadens their applications and increases their value, providing a cost-effective and environmentally beneficial sustainable building method.

7.2.Main conclusions

This research project has contributed towards developing low-carbon cementitious mixtures by developing a scientific understanding and assessing the feasibility of available local waste materials as binders and aggregates. This research has also advanced the development of eco-friendly and cost-efficient feedstocks for concrete 3D printing technology. The following four key points illustrate the conclusions found during this research:

1) The suitability of upcycling end-of-life brick into powder to replace up to 60% fly ash in one-part AAM was studied. The effect of replacing natural sand with brick aggregates on the properties of brick-based one-part AAM and the inclusion of nano-graphite material as a reinforcing agent was also investigated. Brick-based one-part AAM exhibited comparable mechanical performance and transport properties while exhibiting better freeze-thaw resistivity and high temperature resistance than fly ash-based one-part AAM mixture. Brick aggregate incorporation improved brick-based

one-part AAMs' mechanical strength, freeze-thaw and high-temperature resistivity while increasing the water absorption percentage (transport properties). Moreover, adding 0.1% nano-graphite to the weight of the binder improved the flexural strength, freeze-thaw resistivity and high-temperature resistivity while decreasing the water absorption of brick-based one-part AAM containing 70% brick aggregate. These findings show the potential of brick-based AAMs as a sustainable alternative to conventional AAMs. Moreover, the results indicate the suitability of recycling brick aggregates as an alternative source to natural sand, addressing the challenge of natural resource depletion and construction waste recycling.

2) Incorporating up to 50% brick aggregates to replace natural sand significantly improved the green strength, green Young’s modulus and hardened mechanical strength of brick-based one-part AAM. Moreover, the flexural and compressive strength of the printed samples increased with increasing brick aggregate in the mixture. Nonetheless, anisotropic mechanical behaviour also increased with increasing brick aggregate content in the mixture, having the highest strength in the lateral direction. On the other hand, brick aggregate incorporation improved the buildability of the mixtures. These findings reveal the potential for using recycled end-of-life materials to develop an alternative lower carbon feedstock for 3D printing applications. This approach not only addresses the challenge of managing construction and demolition waste but also supports the development of 3D-printable mixtures for small- to medium-scale applications.
3) The suitability of using extra low-grade excavated London clay after being thermally activated at different temperatures was investigated. Calcining excavated London clay at 800 ℃ allowed the clay to exhibit the highest pozzolanic reactivity, showing that excavated London clay can be considered an SCM after activation. Incorporating superplasticiser was beneficial in reducing the water content and achieving better strength performance, where 1% of the binder weight achieved the best strength performance. Nevertheless, VMA was necessary to adjust the fresh behaviour of the mixture to make it 3D printable. Incorporating 0.6% VMA of the binder weight of the mix prepared with 1% SP and 0.3 water content allowed for obtaining the best printing quality, achieving acceptable buildability (maximum height achieved by the printer) with no failure or collapse. This study not only repurposes excavated London clay but also advances the development of alternative feedstocks for 3D printing technology that suits medium- to large-scale applications.

4) Substituting natural sand with brick aggregates while compensating for the water absorption capacity of brick aggregates was beneficial for the different properties of the mixture. Incorporating brick aggregates allowed for better strength performance and freeze-thaw resistivity while having a water absorption percentage comparable to the mix with natural sand. LC3 incorporating brick aggregates was 3D printable up to 50% replacement level. Nonetheless, incorporating VMA was necessary to adjust the flowability of the mixture. The findings suggested the potential and benefits of utilising recycled brick aggregates on the properties of LC3 mixture, presenting a suitable approach for reusing brick waste in construction to develop high-performance construction material.

7.3.Future prospectives

In this section, suggestions for extending the work are listed based on the knowledge established through the completion of this project. The gaps are identified, which should further add value to the research field.

1) **Performance assessment of 3D printed brick-based one-part AAM and LC3:** Most previous studies, including this study, focused on developing low-carbon cementitious binders through considering their performance in the traditional cast method, and only considered investigating the mechanical strength of 3D printed samples. Therefore, the research direction would move towards investigating and studying the performance of 3D printed low-carbon cementitious mixtures rather than cast samples. This would allow gathering a database to develop better insights and understanding of the performance of the developed mix formulations and enhance their practicality for large-scale applications.

2) **The effect of adding extra water on the properties of one-part AAM:** The methodology used in Chapter 4 (i.e., not considering compensating the absorbed water by brick aggregates) raised the problem of limiting the setting time and negatively impacting extrudability while improving the buildability of the mixtures. Hence, it would be interesting to study the effect of treating brick aggregate by compensating the water absorption of brick aggregates or soaking in water on the different properties of one-part AAM.

3) **The reaction of excavated London clay after calcination was found to happen at later ages:** This research investigated the mechanical strength performance and strength growth of the LC3 mixture over a curing period of 28 days. Hence, it is worth investigating the extent of the pozzolanic reaction of calcined London clay by determining the strength development at later ages at 90 and 180 days. Moreover, the effect of calcined London clay particle size on the pozzolanic reactivity and the different properties of LC3 would be an interesting research area. Moreover, the shrinkage and physical properties (e.g., thermal conductivity, and damping ratio) of LC3 mixtures prepared using excavated clays to understand its behaviour, providing more insights and in-depth understanding, to allow for upscaling the utilisation of excavated clays in construction, especially in 3D printing applications.
4) **Assessing the economic feasibility and environmental sustainability for up scaling these products:** The commercial viability of employing these materials in construction lies in costs and carbon emission reductions. Hence, key research to investigate in the future would be on life cycle costing (LCC) and life cycle assessment (LCA) to provide a holistic view of the feasibility of scaling up brick-based one-part AAM and LC3 containing excavated clay.
5) **Scaling up the manufacturing of brick-based one-part AAM and LC3 containing calcined London clay for 3D printing structural elements:** A pilot plant is necessary to allow the transition from laboratory-scale research to commercial production to scale up the manufacturing process of brick powder and excavated London clay, involving drying, crushing, grinding, and other processes, to produce high quantities of these products. Also, scale up the production of mix formulations. Moreover, this can help validate 3D printing technology at a larger scale and resolve issues related to industrial implementation. The next step is to start producing small- to medium-sized structural elements to assess the quality on a larger scale and adapt to the manufacturing process on a larger scale to ensure consistency with the obtained mixtures in the lab. Furthermore, the pilot plant would provide critical insights and data on the LCA and economic feasibility of developing these commercial products.

References:

[1] Hasanbeigi A, Price L, Lin E. Emerging energy-efficiency and CO2 emission-reduction technologies for cement and concrete production: A technical review. Renew Sustain Energy Rev 2012;16:6220–38. https://doi.org/10.1016/j.rser.2012.07.019.

[2] Gunasekara C. Microstructure and strength development of quaternary blend high-volume fly ash concrete. J Mater Sci 2020;55:6441–56. https://doi.org/10.1007/s10853-020-04473-1.

[3] IEA CSI. Technology Roadmap Low-Carbon Transition in the Cement Industry. Fr Geneva, Switzerland IEA, Paris 2018.

[4] Barcelo L, Kline J, Walenta G, Gartner E. Cement and carbon emissions. Mater Struct Constr 2014;47:1055–65. https://doi.org/10.1617/s11527-013-0114-5.

[5] Wangler T, Lloret E, Reiter L, Hack N, Gramazio F, Kohler M, et al. Digital Concrete: Opportunities and Challenges. RILEM Tech Lett 2016;1:67. https://doi.org/10.21809/rilemtechlett.2016.16.

[6] Schutter G De, Lesage K, Mechtcherine V, Naidu V, Habert G, Agusti-juan I. Vision of 3D printing with concrete — Technical , economic and environmental potentials. Cem Concr Res 2018;112:25–36. https://doi.org/10.1016/j.cemconres.2018.06.001.

[7] Wangler T, Roussel N, Bos FP, Salet TAM, Flatt RJ. Digital Concrete: A Review. Cem Concr Res 2019;123. https://doi.org/10.1016/j.cemconres.2019.105780.

[8] Han Y, Yang Z, Ding T, Xiao J. Environmental and economic assessment on 3D printed buildings with recycled concrete. J Clean Prod 2021;278:123884. https://doi.org/10.1016/j.jclepro.2020.123884.

[9] Cicione A, Kruger J, Walls RS, Van Zijl G. An experimental study of the behavior of 3D printed concrete at elevated temperatures. Fire Saf J 2021;120:103075. https://doi.org/10.1016/j.firesaf.2020.103075.

[10] Sanjayan JG, Nematollahi B, Xia M, Marchment T. Effect of surface moisture on inter-layer strength of 3D printed concrete. Constr Build Mater 2018;172:468–75. https://doi.org/10.1016/j.conbuildmat.2018.03.232.

[11] Martirena F, Scrivener K. Low Carbon Cement LC3 in Cuba: Ways to Achieve a

Sustainable Growth of Cement Production in Emerging Economies BT - Calcined Clays for Sustainable Concrete. In: Martirena F, Favier A, Scrivener K, editors., Dordrecht: Springer Netherlands; 2018, p. 318–21.

[12] Avet F, Li X, Scrivener K. Determination of the amount of reacted metakaolin in calcined clay blends. Cem Concr Res 2018;106:40–8. https://doi.org/10.1016/j.cemconres.2018.01.009.

[13] Hardjito D, Wallah SE, Sumajouw DMJ, Rangan BV. On the development of fly ash-based geopolymer concrete. ACI Mater J 2004;101:467–72. https://doi.org/10.14359/13485.

[14] Gholampour A, Ozbakkaloglu T, Ng CT. Ambient- and oven-cured geopolymer concretes under active confinement. Constr Build Mater 2019;228:116722. https://doi.org/10.1016/j.conbuildmat.2019.116722.

[15] Panda B, Tan MJ. Rheological behavior of high volume fly ash mixtures containing micro silica for digital construction application. Mater Lett 2019;237:348–51. https://doi.org/10.1016/j.matlet.2018.11.131.

[16] Panda B, Ruan S, Unluer C, Tan MJ. Improving the 3D printability of high volume fly ash mixtures via the use of nano attapulgite clay. Compos Part B Eng 2019;165:75–83. https://doi.org/10.1016/j.compositesb.2018.11.109.

[17] Dey D, Srinivas D, Panda B, Suraneni P, Sitharam TG. Use of industrial waste materials for 3D printing of sustainable concrete: A review. J Clean Prod 2022;340:130749. https://doi.org/10.1016/j.jclepro.2022.130749.

[18] Le TT, Austin SA, Lim S, Buswell RA, Gibb AGF, Thorpe T. Mix design and fresh properties for high-performance printing concrete 2012:1221–32. https://doi.org/10.1617/s11527-012-9828-z.

[19] Nerella VN, Näther M, Iqbal A, Butler M, Mechtcherine V. Inline quantification of extrudability of cementitious materials for digital construction. Cem Concr Compos 2019;95:260–70. https://doi.org/10.1016/j.cemconcomp.2018.09.015.

[20] Scrivener K, Martirena F, Bishnoi S, Maity S. Calcined clay limestone cements (LC3). Cem Concr Res 2018;114:49–56. https://doi.org/10.1016/j.cemconres.2017.08.017.

[21] Glavind M. Sustainability of cement, concrete and cement replacement materials in

construction. Woodhead Publishing Limited; n.d. https://doi.org/10.1533/9781845695842.120.

[22] Snellings R. Assessing , Understanding and Unlocking Supplementary Cementitious Materials 2016:50–5. https://doi.org/10.21809/rilemtechlett.2016.12.

[23] Environment UN, Scrivener KL, John VM, Gartner EM, Polytechnique É, Lausanne F De. Eco-efficient cements : Potential economically viable solutions for a low-CO 2 cement-based materials industry ☆. Cem Concr Res 2018;114:2–26. https://doi.org/10.1016/j.cemconres.2018.03.015.

[24] Chen Y, Chaves Figueiredo S, Li Z, Chang Z, Jansen K, Çopuroğlu O, et al. Improving printability of limestone-calcined clay-based cementitious materials by using viscosity-modifying admixture. Cem Concr Res 2020;132. https://doi.org/10.1016/j.cemconres.2020.106040.

[25] Maglad AM, Zaid O, Arbili MM, Ascens G, Adrian AS, Qaidi SMA. A Study on the Properties of Geopolymer Concrete Modified with Nano Graphene Oxide 2022.

[26] El-seidy E, Sambucci M, Chougan M, Al-kheetan MJ. Mechanical and physical characteristics of alkali- activated mortars incorporated with recycled polyvinyl chloride and rubber aggregates. J Build Eng 2022;60:105043. https://doi.org/10.1016/j.jobe.2022.105043.

[27] Alghamdi H, Shoukry H, Abadel AA, Khawaji M. Performance assessment of limestone calcined clay cement (LC3)-Based lightweight green mortars incorporating recycled waste aggregate. J Mater Res Technol 2023;23:2065–74. https://doi.org/10.1016/j.jmrt.2023.01.133.

[28] Chilamkurthy K, Marckson A V, Chopperla ST, Santhanam M. A statistical overview of sand demand in Asia and Europe. Proc. Int. Conf. UKIERE CTMC, vol. 16, 2016, p. 15.

[29] Lu W. Big data analytics to identify illegal construction waste dumping: A Hong Kong study. Resour Conserv Recycl 2019;141:264–72. https://doi.org/10.1016/j.resconrec.2018.10.039.

[30] Ouda AS, Gharieb M. Development the properties of brick geopolymer pastes using concrete waste incorporating dolomite aggregate. J Build Eng 2020;27:100919.

https://doi.org/10.1016/j.jobe.2019.100919.

[31] Paul SC, Babafemi AJ, Anggraini V, Rahman MM. Properties of normal and recycled brick aggregates for production of medium range (25-30 MPa) structural strength concrete. Buildings 2018;8. https://doi.org/10.3390/BUILDINGS8050072.

[32] El-seidy E, Chougan M, Sambucci M, Al-kheetan MJ, Biblioteca I, Valente M, et al. Lightweight alkali-activated materials and ordinary Portland cement composites using recycled polyvinyl chloride and waste glass aggregates to fully replace natural sand. Constr Build Mater 2023;368:130399. https://doi.org/10.1016/j.conbuildmat.2023.130399.

[33] Peng C. Calculation of a building ' s life cycle carbon emissions based on Ecotect and building information modeling. J Clean Prod 2016;112:453–65. https://doi.org/10.1016/j.jclepro.2015.08.078.

[34] Oikonomou ND. Recycled concrete aggregates 2005;27:315–8. https://doi.org/10.1016/j.cemconcomp.2004.02.020.

[35] Reig L, Tashima MM, Borrachero M V, Monzó J, Cheeseman CR, Payá J. Properties and microstructure of alkali-activated red clay brick waste. Constr Build Mater 2013;43:98–106. https://doi.org/10.1016/j.conbuildmat.2013.01.031.

[36] Fatta D, Papadopoulos A, Avramikos E, Sgourou E, Moustakas K, Kourmoussis F, et al. Generation and management of construction and demolition waste in Greece — an existing challenge 2003;40:81–91. https://doi.org/10.1016/S0921-3449(03)00035-1.

[37] Li Y, Yi P, Du H, Liu W, Mi T, Huang L. Activation of locally excavated spoil for utilization in limestone calcined clay cement (LC3). Constr Build Mater 2024;420:135518. https://doi.org/10.1016/j.conbuildmat.2024.135518.

[38] Dadsetan S, Siad H, Lachemi M, Sahmaran M. Construction and demolition waste in geopolymer concrete technology: A review. Mag Concr Res 2019;71:1232–52. https://doi.org/10.1680/jmacr.18.00307.

[39] Robayo RA, Mulford A, Munera J, Mejía de Gutiérrez R. Alternative cements based on alkali-activated red clay brick waste. Constr Build Mater 2016;128:163–9. https://doi.org/10.1016/j.conbuildmat.2016.10.023.

[40] Long Y, Pan J, Zhang Q, Hao Y. 3D printing technology and its impact on Chinese

manufacturing. Int J Prod Res 2017;7543:1–10. https://doi.org/10.1080/00207543.2017.1280196.

[41] El-seidy E, Sambucci M, Chougan M, Ai-noaimat YA, Al-kheetan MJ, Biblioteca I, et al. Alkali activated materials with recycled unplasticised polyvinyl chloride aggregates for sand replacement. Constr Build Mater 2023;409:134188. https://doi.org/10.1016/j.conbuildmat.2023.134188.

[42] Pegna J. Exploratory investigation of solid freeform construction. Autom Constr 1997;5:427–37. https://doi.org/10.1016/S0926-5805(96)00166-5.

[43] Ghaffar S, Mullett P. Commentary: 3D printing set to transform the construction industry. Proc Inst Civ Eng Struct Build 2021;174:336–7. https://doi.org/10.1680/jstbu.21.00024.

[44] Kruger J, Zeranka S, van Zijl G. An ab initio approach for thixotropy characterisation of (nanoparticle-infused) 3D printable concrete. Constr Build Mater 2019;224:372–86. https://doi.org/10.1016/j.conbuildmat.2019.07.078.

[45] Panda B, Unluer C, Tan MJ. Investigation of the rheology and strength of geopolymer mixtures for extrusion-based 3D printing. Cem Concr Compos 2018;94:307–14. https://doi.org/10.1016/j.cemconcomp.2018.10.002.

[46] Panda B, Tan MJ. Experimental study on mix proportion and fresh properties of fly ash based geopolymer for 3D concrete printing. Ceram Int 2018;44:10258–65. https://doi.org/10.1016/j.ceramint.2018.03.031.

[47] Rahul A V., Santhanam M, Meena H, Ghani Z. 3D printable concrete: Mixture design and test methods. Cem Concr Compos 2019;97:13–23. https://doi.org/10.1016/j.cemconcomp.2018.12.014.

[48] De Schutter G, Lesage K, Mechtcherine V, Nerella VN, Habert G, Agusti-Juan I. Vision of 3D printing with concrete — Technical, economic and environmental potentials. Cem Concr Res 2018;112:25–36. https://doi.org/10.1016/j.cemconres.2018.06.001.

[49] Agustí-Juan I, Müller F, Hack N, Wangler T, Habert G. Potential benefits of digital fabrication for complex structures: Environmental assessment of a robotically fabricated concrete wall. J Clean Prod 2017;154:330–40.

https://doi.org/10.1016/j.jclepro.2017.04.002.

[50] Weng Y, Li M, Ruan S, Wong TN, Tan MJ, Ow Yeong KL, et al. Comparative economic, environmental and productivity assessment of a concrete bathroom unit fabricated through 3D printing and a precast approach. J Clean Prod 2020;261:121245. https://doi.org/10.1016/j.jclepro.2020.121245.

[51] Grassl P, Wong HS, Buenfeld NR. Influence of aggregate size and volume fraction on shrinkage induced micro-cracking of concrete and mortar. Cem Concr Res 2010;40:85–93. https://doi.org/10.1016/j.cemconres.2009.09.012.

[52] Hardjito D, Rangan BV. Development and properties of low-calcium fly ash-based geopolymer concrete. Res Rep GC 2005:94.

[53] Phoo-Ngernkham T, Maegawa A, Mishima N, Hatanaka S, Chindaprasirt P. Effects of sodium hydroxide and sodium silicate solutions on compressive and shear bond strengths of FA-GBFS geopolymer. Constr Build Mater 2015;91:1–8. https://doi.org/10.1016/j.conbuildmat.2015.05.001.

[54] Aupoil J, Champenois JB, d'Espinose de Lacaillerie JB, Poulesquen A. Interplay between silicate and hydroxide ions during geopolymerization. Cem Concr Res 2019;115:426–32. https://doi.org/10.1016/j.cemconres.2018.09.012.

[55] Vinai R, Soutsos M. Production of sodium silicate powder from waste glass cullet for alkali activation of alternative binders. Cem Concr Res 2019;116:45–56. https://doi.org/10.1016/j.cemconres.2018.11.008.

[56] Hu W, Nie Q, Huang B, Su A, Du Y, Shu X, et al. Mechanical property and microstructure characteristics of geopolymer stabilized aggregate base. Constr Build Mater 2018;191:1120–7. https://doi.org/10.1016/j.conbuildmat.2018.10.081.

[57] Nie Q, Hu W, Ai T, Huang B, Shu X, He Q. Strength properties of geopolymers derived from original and desulfurized red mud cured at ambient temperature. Constr Build Mater 2016;125:905–11. https://doi.org/10.1016/j.conbuildmat.2016.08.144.

[58] van Deventer JSJ, Provis JL, Duxson P, Lukey GC. Reaction mechanisms in the geopolymeric conversion of inorganic waste to useful products. J Hazard Mater 2007;139:506–13. https://doi.org/10.1016/j.jhazmat.2006.02.044.

[59] Adesanya E, Ohenoja K, Luukkonen T, Kinnunen P, Illikainen M. One-part

geopolymer cement from slag and pretreated paper sludge. J Clean Prod 2018;185:168–75. https://doi.org/10.1016/j.jclepro.2018.03.007.

[60] Luukkonen T, Abdollahnejad Z, Yliniemi J, Kinnunen P, Illikainen M. Comparison of alkali and silica sources in one-part alkali-activated blast furnace slag mortar. J Clean Prod 2018;187:171–9. https://doi.org/10.1016/j.jclepro.2018.03.202.

[61] Luukkonen T, Abdollahnejad Z, Yliniemi J, Kinnunen P, Illikainen M. One-part alkali-activated materials: A review. Cem Concr Res 2018;103:21–34. https://doi.org/10.1016/j.cemconres.2017.10.001.

[62] Nawaz M, Heitor A, Sivakumar M. Geopolymers in construction - recent developments. Constr Build Mater 2020;260:120472. https://doi.org/10.1016/j.conbuildmat.2020.120472.

[63] ASTM C618 - 03. Standard Specification for Coal Fly Ash and Raw or Calcined Natural Pozzolan for Use West Conshohocken, PA, 2001. Annu B ASTM Stand 2010:3–6. https://doi.org/10.1520/C0618-08.

[64] Chaves Figueiredo S, Romero Rodríguez C, Ahmed ZY, Bos DH, Xu Y, Salet TM, et al. An approach to develop printable strain hardening cementitious composites. Mater Des 2019;169. https://doi.org/10.1016/j.matdes.2019.107651.

[65] Das SK, Singh SK, Mishra J, Mustakim SM. Effect of Rice Husk Ash and Silica Fume as Strength-Enhancing Materials on Properties of Modern Concrete—A Comprehensive Review BT - Emerging Trends in Civil Engineering. In: Babu KG, Rao HS, Amarnath Y, editors., Singapore: Springer Singapore; 2020, p. 253–66.

[66] Astm C989-04. Standard Specification for Ground Granulated Blast-Furnace Slag for Use in Concrete. Annu B ASTM Stand 2004;i:1–5. https://doi.org/10.1520/C0989-04.

[67] Alujas A, Fernández R, Quintana R, Scrivener KL, Martirena F. Pozzolanic reactivity of low grade kaolinitic clays: Influence of calcination temperature and impact of calcination products on OPC hydration. Appl Clay Sci 2015;108:94–101. https://doi.org/10.1016/j.clay.2015.01.028.

[68] Pasupathy K, Ramakrishnan S, Sanjayan J. 3D concrete printing of eco-friendly geopolymer containing brick waste. Cem Concr Compos 2023;138:104943. https://doi.org/10.1016/j.cemconcomp.2023.104943.

[69] Ilcan H, Sahin O, Kul A, Yildirim G, Sahmaran M. Rheological properties and compressive strength of construction and demolition waste-based geopolymer mortars for 3D-Printing. Constr Build Mater 2022;328:127114. https://doi.org/10.1016/j.conbuildmat.2022.127114.

[70] Migunthanna J, Rajeev P. Waste Clay Bricks as a Geopolymer Binder for Pavement Construction. Sustainability 2022;14:6456.

[71] Nodehi M, Taghvaee VM. Alkali-Activated Materials and Geopolymer: a Review of Common Precursors and Activators Addressing Circular Economy. Circ Econ Sustain 2022;2:165–96. https://doi.org/10.1007/s43615-021-00029-w.

[72] Provis, J. L., & Van Deventer JS. Alkali activated materials: state-of-the-art report. 2013. https://doi.org/https://doi.org/10.1007/978-94-007-7672-21.

[73] Elzeadani M, Bompa D V, Elghazouli AY. One part alkali activated materials : A state-of-the-art review Ordinary Portland cement. J Build Eng 2022;57:104871. https://doi.org/10.1016/j.jobe.2022.104871.

[74] Lazorenko G, Kasprzhitskii A. Geopolymer additive manufacturing: A review. Addit Manuf 2022;55:102782. https://doi.org/10.1016/j.addma.2022.102782.

[75] Jolin M, Burns D, Bissonnette B, Gagnon F, Bolduc L-S. Understanding the pumpability of concrete. Shotcrete Undergr Support XI Eng Conf Int 2009:193–207.

[76] Bos F, Wolfs R, Ahmed Z, Salet T. Additive manufacturing of concrete in construction: potentials and challenges of 3D concrete printing. Virtual Phys Prototyp 2016;11:209–25. https://doi.org/10.1080/17452759.2016.1209867.

[77] Mechtcherine V, Nerella VN, Kasten K. Testing pumpability of concrete using Sliding Pipe Rheometer. Constr Build Mater 2014;53:312–23. https://doi.org/10.1016/j.conbuildmat.2013.11.037.

[78] Muthukrishnan S, Ramakrishnan S, Sanjayan J. Effect of alkali reactions on the rheology of one-part 3D printable geopolymer concrete. Cem Concr Compos 2021;116:103899. https://doi.org/10.1016/j.cemconcomp.2020.103899.

[79] Guo X, Yang J, Xiong G. Influence of supplementary cementitious materials on rheological properties of 3D printed fly ash based geopolymer. Cem Concr Compos 2020;114:103820. https://doi.org/10.1016/j.cemconcomp.2020.103820.

[80] Shah SFA, Chen B, Oderji SY, Haque MA, Ahmad MR. Improvement of early strength of fly ash-slag based one-part alkali activated mortar. Constr Build Mater 2020;246:118533. https://doi.org/10.1016/j.conbuildmat.2020.118533.

[81] Yousefi Oderji S, Chen B, Ahmad MR, Shah SFA. Fresh and hardened properties of one-part fly ash-based geopolymer binders cured at room temperature: Effect of slag and alkali activators. J Clean Prod 2019;225:1–10. https://doi.org/10.1016/j.jclepro.2019.03.290.

[82] Bong SH, Nematollahi B, Xia M, Nazari A, Sanjayan J. Properties of one-part geopolymer incorporating wollastonite as partial replacement of geopolymer precursor or sand. Mater Lett 2020;263:127236. https://doi.org/10.1016/j.matlet.2019.127236.

[83] Bong SH, Nematollahi B, Xia M, Ghaffar SH, Pan J, Dai JG. Properties of additively manufactured geopolymer incorporating mineral wollastonite microfibers. Constr Build Mater 2022;331:127282. https://doi.org/10.1016/j.conbuildmat.2022.127282.

[84] Roussel N. Rheological requirements for printable concretes. Cem Concr Res 2018;112:76–85. https://doi.org/10.1016/j.cemconres.2018.04.005.

[85] Felekoğlu B, Türkel S, Baradan B. Effect of water/cement ratio on the fresh and hardened properties of self-compacting concrete. Build Environ 2007;42:1795–802. https://doi.org/10.1016/j.buildenv.2006.01.012.

[86] Cheng Y, Cong P, Hao H, Zhao Q, Mei L, Zhang A, et al. Improving workability and mechanical properties of one-part waste brick power based-binders with superplasticizers. Constr Build Mater 2022;335:127535. https://doi.org/10.1016/j.conbuildmat.2022.127535.

[87] Alrefaei Y, Wang YS, Dai JG, Xu QF. Effect of superplasticizers on properties of one-part Ca(OH)2/Na2SO4 activated geopolymer pastes. Constr Build Mater 2020;241:117990. https://doi.org/10.1016/j.conbuildmat.2019.117990.

[88] Kazemian A, Yuan X, Cochran E, Khoshnevis B. Cementitious materials for construction-scale 3D printing: Laboratory testing of fresh printing mixture. Constr Build Mater 2017;145:639–47. https://doi.org/10.1016/j.conbuildmat.2017.04.015.

[89] Bong SH, Nematollahi B, Nazari A, Xia M, Sanjayan J. Efficiency of different superplasticizers and retarders on properties of “one-part” fly ash-slag blended

geopolymers with different activators. Materials (Basel) 2019;12. https://doi.org/10.3390/ma12203410.

[90] Bong SH, Xia M, Nematollahi B, Shi C. Ambient temperature cured ‘just-add-water’ geopolymer for 3D concrete printing applications. Cem Concr Compos 2021;121:104060. https://doi.org/10.1016/j.cemconcomp.2021.104060.

[91] Chougan M, Hamidreza Ghaffar S, Jahanzat M, Albar A, Mujaddedi N, Swash R. The influence of nano-additives in strengthening mechanical performance of 3D printed multi-binder geopolymer composites. Constr Build Mater 2020;250:118928. https://doi.org/10.1016/j.conbuildmat.2020.118928.

[92] Chougan M, Ghaffar SH, Sikora P, Chung SY, Rucinska T, Stephan D, et al. Investigation of additive incorporation on rheological, microstructural and mechanical properties of 3D printable alkali-activated materials. Mater Des 2021;202. https://doi.org/10.1016/j.matdes.2021.109574.

[93] Panda B, Singh GB, Unluer C, Tan MJ. Synthesis and characterization of one-part geopolymers for extrusion based 3D concrete printing. J Clean Prod 2019;220:610–9. https://doi.org/10.1016/j.jclepro.2019.02.185.

[94] Abdollahnejad Z, Luukkonen T, Mastali M, Giosue C, Favoni O, Ruello ML, et al. Microstructural Analysis and Strength Development of One-Part Alkali-Activated Slag/Ceramic Binders Under Different Curing Regimes. Waste and Biomass Valorization 2020;11:3081–96. https://doi.org/10.1007/s12649-019-00626-9.

[95] Ma G, Yan Y, Zhang M, Sanjayan J. Effect of steel slag on 3D concrete printing of geopolymer with quaternary binders. Ceram Int 2022. https://doi.org/10.1016/j.ceramint.2022.05.305.

[96] Panda B, Ruan S, Unluer C, Tan MJ. Investigation of the properties of alkali-activated slag mixes involving the use of nanoclay and nucleation seeds for 3D printing. Compos Part B Eng 2020;186:107826. https://doi.org/10.1016/j.compositesb.2020.107826.

[97] Yang T, Gao X, Zhang J, Zhuang X, Wang H, Zhang Z. Sulphate resistance of one-part geopolymer synthesized by calcium carbide residue-sodium carbonate-activation of slag. Compos Part B 2022;242:110024.

https://doi.org/10.1016/j.compositesb.2022.110024.

[98] Gao X, Yao X, Yang T, Zhou S, Wei H, Zhang Z. Calcium carbide residue as auxiliary activator for one-part sodium carbonate-activated slag cements : compressive strength , phase assemblage and environmental benefits. Constr Build Mater 2021;308:125015. https://doi.org/10.1016/j.conbuildmat.2021.125015.

[99] Yang T, Zhang Z, Zhang F, Gao Y, Wu Q. Chloride and heavy metal binding capacities of hydrotalcite-like phases formed in greener one-part sodium carbonate-activated slag cements. J Clean Prod 2020;253:120047. https://doi.org/10.1016/j.jclepro.2020.120047.

[100] Shi C, Qu B, Provis JL. Recent progress in low-carbon binders. Cem Concr Res 2019;122:227–50. https://doi.org/10.1016/j.cemconres.2019.05.009.

[101] Pangdaeng S, Phoo-ngernkham T, Sata V, Chindaprasirt P. Influence of curing conditions on properties of high calcium fly ash geopolymer containing Portland cement as additive. Mater Des 2014;53:269–74. https://doi.org/10.1016/j.matdes.2013.07.018.

[102] Zhang C, Nerella VN, Krishna A, Wang S, Zhang Y, Mechtcherine V, et al. Mix design concepts for 3D printable concrete: A review. Cem Concr Compos 2021;122:104155. https://doi.org/10.1016/j.cemconcomp.2021.104155.

[103] Lu C, Zhang Z, Shi C, Li N, Jiao D, Yuan Q. Rheology of alkali-activated materials: A review. Cem Concr Compos 2021;121:104061. https://doi.org/10.1016/j.cemconcomp.2021.104061.

[104] Roussel N. A thixotropy model for fresh fluid concretes: Theory, validation and applications. Cem Concr Res 2006;36:1797–806. https://doi.org/10.1016/j.cemconres.2006.05.025.

[105] Rodrigue C, Lecomte-nana L, Adesina A. Influence of mineralogy and activator type on the rheology behaviour and setting time of laterite based geopolymer paste 2022;126. https://doi.org/10.1016/j.cemconcomp.2021.104345.

[106] Kaze CR, Alomayri T, Hasan A, Tome S, Lecomte-Nana GL, Nemaleu JGD, et al. Reaction kinetics and rheological behaviour of meta-halloysite based geopolymer cured at room temperature: Effect of thermal activation on physicochemical and

microstructural properties. Appl Clay Sci 2020;196:105773. https://doi.org/10.1016/j.clay.2020.105773.

[107] Chen M, Yang L, Zheng Y, Huang Y, Li L, Zhao P, et al. Yield stress and thixotropy control of 3D-printed calcium sulfoaluminate cement composites with metakaolin related to structural build-up. Constr Build Mater 2020;252:119090. https://doi.org/10.1016/j.conbuildmat.2020.119090.

[108] Liu C, Wang X, Chen Y, Zhang C, Ma L, Deng Z, et al. Influence of hydroxypropyl methylcellulose and silica fume on stability, rheological properties, and printability of 3D printing foam concrete. Cem Concr Compos 2021;122:104158. https://doi.org/10.1016/j.cemconcomp.2021.104158.

[109] Tang Q, Ma Z, Wu H, Wang W. The utilization of eco-friendly recycled powder from concrete and brick waste in new concrete: A critical review. Cem Concr Compos 2020;114:103807. https://doi.org/10.1016/j.cemconcomp.2020.103807.

[110] Chen M, Liu B, Li L, Cao L, Huang Y, Wang S, et al. Rheological parameters, thixotropy and creep of 3D-printed calcium sulfoaluminate cement composites modified by bentonite. Compos Part B Eng 2020;186:107821. https://doi.org/10.1016/j.compositesb.2020.107821.

[111] Rodrigue C, Adesina A, Alomayri T, Assaedi H, Kamseu E, Chinje U, et al. Characterization , reactivity and rheological behaviour of metakaolin and Meta-halloysite based geopolymer binders. Clean Mater 2021;2:100025. https://doi.org/10.1016/j.clema.2021.100025.

[112] Kaze CR, Adesina A, Lecomte-Nana GL, Alomayri T, Kamseu E, Melo UC. Alkali-activated laterite binders: Influence of silica modulus on setting time, Rheological behaviour and strength development. Clean Eng Technol 2021;4. https://doi.org/10.1016/j.clet.2021.100175.

[113] Mechtcherine V, Bos FP, Perrot A, da Silva WRL, Nerella VN, Fataei S, et al. Extrusion-based additive manufacturing with cement-based materials – Production steps, processes, and their underlying physics: A review. Cem Concr Res 2020;132:106037. https://doi.org/10.1016/j.cemconres.2020.106037.

[114] Alghamdi H, Nair SAO, Neithalath N. Insights into material design, extrusion

rheology, and properties of 3D-printable alkali-activated fly ash-based binders. Mater Des 2019;167:107634. https://doi.org/10.1016/j.matdes.2019.107634.

[115] Xie J, Wang J, Rao R, Wang C, Fang C. Effects of combined usage of GGBS and fly ash on workability and mechanical properties of alkali activated geopolymer concrete with recycled aggregate. Compos Part B Eng 2019;164:179–90. https://doi.org/10.1016/j.compositesb.2018.11.067.

[116] Fang G, Ho WK, Tu W, Zhang M. Workability and mechanical properties of alkali-activated fly ash-slag concrete cured at ambient temperature. Constr Build Mater 2018;172:476–87. https://doi.org/10.1016/j.conbuildmat.2018.04.008.

[117] Dong M, Elchalakani M, Karrech A. Development of high strength one-part geopolymer mortar using sodium metasilicate. Constr Build Mater 2020;236:117611. https://doi.org/10.1016/j.conbuildmat.2019.117611.

[118] Ma C, Zhao B, Guo S, Long G, Xie Y. Properties and characterization of green one-part geopolymer activated by composite activators. J Clean Prod 2019;220:188–99. https://doi.org/10.1016/j.jclepro.2019.02.159.

[119] Sun C, Xiang J, Xu M, He Y, Tong Z, Cui X. 3D extrusion free forming of geopolymer composites: Materials modification and processing optimization. J Clean Prod 2020;258:120986. https://doi.org/10.1016/j.jclepro.2020.120986.

[120] Abdollahnejad Z, Luukkonen T, Mastali M, Kinnunen P, Illikainen M. Development of One-Part Alkali-Activated Ceramic/Slag Binders Containing Recycled Ceramic Aggregates. J Mater Civ Eng 2019;31:1–13. https://doi.org/10.1061/(asce)mt.1943-5533.0002608.

[121] Nuaklong P, Sata V, Chindaprasirt P. Properties of metakaolin-high calcium fly ash geopolymer concrete containing recycled aggregate from crushed concrete specimens. Constr Build Mater 2018;161:365–73. https://doi.org/10.1016/j.conbuildmat.2017.11.152.

[122] Tuyan M, Andiç-Çakir Ö, Ramyar K. Effect of alkali activator concentration and curing condition on strength and microstructure of waste clay brick powder-based geopolymer. Compos Part B Eng 2018;135:242–52. https://doi.org/10.1016/j.compositesb.2017.10.013.

[123] Chen Z, Li Z, Li J, Liu C, Lao C, Fu Y, et al. 3D printing of ceramics: A review. J Eur Ceram Soc 2019;39:661–87. https://doi.org/10.1016/j.jeurceramsoc.2018.11.013.

[124] Panda B, Chandra Paul S, Jen Tan M. Anisotropic mechanical performance of 3D printed fiber reinforced sustainable construction material. Mater Lett 2017;209:146–9. https://doi.org/10.1016/j.matlet.2017.07.123.

[125] Rahul A V., Santhanam M, Meena H, Ghani Z. Mechanical characterization of 3D printable concrete. Constr Build Mater 2019;227:116710. https://doi.org/10.1016/j.conbuildmat.2019.116710.

[126] Guo S, Ma C, Long G, Xie Y. Cleaner one-part geopolymer prepared by introducing fly ash sinking spherical beads: Properties and geopolymerization mechanism. J Clean Prod 2019;219:686–97. https://doi.org/10.1016/j.jclepro.2019.02.116.

[127] Arunothayan AR, Nematollahi B, Ranade R, Bong SH, Sanjayan J. Development of 3D-printable ultra-high performance fiber-reinforced concrete for digital construction. Constr Build Mater 2020;257:119546. https://doi.org/10.1016/j.conbuildmat.2020.119546.

[128] Nerella VN, Hempel S, Mechtcherine V. Effects of layer-interface properties on mechanical performance of concrete elements produced by extrusion-based 3D-printing. Constr Build Mater 2019;205:586–601. https://doi.org/10.1016/j.conbuildmat.2019.01.235.

[129] Chen Y, Jia L, Liu C, Zhang Z, Ma L, Chen C, et al. Mechanical anisotropy evolution of 3D-printed alkali-activated materials with different GGBFS/FA combinations. J Build Eng 2022;50:104126. https://doi.org/10.1016/j.jobe.2022.104126.

[130] Xiao J, Liu H, Ding T. Finite element analysis on the anisotropic behavior of 3D printed concrete under compression and flexure. Addit Manuf 2021;39:101712. https://doi.org/10.1016/j.addma.2020.101712.

[131] Ding T, Xiao J, Zou S, Yu J. Flexural properties of 3D printed fibre-reinforced concrete with recycled sand. Constr Build Mater 2021;288:123077. https://doi.org/10.1016/j.conbuildmat.2021.123077.

[132] Batikha M, Jotangia R, Baaj MY, Mousleh I. 3D concrete printing for sustainable and economical construction: A comparative study. Autom Constr 2022;134:104087.

https://doi.org/10.1016/j.autcon.2021.104087.

[133] García de Soto B, Agustí-Juan I, Hunhevicz J, Joss S, Graser K, Habert G, et al. Productivity of digital fabrication in construction: Cost and time analysis of a robotically built wall. Autom Constr 2018;92:297–311. https://doi.org/10.1016/j.autcon.2018.04.004.

[134] Panda B, Paul SC, Hui LJ, Tay YWD, Tan MJ. Additive manufacturing of geopolymer for sustainable built environment. J Clean Prod 2017;167:281–8. https://doi.org/10.1016/j.jclepro.2017.08.165.

[135] McLellan BC, Williams RP, Lay J, Van Riessen A, Corder GD. Costs and carbon emissions for geopolymer pastes in comparison to ordinary portland cement. J Clean Prod 2011;19:1080–90. https://doi.org/10.1016/j.jclepro.2011.02.010.

[136] Abbas R, Khereby MA, Ghorab HY, Elkhoshkhany N. Preparation of geopolymer concrete using Egyptian kaolin clay and the study of its environmental effects and economic cost. Clean Technol Environ Policy 2020;22:669–87. https://doi.org/10.1007/s10098-020-01811-4.

[137] Yang KH, Lee KH, Song JK, Gong MH. Properties and sustainability of alkali-activated slag foamed concrete. J Clean Prod 2014;68:226–33. https://doi.org/10.1016/j.jclepro.2013.12.068.

[138] Ma C, Long G, Shi Y, Xie Y. Preparation of cleaner one-part geopolymer by investigating different types of commercial sodium metasilicate in China. J Clean Prod 2018;201:636–47. https://doi.org/10.1016/j.jclepro.2018.08.060.

[139] Habert G, Ouellet-Plamondon C. Recent update on the environmental impact of geopolymers. RILEM Tech Lett 2016;1:17. https://doi.org/10.21809/rilemtechlett.v1.6.

[140] Mohammad M, Masad E, Al-Ghamdi SG. 3D Concrete Printing Sustainability: A Comparative Life Cycle Assessment of Four Construction Method Scenarios. Buildings 2020;10:245. https://doi.org/10.3390/buildings10120245.

[141] Mohan MK, Rahul A V., Van Tittelboom K, De Schutter G. Rheological and pumping behaviour of 3D printable cementitious materials with varying aggregate content. Cem Concr Res 2021;139:106258. https://doi.org/10.1016/j.cemconres.2020.106258.

[142] Yao Y, Hu M, Di Maio F, Cucurachi S. Life cycle assessment of 3D printing geo-

polymer concrete: An ex-ante study. J Ind Ecol 2020;24:116–27. https://doi.org/10.1111/jiec.12930.

[143] Liu S, Lu B, Li H, Pan Z, Jiang J, Qian S. A comparative study on environmental performance of 3D printing and conventional casting of concrete products with industrial wastes. Chemosphere 2022;298. https://doi.org/10.1016/j.chemosphere.2022.134310.

[144] Kwek SY, Awang H, Cheah CB. Influence of liquid-to-solid and alkaline activator (Sodium silicate to sodium hydroxide) ratios on fresh and hardened properties of alkali-activated palm oil fuel ash geopolymer. Materials (Basel) 2021;14. https://doi.org/10.3390/ma14154253.

[145] Turner LK, Collins FG. Carbon dioxide equivalent (CO2-e) emissions: A comparison between geopolymer and OPC cement concrete. Constr Build Mater 2013;43:125–30. https://doi.org/10.1016/j.conbuildmat.2013.01.023.

[146] Petrillo A, Cioffi R, Ferone C, Colangelo F, Borrelli C. Eco-sustainable Geopolymer Concrete Blocks Production Process. Agric Agric Sci Procedia 2016;8:408–18. https://doi.org/10.1016/j.aaspro.2016.02.037.

[147] Paul SC, Tay YWD, Panda B, Tan MJ. Fresh and hardened properties of 3D printable cementitious materials for building and construction. Arch Civ Mech Eng 2018;18:311–9. https://doi.org/10.1016/j.acme.2017.02.008.

[148] CEMBUREAU. Activity Report 2020, CEMBUREAU: The European Association 2020. https://cembureau.eu/media/1sjf4sk4/cembureau-activity-report-2020.pdf (accessed August 1, 2022).

[149] Chen Y, Veer F, Çopuroğlu O. A critical review of 3D concrete printing as a low CO2 concrete approach. Heron 2017;62:167–94.

[150] Chen Y, Veer F, Copuroglu O, Schlangen E. Feasibility of using low CO2 concrete alternatives in extrusion-based 3D concrete printing. vol. 19. Springer International Publishing; 2019. https://doi.org/10.1007/978-3-319-99519-9_25.

[151] Antoni M, Rossen J, Martirena F, Scrivener K. Cement substitution by a combination of metakaolin and limestone. Cem Concr Res 2012;42:1579–89. https://doi.org/10.1016/j.cemconres.2012.09.006.

[152] Avet F, Snellings R, Alujas A, Ben M, Scrivener K. Development of a new rapid , relevant and reliable (R3) test method to evaluate the pozzolanic reactivity of calcined kaolinitic clays. Cem Concr Res 2016;85:1–11. https://doi.org/10.1016/j.cemconres.2016.02.015.

[153] Avet F, Scrivener K. Investigation of the calcined kaolinite content on the hydration of Limestone Calcined Clay Cement (LC3). Cem Concr Res 2018;107:124–35. https://doi.org/10.1016/j.cemconres.2018.02.016.

[154] Avet F, Boehm-Courjault E, Scrivener K. Investigation of C-A-S-H composition, morphology and density in Limestone Calcined Clay Cement (LC3). Cem Concr Res 2019;115:70–9. https://doi.org/10.1016/j.cemconres.2018.10.011.

[155] Patil SS, Jadhav VS, Nalavade SS, Maske MM. Limestone Calcined Clay Cement as A Green Construction Material. ASEAN J Sci Eng 2021;2:157–66. https://doi.org/10.17509/ajse.v2i2.37977.

[156] Tregger NA, Pakula ME, Shah SP. Influence of clays on the rheology of cement pastes. Cem Concr Res 2010;40:384–91. https://doi.org/10.1016/j.cemconres.2009.11.001.

[157] Ronald T, Hou P, Kawashima S, Sui T. The role of limestone and calcined clay on the rheological properties of LC3. Cem Concr Compos 2020;107:103516. https://doi.org/10.1016/j.cemconcomp.2020.103516.

[158] Fernandez R, Martirena F, Scrivener KL. The origin of the pozzolanic activity of calcined clay minerals: A comparison between kaolinite, illite and montmorillonite. Cem Concr Res 2011;41:113–22. https://doi.org/10.1016/j.cemconres.2010.09.013.

[159] Samet B. Use of a kaolinitic clay as a pozzolanic material for cements : Formulation of blended cement 2007;29:741–9. https://doi.org/10.1016/j.cemconcomp.2007.04.012.

[160] Vizcayno C, Gutiérrez RM De, Castello R, Rodriguez E, Guerrero CE. Pozzolan obtained by mechanochemical and thermal treatments of kaolin. Appl Clay Sci 2010;49:405–13. https://doi.org/10.1016/j.clay.2009.09.008.

[161] Kloprogge JT, Frost RL. Mechanochemical Treatment of Kaolinite. J Colloid Interface Sci 2001;466:458–66. https://doi.org/10.1006/jcis.2001.7591.

[162] Amin NU, Alam S, Gul S, Muhammad K. Activation of clay in cement mortar

applying mechanical, chemical and thermal techniques. Adv Cem Res 2012;24:319–24. https://doi.org/10.1680/adcr.11.00020.

[163] Muzenda TR, Hou P, Kawashima S, Sui T, Cheng X. The role of limestone and calcined clay on the rheological properties of LC3. Cem Concr Compos 2020;107:103516. https://doi.org/10.1016/j.cemconcomp.2020.103516.

[164] He C, Makovicky E, Osbæck B. Thermal stability and pozzolanic activity of raw and calcined mixed-layer mica/smectite. Appl Clay Sci 2000;17:141–61. https://doi.org/10.1016/S0169-1317(00)00011-9.

[165] Avet F, Scrivener K. Simple and Reliable Quantification of Kaolinite in Clay Using an Oven and a Balance BT - Calcined Clays for Sustainable Concrete. In: Bishnoi S, editor., Singapore: Springer Singapore; 2020, p. 147–56.

[166] Chen Y, Jansen K, Zhang H, Romero Rodriguez C, Gan Y, Çopuroğlu O, et al. Effect of printing parameters on interlayer bond strength of 3D printed limestone-calcined clay-based cementitious materials: An experimental and numerical study. Constr Build Mater 2020;262. https://doi.org/10.1016/j.conbuildmat.2020.120094.

[167] Ferreiro S, Canut MMC, Lund J, Herfort D, A CHS, S APA. Influence of fineness of raw clay and calcination temperature on the performance of calcined clay-limestone blended cements. Appl Clay Sci 2019;169:81–90. https://doi.org/10.1016/j.clay.2018.12.021.

[168] Ferreiro S, Herfort D, Damtoft JS. Effect of raw clay type , fi neness , water-to-cement ratio and fly ash addition on workability and strength performance of calcined clay – Limestone Portland cements. Cem Concr Res 2017;101:1–12. https://doi.org/10.1016/j.cemconres.2017.08.003.

[169] Skibsted J, Snellings R. Reactivity of supplementary cementitious materials (SCMs) in cement blends. Cem Concr Res 2019;124:105799. https://doi.org/10.1016/j.cemconres.2019.105799.

[170] Chen, Li, Chaves Figueiredo, Çopuroğlu, Veer, Schlangen. Limestone and Calcined Clay-Based Sustainable Cementitious Materials for 3D Concrete Printing: A Fundamental Study of Extrudability and Early-Age Strength Development. Appl Sci 2019;9:1809. https://doi.org/10.3390/app9091809.

[171] Tironi A, Ph D, Scian AN, Ph D, Irassar EF, Eng C. Blended Cements with Limestone Filler and Kaolinitic Calcined Clay : Filler and Pozzolanic Effects 2017;29:1–8. https://doi.org/10.1061/(ASCE)MT.1943-5533.0001965.

[172] Dhandapani Y, Sakthivel T, Santhanam M, Gettu R, Pillai RG. Mechanical properties and durability performance of concretes with Limestone Calcined Clay Cement (LC3). Cem Concr Res 2018;107:136–51. https://doi.org/10.1016/j.cemconres.2018.02.005.

[173] Huang W, Kazemi-kamyab H, Sun W, Scrivener K. Effect of replacement of silica fume with calcined clay on the hydration and microstructural development of eco-UHPFRC. Mater Des 2017;121:36–46. https://doi.org/10.1016/j.matdes.2017.02.052.

[174] Dhandapani Y, Santhanam M. Assessment of pore structure evolution in the limestone calcined clay cementitious system and its implications for performance. Cem Concr Compos 2017;84:36–47. https://doi.org/10.1016/j.cemconcomp.2017.08.012.

[175] Tironi A, Trezza MA, Scian AN, Irassar EF. Potential use of Argentine kaolinitic clays as pozzolanic material. Appl Clay Sci 2014;101:468–76. https://doi.org/10.1016/j.clay.2014.09.009.

[176] Minard H, Garrault S, Regnaud L, Nonat A. Mechanisms and parameters controlling the tricalcium aluminate reactivity in the presence of gypsum. Cem Concr Res 2007;37:1418–26. https://doi.org/10.1016/j.cemconres.2007.06.001.

[177] Hay R, Li L, Celik K. Shrinkage , hydration , and strength development of limestone calcined clay cement (LC 3) with different sulfation levels. Cem Concr Compos 2022;127:104403. https://doi.org/10.1016/j.cemconcomp.2021.104403.

[178] Briki Y, Avet F, Zajac M, Bowen P, Haha M Ben, Scrivener K. Understanding of the factors slowing down metakaolin reaction in limestone calcined clay cement (LC3) at late ages. Cem Concr Res 2021;146:106477. https://doi.org/10.1016/j.cemconres.2021.106477.

[179] Mishra G, Emmanuel AC, Bishnoi S. Influence of temperature on hydration and microstructure properties of limestone-calcined clay blended cement. Mater Struct 2019;52:1–13. https://doi.org/10.1617/s11527-019-1390-5.

[180] Bonavetti VL, Rahhal VF, Irassar EF. Studies on the carboaluminate formation in limestone filler-blended cements 2001;31.

[181] Krishnan S, Singh A, Bishnoi S. Impact of Alkali Salts on the Hydration of Ordinary Portland Cement and Limestone – Calcined Clay Cement 2021;33:1–13. https://doi.org/10.1061/(ASCE)MT.1943-5533.0003861.

[182] Chen Y, He S, Zhang Y, Wan Z, Schlangen E, Çopuroğlu O. 3D printing of calcined clay-limestone-based cementitious materials. Cem Concr Res 2021;149. https://doi.org/10.1016/j.cemconres.2021.106553.

[183] Shah V, Medepalli S, Krishnan S, Parashar A, Bishnoi S, Mishra G. Influence of cement replacement by limestone calcined clay pozzolan on the engineering properties of mortar and concrete. Adv Cem Res 2020;32:101–11. https://doi.org/https://doi.org/10.1680/jadcr.18.00073.

[184] Chen Y, Rodriguez CR, Li Z, Chen B, Schlangen E. Effect of different grade levels of calcined clays on fresh and hardened properties of ternary-blended cementitious materials for 3D printing. Cem Concr Compos 2020;114. https://doi.org/10.1016/j.cemconcomp.2020.103708.

[185] Long WJ, Lin C, Tao JL, Ye TH, Fang Y. Printability and particle packing of 3D-printable limestone calcined clay cement composites. Constr Build Mater 2021;282:122647. https://doi.org/10.1016/j.conbuildmat.2021.122647.

[186] Shantanu B, Smrati J, Manu S. Criticality of binder-aggregate interaction for buildability of 3D printed concrete containing limestone calcined clay. Cem Concr Compos 2023;136:104853. https://doi.org/10.1016/j.cemconcomp.2022.104853.

[187] Chen Y, Figueiredo SC, Yalçinkaya Ç, Çopuroğlu O, Veer F, Schlangen E. The effect of viscosity-modifying admixture on the extrudability of limestone and calcined clay-based cementitious material for extrusion-based 3D concrete printing. Materials (Basel) 2019;12:9–12. https://doi.org/10.3390/ma12091374.

[188] Wang Y, Chen M, Zhang T, Zhang M. Hardening properties and microstructure of 3D printed engineered cementitious composites based on limestone calcined clay cement. Cem Concr Compos 2024;152:105641. https://doi.org/10.1016/j.cemconcomp.2024.105641.

[189] Hosseini E, Zakertabrizi M, Habibnejad A, Xu G. A novel method to enhance the interlayer bonding of 3D printing concrete : An experimental and computational

investigation. Cem Concr Compos 2019;99:112–9. https://doi.org/10.1016/j.cemconcomp.2019.03.008.

[190] Lim S, Buswell RA, Le TT, Austin SA, Gibb AGF, Thorpe T. Developments in construction-scale additive manufacturing processes. Autom Constr 2012;21:262–8. https://doi.org/10.1016/j.autcon.2011.06.010.

[191] Kruger J, Zeranka S, Zijl G Van. 3D concrete printing : A lower bound analytical model for buildability performance quantification. Autom Constr 2019;106:102904. https://doi.org/10.1016/j.autcon.2019.102904.

[192] Muzenda TR, Hou P, Kawashima S, Sui T, Cheng X. The role of limestone and calcined clay on the rheological properties of LC3. Cem Concr Compos 2020;107:103516. https://doi.org/10.1016/j.cemconcomp.2020.103516.

[193] Beigh MAB, Nerella VN, Schröfl C, Mechtcherine V. Studying the Rheological Behavior of Limestone Calcined Clay Cement (LC3) Mixtures in the Context of Extrusion-Based 3D-Printing BT - Calcined Clays for Sustainable Concrete. In: Bishnoi S, editor., Singapore: Springer Singapore; 2020, p. 229–36.

[194] Aramburo C, Pedrajas C, Rahhal V, González M, Talero R. Calcined clays for low carbon cement : Rheological behaviour in fresh Portland cement pastes. Mater Lett 2019;239:24–8. https://doi.org/10.1016/j.matlet.2018.12.050.

[195] Beigh MAB, Nerella VN, Secrieru E, Mechtcherine V. Structural build-up behavior of limestone calcined clay cement (LC^3) pastes in the context of digital concrete construction . n.d.:1–8.

[196] Hou P, Ronald T, Li Q, Chen H, Kawashima S, Sui T, et al. Mechanisms dominating thixotropy in limestone calcined clay cement (LC3). Cem Concr Res 2021;140:106316. https://doi.org/10.1016/j.cemconres.2020.106316.

[197] Kawashima S, Chaouche M, Corr DJ, Shah SP. Rate of thixotropic rebuilding of cement pastes modified with highly purified attapulgite clays. Cem Concr Res 2013;53:112–8. https://doi.org/10.1016/j.cemconres.2013.05.019.

[198] Perrot A, Rangeard D, Pierre A. Structural built-up of cement-based materials used for 3D-printing extrusion techniques. Mater Struct Constr 2016;49:1213–20. https://doi.org/10.1617/s11527-015-0571-0.

[199] Marchon D, Kawashima S, Bessaies-bey H, Mantellato S, Ng S. Hydration and rheology control of concrete for digital fabrication : Potential admixtures and cement chemistry. Cem Concr Res 2018;112:96–110. https://doi.org/10.1016/j.cemconres.2018.05.014.

[200] Matos PR De, Zat T, Moraes M, Andrade S, Tramontin M, Davi E. Effect of the superplasticizer addition time on the fresh properties of 3D printed limestone calcined clay cement (LC3) concrete. Case Stud Constr Mater 2023;19. https://doi.org/10.1016/j.cscm.2023.e02419.

[201] Palacios M, Flatt RJ. Working mechanism of viscosity-modifying admixtures. vol. i. Elsevier Ltd; 2016. https://doi.org/10.1016/B978-0-08-100693-1.00020-5.

[202] Kazemian A, Yuan X, Cochran E, Khoshnevis B. Cementitious materials for construction-scale 3D printing : Laboratory testing of fresh printing mixture. Constr Build Mater 2017;145:639–47. https://doi.org/10.1016/j.conbuildmat.2017.04.015.

[203] Vance K, Kumar A, Sant G, Neithalath N. The rheological properties of ternary binders containing Portland cement , limestone , and metakaolin or fl y ash. Cem Concr Res 2013;52:196–207. https://doi.org/10.1016/j.cemconres.2013.07.007.

[204] Chen JJ, Kwan AKH. Superfine cement for improving packing density , rheology and strength of cement paste. Cem Concr Compos 2012;34:1–10. https://doi.org/10.1016/j.cemconcomp.2011.09.006.

[205] Fung WWS, Kwan AKH. Role of water film thickness in rheology of CSF mortar. Cem Concr Compos 2010;32:255–64. https://doi.org/10.1016/j.cemconcomp.2010.01.005.

[206] Liu H, Sun X, Du H, Lu H, Ma Y, Shen W, et al. Effects and threshold of water film thickness on multi-mineral cement paste. Cem Concr Compos 2020;112:103677. https://doi.org/10.1016/j.cemconcomp.2020.103677.

[207] Li LG, Kwan AKH. Concrete mix design based on water film thickness and paste film thickness. Cem Concr Compos 2013;39:33–42. https://doi.org/10.1016/j.cemconcomp.2013.03.021.

[208] Li LG, Kwan AKH. Mortar design based on water film thickness 2011;25:2381–90. https://doi.org/10.1016/j.conbuildmat.2010.11.038.

[209] Lothenbach B, Scrivener K, Hooton RD. Supplementary cementitious materials. Cem Concr Res 2011;41:1244–56. https://doi.org/10.1016/j.cemconres.2010.12.001.

[210] Ma G, Wang L. A critical review of preparation design and workability measurement of concrete material for largescale 3D printing 2018;12:382–400.

[211] Tay YWD, Heng G, Ting A, Qian Y, Panda B, Tan MJ, et al. Time gap effect on bond strength of 3D-printed concrete Time gap e ff ect on bond strength of 3D-printed concrete 2019;2759. https://doi.org/10.1080/17452759.2018.1500420.

[212] Keita E, Bessaies-bey H, Zuo W, Belin P, Roussel N. Weak bond strength between successive layers in extrusion-based additive manufacturing : measurement and physical origin. Cem Concr Res 2019;123:105787. https://doi.org/10.1016/j.cemconres.2019.105787.

[213] Zhou Y, Gong G, Xi B, Guo M, Xing F, Chen C. Sustainable lightweight engineered cementitious composites using limestone calcined clay cement (LC 3). Compos Part B 2022;243:110183. https://doi.org/10.1016/j.compositesb.2022.110183.

[214] Liu D, Šavija B, Smith GE, Flewitt PEJ, Lowe T. Towards understanding the influence of porosity on mechanical and fracture behaviour of quasi-brittle materials : experiments and modelling 2017:57–72. https://doi.org/10.1007/s10704-017-0181-7.

[215] Maraghechi H, Avet F, Wong H, Kamyab H. Performance of Limestone Calcined Clay Cement (LC3) with various kaolinite contents with respect to chloride transport. Mater Struct 2019;51:1–17. https://doi.org/10.1617/s11527-018-1255-3.

[216] Roussel N, Cussigh F. Distinct-layer casting of SCC : The mechanical consequences of thixotropy 2008;38:624–32. https://doi.org/10.1016/j.cemconres.2007.09.023.

[217] Zareiyan B, Khoshnevis B. Effects of interlocking on interlayer adhesion and strength of structures in 3D printing of concrete. Autom Constr 2017;83:212–21. https://doi.org/10.1016/j.autcon.2017.08.019.

[218] Wolfs RJM, Bos FP, Salet TAM. Hardened properties of 3D printed concrete : The influence of process parameters on interlayer adhesion. Cem Concr Res 2019;119:132–40. https://doi.org/10.1016/j.cemconres.2019.02.017.

[219] Le TT, Austin SA, Lim S, Buswell RA, Law R, Gibb AGF, et al. Hardened properties of high-performance printing concrete. Cem Concr Res 2012;42:558–66.

https://doi.org/10.1016/j.cemconres.2011.12.003.

[220] Putten J Van Der, Schutter G De, Tittelboom K Van. Surface modification as a technique to improve inter - layer bonding strength in 3D printed cementitious materials 2019:1–6.

[221] Ibrahim KA, van Zijl GPAG, Babafemi AJ. Influence of limestone calcined clay cement on properties of 3D printed concrete for sustainable construction. J Build Eng 2023;69:106186. https://doi.org/10.1016/j.jobe.2023.106186.

[222] Matschei T, Lothenbach B, Glasser FP. The role of calcium carbonate in cement hydration 2007;37:551–8. https://doi.org/10.1016/j.cemconres.2006.10.013.

[223] Elgalhud AA, Dhir RK, Ghataora G. Limestone addition effects on concrete porosity. Cem Concr Compos 2016;72:222–34. https://doi.org/10.1016/j.cemconcomp.2016.06.006.

[224] Figueiredo SC, Çopuroğlu O, Schlangen E. Effect of viscosity modifier admixture on Portland cement paste hydration and microstructure. Constr Build Mater 2019;212:818–40. https://doi.org/10.1016/j.conbuildmat.2019.04.020.

[225] Sánchez-Berriel S, Favier A, Rosa-Domínguez E, Sánchez-Machado IR, Heierli U, Scrivener KL, et al. Assessing the environmental and economic potential of Limestone Calcined Clay Cement in Cuba. J Clean Prod 2016;124:361–9. https://doi.org/10.1016/j.jclepro.2016.02.125.

[226] Yao ZT, Ji XS, Sarker PK, Tang JH, Ge LQ, Xia MS, et al. Earth-Science Reviews A comprehensive review on the applications of coal fl y ash 2015;141:105–21. https://doi.org/10.1016/j.earscirev.2014.11.016.

[227] Hemalatha T, Ramaswamy A. A review on fly ash characteristics e Towards promoting high volume utilization in developing sustainable concrete. J Clean Prod 2017;147:546–59. https://doi.org/10.1016/j.jclepro.2017.01.114.

[228] Siddique R. Utilisation of silica fume in concrete : Review of hardened properties. "Resources, Conserv Recycl 2011;55:923–32. https://doi.org/10.1016/j.resconrec.2011.06.012.

[229] Wang D, Shi C, Farzadnia N, Shi Z, Jia H, Ou Z. A review on use of limestone powder in cement-based materials : Mechanism , hydration and microstructures. Constr Build

Mater 2018;181:659–72. https://doi.org/10.1016/j.conbuildmat.2018.06.075.

[230] Tran YT, Lee J, Kumar P, Kim K, Lee SS. Natural zeolite and its application in concrete composite production. Compos Part B 2019;165:354–64. https://doi.org/10.1016/j.compositesb.2018.12.084.

[231] Li J, Zhang W, Li C, Monteiro PJM. Green concrete containing diatomaceous earth and limestone : Workability , mechanical properties , and life-cycle assessment *. J Clean Prod 2019;223:662–79. https://doi.org/10.1016/j.jclepro.2019.03.077.

[232] Gettu R, Patel A, Rathi V, Prakasan S, Basavaraj AS, Palaniappan S, et al. Influence of supplementary cementitious materials on the sustainability parameters of cements and concretes in the Indian context. Mater Struct 2019;52:1–11. https://doi.org/10.1617/s11527-019-1321-5.

[233] Salvi C, Rubens M, Danieli S, Gonçalves V, Paula A. Environmental and technical assessment to support sustainable strategies for limestone calcined clay cement production in Brazil. Constr Build Mater 2021;310:125261. https://doi.org/10.1016/j.conbuildmat.2021.125261.

[234] Cancio Y, Heierli U, Favier AR, Machado RS, Scrivener KL, Fernando J, et al. Limestone calcined clay cement as a low-carbon solution to meet expanding cement demand in emerging economies 2017;2:82–91. https://doi.org/10.1016/j.deveng.2017.06.001.

[235] Pillai RG, Gettu R, Santhanam M, Rengaraju S, Dhandapani Y, Rathnarajan S, et al. Service life and life cycle assessment of reinforced concrete systems with limestone calcined clay cement (LC3). Cem Concr Res 2019;118:111–9. https://doi.org/10.1016/j.cemconres.2018.11.019.

[236] Ghaffar SH, Corker J, Fan M. Additive manufacturing technology and its implementation in construction as an eco-innovative solution. Autom Constr 2018;93:1–11. https://doi.org/10.1016/j.autcon.2018.05.005.

[237] Schuldt SJ, Jagoda JA, Hoisington AJ, Delorit JD. A systematic review and analysis of the viability of 3D-printed construction in remote environments. Autom Constr 2021;125. https://doi.org/10.1016/j.autcon.2021.103642.

[238] Diaz YC, Fernando J, Hernandez M. Economic and ecological assessment of Cuban

housing solutions using alternative cement. Sustain. Built Environ., 2016.

[239] Dang J, Zhao J, Hu W, Du Z, Gao D. Properties of mortar with waste clay bricks as fine aggregate. Constr Build Mater 2018;166:898–907. https://doi.org/10.1016/j.conbuildmat.2018.01.109.

[240] Zhang Z, Choy Y, Arulrajah A, Horpibulsuk S. A review of studies on bricks using alternative materials and approaches. Constr Build Mater 2018;188:1101–18. https://doi.org/10.1016/j.conbuildmat.2018.08.152.

[241] Wong CL, Mo KH, Yap SP, Alengaram UJ, Ling TC. Potential use of brick waste as alternate concrete-making materials: A review. J Clean Prod 2018;195:226–39. https://doi.org/10.1016/j.jclepro.2018.05.193.

[242] Arif R, Khitab A, Serkan M, Bilal R, Khan N. Experimental analysis on partial replacement of cement with brick powder in concrete. Case Stud Constr Mater 2021;15:e00749. https://doi.org/10.1016/j.cscm.2021.e00749.

[243] Rovnaník P, Rovnaníková P, Vyšvařil M, Grzeszczyk S, Janowska-Renkas E. Rheological properties and microstructure of binary waste red brick powder/metakaolin geopolymer. Constr Build Mater 2018;188:924–33. https://doi.org/10.1016/j.conbuildmat.2018.08.150.

[244] Bayraktar OY, Citoglu GS, Belgin CM, Cetin S, Cetin M. Investigation of effect of brick dust and silica fume on the properties of portland cement mortar 2019.

[245] Bayraktar OY, Citoglu GS, Belgin CM, Cetin M. INVESTIGATION OF THE MECHANICAL PROPERTIES OF MARBLE DUST AND SILICA FUME SUBSTITUTED PORTLAND CEMENT SAMPLES UNDER HIGH 2019.

[246] Zeng Q, Jike N, Xu C, Yang R, Peng Y, Wang J, et al. Total recycling of low-quality urban-fringe construction and demolition waste towards the development of sustainable cement-free pervious concrete: The proof of concept. J Clean Prod 2022;352:131464. https://doi.org/10.1016/j.jclepro.2022.131464.

[247] Migunthanna J, Rajeev P, Sanjayan J. Investigation of waste clay brick as partial replacement of geopolymer binders for rigid pavement application. Constr Build Mater 2021;305:124787. https://doi.org/10.1016/j.conbuildmat.2021.124787.

[248] BS EN 450-1: Fly ash for concrete - Part 1: Definitions, specifications and conformity

criteria, 2012 n.d.

[249] BS EN 15167-1: Ground granulated blast furnace slag for use in concrete, mortar and grout - Part 1: Definitions, specifications and conformity criteria, 2006, (n.d.). n.d.

[250] Zawrah MF, Gado RA, Feltin N, Ducourtieux S, Devoille L. Recycling and utilization assessment of waste fired clay bricks (Grog) with granulated blast-furnace slag for geopolymer production. Process Saf Environ Prot 2016;103:237–51. https://doi.org/10.1016/j.psep.2016.08.001.

[251] BS EN 12620: Aggregates for concrete 2013.

[252] Nematollahi B, Sanjayan J, Uddin F, Shaikh A. Synthesis of heat and ambient cured one-part geopolymer mixes with different grades of sodium silicate. Ceram Int 2015;41:5696–704. https://doi.org/10.1016/j.ceramint.2014.12.154.

[253] Kong DLY, Sanjayan JG. Effect of elevated temperatures on geopolymer paste , mortar and concrete. Cem Concr Res 2010;40:334–9. https://doi.org/10.1016/j.cemconres.2009.10.017.

[254] BS EN 1015-3: Methods of test for mortar for masonry- Part 3: Determination of consistence of fresh mortar (by flow table), 1999. n.d.

[255] BS EN 196-1: Methods of testing cement - Part 1: Determination of cement, 2016 n.d.

[256] BS 1881-122: Testing concrete - Part 122: Method for determination of water absorption, 2011. n.d.

[257] Wang Y, Cao Y, Zhang P, Ma Y, Zhao T, Wang H, et al. Water absorption and chloride diffusivity of concrete under the coupling effect of uniaxial compressive load and freeze–thaw cycles. Constr Build Mater 2019;209:566–76. https://doi.org/10.1016/j.conbuildmat.2019.03.091.

[258] Li L, Liu W, You Q, Chen M, Zeng Q, Zhou C, et al. Relationships between microstructure and transport properties in mortar containing recycled ceramic powder. J Clean Prod 2020;263. https://doi.org/10.1016/j.jclepro.2020.121384.

[259] Pandey A, Kumar B. Evaluation of water absorption and chloride ion penetration of rice straw ash and microsilica admixed pavement quality concrete. Heliyon 2019;5:e02256. https://doi.org/10.1016/j.heliyon.2019.e02256.

[260] PN-85/B-04500: Construction mortars. Research of physical and strength characteristics. Polish committee for standardization; Warsaw, Poland, 1985. n.d.

[261] Wong CL, Mo KH, Alengaram UJ, Yap SP. Mechanical strength and permeation properties of high calcium fly ash-based geopolymer containing recycled brick powder. J Build Eng 2020;32:101655. https://doi.org/10.1016/j.jobe.2020.101655.

[262] Chindaprasirt P, Chareerat T, Hatanaka S, Cao T. High-Strength Geopolymer Using Fine High-Calcium Fly Ash. J Mater Civ Eng 2011;23:264–70. https://doi.org/10.1061/(asce)mt.1943-5533.0000161.

[263] Álvarez-Ayuso E, Querol X, Plana F, Alastuey A, Moreno N, Izquierdo M, et al. Environmental, physical and structural characterisation of geopolymer matrixes synthesised from coal (co-)combustion fly ashes. J Hazard Mater 2008;154:175–83. https://doi.org/10.1016/j.jhazmat.2007.10.008.

[264] Hwang CL, Yehualaw MD, Vo DH, Huynh TP, Largo A. Performance evaluation of alkali activated mortar containing high volume of waste brick powder blended with ground granulated blast furnace slag cured at ambient temperature. Constr Build Mater 2019;223:657–67. https://doi.org/10.1016/j.conbuildmat.2019.07.062.

[265] Navrátilová E, Rovnaníková P. Pozzolanic properties of brick powders and their effect on the properties of modified lime mortars. Constr Build Mater 2016;120:530–9. https://doi.org/10.1016/j.conbuildmat.2016.05.062.

[266] Pan Z, Sanjayan JG, Collins F. Effect of transient creep on compressive strength of geopolymer concrete for elevated temperature exposure. Cem Concr Res 2014;56:182–9. https://doi.org/10.1016/j.cemconres.2013.11.014.

[267] Wu H, Liang C, Wang C, Ma Z. Properties of green mortar blended with waste concrete-brick powder at various components , replacement ratios and particle sizes. Constr Build Mater 2022;342:128050. https://doi.org/10.1016/j.conbuildmat.2022.128050.

[268] Yusuf MO, Johari MAM, Ahmad ZA, Maslehuddin M. Effects of addition of Al(OH)3 on the strength of alkaline activated ground blast furnace slag-ultrafine palm oil fuel ash (AAGU) based binder. Constr Build Mater 2014;50:361–7. https://doi.org/10.1016/j.conbuildmat.2013.09.054.

[269] Criado M, Fernández-Jiménez A, Palomo A. Alkali activation of fly ash: Effect of the SiO2/Na2O ratio. Part I: FTIR study. Microporous Mesoporous Mater 2007;106:180–91. https://doi.org/10.1016/j.micromeso.2007.02.055.

[270] Xing Z, Beaucour AL, Hebert R, Noumowe A, Ledesert B. Aggregate's influence on thermophysical concrete properties at elevated temperature. Constr Build Mater 2015;95:18–28. https://doi.org/10.1016/j.conbuildmat.2015.07.060.

[271] Donza H, Cabrera O, Irassar EF. High-strength concrete with different fine aggregate. Cem Concr Res 2002;32:1755–61. https://doi.org/10.1016/S0008-8846(02)00860-8.

[272] Siregar APN, Rafiq MI, Mulheron M. Experimental investigation of the effects of aggregate size distribution on the fracture behaviour of high strength concrete. Constr Build Mater 2017;150:252–9. https://doi.org/10.1016/j.conbuildmat.2017.05.142.

[273] Li S, Chen G, Xu Z, Luo X, Gao J. Particle-size effect of recycled clay brick powder on the pore structure of blended cement paste. Constr Build Mater 2022;344:128288. https://doi.org/10.1016/j.conbuildmat.2022.128288.

[274] Farrell MO, Wild S, Sabir BB. Pore size distribution and compressive strength of waste clay brick mortar 2001;23:81–91.

[275] Kumar R, Bhattacharjee B. Study on some factors affecting the results in the use of MIP method in concrete research 2003;33:417–24.

[276] Dong Q, Wan L, Luan C, Wang J, Du P. Effect of Graphene Oxide on Properties of Alkali-Activated Slag. Materials (Basel) 2021;14:1–13.

[277] Ranjbar N, Mehrali M, Mehrali M, Alengaram UJ, Jumaat MZ. Graphene nanoplatelet-fly ash based geopolymer composites. Cem Concr Res 2015;76:222–31. https://doi.org/10.1016/j.cemconres.2015.06.003.

[278] Bellum RR, Muniraj K, Indukuri CSR, Madduru SRC. Investigation on Performance Enhancement of Fly ash-GGBFS Based Graphene Geopolymer Concrete. J Build Eng 2020;32:101659. https://doi.org/10.1016/j.jobe.2020.101659.

[279] Long WJ, Ye TH, Luo QL, Wang Y, Mei L. Reinforcing mechanism of reduced graphene oxide on flexural strength of geopolymers: A synergetic analysis of hydration and chemical composition. Nanomaterials 2019;9. https://doi.org/10.3390/nano9121723.

[280] Li Y, Shen J, Lin H, Lv J, Feng S, Ci J. Properties and environmental assessment of eco-friendly brick powder geopolymer binders with varied alkali dosage. J Build Eng 2022;58:105020. https://doi.org/10.1016/j.jobe.2022.105020.

[281] Zhuang S, Wang Q, Zhang M. Water absorption behaviour of concrete: Novel experimental findings and model characterization. J Build Eng 2022;53:104602. https://doi.org/10.1016/j.jobe.2022.104602.

[282] Du H, Pang SD. Enhancement of barrier properties of cement mortar with graphene nanoplatelet. Cem Concr Res 2015;76:10–9. https://doi.org/10.1016/j.cemconres.2015.05.007.

[283] Chougan M, Marotta E, Lamastra FR, Vivio F, Montesperelli G, Ianniruberto U, et al. High performance cementitious nanocomposites: The effectiveness of nano-Graphite (nG). Constr Build Mater 2020;259:119687. https://doi.org/10.1016/j.conbuildmat.2020.119687.

[284] Indukuri CSR, Nerella R. Enhanced transport properties of graphene oxide based cement composite material. J Build Eng 2021;37. https://doi.org/10.1016/j.jobe.2021.102174.

[285] Fu C, Xie C, Liu J, Wei X, Wu D. A Comparative Study on the Effects of Three Nano-Materials on the Properties of Cement-Based Composites. Materials (Basel) 2020;13.

[286] Wang W, Zhong Z, Kang X, Ma X. Physico-mechanical properties and micromorphological characteristics of graphene oxide reinforced geopolymer foam concrete. J Build Eng 2023;72:106732. https://doi.org/10.1016/j.jobe.2023.106732.

[287] Guo X, Shi H, Wei X. Pore properties , inner chemical environment , and microstructure of nano-modi fi ed CFA-WBP (class C fl y ash-waste brick powder) based geopolymers. Cem Concr Compos 2017;79:53–61. https://doi.org/10.1016/j.cemconcomp.2017.01.007.

[288] Ozcan A. Effect of binder content and recycled concrete aggregate on freeze-thaw and sulfate resistance of GGBFS based geopolymer concretes 2021;301. https://doi.org/10.1016/j.conbuildmat.2021.124246.

[289] Lu Z, Feng Z, Yao D, Li X, Ji H. Freeze-thaw resistance of Ultra-High performance concrete : Dependence on concrete composition. Constr Build Mater

2021;293:123523. https://doi.org/10.1016/j.conbuildmat.2021.123523.

[290] Ebrahimi K, Daiezadeh MJ, Zakertabrizi M, Zahmatkesh F, Habibnejad Korayem A. A review of the impact of micro- and nanoparticles on freeze-thaw durability of hardened concrete: Mechanism perspective. Constr Build Mater 2018;186:1105–13. https://doi.org/10.1016/j.conbuildmat.2018.08.029.

[291] Giannopoulou I, Robert PM, Sakkas KM, Petrou MF, Nicolaides D. High temperature performance of geopolymers based on construction and demolition waste. J Build Eng 2023;72:106575. https://doi.org/10.1016/j.jobe.2023.106575.

[292] Ahmad R, Ibrahim WMW, Abdullah MMAB, Pakawanit P, Vizureanu P, Abdullah AS, et al. Geopolymer-Based Nepheline Ceramics: Effect of Sintering Profile on Morphological Characteristics and Flexural Strength. Crystals 2022;12:1–9. https://doi.org/10.3390/cryst12091313.

[293] He R, Dai N, Wang Z. Thermal and Mechanical Properties of Geopolymers Exposed to High Temperature: A Literature Review. Adv Civ Eng 2020;2020. https://doi.org/10.1155/2020/7532703.

[294] Sun Z, Cui H, An H, Tao D, Xu Y, Zhai J, et al. Synthesis and thermal behavior of geopolymer-type material from waste ceramic. Constr Build Mater 2013;49:281–7. https://doi.org/10.1016/j.conbuildmat.2013.08.063.

[295] Tu W, Fang G, Dong B, Hu Y, Zhang M. Behaviour of alkali-activated fly ash-slag paste at elevated temperatures: An experimental study. Cem Concr Compos 2024;147:105438. https://doi.org/10.1016/j.cemconcomp.2024.105438.

[296] Abd Razak SN, Shafiq N, Hasan Nikbakht E, Mohammed BS, Guillaumat L, Farhan SA. Fire performance of fly-ash-based geopolymer concrete: Effect of burning temperature on mechanical and microstructural properties. Mater Today Proc 2022;66:2665–9. https://doi.org/10.1016/j.matpr.2022.06.491.

[297] Kodur VKR, Phan L. Critical factors governing the fire performance of high strength concrete systems. Fire Saf J 2007;42:482–8. https://doi.org/10.1016/j.firesaf.2006.10.006.

[298] Sarker PK, Kelly S, Yao Z. Effect of fire exposure on cracking, spalling and residual strength of fly ash geopolymer concrete. Mater Des 2014;63:584–92.

https://doi.org/10.1016/j.matdes.2014.06.059.

[299] Luo Y, Li SH, Klima KM, Brouwers HJH, Yu Q. Degradation mechanism of hybrid fly ash / slag based geopolymers exposed to elevated temperatures 2022;151. https://doi.org/10.1016/j.cemconres.2021.106649.

[300] Chan CL, Zhang M. Behaviour of strain hardening geopolymer composites at elevated temperatures. Cem Concr Compos 2022;132:104634. https://doi.org/10.1016/j.cemconcomp.2022.104634.

[301] Rickard WDA, Temuujin J, Riessen A Van. Thermal analysis of geopolymer pastes synthesised from five fly ashes of variable composition. J Non Cryst Solids 2012;358:1830–9. https://doi.org/10.1016/j.jnoncrysol.2012.05.032.

[302] Liang G, Luo L, Yao W. Reusing waste red brick powder as partial mineral precursor in eco-friendly binders: Reaction kinetics, microstructure and life-cycle assessment. Resour Conserv Recycl 2022;185:106523. https://doi.org/10.1016/j.resconrec.2022.106523.

[303] Fořt J, Robert C. Transition to circular economy in the construction industry : Environmental aspects of waste brick recycling scenarios 2020;118:510–20. https://doi.org/10.1016/j.wasman.2020.09.004.

[304] Pacheco J, de Brito J, Chastre C, Evangelista L. Experimental investigation on the variability of the main mechanical properties of concrete produced with coarse recycled concrete aggregates. Constr Build Mater 2019;201:110–20. https://doi.org/10.1016/j.conbuildmat.2018.12.200.

[305] Rodrigues F, Evangelista L, Britoa J De. A new method to determine the density and water absorption of fine recycled aggregates. Mater Res 2013;16:1045–51. https://doi.org/10.1590/S1516-14392013005000074.

[306] BS EN 12350-2: Testing fresh concrete-Part 2: Slump-test, 2009 n.d.

[307] ASTM C1437-01. Standard Test Method for Flow of Hydraulic Cement Mortar. Standard 2001:7–8.

[308] Skibicki S, Jakubowska P, Kaszyńska M, Sibera D, Cendrowski K, Hoffmann M. Early-Age Mechanical Properties of 3D-Printed Mortar with Spent Garnet. Materials. Materials (Basel) 2022;15:1–16.

[309] Panda B, Lim JH, Tan MJ. Mechanical properties and deformation behaviour of early age concrete in the context of digital construction. Compos Part B 2019;165:563–71. https://doi.org/10.1016/j.compositesb.2019.02.040.

[310] Wolfs RJM, Bos FP, Salet TAM. Cement and Concrete Research Early age mechanical behaviour of 3D printed concrete : Numerical modelling and experimental testing. Cem Concr Res 2018;106:103–16. https://doi.org/10.1016/j.cemconres.2018.02.001.

[311] Ding T, Xiao J, Qin F, Duan Z. Mechanical behavior of 3D printed mortar with recycled sand at early ages. Constr Build Mater 2020;248:118654. https://doi.org/10.1016/j.conbuildmat.2020.118654.

[312] Casagrande L, Esposito L, Menna C, Asprone D, Auricchio F. Effect of testing procedures on buildability properties of 3D-printable concrete. Constr Build Mater 2020;245:118286. https://doi.org/10.1016/j.conbuildmat.2020.118286.

[313] BS EN 480: Admixtures for concrete, mortar and grout-Test methods-Part 2: Determination of setting time-2006 n.d.

[314] ASTM C191-08. Standard test method for normal consistency and setting time of hydraulic cement 2008.

[315] Ma G, Li Z, Wang L. Printable properties of cementitious material containing copper tailings for extrusion based 3D printing. Constr Build Mater 2018;162:613–27. https://doi.org/10.1016/j.conbuildmat.2017.12.051.

[316] Bhowmick A, Ghosh S. Effect of synthesizing parameters on workability and compressive strength of Fly ash based Geopolymer mortar. Int J Struct Civ Eng 2012;3:168–77. https://doi.org/10.6088/ijcser.201203013016.

[317] Tran M V., Vu TH, Nguyen THY. Simplified assessment for one-part 3D-printable geopolymer concrete based on slump and slump flow measurements. Case Stud Constr Mater 2023;18:e01889. https://doi.org/10.1016/j.cscm.2023.e01889.

[318] Zhong H, Zhang M. 3D printing geopolymers: A review. Cem Concr Compos 2022;128:104455. https://doi.org/10.1016/j.cemconcomp.2022.104455.

[319] Bong SH, Nematollahi B, Nerella VN, Mechtcherine V. Method of formulating 3D-printable strain-hardening alkali-activated composites for additive construction. Cem

Concr Compos 2022;134:104780. https://doi.org/10.1016/j.cemconcomp.2022.104780.

[320] Kondepudi K, Subramaniam KVL, Nematollahi B, Bong SH, Sanjayan J. Study of particle packing and paste rheology in alkali activated mixtures to meet the rheology demands of 3D Concrete Printing. Cem Concr Compos 2022;131:104581. https://doi.org/10.1016/j.cemconcomp.2022.104581.

[321] Dai X, Tao Y, Van Tittelboom K, De Schutter G. Rheological and mechanical properties of 3D printable alkali-activated slag mixtures with addition of nano clay. Cem Concr Compos 2023;139:104995. https://doi.org/10.1016/j.cemconcomp.2023.104995.

[322] Kondepudi K, Subramaniam KVL. Formulation of alkali-activated fly ash-slag binders for 3D concrete printing. Cem Concr Compos 2021;119. https://doi.org/10.1016/j.cemconcomp.2021.103983.

[323] Jones SZ, Bentz DP, Martys NS, George WL, Thomas A. Rheological control of 3D printable cement paste and mortars. vol. 19. Springer International Publishing; 2019. https://doi.org/10.1007/978-3-319-99519-9_7.

[324] Christen H, Cho S, van Zijl G, de Villiers W. Phase change material infused recycled brick aggregate in 3D printed concrete. Heliyon 2022;8:e11598. https://doi.org/10.1016/j.heliyon.2022.e11598.

[325] Christen H, van Zijl G, de Villiers W. The incorporation of recycled brick aggregate in 3D printed concrete. Clean Mater 2022;4:100090. https://doi.org/10.1016/j.clema.2022.100090.

[326] Panda B, Unluer C, Tan MJ. Extrusion and rheology characterization of geopolymer nanocomposites used in 3D printing. Compos Part B Eng 2019;176:107290. https://doi.org/10.1016/j.compositesb.2019.107290.

[327] Elyamany HE, Abd Elmoaty AEM, Elshaboury AM. Setting time and 7-day strength of geopolymer mortar with various binders. Constr Build Mater 2018;187:974–83. https://doi.org/10.1016/j.conbuildmat.2018.08.025.

[328] BS EN 197-1: Cement - Composition, specifications and conformity criteria for common cements n.d.

[329] American Concrete Institute. Building Code Requirements for Structural Concrete

(ACI 318M-05) and Commentary 2005.

[330] Ma G, Zhang J, Wang L, Li Z, Sun J. Mechanical characterization of 3D printed anisotropic cementitious material by the electromechanical transducer. Smart Mater Struct 2018;27. https://doi.org/10.1088/1361-665X/aac789.

[331] Sikora P, Techman M, Federowicz K, El-Khayatt AM, Saudi HA, Abd Elrahman M, et al. Insight into the microstructural and durability characteristics of 3D printed concrete: Cast versus printed specimens. Case Stud Constr Mater 2022;17:e01320. https://doi.org/10.1016/j.cscm.2022.e01320.

[332] Jiang X, Zhang Y, Xiao R, Polaczyk P, Zhang M, Hu W, et al. A comparative study on geopolymers synthesized by different classes of fly ash after exposure to elevated temperatures. J Clean Prod 2020;270:122500. https://doi.org/10.1016/j.jclepro.2020.122500.

[333] Lo TY, Cui H, Memon SA, Noguchi T. Manufacturing of sintered lightweight aggregate using high-carbon fly ash and its effect on the mechanical properties and microstructure of concrete. J Clean Prod 2016;112:753–62. https://doi.org/10.1016/j.jclepro.2015.07.001.

[334] Al-noaimat YA, Akis T. Influence of Cement Replacement by Calcinated Kaolinitic and Montmorillonite Clays on the Properties of Mortars. Arab J Sci Eng 2023. https://doi.org/10.1007/s13369-023-08041-y.

[335] Du H, Dai S. Value-added utilization of marine clay as cement replacement for sustainable concrete production. J Clean Prod 2018;198:867–73. https://doi.org/10.1016/j.jclepro.2018.07.068.

[336] Yanguatin H, Ramírez JH, Tironi A, Tobón JI. Effect of thermal treatment on pozzolanic activity of excavated waste clays. Constr Build Mater 2019;211:814–23. https://doi.org/10.1016/j.conbuildmat.2019.03.300.

[337] Pereira VM, Baldusco R, Nobre T, Quarcioni VA, Vieira AC, Angulo SC. High activity pozzolan obtained from selection of excavation soils in a Construction and Demolition Waste landfill. J Build Eng 2024;84:108494. https://doi.org/10.1016/j.jobe.2024.108494.

[338] Ayati B, Newport D, Wong H, Cheeseman C. Low-carbon cements : Potential for low-

grade calcined clays to form supplementary cementitious materials. Clean Mater 2022;5:100099. https://doi.org/10.1016/j.clema.2022.100099.

[339] Dhandapani Y, Marsh ATM, Rahmon S, Kanavaris F, Papakosta A, Bernal SA. Suitability of excavated London clay as a supplementary cementitious material: mineralogy and reactivity. Mater Struct Constr 2023;56:1–21. https://doi.org/10.1617/s11527-023-02260-3.

[340] De la Varga I, Castro J, Bentz DP, Zunino F, Weiss J. Evaluating the hydration of high volume fly ash mixtures using chemically inert fillers. Constr Build Mater 2018;161:221–8. https://doi.org/10.1016/j.conbuildmat.2017.11.132.

[341] Mendoza O, Tobón JI. An alternative thermal method for identification of pozzolanic activity in Ca(OH)2/pozzolan pastes. J Therm Anal Calorim 2013;114:589–96. https://doi.org/10.1007/s10973-013-2973-y.

[342] Payá J, Monzó J, Borrachero M V., Velázquez S, Bonilla M. Determination of the pozzolanic activity of fluid catalytic cracking residue. Thermogravimetric analysis studies on FC3R-lime pastes. Cem Concr Res 2003;33:1085–91. https://doi.org/10.1016/S0008-8846(03)00014-0.

[343] Borges PHR, Costa JO, Milestone NB, Lynsdale CJ, Streatfield RE. Carbonation of CH and C-S-H in composite cement pastes containing high amounts of BFS. Cem Concr Res 2010;40:284–92. https://doi.org/10.1016/j.cemconres.2009.10.020.

[344] Borges AL, Soares SM, Freitas TOG, Junior AO, Ferreira EB, Ferreira FGS. Evaluation of the pozzolanic activity of glass powder in three maximum grain sizes. Mater Res 2021;24. https://doi.org/10.1590/1980-5373-MR-2020-0496.

[345] Zhou D, Wang R, Tyrer M, Wong H, Cheeseman C. Sustainable infrastructure development through use of calcined excavated waste clay as a supplementary cementitious material. J Clean Prod 2017;168:1180–92. https://doi.org/10.1016/j.jclepro.2017.09.098.

[346] Zheng D, Liang X, Cui H, Tang W, Liu W, Zhou D. Study of performances and microstructures of mortar with calcined low-grade clay. Constr Build Mater 2022;327:126963. https://doi.org/10.1016/j.conbuildmat.2022.126963.

[347] Madejová J. FTIR techniques in clay mineral studies. Vib Spectrosc 2003;31:1–10.

https://doi.org/10.1016/S0924-2031(02)00065-6.

[348] Nayak PS, Singh BK. Instrumental characterization of clay by FTIR, XRF, BET and, TPD-NH3. Bull Mater Sci 2007;30:235–8.

[349] Kanavaris F, Papakosta A, Zunino F, Pantelidou H, Bernal A, Szanser J, et al. Suitability of excavated London Clay from tunnelling operations as a supplementary cementitious material and expanded clay aggregate n.d.:1–9.

[350] Mehdizadeh H, Jia X, Mo KH, Ling TC. Effect of water-to-cement ratio induced hydration on the accelerated carbonation of cement pastes. Environ Pollut 2021;280:116914. https://doi.org/10.1016/j.envpol.2021.116914.

[351] Bakolas A, Aggelakopoulou E, Moropoulou A. Evaluation of pozzolanic activity and physico-mechanical characteristics in ceramic powder-lime pastes. J Therm Anal Calorim 2008;92:345–51. https://doi.org/10.1007/s10973-007-8858-1.

[352] Go SS, Chung CW, Struble LJ, Lee HC. Pozzolanic activity of Hwangtoh clay. Constr Build Mater 2010;24:2638–45. https://doi.org/10.1016/j.conbuildmat.2010.04.061.

[353] Cao Y, Wang Y, Zhang Z, Ma Y, Wang H. Turning sandstone clay into supplementary cementitious material: activation and pozzolanic reactivity evaluation. Compos Part B Eng 2021;223:109137. https://doi.org/10.1016/j.compositesb.2021.109137.

[354] Li LG, Kwan AKH. Effects of superplasticizer type on packing density , water film thickness and flowability of cementitious paste 2015;86:113–9. https://doi.org/10.1016/j.conbuildmat.2015.03.104.

[355] Kai K, Heng Y, Yingbin W. Effect of chemical structure on dispersity of polycarboxylate superplasticiser in cement paste. Adv Cem Res 2020;32:456–64.

[356] Zeyad AM, Almalki A. Influence of mixing time and superplasticizer dosage on self-consolidating concrete properties. Integr Med Res 2020;9:6101–15. https://doi.org/10.1016/j.jmrt.2020.04.013.

[357] Zunino F, Scrivener K. The influence of the filler effect on the sulfate requirement of blended cements. Cem Concr Res 2019;126:105918. https://doi.org/10.1016/j.cemconres.2019.105918.

[358] Tambara Júnior LUD, dos Santos Lima GT, Silvestro L, Ruviaro AS, Gleize PJP, de

Azevedo ARG. Influence of polycarboxylate superplasticizer and calcium sulfoaluminate cement on the rheology, hydration kinetics, and porosity of Portland cement pastes. J Build Eng 2023;68:106120. https://doi.org/10.1016/j.jobe.2023.106120.

[359] He Y, Zhang X, Shui L, Wang Y, Gu M, Wang X, et al. Effects of PCEs with various carboxylic densities and functional groups on the fluidity and hydration performances of cement paste. Constr Build Mater 2019;202:656–68. https://doi.org/10.1016/j.conbuildmat.2018.12.216.

[360] Kong FR, Pan LS, Wang CM, Zhang D La, Xu N. Effects of polycarboxylate superplasticizers with different molecular structure on the hydration behavior of cement paste. Constr Build Mater 2016;105:545–53. https://doi.org/10.1016/j.conbuildmat.2015.12.178.

[361] Matos PR de, Neto JSA, Sakata RD, Kirchheim AP, Rodríguez ED. Effect of superplasticizer addition time and metakaolin source on the early-age hydration of limestone calcined clay. Mater Struct 2022. https://doi.org/10.1617/s11527-022-02049-w.

[362] Khayat KH, Mikanovic N. Viscosity-enhancing admixtures and the rheology of concrete. Woodhead Publishing Limited; 2012. https://doi.org/10.1533/9780857095282.2.209.

[363] Fellows CM, Doherty WOS. Insights into bridging flocculation. Macromol Symp 2005;231:1–10. https://doi.org/10.1002/masy.200590012.

[364] Palacios M, Flatt RJ, Puertas F, Sanchez-Herencia A. Compatibility between polycarboxylate and viscosity-modifying admixtures in cement pastes. Am Concr Institute, ACI Spec Publ 2012:29–42. https://doi.org/10.14359/51684218.

[365] Ma B, Peng Y, Tan H, Jian S, Zhi Z, Guo Y, et al. Effect of hydroxypropyl-methyl cellulose ether on rheology of cement paste plasticized by polycarboxylate superplasticizer. Constr Build Mater 2018;160:341–50. https://doi.org/10.1016/j.conbuildmat.2017.11.010.

[366] Pourchez J, Peschard A, Grosseau P, Guyonnet R, Guilhot B, Valle F. HPMC and HEMC influence on cement hydration 2006;36:288–94.

https://doi.org/10.1016/j.cemconres.2005.08.003.

[367] Pourchez J, Grosseau P, Ruot B. Changes in C3S hydration in the presence of cellulose ethers. Cem Concr Res 2010;40:179–88. https://doi.org/10.1016/j.cemconres.2009.10.008.

[368] Van Der Putten J, Deprez M, Cnudde V, De Schutter G, Van Tittelboom K. Microstructural characterization of 3D printed cementitious materials. Materials (Basel) 2019;12. https://doi.org/10.3390/ma12182993.

[369] Huang Q, Zhu X, Xiong G, Wang C, Liu D, Zhao L. Recycling of crushed waste clay brick as aggregates in cement mortars: An approach from macro- and micro-scale investigation. Constr Build Mater 2021;274:122068. https://doi.org/10.1016/j.conbuildmat.2020.122068.

[370] Bektas F, Wang K, Ceylan H. Effects of crushed clay brick aggregate on mortar durability. Constr Build Mater 2009;23:1909–14. https://doi.org/10.1016/j.conbuildmat.2008.09.006.

[371] Cachim PB. Mechanical properties of brick aggregate concrete. Constr Build Mater 2009;23:1292–7. https://doi.org/10.1016/j.conbuildmat.2008.07.023.

[372] Zhang S, He P, Niu L. Mechanical properties and permeability of fiber-reinforced concrete with recycled aggregate made from waste clay brick. J Clean Prod 2020;268:121690. https://doi.org/10.1016/j.jclepro.2020.121690.

[373] Ge Z, Feng Y, Zhang H, Xiao J, Sun R, Liu X. Use of recycled fine clay brick aggregate as internal curing agent for low water to cement ratio mortar. Constr Build Mater 2020;264:120280. https://doi.org/10.1016/j.conbuildmat.2020.120280.

[374] El-seidy E, Chougan M, Al-noaimat YA, Al-kheetan MJ, Ghaffar H. The impact of waste brick and geo-cement aggregates as sand replacement on the mechanical and durability properties of alkali – activated mortar composites. Results Eng 2024;21:101797. https://doi.org/10.1016/j.rineng.2024.101797.

[375] Dang J, Zhao J, Dai S, Zhao S. Durability and microstructural properties of concrete with recycled brick as fine aggregates. Constr Build Mater 2020;262:120032. https://doi.org/10.1016/j.conbuildmat.2020.120032.

[376] Tavakoli D, Fakharian P, Brito J De. Mechanical properties of roller-compacted

concrete pavement containing recycled brick aggregates and silica fume. ROAD Mater PAVEMENT Des 2022;23:1793–814. https://doi.org/10.1080/14680629.2021.1924236.

[377] Allahverdi A, Mahdi M, Rasht B, Anwar KM, Lachemi M. Cold Regions Science and Technology Resistance of chemically-activated high phosphorous slag content cement against freeze – thaw cycles. Cold Reg Sci Technol 2014;103:107–14. https://doi.org/10.1016/j.coldregions.2014.03.012.

[378] Ji Y, Pei Z, Xu W, Li Z, Li Y, Jia Y. Deterioration performance analysis of recycled brick concrete subjected to freezing and thawing effect. Case Stud Constr Mater 2024;20:e02722. https://doi.org/10.1016/j.cscm.2023.e02722.

[379] Kanagaraj B, Anand N, Samuvel Raj R, Lubloy E. Techno-socio-economic aspects of Portland cement, Geopolymer, and Limestone Calcined Clay Cement (LC3) composite systems: A-State-of-Art-Review. Constr Build Mater 2023;398:132484. https://doi.org/10.1016/j.conbuildmat.2023.132484.

[380] Tay YWD, Qian Y, Tan MJ. Printability region for 3D concrete printing using slump and slump flow test. Compos Part B Eng 2019;174:106968. https://doi.org/10.1016/j.compositesb.2019.106968.

[381] Bessaies-bey H, Khayat KH, Palacios M, Schmidt W, Roussel N. Viscosity modifying agents : Key components of advanced cement-based materials with adapted rheology. Cem Concr Res 2022;152:106646. https://doi.org/10.1016/j.cemconres.2021.106646.

[382] Ge Z, Feng Y, Yuan H, Zhang H, Sun R, Wang Z. Durability and shrinkage performance of self-compacting concrete containing recycled fine clay brick aggregate. Constr Build Mater 2021;308:125041. https://doi.org/10.1016/j.conbuildmat.2021.125041.